VOLUME 80 JANUARY 15, 1976 NUMBER 2

JPCHAx

THE JOURNAL OF PHYSICAL CHEMISTRY

PUBLISHED BIWEEKLY BY THE AMERICAN CHEMICAL SOCIETY

THE JOURNAL OF

PHYSICAL CHEMISTRY

Published by the
AMERICAN CHEMICAL SOCIETY
BOOKS AND JOURNALS DIVISION
D. H. Michael Bowen, Director

Editorial Department: Charles R. Bertsch, Head; Marianne C. Brogan, Associate Head; Celia B. McFarland, Joseph E. Yurvati, Assistant Editors
Graphics and Production Department: Bacil Guiley, Head
Research and Development Department: Seldon W. Terrant, Head

Advertising Office: Centcom, Ltd., 50 W. State St., Westport, Conn. 06880.

Published biweekly by the American Chemical Society at 20th and Northampton Sts., Easton, Pennsylvania 18042. Second class postage paid at Washington, D.C. and at additional mailing offices.

Editorial Information

Instructions for authors are printed in the first issue of each volume. Please conform to these instructions when submitting manuscripts.

Manuscripts for publication should be submitted to *The Journal of Physical Chemistry*, Department of Chemistry, University of Minnesota, Minneapolis, Minn. 55455. Correspondence regarding accepted papers and proofs should be directed to the Editorial Department at the ACS Easton address.

Page charges of $60.00 per page are assessed for papers published in this journal. Ability to pay does not affect acceptance or scheduling of papers.

Bulk reprints or photocopies of individual articles are available. For information write to Business Operations, Books and Journals Division at the ACS Washington address.

Requests for **permission to reprint** should be directed to Permissions, Books and Journals Division at the ACS Washington address. The American Chemical Society and its Editors assume no responsibility for the statements and opinions advanced by contributors.

Subscription and Business Information

1976 Subscription rates—including surface postage

	U.S.	PUAS	Canada, Foreign
Member	$24.00	$29.75	$30.25
Nonmember	96.00	101.75	102.25
Supplementary material	15.00	19.00	20.00

Air mail and air freight rates are available from Membership & Subscription Services, at the ACS Columbus address.

New and renewal subscriptions should be sent with payment to the Office of the Controller at the ACS Washington address. **Changes of address** must include both old and new addresses with ZIP code and a recent mailing label. Send all address changes to the ACS Columbus address. Please allow six weeks for change to become effective. **Claims** for missing numbers will not be allowed if loss was due to failure of notice of change of address to be received in the time specified; if claim is dated (a) North America—more than 90 days beyond issue date, (b) all other foreign—more than 1 year beyond issue date; or if the reason given is "missing from files". Hard copy claims are handled at the ACS Columbus address.

Microfiche subscriptions are available at the same rates but are mailed first class to U.S. subscribers, air mail to the rest of the world. Direct all inquiries to Business Operations, Books and Journals Division, at the ACS Washington address or call (202) 872-4444. **Single issues** in hard copy and/or microfiche are available from Special Issues Sales at the ACS Washington address. Current year $4.75. Back issue rates available from Special Issues Sales. **Back volumes** are available in hard copy and/or microform. Write to Special Issues Sales at the ACS Washington address for further information. **Microfilm** editions of ACS periodical publications are available from volume 1 to the present. For further information, contact Special Issues Sales at the ACS Washington address. **Supplementary material** must be ordered directly from Business Operations, Books and Journals Division, at the ACS Washington address.

	U.S.	PUAS, Canada	Other Foreign
Microfiche	$2.50	$3.00	$3.50
Photocopy			
1-7 pages	4.00	5.50	7.00
8-20 pages	5.00	6.50	8.00

Orders over 20 pages are available only on microfiche, 4 × 6 in., 24X, negative, silver halide. Orders must state photocopy or microfiche if both are available. Full bibliographic citation including names of all authors and prepayment are required. Prices are subject to change.

American Chemical Society
1155 16th Street, N.W.
Washington, D.C. 20036
(202) 872-4600

Member & Subscription Services
American Chemical Society
P.O. Box 3337
Columbus, Ohio 43210
(314) 421-7230

Editorial Department
American Chemical Society
20th and Northampton Sts.
Easton, Pennsylvania 18042
(215) 258-9111

Notice to Authors last printed in the issue of January 1, 1976

THE JOURNAL OF

PHYSICAL CHEMISTRY

Volume 80, Number 2 January 15, 1976

JPCHAx 80(2) 91-216 (1976)

ISSN 0022-3654

COMMUNICATIONS TO THE EDITOR

■ Supplementary material for this paper is available separately (consult the masthead page for ordering information); it will also appear following the paper in the microfilm edition of this journal.

* In papers with more than one author, the asterisk indicates the name of the author to whom inquiries about the paper should be addressed.

AUTHOR INDEX

THE JOURNAL OF
PHYSICAL CHEMISTRY

VOLUME 80, NUMBER 2 JANUARY 15, 1976

Collisional Quenching of Electronically Excited Tin Atoms, Sn($5p^2\ ^3P_1$) and Sn($5p^2\ ^3P_2$), by Time-Resolved Attenuation of Atomic Resonance Radiation

P. D. Foo, J. R. Wiesenfeld,* M. J. Yuen,

Department of Chemistry, Cornell University, Ithaca, New York 14853

and D. Husain

The Department of Physical Chemistry, The University of Cambridge, Cambridge CB2 1EP, England *(Received September 15, 1975)*

Publication costs assisted by the Petroleum Research Fund

An investigation of the collisional behavior of the gaseous tin atom in the $5p^2(^3P_1)$ and $5p^2(^3P_2)$ spin–orbit states, 0.210 and 0.425 eV above the $5p^2(^3P_0)$ electronic ground state, respectively, has been carried out. The transient, optically metastable atoms were generated by the pulsed irradiation of $SnMe_4$ and monitored photoelectrically in absorption by the time-resolved attenuation of atomic resonance radiation derived from a microwave-powered sealed discharge. Modification of the lifetime of the two spin–orbit states by added quenching gases has been studied in detail and has led to absolute rate constants (k_Q) at 300 K for collisional quenching of both the $^3P_1$ and $^3P_2$ states by the gases Ar, Kr, Xe, H_2, D_2, HD, N_2, O_2, CO, NO, CO_2, CH_4, CF_3H, CF_4, C_2H_4, C_2D_4, C_2H_2, C_2D_2, and $SnMe_4$. The results are compared with the analogous data for the low-lying spin–orbit states of the lead atom, $Pb(6p^2(^3P_{1,2}))$. Discussion of quenching by the noble gases is principally in terms of the Hund's coupling case (c) components arising from the interaction on collision; detailed consideration is given to quenching by the hydrogen isotopes especially in terms of the effects of long-range quadrupole–quadrupole coupling and selection rules for rotation for near-resonance transfer processes on collision; diatomic molecules in general are discussed in terms of correlation diagrams based on (J,Ω) coupling and the effects of E → V,R transfer; quenching by polyatomic molecules is briefly considered, principally in terms of the interaction on collision and the observation of an approximate trend of k_Q with the ionization potential for the larger molecules.

Introduction

While there has been some recent development in direct measurements of the collisional behavior of heavy atoms in electronically excited states, many of the results have been dealt with on an individual basis, with little reference being made to a unified treatment for considering the relationship between electronic structure and atomic reactivity.[1-3] The fundamental reason for this is that the most widely used general structure for discussing atomic reactivity in excited states has been based on correlations between initial and final states derived from the weak spin–orbit coupling approximation.[4-6] With the main exception of recent work by Callear and McGurk,[7] who have considered in a detailed manner the nature of the molecular orbitals involved in the collision complex, this hitherto prevailing attitude toward heavy atom chemistry applied even to the vast body of data, for example, on quenching of electronically excited mercury atoms.[8] Indeed, the now large number of absolute rate measurements on various highly energized spin–orbit states arising out of the electronic ground state configuration, such as $I(5p^5\ ^2P_{1/2})$ (0.943 eV),[3,9-11] $Tl(6p\ ^2P_{3/2})$ (0.966 eV),[12-14] $Te(5p^4\ ^3P_{0,1})$ (0.584 and 0.589 eV, respectively),[15] and $Br(4p^5\ ^2P_{1/2})$ (0.457 eV)[3,16,17] also fell outside this general structure, which, by definition, must omit the effects of J splittings.

Very recently, Brown and Husain[18] have shown that (J, Ω) coupling, presented in general form for heavy atom–molecule collisions by Husain,[19] provides the best framework within which to consider the chemistry of the $np^2\ ^1S_0$ and $^1D_2$ states of atomic tin[18,20] and lead.[20,22] Similarly, we have shown in a preliminary investigation[23] that the low-lying spin–orbit states of the tin atom, Sn($5p^2\ ^3P_1$) and Sn($5p^2\ ^3P_2$), respectively, 0.210 and 0.425 eV above the

$5p^2\,^3P_0$ ground state,[24] and also those of $Pb(6p^2\,^3P_{1,2})$,[25] can be best discussed within the same context. This present paper describes detailed and extensive absolute rate measurements for the collisional quenching of the 5^3P_1 and 5^3P_2 states of the tin atom. The resulting data for deactivation by small molecules are compared with those for $Pb(6^3P_{1,2})$ and are discussed within the (J, Ω) framework, the nature of the interaction on collision with polyatomic molecules also being taken into account. The overall objective of this present work should be viewed within a broader program of seeking a general fundamental structure for considering the reactions of both light and heavy atoms. One may also stress, in the present context, current interest in electronic transition atomic lasers and especially visible chemical lasers arising from heavy atom–molecule collisions.[26-29]

Experimental Section

The general nature of the experimental arrangement has been given hitherto for the kinetic study of $Tl(6^2P_{3/2})$[13,14] and briefly referred to in our preliminary communication.[23] We will here limit consideration to the salient features of the system and a few aspects not discussed previously. The basis of the method is to generate $Sn(5^3P_1)$ and $Sn(5^3P_2)$ by the pulsed irradiation (E = 400 J) of low pressures of $SnMe_4$ (1.5–3.5 × 10^{-4} Torr) in the presence of excess argon buffer gas (p_{Ar}:p_{SnMe_4} = ca. 100 000:1) in order to prevent any significant rise above ambient temperature on photolysis. Einstein coefficients, both magnetic dipole and electric quadrupole for spontaneous emission from these spin–orbit states, have been calculated by Garstang[30] and indicate quantitatively the high optical metastability of these species. Thus they can be readily monitored photoelectrically in absorption by time-resolved attenuation of the following two resonance transitions:

Transition	λ, nm	10^{-8}gA, sec^{-1} [31]	γ [23]
$6s(^3P_2^0) \rightarrow 5p^2(^3P_1)$	270.65	10.0	0.77 ± 0.04
$6s(^3P_2^0) \rightarrow 5p^2(^3P_2)$	284.00	21.0	0.67 ± 0.09

These were derived from a microwave-powered (incident power = ca. 10 W) sealed source (E.M.I. electrodeless discharge tube) and optically separated by means of a 0.5-m grating monochromator. The resonance absorption signals were detected by means of a photomultiplier tube (RCA Corp., 1P28) mounted at the exit slit, monitored on an oscilloscope and photographed for subsequent kinetic analysis.

The appropriate plots leading to the above γ values for the conditions employed using the now standard modified Beer–Lambert law[32]

$$I_{tr} = I_0 \exp(-\epsilon(cl)^\gamma) \qquad \text{(i)}$$

(where the symbols have their usual significance[32]) have been given in the preliminary communication.[23] Various aspects of this modified law have been discussed in a number of papers concerned with attenuation of resonance radiation (see references in reviews, ref 1 and 2). Three points merit mention. First, ε in eq i is *not* the standard extinction coefficient but an arbitrary constant, of dimensions $(cl)^{-\gamma}$, in a given set of experiments, depending on the value of γ. We have by custom adopted eq i here but could equally employ the equation

$$I_{tr} = I_0 \exp(-(\epsilon cl)^\gamma) \qquad \text{(ii)}$$

where the new ε would be of the standard dimensions, $(cl)^{-1}$. Secondly, the plots used to determine γ, i.e., the first-order intercepts, ln (ln $(I_0/I_{tr}))_{t=0}$ vs. ln (p_{SnMe_4}) in this instance, simply constitute a device for determining *relative* values of atomic concentrations, using the weak light absorption approximation (by the parent molecule), for decays which are found experimentally to be kinetically first order. Thirdly, Bemand and Clyne[33] have used the better procedure of employing a power series for resonance absorption by $O(2^3P_J)$ where the *absolute* concentrations can be determined by titration techniques. Unfortunately, we have no chemical titration technique for $Sn(5^3P_1)$ and $Sn(5^3P_2)$, analogous to that for the oxygen atom in a discharge flow system, and eq i or ii is, at present, the only convenient route to relative measurements of the concentrations of the excited atoms.

Materials. Ar (Research Grade, Matheson Co.) was used directly. Kr, Xe, H_2, D_2, N_2, O_2, CO, NO, CO_2, CH_4, CF_3H, CF_4, C_2H_4, C_2H_2, and $SnMe_4$ were prepared essentially as described in previous publications (ref 18 and references contained therein). HD (Merck and Co., 98% mole purity) was used directly, as was C_2D_2 and C_2D_4 (Merck and Co.).

Results and Discussion

Figure 1 shows typical oscilloscopic traces indicating both time-resolved resonance absorption by $Sn(5^3P_2)$, as an example of the type of raw data obtained in these experiments, and also modification of the lifetime of the transient species by the addition of carbon monoxide. Figure 2 shows first-order kinetic plots derived from the data of Figure 1. Similar sets of data to those presented in Figures 1 and 2 were obtained for the decay of $Sn(5^3P_2)$ and $Sn(5^3P_1)$ in the presence of the various quenching gases. When $SnMe_4$ is flash photolyzed in the Spectrosil region (λ ≳ 165 nm), all of the states, $Sn(5^1D_2)$, $Sn(5^3P_2)$, $Sn(5^3P_1)$, and $Sn(5^3P_0)$, are generated in significantly decreasing yields;[18,34] $Sn(5^1S_0)$ is *not* produced in any significant yield.[18] The present method, however, was not sufficiently sensitive to permit detection of population following relaxation from higher states and the decays for both $Sn(5^3P_2)$ and $Sn(5^3P_1)$ are taken to be first order. The sensible linearity of plots of the type given in Figure 2 for both spin–orbit states in the presence of all the added quenching gases indicates the reasonable nature of the approximation.

The slopes of the first-order plots in individual experiments (e.g., Figure 2) are given by $-\gamma k'$ where k', the overall first-order decay coefficient derived by means of the appropriate value of γ (see earlier), is taken to satisfy the form

$$k' = k_Q[Q] + K \qquad \text{(iii)}$$

and k_Q is the absolute second-order rate constant for collisional removal of the individual spin–orbit state by the added quenching gas, Q. K is taken to be a constant in a given series of kinetic runs in which [Q] is varied. It comprises contributions to the first-order decay from weak spontaneous emission,[30] diffusion, and quenching by the buffer gas, impurities, products of photolysis, and the undissociated parent molecule. In fact, it is the latter that principally governs the magnitude of K in these experiments. Figures 3 and 4 show examples of the variation of $\gamma k'$ for the two spin–orbit states with added quenching gases, including carbon monoxide. The slopes of the plots given in Figures 3 and 4, in conjunction with the appropriate values of γ, yield the absolute values of k_Q for collision-

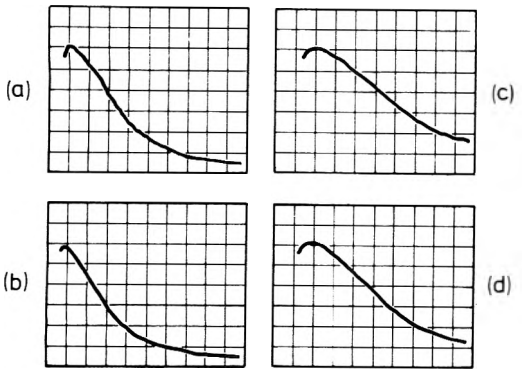

Figure 1. Typical oscilloscopic traces for the decay of $Sn(5^3P_2)$ in the presence of carbon monoxide obtained by attenuation of atomic resonance radiation at λ 284.00 nm. $p_{SnMe_4} = 3.3 \times 10^{-4}$ Torr, p_{total} with Ar = 30 Torr; E = 400 J. (a, b) 100 μsec/division; (c, d) 50 μsec/division 10^3 p_{CO} (Torr): (a) 0.0; (b) 3.2; (c) 7.4; (d) 9.8.

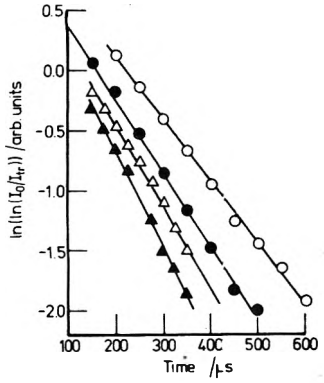

Figure 2. Pseudo-first-order plots for the decay of $Sn(5^3P_2)$ in the presence of different pressures of carbon monoxide. $10^3 p_{CO}$ (Torr): (○) 0.0; (●) 3.2; (△) 7.4; (▲) 9.8.

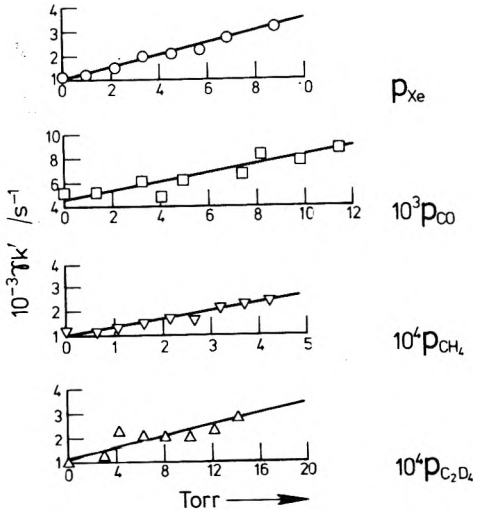

Figure 3. Pseudo-first-order rate coefficients ($\gamma k'$) for the decay of $Sn(5^3P_2)$ in the presence of different quenching gases.

al removal of $Sn(5^3P_2)$ and $Sn(5^3P_1)$. Table I includes all the quenching data for $Sn(5^3P_{1,2})$ obtained in this investigation and the preliminary communication.[23] It constitutes, to the best of our knowledge, the only body of rate data for these two spin–orbit states. Included in Table I are

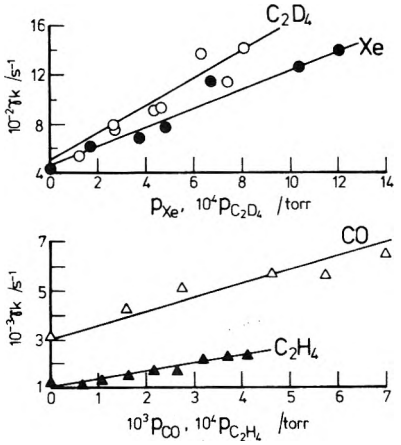

Figure 4. Psuedo-first-order rate coefficients ($\gamma k'$) for the decay of $Sn(5^3P_1)$ in the presence of different quenching gases.

the analogous data for $Pb(6^3P_{1,2})$ obtained by Husain and Littler[35] and subsequently by Ewing et al.[36,37]

Noble Gases. The general behavior for the collisional quenching of $Sn(5^3P_1)$ and $Sn(5^3P_2)$ by the noble gases, Ar, Kr, and Xe, essentially follows that observed hitherto for the analogous states of the lead atom (Table I). First, quenching is relatively inefficient. Secondly, the more energized $^3P_2$ state is deactivated more efficiently than the $^3P_1$ state for a given noble gas deactivator. Thirdly, the deactivation efficiency increases with increasing atomic weight of the noble gas partner. The standard, general principle in such processes must clearly operate, namely, that the transfer of large quantities of electronic energy to translational energy can only occur with any significant probability if the potential curves describing the initial and final states either cross or approach sufficiently closely for quantum mechanical tunneling to become significant. Further, such crossing in a low order to approximation must be accompanied by a mixing following the inclusion of higher order terms in the Hamiltonian in order for a so-called "nonadiabatic transition" (NAT) to take place. If we designate states in Hund's coupling case (c) in the standard manner,[38] then the molecular Ω values clearly indicate the mechanism for relaxation from the $^3P_2$ to the $^3P_1$ level. Thus, for $Sn(^3P_2)$ + noble gas ($^1S_0$), the states arising from $2_g + 0_g$ are 2, 1, and 0^+, while the $Sn(^3P_1)$ noble gas interaction, $1_g + 0_g$, yields 1 and 0^- and $\Delta\Omega = 0$ for $\Omega = 1 \rightarrow 1$. By contrast, no common case (c) components arise from the $^3P_1$ and $^3P_0$ states as the $^3P_0 + {}^1S_0$ interaction corresponding to $0_g + 0_g$ yields only 0^+. Alternatively, designating the states in Hund's cases (a) or (b),[38] we see that $^3P_g + {}^1S_g \rightarrow {}^3\Sigma^- + {}^3\Pi$. On this basis, Ewing et al.[37] have constructed arbitrary repulsive curves for the Pb + noble gas atom interactions, designating $^3P_1$ and $^3P_0$ + noble gas in case (c) at large interatomic distances, merging into a common $^3\Sigma^-$ state at closer internuclear separation. Critical to such a discussion are the regions of crossing, which, as Ewing et al.[36] point out, could be probed by temperature dependent studies. Similar considerations will, of course, apply to the lighter tin atom where the case (a) and (b) designations at close internuclear separations will constitute somewhat better descriptions of the interactions. Further, a partial minimum, estimated by an approximate Lennard-Jones interaction[39] should assist such a mechanism by an acceleration effect. The foregoing discussion may be contrasted with the similar but far more detailed argument for the

TABLE I: Rate Constants (k_Q, cm^3 molecule^{-1} sec^{-1}, 300 K) for the Collisional Removal of the $np^2(^3P_{1,2})$ Spin–Orbit States of Atomic Tin (n = 5) and Lead (n = 6) by Various Gases (M)[a]

M	Sn(5^3P_1) (0.210 eV)	Sn(5^3P_2) (0.425 eV)	Pb(6^3P_1) (0.969 eV)	Pb(6^3P_2) (1.320 eV)
Ar	$<5 \times 10^{-16}$ [b]	$<1 \times 10^{-16}$ [b]	$0 \pm 1.0 \times 10^{-16}$ [c] $<2.3 \times 10^{-16}$ [d]	$2.0 \pm 0.5 \times 10^{-15}$ [c] $<2.0 \times 10^{-15}$ [d]
Kr	$1.1 \pm 0.3 \times 10^{-15}$	$1.6 \pm 0.2 \times 10^{-15}$		
Xe	$3.2 \pm 0.3 \times 10^{-15}$	$1.2 \pm 0.3 \times 10^{-14}$	$<6 \times 10^{-16}$ [d]	2.3×10^{-13} [d]
H_2	$<2 \times 10^{-12}$ [b]	$1.15 \pm 0.3 \times 10^{-12}$ [b]	$2.9 \pm 0.4 \times 10^{-15}$ [c] $<5.7 \times 10^{-15}$ [d,e]	$1 \pm 1 \times 10^{-12}$ [c] 1.5×10^{-13} [d,e]
D_2	$1.09 \pm 0.3 \times 10^{-12}$ [b]	$1.62 \pm 0.5 \times 10^{-11}$ [b]	$<6 \times 10^{-16}$ [c] $<5.5 \times 10^{-15}$ [d,e]	$<10^{-12}$ [c] $<8.7 \times 10^{-12}$ [d,e]
HD	$1.5 \pm 0.4 \times 10^{-12}$	$5.4 \pm 0.8 \times 10^{-12}$		
N_2	$<2.5 \times 10^{-13}$	$<2.9 \times 10^{-13}$	$2.0 \pm 2.0 \times 10^{-15}$ [c] 1.7×10^{-15} [d]	$8.0 \pm 8.0 \times 10^{-15}$ [c] 4.1×10^{-13} [d]
O_2	$8.2 \pm 0.5 \times 10^{-11}$ [b]	$4.91 \pm 0.3 \times 10^{-11}$ [b]	$7.0 \pm 5.0 \times 10^{-12}$ [c] 4.5×10^{-11} [d]	$4.0 \pm 1.0 \times 10^{-11}$ [c] 4.6×10^{-11} [d]
CO	$1.7 \pm 0.2 \times 10^{-12}$	$1.5 \pm 0.2 \times 10^{-11}$	$2.3 \pm 0.7 \times 10^{-12}$ [c]	$4.7 \pm 0.3 \times 10^{-13}$ [c]
NO	$6.7 \pm 1.0 \times 10^{-11}$	$5.9 \pm 0.6 \times 10^{-11}$	$9.1 \pm 1.0 \times 10^{-12}$ [c]	$4.3 \pm 0.9 \times 10^{-11}$ [c]
CO_2	$3.2 \pm 0.2 \times 10^{-13}$	$6.2 \pm 0.6 \times 10^{-12}$	$<10^{-14}$ [c]	$2.2 \pm 0.4 \times 10^{-11}$ [c]
CH_4	$1.5 \pm 0.2 \times 10^{-11}$	$1.4 \pm 0.1 \times 10^{-10}$	$0 \pm 2 \times 10^{-15}$ [c]	$1.6 \pm 0.3 \times 10^{-11}$ [c]
CF_3H	$7.6 \pm 0.5 \times 10^{-12}$	$8.0 \pm 0.9 \times 10^{-12}$		
CF_4	$2.6 \pm 0.2 \times 10^{-12}$	$5.6 \pm 0.9 \times 10^{-12}$	$0 \pm 4 \times 10^{-15}$ [c]	$3 \pm 2 \times 10^{-11}$ [c]
C_2H_4	$5.7 \pm 0.4 \times 10^{-11}$	$1.6 \pm 0.1 \times 10^{-10}$	$8.2 \pm 0.2 \times 10^{-13}$	$2.3 \pm 0.3 \times 10^{-11}$ [c]
C_2D_4	$3.6 \pm 0.7 \times 10^{-11}$	$5.2 \pm 0.8 \times 10^{-11}$		
C_2H_2	$1.4 \pm 0.1 \times 10^{-10}$	$1.5 \pm 0.2 \times 10^{-10}$	$3.5 \pm 0.3 \times 10^{-12}$ [c]	$1.7 \pm 0.2 \times 10^{-11}$ [c]
C_2D_2	$8.1 \pm 0.1 \times 10^{-11}$	$1.5 \pm 0.02 \times 10^{-10}$		
$SnMe_4$	$2.00 \pm 0.05 \times 10^{-10}$ [b]	$3.41 \pm 0.24 \times 10^{-10}$ [b]		

[a] Values not referenced are from this work. [b] Reference 23. [c] Reference 35. [d] Reference 37. [e] Reference 36.

large difference in the Xe quenching rates of $O(2^1D_2)$ and $O(2^1S_0)$ by Donovan, Husain, and Kirsch[40] where sufficient spectroscopic data on XeO[41] permitted semiempirical construction of the appropriate potential energy curves.

H_2, D_2, and HD. There have recently been some particularly significant developments in the quenching of electronically excited atoms by the isotopes of molecular hydrogen, especially with respect to assessing the importance of near-resonance processes involved in E → V, R (electronic → vibrational, rotational) transfer. Our preliminary communication[23] on the rate constants for the collisional quenching of both Sn(5^3P_1) and Sn(5^3P_2) by H_2 and D_2 was clearly confined to a very brief consideration of this topic. The inclusion here of the quenching data for HD for both of these atomic states of tin, a highly pertinent aspect of this problem, further indicates the merit of separate and more complete consideration of this group of collision partners. Indeed, Butcher et al.[42] have recently given a highly detailed description of the collisional deactivation of $I(5^2P_{1/2})$ by H_2, D_2, and HD which will be seen to be relevant to the present experiments. Further, Ewing[36] has given a detailed calculation on the quenching of Pb(6^3P_1) and Pb(6^3P_2) by H_2 and D_2. Before proceeding with a discussion which is principally centered on E → V, R transfer, it should, of course, first be stated that correlations based on (J, Ω) coupling lead one to expect no differences in the collisional behavior between the $^3P_1$ or $^3P_2$ states of tin or lead arising from differences in the symmetry of the appropriate potential surfaces. All chemical reactions would be endothermic and this relaxation clearly arises from NAT's between surfaces connecting with the states $^3P_2 + {}^1\Sigma_g^+(3A' + 2A'')$, $^3P_1 + {}^1\Sigma_g^+(A' + 2A'')$ and $^3P_0 + {}^1\Sigma_g^+(A')$.

Now, although no significant differences in chemistry for any of these atomic states with these quenching molecules are predicted, relaxation and energy transfer would be expected to be profoundly affected by the *electronic* factors governing the nature of interaction on collision. Ewing's calculation[36] has employed an approximate version of the Sharma–Brau theory[43,44] based on *long-range* quadrupole–quadrupole coupling for the near-resonance E → V, R transfer process

$$Pb(6^3P_2) + D_2(v'' = 0, J = 2) \rightarrow Pb(6^3P_1) + D_2(v'' = 1, J = 0) \qquad \Delta E = +18\ cm^{-1} \quad (1)$$

The calculation in general yields a selection rule for the change in the rotational quantum number of $\Delta J = \pm 2$, and the resulting calculated value for the collisional cross section of process 1 is in reasonable agreement with experiment for a calculation of this type, i.e., σ^2(300 K, theory) = 10 Å^2; σ^2(expt) < 2.5×10^{-2} (ref 35) and 0.22 Å^2 (ref 36 and 37). Further, the $^3P_1$ and $^3P_0$ states are not coupled by any electric multipole for near-resonance processes, and the considerably smaller cross sections for Pb(6^3P_1) (Table I) are in accord with this. Following Ewing,[36] we may expect that the process

$$Sn(5^3P_2) + H_2(v'' = 0, J = 1) \rightarrow Sn(5^3P_1) + H_2(v'' = 0, J = 5) \qquad \Delta E = -96\ cm^{-1} \quad (2)$$

be rapid compared to the analogous process

$$Sn(5^3P_1) + H_2(v'' = 0, J = 1) \rightarrow Sn(5^3P_2) + H_2(v'' = 0, J = 5) \qquad \Delta E = -52\ cm^{-1} \quad (3)$$

Here the coupling is between the atomic quadrupole and the molecular hexadecapole, but process 3 is forbidden for a quadruple transition ($J = 0 \nleftrightarrow J = 1$). Unfortunately, the data for Sn(5^3P_1) and Sn(5^3P_2) + H_2 do not at present appear to be in accord with the extension of this theory for E → R transfer (Table I).

Within the confines of the same approach, Butcher et al.[42] have concentrated on the effect of the $\Delta J = \pm 2$ selection rule in the quenching of $I(5^2P_{1/2})$ by H_2 and D_2 in E → V, R transfer and, on this basis, have successfully accounted for the nature of the temperature dependence of the relaxation processes.[45] By contrast, the $\Delta J = \pm 2$ rule will not prevail for HD and this has also been suitably included in

Butcher et al.'s treatment of $I(5^2P_{1/2})$ relaxation. The extension of such an approach to $Sn(5^3P_{1,2})$ is not fully clear. For quenching of $Sn(^3P_2) \rightarrow Sn(^3P_1)$ by D_2 via quadrupole–hexadecapole coupling, only

$$Sn(^3P_2) + D_2(v'' = 0, J = 5) \rightarrow Sn(^3P_1) + D_2(v'' = 0, J = 9) \quad \Delta E = -23\ cm^{-1} \quad (4)$$

is near resonance. As no rotational selection rules pertain for the quadrupole transition in HD, deactivation by HD might proceed via

$$Sn(^3P_2) + HD(v'' = 0, J = 5) \rightarrow Sn(^3P_1) + HD(v'' = 0, J = 8) \quad \Delta E = +31\ cm^{-1} \quad (5)$$

However, as the thermal populations of the $J = 5$ level of D_2 and HD at 300 K are very small, 1.5 and 0.4%, respectively, the relaxation of $Sn(^3P_2)$ to $Sn(^3P_1)$ by D_2 (4) and HD (5) might be expected to be relatively slow in comparison to deactivation by H_2 (2) (approximately 70% of the thermal population is in $J = 1$). The experimental results (Table I) indicate that quite the opposite is true; deactivation of $Sn(^3P_2)$ by HD and D_2 is much more efficient than by H_2, a trend which is especially clear when the rate coefficients are converted to quenching cross sections, σ_Q

Q	σ_Q, Å^2
H_2	0.064
HD	0.37
D_2	1.26

Other possible channels for near-resonant energy transfer might also be considered, although these would involve deactivation of $Sn(^3P_2)$ to $Sn(^3P_0)$, a process which is electric quadrupole allowed ($\Delta J = 0, 1, 2$)[36] with an Einstein coefficient, A_q, approximately a factor of 10 larger than $Sn(^3P_2) \rightarrow Sn(^3P_1)$[30]

$$Sn(5^3P_2) + H_2(v'' = 0, J = 4) \longrightarrow Sn(5^3P_0) + H_2(v'' = 1, J = 2) \quad \Delta E = -99\ cm^{-1} \quad (6)$$

$$Sn(5^3P_2) + HD(v'' = 0, J = 1) \longrightarrow Sn(5^3P_0) + HD(v'' = 1, J = 0) \quad \Delta E = +115\ cm^{-1} \quad (7)$$

$(v'' = 0, J = 2)$	$(v'' = 1, J = 0)$	−63
$(v'' = 0, J = 2)$	$(v'' = 1, J = 1)$	+22
$(v'' = 0, J = 3)$	$(v'' = 1, J = 2)$	−73

$$Sn(5^3P_2) + D_2(v'' = 0, J = 0) \longrightarrow Sn(5^3P_0) + D_2(v'' = 1, J = 4) \quad \Delta E = -138\ cm^{-1} \quad (8)$$

$(v'' = 0, J = 1)$	$(v'' = 1, J = 3)$	−150
$(v'' = 0, J = 2)$	$(v'' = 1, J = 4)$	−41
$(v'' = 0, J = 3)$	$(v'' = 1, J = 5)$	+64
$(v'' = 0, J = 4)$	$(v'' = 1, J = 6)$	+165

Here, the low thermal population of H_2 ($J = 4$) would make quenching of $Sn(^3P_2)$ via (6) a relatively slow process in comparison with (7) and (8), more in qualitative agreement with experiment. Indeed, it would seem that the relative rates of (2) + (6), (4) + (8), and (5) + (7) must be taken into account when calculating the overall rate constant for deactivation of $Sn(^3P_2)$ by H_2, D_2, and HD, respectively. It would be of considerable interest to monitor the temporal profiles of the spin–orbit levels of the Sn atoms following energy transfer as such data would yield further information concerning the relative contributions of the possible quadrupole–multipole relaxations. As indicated above, such a measurement is not feasible with the present experimental arrangement.

A number of factors in this area require theoretical explanation, the most difficult of which clearly being those concerned with quenching of different electronic states by the same molecule. Whether the potential curves involving $I(5^2P_{1/2})$ + H_2, D_2, HD and even, for that matter, $Sn(5^3P_{1,2})$ + H_2, D_2, HD are parallel, especially as the interactions may involve species such as SnH_2, is, in our opinion, still open to question. Even the propensity rule[36,42] for H_2 and D_2 may be open to conjecture. All the atomic states that have been considered within this context, namely, $I(5^2P_{1/2})$,[42] $Tl(6^2P_{3/2})$,[12-14,42] $Pb(6^3P_{1,2})$,[35-37] and $Sn(5^3P_{1,2})$ (this work) have magnetic moments. Thus the time and space variable magnetic fields generated on collision with H_2 or D_2 may well increase the magnitudes of the appropriate magnetic dipole matrix elements sufficiently to bring about ortho–para conversion ($\Delta J = \pm 1$), a mechanism well established for collisions with molecules such as NO and O_2.[46] Finally, the theoretical basis of treatments concerned with explanation of energy transfer by E → V, R long-range quadrupole–multipole interaction[36,42] must still be reconciled with those dealing with the effects of quantum resonance on collisions of electronically excited atoms with molecules.[47,48]

N_2 and CO. The thermochemistry clearly indicates that the chemical reaction between $Sn(5^3P_1)$ and $Sn(5^3P_2)$ with either N_2 or CO will not occur. Physical relaxation will take place via NAT's between the appropriate surfaces correlating with the three spin–orbit states of the $5p^2$ configuration: (N_2, CO = $^1\Sigma^+(0^+)$) $O^+ + {}^3P_2(2_g) = 3A' + 2A''$, $O^+ + {}^3P_1(1_g) = (A' + 2A'')$, and $O^+ + {}^3P_0(0_g) = A'$. The slow rates for the quenching of both $Sn(5^3P_1)$ and $Sn(5^3P_2)$ by N_2 (Table I) are not inconsistent with the energy discrepancies involved in E → V transfer ($v'' = 0 \rightarrow 1$) for $^3P_2 \rightarrow {}^3P_1$ and $^3P_1 \rightarrow {}^3P_0$. The present experiments permit no further detailed discussion of the mechanism of this nonadiabatic process. By contrast, rapid rates for the quenching of both spin–orbit states by CO, which has a comparable fundamental vibrational frequency to that of N_2[49] presumably involves some specific chemical interaction between this molecule and the metal, an interaction commonly encountered with other metals in inorganic chemistry.

O_2 and NO. Chemical reaction between either $Sn(5^3P_2)$ or $Sn(5^3P_1)$ with nitric oxide would be highly endothermic and hence physical relaxation takes place. There are a relatively large number of surfaces that correlate with the spin–orbit states, namely, $^3P_2 + NO(X^2\Pi_{1/2,3/2}) = 10E_{1/2}(\text{total})$, $^3P_1 + NO(X^2\Pi_{1/2,3/2}) = 6E_{1/2}(\text{total})$, and $^3P_0 + NO(X^2\Pi_{1/2,3/2}) = 2E_{1/2}(\text{total})$, and hence one may expect a suitable number of surface crossings with NAT's of appropriate magnitude in probability. Further, E → V transfer is sufficiently close to resonance to account for the observed rapid rates (Table I)

$$Sn(5^3P_2) + NO(v'' = 0) \rightarrow Sn(5^3P_1) + NO(v'' = 1) \quad \Delta E = +139\ cm^{-1}$$

$$Sn(5^3P_1) + NO(v'' = 0) \rightarrow Sn(5^3P_0) + NO(v'' = 1) \qquad \Delta E = +183\ cm^{-1}$$

It may be noted that Husain and Littler[50] have observed that the removal of ground state lead atoms, $Pb(6^3P_0)$, by NO is characterized by kinetics which are overall third order, indicating the formation of a PbNO* intermediate. Further, these third-order processes were found to be characterized by relatively large negative temperature rate coefficients,[51] indicating the magnitude of the Pb–NO interaction. It would seem reasonable to invoke comparable interactions for the higher spin–orbit states which presumably account in part for the relatively rapid quenching of $Sn(5^3P_{1,2})$ and $Pb(6^3P_{1,2})$ by this molecule.

We have already presented the data for the quenching of $Sn(5^3P_{1,2})$ and $Pb(6^3P_{1,2})$ by molecular oxygen in our preliminary communication[22] and reported a relatively detailed discussion of the mechanisms involved. Essentially, the data for $Sn(5^3P_{1,2}) + O_2$ are in accord with a correlation diagram based on (J, Ω) coupling, which has been given.[22] Briefly, there are potential surfaces (4A′ + 2A″, total) directly connecting $Sn(5^3P_1) + O_2$ ($X^3\Sigma_g^-(0^-, 1)$) exothermically to the chemical products $SnO(X^1\Sigma^+(0^+)) + O(2^3P_{2,1,0})$. Although similar symmetry considerations apply to $Pb(6^3P_{0,1,2}) + O_2$, for which the (J, Ω) correlation diagram has also been given,[22] there is a sizeable body of kinetic evidence[23,51] which supports the further complication of a rapidly established, near-resonance electronic energy exchange equilibrium, $Pb(6^3P_1) + O_2(X^3\Sigma_g^-) = Pb(6^3P_0) + O_2(a^1\Delta_g)$, $\Delta E = 105\ cm^{-1}$, similar to that reported by Derwent and Thrush[52] for $I(5^2P_{1/2}) + O_2$ and Wiesenfeld et al.[13,14] for $Tl(6^2P_{3/2}) + O_2$.

CO_2. Although the correlation diagram in (J, Ω) coupling connecting the states of Pb + CO_2 and PbO + CO assuming C_s symmetry in the collision complex has been presented hitherto,[18] the analogous diagram for the tin atom has not and is given here (Figure 5). It differs from that of lead in two principal respects. First, the differences in thermochemistry cause fundamental differences in the nature of the diagrams (see Figure 7, ref 18). Secondly, there is a fundamental difference between the ordering of the states of SnO and those of PbO. The ordering of the low-lying states of SnO is a matter of some controversy.[53–55] Figure 5 is constructed following the ordering given by Deutsch and Barrow[54] whose work is spectroscopically more detailed. While chemical reaction between Sn + CO_2 is essentially thermoneutral[38,49,56]

$$Sn + CO_2 = SnO + CO \qquad \Delta H = +0.053\ eV$$

Figure 5 clearly shows that, for the analogous exothermic reactions of $Sn(5^3P_1)$ and $Sn(5^3P_2)$, there are no pathways leading directly to ground state chemical products. Hence chemical reaction or physical relaxation must occur via NAT's between the appropriate surfaces shown in Figure 5. It is tempting to attribute the enhancement in the relaxation rate for the upper level (Table I) to the availability of more suitable vibrational modes in the quenching molecule. The degenerate bending mode (ν_2) at 667 cm^{-1} and the symmetric stretch (ν_1) at 1388 cm^{-1} are available both to the $^3P_1$ level (1692 cm^{-1}) and $^3P_{2\rightarrow1}$ transition (1736 cm^{-1}) while the asymmetric stretch (ν_3) at 2349 cm^{-1} is principally accessible to the $^3P_2$ level (3428 cm^{-1}). On the other hand, the explanation may well lie in those types of electronic factors that were discussed when considering quenching by the hydrogen isotopes. In particular, the

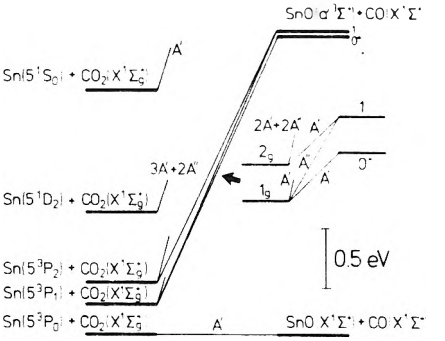

Figure 5. Correlation diagram in (J, Ω) coupling connecting the states of Sn + CO_2 and SnO + CO assuming C_s symmetry in the collision complex.

greater rate for the $^3P_2$ level may lie with the more favorable coupling between the electronic $J = 2$ and $J = 1$ atomic levels with this $^1\Sigma_g^+$ molecule compared to that between the $^3P_1$ and $^3P_0$ levels.

Polyatomic Molecules. There are no effects sufficiently dramatic when considering quenching of both the $^3P_1$ and $^3P_2$ levels by the polyatomic molecules investigated (Table I) to merit detailed discussion. Indeed the complexity involved when considering deactivation by diatomic molecules alone indicates the inadequacy of present methods to deal with data for the polyatomic species within the context of a detailed, physical, and unified structure. One may note generally slower rates for the deuterated alkenes compared to the hydrogenated analogues. The most striking aspect of all of this group of data is the comparatively fast rates for all molecules from CH_4 onward for both atomic states. There is a rough, weak correlation (in the classical sense) between log k_Q for the $^3P_1$ and $^3P_2$ levels and the ionization potential[57] for the polyatomic molecules, with the exception of relaxation by CF_4, which, by this criterion, is very fast. For many atomic states studied hitherto[1–3,5] large differences have been observed in the quenching rates between, e.g., CF_4 and CF_3H, the latter molecule being generally more efficient and the effect attributed to chemical interaction with the hydrogen atom. The comparably rapid rates observed here (Table I) may arise from the relatively small energies to be transferred which can readily be taken up in vibration, although a specific chemical interaction similar to that suggested[14] for $Tl(6^2P_{3/2}) + CF_4$ may also facilitate physical deactivation.

Acknowledgment. We wish to acknowledge the generous support of the General Electric Company and donors of the Petroleum Research Fund, administered by the American Chemical Society.

References and Notes

(1) R. J. Donovan and D. Husain, *Annu. Rep. Prog. Chem., Sect. A*, **68**, 124 (1972).
(2) R. J. Donovan, D. Husain, and L. J. Kirsch, *Annu. Rep. Prog. Chem., Sect. A*, **69**, 19 (1973).
(3) D. Husain and R. J. Donovan, *Adv. Photochem.*, **8**, 1 (1970).
(4) K. E. Shuler, *J. Chem. Phys.*, **21**, 624 (1953).
(5) R. J. Donovan and D. Husain, *Chem. Rev.*, **70**, 489 (1970).
(6) B. H. Mahan, *Acc. Chem. Res.*, **8**, 55 (1975).
(7) A. B. Callear and J. C. McGurk, *J. Chem. Soc., Faraday Trans. 2*, **69**, 97 (1973).
(8) J. G. Calvert and J. N. Pitts, "Photochemistry", Wiley-Interscience, New York, N.Y., 1966.
(9) D. Husain and J. R. Wiesenfeld, *Trans. Faraday Soc.*, **63**, 1349 (1967).
(10) J. J. Deakin and D. Husain, *J. Chem. Soc., Faraday Trans. 2*, **68**, 41 (1972).
(11) J. J. Deakin, D. Husain, and J. R. Wiesenfeld, *Chem. Phys. Lett.*, **10**,

146 (1971).
(12) J. A. Bellisio and P. Davidovits, *J. Chem. Phys.*, **53**, 3474 (1970).
(13) J. R. Wiesenfeld, *Chem. Phys. Lett.*, **21**, 517 (1973).
(14) P. D. Foo, T. Lohman, J. Podolske, and J. R. Wiesenfeld, *J. Phys. Chem.*, **79**, 414 (1975).
(15) R. J. Donovan and D. J. Little, *J. Chem. Soc., Faraday Trans. 2*, **69**, 952 (1973).
(16) R. J. Donovan and D. Husain, *Trans. Faraday Soc.*, **62**, 2643 (1966).
(17) R. J. Donovan and D. Husain, *Trans. Faraday Soc.*, **62**, 2987 (1966).
(18) A. Brown and D. Husain, *J. Chem. Soc., Faraday Trans. 2*, **71**, 699 (1975).
(19) D. Husain, *Acc. Chem. Res.*, manuscript in preparation.
(20) A. Brown and D. Husain, *Int. J. Chem. Kinet.*, **7**, 77 (1975).
(21) D. Husain and J. G. F. Littler, *J. Chem. Soc., Faraday Trans. 2*, **69**, 842 (1973).
(22) D. Husain and J. G. F. Littler, *J. Chem. Soc., Faraday Trans. 2*, **68**, 2110 (1972).
(23) P. D. Foo, J. R. Wiesenfeld, and D. Husain, *Chem. Phys. Lett.*, **32**, 443 (1975).
(24) C. E. Moore, Ed., *Natl. Bur. Stand. Circ.* **No. 467** (1958).
(25) D. Husain and J. G. F. Littler, *Int. J. Chem. Kinet.*, VI, **61** (1974).
(26) C. R. Jones and H. P. Broida, *J. Chem. Phys.*, **60**, 4369 (1974).
(27) R. W. Field, C. R. Jones, and H. P. Broida, *J. Chem. Phys.*, **60**, 4377 (1974).
(28) D. Husain and J. R. Wiesenfeld, *J. Chem. Phys.*, **62**, 2010 (1975).
(29) R. W. Field, C. R. Jones, and H. P. Broida, *J. Chem. Phys.*, **62**, 2012 (1975).
(30) R. H. Garstang, *J. Res. Natl. Bur. Stand., Sect. A*, **68**, 61 (1964).
(31) C. H. Corliss and W. R. Bozman, *Natl. Bur. Stand. Monogr.*, **No. 53** (1962).
(32) R. J. Donovan, D. Husain, and L. J. Kirsch, *Trans. Faraday Soc.*, **66**, 2551 (1970).
(33) P. P. Bemand and M. A. A. Clyne, *J. Chem. Soc., Faraday Trans. 2*, **69**, 1643 (1973).
(34) A. Brown and D. Husain, unpublished results.
(35) D. Husain and J. G. F. Littler, *Int. J. Chem. Kinet.*, VI, 61 (1974).
(36) J. J. Ewing, *Chem. Phys. Lett.*, **29**, 50 (1974).
(37) J. J. Ewing, D. W. Trainor, and S. Yatsiv, *J. Chem. Phys.*, **61**, 4433 (1974).
(38) A. G. Gaydon, "Dissociation Energies and Spectra of Diatomic Molecules", 3rd ed, Chapman and Hall, London, 1968.
(39) J. O. Hirschfelder, C. F. Curtiss, and R. B. Bird, "Molecular Theory of Gases and Liquids", Wiley, New York, N.Y., 1954.
(40) R. J. Donovan, D. Husain, and L. J. Kirsch, *Trans. Faraday Soc.*, **66**, 774 (1970).
(41) C. D. Cooper, G. C. Cobb, and E. L. Tolnas, *J. Mol. Spectrosc.*, **7**, 223 (1961).
(42) R. J. Butcher, R. J. Donovan, and R. H. Strain, *J. Chem. Soc., Faraday Trans. 2*, **70**, 1837 (1974).
(43) R. D. Sharma and C. A. Brau, *Phys. Rev. Lett.*, **19**, 1273 (1967).
(44) R. D. Sharma and C. A. Brau, *J. Chem. Phys.*, **50**, 924 (1969).
(45) J. J. Deakin and D. Husain, *J. Chem. Soc., Faraday Trans. 2*, **68**, 1603 (1972).
(46) A. Farkes, "Light and Heavy Hydrogen (Orthohydrogen, Parahydrogen and Heavy Hydrogen)", Cambridge University Press, New York, N.Y., 1935, p 79.
(47) J. C. Tully, *J. Chem. Phys.*, **60**, 3042 (1974).
(48) I. H. Zimmerman and T. F. George, *J. Chem. Phys.*, **61**, 2468 (1974).
(49) G. Herzberg, "Spectra of Diatomic Molecules", Van Nostrand, New York, N.Y., 1961.
(50) D. Husain and J. G. F. Littler, *J. Photochem.*, **2**, 247 (1973–1974).
(51) D. Husain and J. G. F. Littler, *Combus. Flame*, **22**, 295 (1974).
(52) R. G. Derwent and B. A. Thrush, *Chem. Phys. Lett.*, **9**, 591 (1971).
(53) J. J. Smith and B. Meyer, *J. Mol. Spectrosc.*, **27**, 304 (1968).
(54) B. Meyer, J. J. Smith, and K. Spitzer, *J. Chem. Phys.*, **53**, 3616 (1970).
(55) E. W. Deutsch and R. F. Barrow, *Nature (London)*, **201**, 815 (1964).
(56) G. Herzberg, "Electronic Spectra of Polyatomic Molecules", Van Nostrand, New York, N.Y., 1966.
(57) J. L. Franklin, J. G. Dillard, H. M. Rosenstock, and K. Draxl, *Natl. Stand. Ref. Data Ser., Natl. Bur. Stand.*, **No. 26** (1969).

Quenching of the Luminescence of the Tris(2,2'-bipyridine) Complexes of Ruthenium(II) and Osmium(II). Kinetic Considerations and Photogalvanic Effects

Chin-Tung Lin and Norman Sutin*

Chemistry Department, Brookhaven National Laboratory, Upton, New York 11973 *(Received July 11, 1975)*

Publication costs assisted by Brookhaven National Laboratory

The quenching of the charge-transfer excited states of $Ru(bpy)_3^{2+}$ and $Os(bpy)_3^{2+}$ by O_2, Fe^{3+}, $Co(phen)_3^{3+}$, $Ru(NH_3)_6^{3+}$, $Os(bpy)_3^{3+}$, and $Fe(CN)_6^{3-}$ has been studied by a spectrofluorimetric method. The lifetime of the emitting state of the osmium(II) complex and the rate of its reaction with $Ru(NH_3)_6^{3+}$ were measured by a single-photon counting technique. A value of −0.96 V was estimated for the reduction potential of the $Os(bpy)_3^{3+}|{}^*Os(bpy)_3^{2+}$ couple. Emission intensity measurements were used to determine the steady-state concentrations of the Fe^{2+} and $Ru(bpy)_3^{3+}$ formed in the reaction of Fe^{3+} with the emitting state of $Ru(bpy)_3^{2+}$. The steady-state concentrations of the electron-transfer products increase in the order HCl < H_2SO_4 < $HClO_4$ ~ CF_3SO_3H and in 0.5 *M* $HClO_4$ amount to about 25% of the initial $Ru(bpy)_3^{2+}$ concentration under the conditions used. The $Ru(bpy)_3^{2+}$–Fe^{3+} system exhibits a large photogalvanic effect. The mechanisms of the reactions are discussed and general equations describing the steady-state characteristics of these systems are derived.

The quenching of the tris(2,2'-bipyridine)ruthenium(II) luminescence by various inorganic and organic substrates is a subject of much current interest.[1-8] Recent studies have shown that depending on the nature of the substrate the quenching reaction may proceed by an energy-transfer[3,4] or an electron-transfer mechanism[5-10] (or both). Since the emitting state of $Ru(bpy)_3^{2+}$ has both very strong reducing[1,5-9] and moderately strong oxidizing[10] properties, electron transfer can occur rapidly to substrates that are either oxidizing or reducing. Proof that the emitting state is acting as an electron donor (oxidative quenching) requires the use of a substrate to which energy transfer cannot readily occur and which accepts electrons to give a reduced product that is not rapidly oxidized by $Ru(bpy)_3^{3+}$.[6-8] Similarly, demonstration of reductive quenching requires the use of a substrate to which energy transfer is inefficient and which

donates electrons to give an oxidized product that does not rapidly react with $Ru(bpy)_3^{+}$. Evidence for electron-transfer quenching has been obtained in flash experiments[5] and also from product analysis studies.[1,6,7] (The interpretation of even experiments such as these is, however, not free of ambiguities.[2,9]) Less direct evidence for electron-transfer quenching mechanisms has also been obtained from steady-state,[9] relative rate,[6] and spectroscopic considerations.[6,10]

In the present paper we report the results of a study of the quenching of the tris(2,2′-bipyridine)ruthenium(II) and -osmium(II) luminescence by a variety of inorganic compounds. The reactivities of the emitting states of $Ru(bpy)_3^{2+}$ and $Os(bpy)_3^{2+}$ are compared. The presence or absence of photogalvanic effects in these systems is revealed by the quenching studies. Evidence is presented for the buildup of appreciable concentrations of electron-transfer products upon continuous illumination of the $Ru(bpy)_3^{2+}$–Fe^{3+} system and the accompanying free energy increase is related to the photogalvanic potentials observed in this system.

Experimental Section

Materials. Commercial $[Ru(bpy)_3]Cl_2 \cdot 6H_2O$ was purified by recrystallization from water while $[Os(bpy)_3]Br_2 \cdot 3H_2O$ and $[Os(bpy)_3](ClO_4)_2 \cdot H_2O$ were prepared and purified using literature methods.[11] Tris(1,10-phenanthroline)cobalt(III) chloride was prepared following the procedure of Pfeiffer and Werdelmann.[12] The europium(III) source was 99.9% pure europium(III) chloride (Ventron) or 99.99% pure europium oxide (Alfa). Commercial $[Ru(NH_3)_6]Cl_3$ was purified using published procedures.[13] Iron(III) perchlorate was purified by recrystallization from perchloric acid. The other chemicals used were of reagent grade. The samples were freshly prepared with triply distilled water and the ionic strengths and the acid concentrations of the solutions were adjusted with NaCl, H_2SO_4, $HClO_4$, HCl, or CF_3SO_3H. The samples were deaerated by argon bubbling immediately prior to use (except those using oxygen as a quencher).

Emission Intensity Measurements. The emission from the bipyridine complexes was measured on a Perkin-Elmer Model MPF-4 fluorescence spectrophotometer equipped with a 150-W xenon lamp. Incident light intensity was measured using ferrioxolate actinometry.[14] Excitation wavelengths in the range 420–460 and 440–500 nm were used for $Ru(bpy)_3^{2+}$ (λ_{max} 452 nm, ϵ 1.46×10^4 M^{-1} cm^{-1}) and $Os(bpy)_3^{2+}$ (λ_{max} 483 nm, ϵ 1.30×10^4 M^{-1} cm^{-1}), respectively. The emission was monitored in the range 560–760 nm; the (uncorrected) maximum emission intensity is at 608 nm for $Ru(bpy)_3^{2+}$ and at 715 nm for $Os(bpy)_3^{2+}$. The emission intensities were corrected for absorption of the incident light by the quenchers.[1b,6] The absorption spectra of the solutions containing the donor and various amounts of quenchers were essentially equal within experimental error to the combined spectra of donor and quenchers. Absorption by the quenchers at the emitting wavelengths was negligible except in the case of $Os(bpy)_3^{3+}$, where a correction to the emission below 690 nm was necessary. All of the measurements were made with 1-cm^2 cells at 25°.

Single-Photon Counting. The lifetime of the emitting state of $Os(bpy)_3^{2+}$ in the absence and in the presence of $Ru(NH_3)_6^{3+}$ was measured on an Ortec-based single-photon counting apparatus. The $Os(bpy)_3^{2+}$ solutions were deaerated by argon bubbling and the serum-capped cells were sealed with wax prior to measurement. The solutions were irradiated at 400 or 480 nm with a pulsed argon–hydrogen lamp. The pulses were 10 μsec apart and each pulse had a full-width at half-maximum of 5.3 nsec. Filters that cutoff wavelengths below 640 nm were placed between the irradiated solution and the detecting photomultiplier. The performance of the single-photon counting equipment was checked by measuring the emission lifetime of quinine; the value of 18.1 nsec measured with this apparatus is in good agreement with the literature value of 19.0 nsec.[15a]

Photogalvanic Cell. The photogalvanic potentials generated upon illumination of the $Ru(bpy)_3^{2+}$–Fe^{3+} system were measured in a cell consisting of two identical compartments separated by a sintered glass disk. Each of the compartments was filled with 9 ml of a solution containing $Ru(bpy)_3^{2+}$, Fe^{3+}, and acid. The solutions were stirred at a moderate speed. One compartment was exposed to a 500-W tungsten projection lamp (2.3×10^{-7} einstein cm^{-2} sec^{-1} in the range 400–480 nm) while the other was kept in the dark. A Corning glass filter was used to cut off wavelengths below 400 nm. The illuminated compartment had a light path of about 2 cm. A 1-cm^2 bright platinum gauze electrode was placed in the center of each compartment and the electrodes were connected to a high impedance (10 MΩ) voltmeter. The gauze and the connection to it were made of ~0.008-in. diameter platinum wire. To minimize the variation of catalytic effects on the electron transfer reaction as a function of the state of the platinum electrodes and also to facilitate comparisons between various measurements, the same pair of electrodes and the same set of experimental conditions were used. With the exception of two experiments carried out under nitrogen the potential measurements were made in air. A high Fe^{3+} ion concentration (5×10^{-3} M) was used in the latter case so that the Fe^{3+} would compete successfully with the O_2 for reaction with $^*Ru(bpy)_3^{2+}$.

Results

Emission Intensity Measurements. In order to calculate Stern–Volmer constants from the emission intensity measurements it is necessary to correct the observed ratios for the absorption of the incident or emitted light by the quencher and also for any difference in the concentration of the donor (resulting from its net oxidation or reduction by the quencher) in the quenched and unquenched samples. The former corrections (which were significant for quenching by $Os(bpy)_3^{3+}$ and $Co(phen)_3^{3+}$) were made using standard procedures.[1b,6] The corrections for the changes in the concentration of the donor (which were important in the $Ru(bpy)_3^{2+}$–Fe^{3+} system) were made using

$$\left(\frac{I_0}{I}\right)_{cor} = \left(\frac{I_{ref}}{I}\right)\frac{[D]}{[D_{ref}]} \qquad (1a)$$

which is valid when the absorbance of the donor is small. In this equation I_{ref} and I are the observed emission intensities and $[D_{ref}]$ and [D] are the donor concentrations of an unquenched and quenched sample, respectively. The donor concentration of the quenched sample is equal to ($[D_0] - [X]$) where $[D_0]$ is the total donor concentration and [X] is the amount of the donor that has been oxidized (or reduced). Values of [X] were obtained from eq 9 which is discussed later. Once [X] had been evaluated then eq 1a was either used directly (with $[D] = ([D_0] - [X])$) or the emission of an unquenched sample with a donor concentration

equal to ([D_0] − [X]) was measured. The corrected intensity ratios are plotted as a function of the quencher concentration in Figures 1 and 2. The Stern-Volmer constants calculated from the slopes of these plots (eq 1b) are sum-

$$(I_0/I)_{cor} = 1 + K_{SV}[Q] \quad (1b)$$

marized in Table I. The second-order quenching rate constants are also included in this table. These rate constants were calculated from eq 2 where τ_0, the unquenched life-

$$k_q = K_{SV}/\tau_0 = k_{en} + k_{el} \quad (2)$$

time of the emitting state, is 0.60 μsec for $Ru(bpy)_3^{2+}$ [6] and 19.2 nsec for $Os(bpy)_3^{2+}$ (determined in the work) in aqueous solution at 25°.[16] The rate constants k_{en} and k_{el} correspond to energy-transfer and electron-transfer quenching paths, respectively.

In Table II the emission intensity ratios are presented as a function of incident light intensity, acid, Fe(III), and Fe(II) concentrations. It will be seen that the ratios at the two light intensities are drastically decreased by the addition of iron(II) and are smallest in hydrochloric acid. The emission intensities were independent of the light intensity for $*Ru(bpy)_3^{2+}$ quenched by $Ru(NH_3)_6^{3+}$ or $*Os(bpy)_3^{2+}$ quenched by $Co(phen)_3^{3+}$. Furthermore the emission intensity ratios did not vary with the light intensity or with the $Ru(bpy)_3^{2+}$ concentration for $*Ru(bpy)_3^{2+}$ quenched by molecular oxygen. This is in contrast with the observation that the ratios decreased with increasing $Ru(bpy)_3^{2+}$ concentration when Fe^{3+} was used as the quencher. It was also found that the observed emission intensity for an unquenched sample was linearly dependent on the $Ru(bpy)_3^{2+}$ concentration at low ruthenium(II) concentrations but became increasingly insensitive to [$Ru(bpy)_3^{2+}$] at higher concentrations. This nonlinear relationship is presumably due to at least three factors: the exponential decrease of light intensity as a function of absorbance, the decrease in the collection efficiency of the emitted light as a function of (increasing) absorbance, and some self-quenching at the higher $Ru(bpy)_3^{2+}$ concentrations.

Figure 3 contains plots of $Ru(bpy)_3^{2+}$ emission intensity ratios as a function of added europium(III) chloride concentration both in the absence and in the presence of magnesium chloride. It will be seen that there is appreciable quenching at the higher europium(III) concentrations and ionic strengths but that the data do not give linear Stern-Volmer plots. The data also cannot be analyzed in terms of simple static quenching mechanisms involving a nonluminescent $Ru(bpy)_3^{2+}$-Eu(III) complex. No quenching by magnesium chloride was observed.

Although the determination of the Stern-Volmer constant for europium(III) quenching of the $Ru(bpy)_3^{2+}$ emission is hampered by the lack of information concerning the nature and amounts of the europium(III) species present at the high ionic strengths used, the fact that some quenching was observed raised the possibility that one possible product of the quenching reaction, Eu^{2+}, might be used to generate hydrogen in acid. However no hydrogen was detected by gas chromatographic analysis after an argon-deaerated sample containing $Ru(bpy)_3^{2+}$ and Eu(III) in 2 *M* $HClO_4$ or HCl had been irradiated (λ ≥400 nm) in the presence of a platinized platinum wire. These results (together with those from a laser flash experiment) indicate that the quenching process either proceeds primarily by an energy transfer mechanism or that the products of the electron-

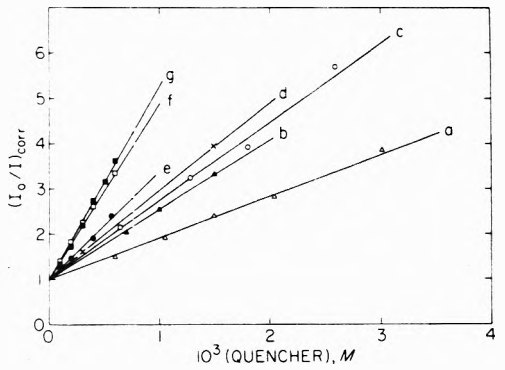

Figure 1. Stern-Volmer plots for the quenching of the $Ru(bpy)_3^{2+}$ emission by a series of quenchers at 25°: (a) Fe^{3+} in 0.11 *M* $HClO_4$; (b) $Ru(NH_3)_6^{3+}$ in 0.50 *M* NaCl; (c) $Co(phen)_3^{3+}$ in 0.50 *M* NaCl; (d) O_2 in H_2O; (e) $Os(bpy)_3^{3+}$ in 0.40 *M* NaCl + 0.10 *M* HCl; (f) $Fe(CN)_6^{3-}$ in 0.50 *M* NaCl; (g) $Fe(CN)_6^{3-}$ in 0.50 *M* H_2SO_4.

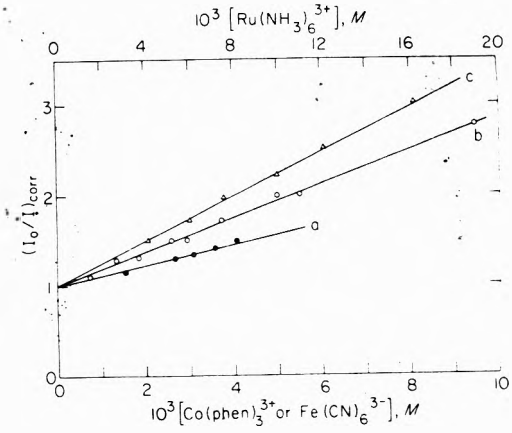

Figure 2. Stern-Volmer plots for the quenching of the $Os(bpy)_3^{2+}$ emission by a series of quenchers in 0.50 *M* NaCl at 25°: (a) $Co(phen)_3^{3+}$; (b) $Ru(NH_3)_6^{3+}$; (c) $Fe(CN)_6^{3-}$.

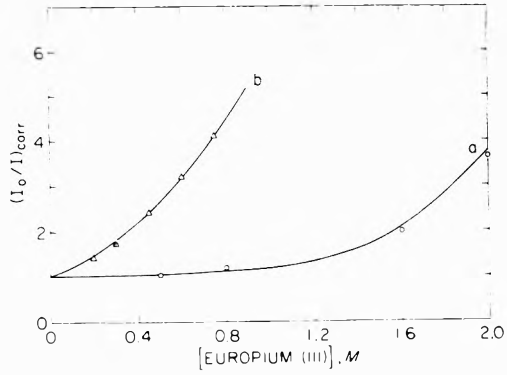

Figure 3. Plots of $(I_0/I)_{cor}$ for $Ru(bpy)_3^{2+}$ emission as a function of europium(III) concentration at 25°: (a) no added $MgCl_2$; the europium concentrations were obtained by dilution of a stock solution of europium(III) chloride in 0.50 *M* hydrochloric acid; (b) in 0.2 *M* HCl with the total europium(III) and magnesium chloride concentrations kept at 4.0 *M*.

transfer path react very rapidly to reverse the quenching redox reaction and to reform Ru(II) and Eu(III) (see eq 7 and 8).

Spectroscopic considerations indicate that energy transfer from $*Ru(bpy)_3^{2+}$ to the 16.9 kK level ($^7F \rightarrow {}^5D$) of Eu^{3+} is a spin-allowed process.[15b] This path may be ruled

TABLE I: Stern–Volmer Constants for the Quenching of the $Ru(bpy)_3^{2+}$ and $Os(bpy)_3^{2+}$ Emission by a Series of Inorganic Quenchers at 25°

Donor	Quencher	Medium	K_{SV}, M^{-1}	$10^{-9}k_q$, M^{-1} sec^{-1}
$Ru(bpy)_3^{2+}$	$Co(phen)_3^{3+}$	0.17 *M* NaCl	$(1.4 \pm 0.1) \times 10^3$	2.3 ± 0.2
		0.50 *M* NaCl	$(1.8 \pm 0.1) \times 10^3$	3.0 ± 0.2
$Ru(bpy)_3^{2+}$	O_2	H_2O	$(2.0 \pm 0.1) \times 10^3$	3.3 ± 0.2
$Ru(bpy)_3^{2+}$	$Ru(NH_3)_6^{3+}$	0.50 *M* NaCl	$(1.6 \pm 0.1) \times 10^3$	2.7 ± 0.1
$Ru(bpy)_3^{2+}$	$Fe(H_2O)_6^{3+}$	0.11 *M* $HClO_4$ [a,b]	$(0.9 \pm 0.1) \times 10^3$	1.5 ± 0.1
		0.50 *M* $HClO_4$ [a,b]	$(1.4 \pm 0.1) \times 10^3$ [c]	2.3 ± 0.1
		0.50 *M* HCl	$(1.6 \pm 0.1) \times 10^3$ [d]	2.7 ± 0.2
		0.50 *M* H_2SO_4	$(1.6 \pm 0.1) \times 10^3$ [d]	2.7 ± 0.2
$Ru(bpy)_3^{2+}$	$Os(bpy)_3^{3+}$	0.40 *M* NaCl + 0.10 *M* HCl	$(2.3 \pm 0.2) \times 10^3$	3.8 ± 0.3
$Ru(bpy)_3^{2+}$	$Fe(CN)_6^{3-}$	0.50 *M* NaCl	$(3.9 \pm 0.1) \times 10^3$	6.5 ± 0.1
		0.50 *M* H_2SO_4 [e]	$\leq(4.4 \pm 0.1) \times 10^3$	$\leq 7.3 \pm 0.1$
$Os(bpy)_3^{2+}$	$Co(phen)_3^{3+}$	0.50 *M* NaCl	$(1.1 \pm 0.1) \times 10^2$	5.7 ± 0.4
$Os(bpy)_3^{2+}$	O_2	H_2O [f]	$(1.0 \pm 0.2) \times 10^2$	5.2 ± 0.9
$Os(bpy)_3^{2+}$	$Ru(NH_3)_6^{3+}$	0.50 *M* NaCl	$(0.92 \pm 0.04) \times 10^2$	4.8 ± 0.2
		0.50 *M* NaCl [g]	$(0.91 \pm 0.04) \times 10^2$	4.7 ± 0.2
$Os(bpy)_3^{2+}$	$Fe(CN)_6^{3-}$	0.50 *M* NaCl	$(2.5 \pm 0.06) \times 10^2$	13.0 ± 0.4

[a] $(I_0/I)_{cor}$ has been corrected for the steady-state concentration of $Ru(bpy)_3^{3+}$, see ref 9. [b] $Os(bpy)_3^{2+}$ is readily oxidized by high concentrations of Fe^{3+}. [c] The Stern–Volmer constant measured at very low incident light intensity ($\sim 1 \times 10^{-10}$ einstein cm^{-2} sec^{-1}) is 1.45×10^3 M^{-1} (D. Marshall and N. Sutin, unpublished observations). [d] This value was determined at very low incident light intensity. [e] $Fe(CN)_6^{3-}$ slowly aquates in acid medium; $Os(bpy)_3^{2+}$ is unstable in acid media with $Fe(CN)_6^{3-}$ as quencher. [f] The O_2 concentration = 1.5×10^{-3} *M*. [g] This value is obtained from Figure 4.

TABLE II: Emission Intensity Ratios from Solutions Containing $Ru(bpy)_3^{2+}$ with and without Added Fe^{3+} as a Function of Incident Light Intensity, and Acid, Fe(III), or Fe(II) Concentrations at 25° [a]

10^6-$[Ru(bpy)_3^{2+}]$, *M*	$10^3[Fe^{3+}]$, *M*	Medium	I_{ref}/I [b,c]	I_{ref}/I [d,e]	10^6-[X], [b,c,f] *M*	10^7-[X], [d–f] *M*
4.46	1.5	0.50 *M* $HClO_4$	3.94	3.21	0.91	0.10
4.46	1.5	0.50 *M* H_2SO_4	3.65	3.26	0.48	0.05
4.46	1.5	0.50 *M* HCl	3.34	3.35	~0	~0
4.46	0.5	0.50 *M* $HClO_4$	2.09	1.71	0.89	0.10
4.46	0.5	0.50 *M* H_2SO_4	1.89	1.77	0.31	0.03
4.46	0.5	0.50 *M* HCl	1.75	1.74	~0	~0
4.46	1.0	0.50 *M* H_2SO_4		2.50		
4.46	2.0	0.50 *M* H_2SO_4		4.00		
4.46	1.0	0.50 *M* HCl		2.49		
4.46	2.0	0.50 *M* HCl		4.26		
4.46	1.5 [g]	0.50 *M* $HClO_4$	3.23	3.23	~0	~0
4.46	1.5 [h]	0.50 *M* $HClO_4$	3.23	3.23	~0	~0
~3.7	1.5	0.10 *M* CF_3SO_3H + 0.05 *M* $HClO_4$	4.32	3.42	0.85	0.10
4.46	1.5	0.10 *M* H_2SO_4 + 0.05 *M* $HClO_4$	4.32	4.04	0.32	0.03
4.46	1.5	0.10 *M* HCl + 0.05 *M* $HClO_4$	3.11	2.93	0.28	0.03
6.15	3.18	0.50 *M* $HClO_4$	1.56	1.29	1.20	0.15
4.92	2.23	0.50 *M* $HClO_4$	1.54	1.17	1.07	0.13
3.69	1.61	0.50 *M* $HClO_4$	1.52	1.18	0.91	0.11
3.07	1.12	0.50 *M* $HClO_4$	1.40	1.12	0.68	0.09
2.46	0.64	0.50 *M* $HClO_4$	1.31	1.02	0.60	0.08

[a] The excitation and emission wavelengths are 452 and 608 nm, respectively, and [X] is the steady-state concentration of $Ru(bpy)_3^{3+}$ or Fe^{2+}. [b] For the first 15 entries the incident light intensity was $\sim 1.3 \times 10^{-8}$ einstein cm^{-2} sec^{-1} and I_{ref} is the emission intensity measured at a $Ru(bpy)_3^{2+}$ concentration of 4.46×10^{-6} *M*. [c] For the last 5 entries the incident light intensity was 1.12×10^{-8} einstein cm^{-2} sec^{-1} and I_0 is the emission intensity measured at a $Ru(bpy)_3^{2+}$ concentration of 1.23×10^{-6} *M* in 0.1 *M* $HClO_4$. [d] The incident light intensity of $\sim 1.3 \times 10^{-8}$ einstein cm^{-2} sec^{-1} was reduced by a factor of 100 for the first 15 entries. [e] The incident light intensity was 1.4×10^{-10} einstein cm^{-2} sec^{-1} for the last 5 entries. [f] The [X] values calculated for the first 15 entries are not as accurate as those calculated for the last 5 entries since the former calculations are based on relatively high I_{ref}/I ratios. [g] The Fe^{2+} concentration added is 3.0×10^{-4} *M*. [h] The Fe^{2+} concentration added is 1.5×10^{-4} *M*.

out, however, since no sensitized emission from europium(III) was observed. On the basis of these observations we may tentatively conclude that the europium(III) quenching of the $Ru(bpy)_3^{2+}$ emission proceeds by an electron-transfer mechanism and that the reverse electron transfer between the $Ru(bpy)_3^{3+}$ and europium(II) produced in this reaction is much more rapid than the platinum-catalyzed reaction of europium(II) with hydronium ions.

Single-Photon Counting. The ratio of the lifetimes of the $Os(bpy)_3^{2+}$ emission τ_0/τ, where τ_0 and τ are the observed lifetimes in the absence and presence of the quencher, respectively, is plotted as a function of $Ru(NH_3)_6^{3+}$ concentration in Figure 4. The Stern–Volmer constant calculated from eq 3 is 91 M^{-1}, in excellent agreement with the

$$\tau_0/\tau = 1 + K_{SV}[Q] \quad (3)$$

value of 92 M^{-1} obtained in the intensity quenching measurements. Hexaammineruthenium(III) was used as the quenching agent for this comparison due to its stability in

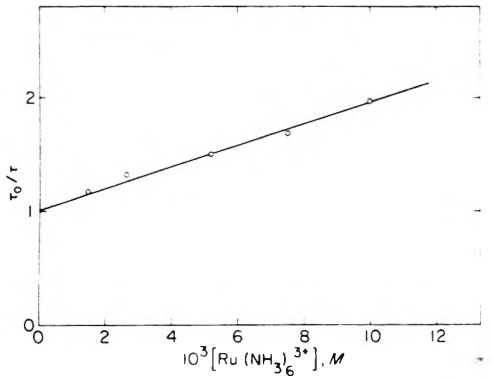

Figure 4. Quenching of the observed lifetime for $Os(bpy)_3^{2+}$ emission by added $Ru(NH_3)_6^{3+}$ in 0.50 *M* NaCl at 25°.

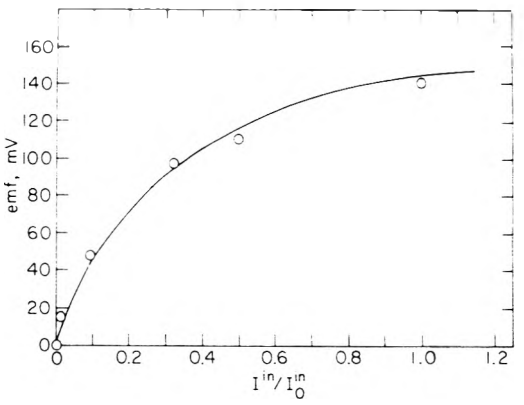

Figure 5. Plot of photogalvanic potentials as a function of incident light intensity: $[Ru(bpy)_3^{2+}] \simeq 3 \times 10^{-5}$ *M*, $[Fe^{3+}] = 2 \times 10^{-3}$ *M*, and $[CF_3SO_3H] = 0.3$ *M*.

aqueous solution and because of its very low absorbance at the exciting and emitting wavelengths. As mentioned above, the lifetime of the emitting state of $Os(bpy)_3^{2+}$ determined in this work is 19.2 nsec in water at 25°. We have also found that the luminescence quantum yield of (unquenched) $Os(bpy)_3^{2+}$ is 2.59 times higher in methanol than in water. Provided the intrinsic radiative lifetime of the emitting state of $Os(bpy)_3^{2+}$ is similar in the two media, this quantum yield comparison implies a lifetime of 49.8 nsec for $*Os(bpy)_3^{2+}$ in methanol at 25°. This lifetime estimate is in good agreement with the value of 49 nsec obtained from a direct measurement.[15c]

Photogalvanic Potential Measurements. In all the experiments reported here the platinum in the illuminated compartment acted as the cathode and the platinum in the dark compartment as the anode; that is, the current in the external circuit flowed from the illuminated to the dark electrode. The dependence of the photogalvanic potential on the incident light intensity is shown in Figure 5 and its dependence on the nature of the medium is shown in Table III. The values in Table III (which are averages of several measurements) show that the photogalvanic potentials decrease in the order: $HClO_4 \sim CF_3SO_3H > H_2SO_4 > HCl$. This is also the order seen in the quenching measurements. The potentials of unstirred solutions tended to be about 45% lower than those of stirred ones. No photogalvanic effect was observed in the presence of either $\sim 10^{-4}$ *M* $Ru(bpy)_3^{3+}$ or $\sim 10^{-4}$ *M* Fe^{2+}. By decreasing the amount of added $Ru(bpy)_3^{3+}$ or Fe^{2+} the potential of the system could be gradually restored. In order to test the long-term stability of the system, an air-saturated solution of 3×10^{-5} *M* $Ru(bpy)_3^{2+}$ and 5×10^{-3} *M* Fe^{3+} in 0.3 *M* CF_3SO_3H was exposed to the tungsten lamp for 10 sec of every minute in a cycle which continued for 6 days.[17] The absorbance measurements made at the end of this time indicated that only about 20% of the $Ru(bpy)_3^{2+}$ had been lost; during this time the potential also declined by about 45%. The system thus appears to be quite reversible in air and is likely to be even more stable in an inert atmosphere.

Discussion

Comparison of Excited State Reactivities. It is evident from the kinetic data presented in Table I that the quenching reactions of $*Os(bpy)_3^{2+}$ proceed about 60–100% faster than those of $*Ru(bpy)_3^{2+}$. The real reactivity difference of the two excited states might even be larger than this factor since the $*Os(bpy)_3^{2+}$ rates are close to the diffusion-controlled limits. (The diffusion-controlled rate constant for the $M(bpy)_3^{2+}$–O_2 reactions calculated from the Smoluchowski equation is 12×10^9 M^{-1} sec^{-1}, assuming encounter radii of 6.2 and 0.9 Å and diffusion coefficients of 0.37×10^{-5} and 2.0×10^{-5} cm^2 sec^{-1} for $Ru(bpy)_3^{2+}$ and O_2, respectively.)

In attempting to rationalize the reactivity difference of the two excited states we will first attempt to ascertain whether there is a correlation between the reactivities of the excited states and their oxidation potentials. The standard potential for the reduction of $M(bpy)_3^{3+}$ to $*M(bpy)_3^{2+}$ (eq 4) can be calculated from the potential for the reduction of $M(bpy)_3^{3+}$ to $M(bpy)_3^{2+}$ (eq 5) and the free energy change for the conversion of $M(bpy)_3^{2+}$ to $*M(bpy)_3^{2+}$ (eq 6). The enthalpy difference between the

$$M(bpy)_3^{3+} + e^- \rightleftharpoons *M(bpy)_3^{2+} \qquad (\Delta G°)^*, (E°)^* \qquad (4)$$

$$M(bpy)_3^{3+} + e^- \rightleftharpoons M(bpy)_3^{2+} \qquad \Delta G°, E° \qquad (5)$$

$$M(bpy)_3^{2+} \rightleftharpoons *M(bpy)_3^{2+} \qquad \Delta G^* \qquad (6)$$

triplet and ground states can be estimated from the average of the maxima of the singlet–triplet absorption and emission bands of $M(bpy)_3^{2+}$.[6] The positions of the low-energy charge-transfer singlet–singlet absorption and singlet–triplet absorption and emission bands of the ruthenium and osmium complexes are compared in Table IV. It will be seen that the bands in the spectrum of the ruthenium complex are shifted about 1–2 kK to higher energies relative to those of the osmium complex. This result is not unexpected in view of the greater ease of oxidation of the metal center in the latter complex.[18] In interpreting the temperature dependence of the luminescence in these complexes it has been proposed[19,20] that the emission does not arise from a single charge-transfer state of triplet multiplicity, but rather from three closely spaced, strongly spin–orbit coupled electronic states (which span 61 cm^{-1} in $Ru(bpy)_3^{2+}$).[18] However our observation of wavelength-independent quenching rates as well as of a single emission lifetime (as was also found to be the case at low temperature[17]) indicates that these states are in very rapid equilibrium. Although we shall, for the sake of convenience, continue to refer to the emitting state as if it were a single state of triplet multiplicity the above reservations concerning the significance of the spin label should be kept in mind.[18,21]

Returning to the estimation of the oxidation potentials of the luminescent states, the enthalpy difference between $Ru(bpy)_3^{2+}$ and $*Ru(bpy)_3^{2+}$, calculated from the average

TABLE III: Photogalvanic Potentials[a] of a Reversible $Ru(bpy)_3^{2+}$–Fe^{3+} System in Various Acids at ~22°[b]

$10^5[Ru(bpy)_3^{2+}]$, M	$10^3[Fe^{3+}]$, M	Medium	ΔE_{obsd}, V
1.9	4.8	0.10 M CF_3SO_3H + 0.024 M $HClO_4$	0.16[c]
2.0	5.0	0.10 M CF_3SO_3H + 0.025 M $HClO_4$	0.17
2.0	5.0	0.125 M $HClO_4$	0.17
2.0	5.0	0.10 M H_2SO_4 + 0.025 M $HClO_4$	0.14
2.0	5.0	0.10 M HCl + 0.025 M $HClO_4$	0.10
2.0	5.0	0.50 M $HClO_4$	0.18
2.0	5.0	0.50 M H_2SO_4	0.14
2.0	5.0	0.50 M HCl	~0.03

[a] Open circuit potentials in volts. The incident light intensity in the range 400–480 nm was ~2.3×10^{-7} einstein cm^{-2} sec^{-1}. In this range, the ϵ_D value for $Ru(bpy)_3^{2+}$ was averaged as 1×10^4 M^{-1} cm^{-1}. [b] Except where noted the solutions were air saturated. No photopotentials were observed for a deaerated solution containing $Ru(bpy)_3^{2+}$ but not Fe^{3+} or an air-saturated solution containing Fe^{3+} but not $Ru(bpy)_3^{2+}$. [c] In a deaerated solution.

TABLE IV: Comparison of the Low-Energy Charge-Transfer Absorptions and Emissions of $Ru(bpy)_3^{2+}$ and $Os(bpy)_3^{2+}$

Transition	$Ru(bpy)_3^{2+}$	Ref	$Os(bpy)_3^{2+}$	Ref
S → S, kK[a,b]	22.1 (452)	d	20.7 (483)	d
	23.6 (423)	d	22.8 (438)	d
S → T, kK[a,b]	18.2 (549)	e	~16.9 (590)	d,f
			~15.4 (650)	d,f
T → S, kK[a,c]	15.9 (630)	d	13.3 (750)	g

[a] The numbers in parentheses are the wavelengths for the transitions. [b] Low-energy charge-transfer absorption maxima. [c] Corrected emission maximum in water at 25°. [d] This work. [e] R. A. Palmer and T. S. Piper, *Inorg. Chem.*, 5, 864 (1966). [f] Reference 19. [g] We are indebted to Professor M. S. Wrighton for this measurement.

of the maxima of the singlet–triplet absorption and emission bands of the ruthenium complex, is 2.11 eV. As far as the corresponding entropy change is concerned, only that part due to the spin multiplicity change (R ln 3) can be calculated. If it is assumed that other contributions to the entropy difference can be neglected, then ΔG^* is calculated to be 2.08 eV. Combining this value with the reduction potential of $Ru(bpy)_3^{3+}$ (1.24 V in 1 M acid[22]) gives $(E°)^* = -0.84$ V.[23,24] The analogous calculation for the osmium complex is complicated by the fact that the singlet–triplet absorption band which is the inverse of the emission band is not clearly resolved.[18] If the absorption maximum at ~16.9 kK is assigned to this band then the enthalpy and free energy changes for the conversion of $Os(bpy)_3^{2+}$ to $*Os(bpy)_3^{2+}$ are calculated to be 1.81 and 1.78 eV, respectively. Combining this value with the reduction potential of $Os(bpy)_3^{3+}$ (0.82 V in 1 M acid[25]) gives $(E°)^* = -0.96$ V. These considerations suggest that the luminescent state of osmium is a somewhat better reducing agent than that of ruthenium. This difference could account for the greater reactivity of $*Os(bpy)_3^{2+}$ provided that the quenching reactions under consideration proceed by electron-transfer mechanisms.[26,27]

Steady-State Considerations. Additional evidence for the conclusion that the quenching reactions proceed, at least in part, by electron-transfer mechanisms is provided by flash experiments. These experiments, which will be described elsewhere, show that the quenching of the ruthenium(II) and osmium(II) luminescence by $Co(phen)_3^{3+}$ and $Ru(NH_3)_6^{3+}$ yields primarily electron-transfer products. The quenching rate constants obtained for these reactions are also consistent with calculations based on Marcus' equations. These observations and the above considerations can be rationalized in terms of the kinetic scheme summarized in[5,9]

$$D \underset{k_0}{\overset{h\nu}{\rightleftharpoons}} {}^*D \tag{7}$$

$$^*D + Q \xrightarrow{k_{el}} D^+ + Q^- \tag{8a}$$

$$D^+ + Q^- \xrightarrow{k_t} D + Q \tag{8b}$$

In this scheme k_t is the second-order rate constant for the back (thermal) electron transfer between D^+ and Q^-. The steady-state approximation for the concentration [X] of D^+ of Q^- gives

$$k_{el}[^*D][Q] = k_t[X]^2 \tag{9a}$$

If the absorbance of the quencher at the excitation wavelength may be neglected and the absorbance of the donor is not too large, then the expression for the concentration of the excited donor in a 1-cm path length cell can be simplified from eq 8 of a previous paper[6] to give

$$[^*D] = \frac{2.3 \times 10^3 I^{in} A_D}{k_0 + k_q[Q]} \tag{9b}$$

where $A_D = \epsilon_D([D_0] - [X])$, A_D and ϵ_D are the absorbance of $Ru(bpy)_3^{2+}$ (corrected for $Ru(bpy)_3^{3+}$ concentration) and its molar absorptivity, respectively, and I^{in} is the incident light intensity (einstein cm^{-2} sec^{-1}). Since the emission intensity (I) is proportional to [*D], the ratio of measured emission intensities (at constant incident light intensity) from a sample containing Q to that from a reference sample without Q is

$$\frac{I}{I_{ref}} = \frac{[^*D]}{[^*D]_{ref}} = \frac{\{[D_0] - [X]\}k_0}{[D]_{ref}\{k_0 + k_q[Q]\}} \tag{9c}$$

provided $Q \gg D_0$. Equations 9a and 9b can be combined to yield

$$\left\{\frac{[X_1]}{[X_2]}\right\}^2 = \frac{I_1^{in}\{[D_0] - [X_1]\}}{I_2^{in}\{[D_0] - [X_2]\}} \tag{9d}$$

which is an expression for the steady-state concentrations in a given sample at two different light intensities. Similarly, eq 9c is an expression for the emission intensities of a given sample relative to that of an unquenched reference sample at two light intensities. Values of [X] as a function of light intensity can now be obtained by the simultaneous solution of eq 9d and 9e.

$$\frac{[D_0] - [X_1]}{[D_0] - [X_2]} = \left[\frac{I}{I_{ref}}\right]_1 \left[\frac{I}{I_{ref}}\right]_2^{-1} \tag{9e}$$

Values of [X] calculated from eq 9d and 9e are presented in Table II. These [X] values were used to obtain the "true" Stern–Volmer constants as described above (eq 1a and 9c). The steady-state concentrations of $Ru(bpy)_3^{3+}$ and Fe^{2+} can evidently attain relatively high levels which amount to about 25% of the initial $Ru(bpy)_3^{2+}$ concentration at the higher quencher concentrations. According to eq 9a the steady-state concentrations are proportional to the square root of the excited state concentration. As a consequence the yield of steady-state products is relatively low in samples containing high donor concentrations. In addition, high donor concentrations reduce the effective incident light intensity. These factors result in the observed emission intensities becoming relatively insensitive to any change in the steady-state concentrations. For these reasons, the steady-state yields are highest and, from a practical point of view, are most readily determined at low donor concentrations and at high incident light intensities.

The square of the steady-state concentrations of $Ru(bpy)_3^{3+}$ or Fe^{2+} are directly proportional to the product of the $*Ru(bpy)_3^{2+}$ and Fe^{3+} concentrations (eq 9a and Figure 6). The value of k_{el}/k_t calculated from the slope of the plot in Figure 6 is 2.6×10^3. Since k_t is equal to 7.2×10^5 M^{-1} sec^{-1} in 0.5 M $HClO_4$ at 25° [28] we calculate that $k_{el} = 1.9 \times 10^9$ M^{-1} sec^{-1} in 0.5 M $HClO_4$. Since the value of k_q determined in this work is 2.3×10^9 M^{-1} sec^{-1} we calculate that $k_{el}/k_q = 0.81 \pm 0.16$ in 0.5 M $HClO_4$ at 25°. *This is an important result since it shows that most (if not all) of the quenching events result in net electron transfer from the excited ruthenium(II) to the iron(III).* It should be emphasized that this conclusion is based on the stopped-flow data and on the analysis of the steady-state emission measurements in terms of eq 9, and that no further assumptions have been introduced.

The effect of the medium on the steady-state concentrations can be rationalized in terms of anion effects on k_t. The data in Table II show that under comparable conditions the steady-state concentrations of $Ru(bpy)_3^{3+}$ or Fe^{2+} decrease in the order 0.5 M $HClO_4$ > 0.5 M H_2SO_4 > 0.5 M HCl. Since this order is determined by k_{el}/k_t and since the data in Table I show that k_q is essentially anion independent (and is about 15% smaller in 0.5 M $HClO_4$) the results imply that, provided k_{el}/k_q is independent of the medium, k_t decreases in the order HCl > H_2SO_4 > $HClO_4$. This conclusion is consistent with the results of stopped-flow studies[29] which have shown that the iron(II) reduction of polypyridine complexes of iron(III) proceed eight times faster in 0.5 M H_2SO_4 than in 0.5 M $HClO_4$.

The relatively low value of k_t/k_q for the $Ru(bpy)_3^{2+}$–Fe^{3+} system results in a relatively high steady-state concentration of the electron-transfer products. The steady-state concentrations are much lower when $Co(phen)_3^{3+}$ or $Ru(NH_3)_6^{3+}$ are used as quenchers. Laser flash studies show that the thermal electron transfer rate in the latter systems approaches the diffusion controlled limit. In comparison with $Ru(bpy)_3^{2+}$, the formation of relatively high steady-state concentrations of electron-transfer products is favored in the $Os(bpy)_3^{2+}$ system on account of the lower reduction potential of the $Os(bpy)_3^{3+}$ complex. On the other hand, the efficient quenching of the short-lived $Os(bpy)_3^{2+}$ excited state (τ = 19.2 nsec at 25°) requires high quencher concentrations. In the case of a highly colored quencher this produces a relatively large decrease of the incident light intensity, or, in the case of Fe^{3+} as quencher, the net oxidation of the osmium(II) complex.

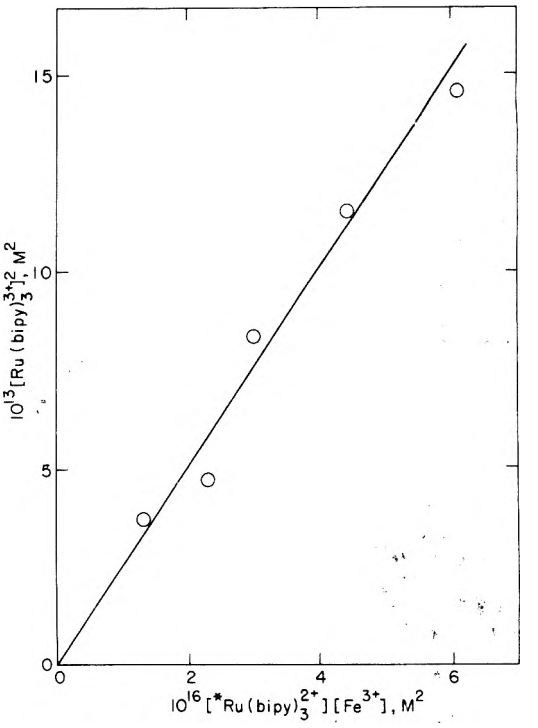

Figure 6. Plot of the square of the steady-state concentration of $Ru(bpy)_3^{3+}$ or Fe^{2+} vs. the product of the $*Ru(bpy)_3^{2+}$ and Fe^{3+} concentrations in 0.5 M $HClO_4$ at an incident light intensity of 1.12×10^{-8} einstein cm^{-2} sec^{-1}.

Overall, the advantage of the slower thermal electron-transfer rates in $Os(bpy)_3^{2+}$ system is overcome by the shorter lifetime of its excited state.

Photogalvanic Cell. The potential changes produced upon illumination of dilute aqueous solutions of redox couples have been recognized for a number of years.[30] These potentials are a consequence of the changed composition of the irradiated solution relative to the unirradiated one. The iron–thionine system provides perhaps the best known example of this type of photogalvanic effect. Cells based upon this system have been extensively studied since 1940[31] and a mathematical model describing some properties of these cells has recently been proposed.[32a] Because of their very low efficiencies, photogalvanic cells have not been seriously considered as a practical means of converting light into electricity. However the recent development of semiconductor electrodes and thin layer devices affords the possibility of greatly enhancing the efficiencies of such cells.

Unlike the iron–thionine system in which the dye is reduced in light and oxidized in the dark, in the $Ru(bpy)_3^{2+}$–Fe^{3+} system the "dye" is oxidized in light and reduced in the dark. The iron–thionine and the $Ru(bpy)_3^{2+}$–Fe^{3+} cells give comparable microamp current outputs under our conditions (using a cell of extremely inefficient design). The latter system possesses some advantages over the former: $*Ru(bpy)_3^{2+}$ is reasonably stable with respect to reaction with oxygen, especially in the presence of an efficient and stable quencher such as Fe^{3+}. Furthermore the maximum absorption peak (452 nm) for the $Ru(bpy)_3^{2+}$ complex is close to the maximum energy peak (~460 nm) of the solar spectrum. No reactive intermediates (which give rise to undesirable side reactions in the iron–thionine cell) are involved in the kinetic scheme (eq 8).

The potentials generated in the $Ru(bpy)_3^{2+}$–Fe^{3+} cell upon illumination are consequences of the differences in

the compositions of the solutions in the dark and illuminated compartments. The disappearance of these potentials on the addition of either $Ru(bpy)_3^{3+}$ or Fe^{2+} clearly establishes that the two active species in the $Ru(bpy)_3^{2+}$–Fe^{3+} system are Ru(III) and Fe(II) generated in the quenching process. Similarly, the dependence of the potential on the incident light intensity (Figure 5) can be rationalized in terms of variations in the concentrations of $Ru(bpy)_3^{3+}$ and Fe^{2+} with light intensity. The photogalvanic potentials can be estimated as follows.[32b] The fluxes at the electrode surface are given by

$$f_{Fe^{3+}} = -f_{Fe^{2+}} = k_{hs1}\,(ae^{-\alpha_1 \Delta U} - be^{(1-\alpha_1)\Delta U}) \quad (10a)$$

and

$$f_{Ru(III)} = -f_{Ru(II)} = k_{hs2}\,(ce^{-\alpha_2 \Delta U} - de^{(1-\alpha_2)\Delta U}) \quad (10b)$$

In these equations k_{hs1} and k_{hs2} are the electrochemical exchange rate constants (in cm sec^{-1}) of the $Fe^{2+}|Fe^{3+}$ and Ru(II)|Ru(III) couples, respectively, α_1 and α_2 are the corresponding electrochemical transfer coefficients, $\Delta U = RT\Delta E/nF$ where $\Delta E = (E_l - E_d)$ is the difference between the light and dark potentials, the subscripts l and d refer to light and dark conditions, respectively, and a, b, c, and d are defined by

$$a = [Fe^{3+}]_l([Fe^{2+}]/[Fe^{3+}])_d^{\alpha_1}$$

$$b = [Fe^{2+}]_l([Fe^{3+}]/[Fe^{2+}])_d^{1-\alpha_1}$$

$$c = [Ru(III)]_l([Ru(II)]/[Ru(III)])_d^{\alpha_2}$$

$$d = [Ru(II)]_l([Ru(III)]/[Ru(II)])_d^{1-\alpha_2} \quad (10c)$$

In this equation the concentrations are those obtaining at the surface of the electrode. If it is assumed that the cell is on open circuit then the flux of electrons at the electrode is zero. Under these conditions the flux of Fe^{3+} at the electrode surface is equal to the Ru(II) flux (while, in the opposite direction, the Fe^{2+} flux is equal to the Ru(III) flux) and eq 10a and 10b may be *added* to give

$$0 = k_{hs1}\,(ae^{-\alpha_1 \Delta U} - be^{(1-\alpha_1)\Delta U}) + k_{hs2}\,(ce^{-\alpha_2 \Delta U} - de^{(1-\alpha_2)\Delta U}) \quad (11)$$

If it is now assumed that $\alpha_1 = \alpha_2 = 0.5$[33] then eq 11 reduces to

$$e^{\Delta U} = \frac{ak_{hs1} + ck_{hs2}}{bk_{hs1} + dk_{hs2}} \quad (12)$$

Finally if $k_{hs2} \gg k_{hs1}$ then eq 12 simplifies to

$$\Delta U = \log \frac{[Ru(II)]_d}{[Ru(III)]_d} - \log \frac{[Ru(II)]_l}{[Ru(III)]_l} \quad (13)$$

which is the potential calculated by substituting the light and dark ruthenium concentrations into the Nernst equation. In other words, provided the electrochemical transfer coefficients for the two couples are each equal to 0.5 and the surface and bulk concentrations are equal, the open-circuit potential will be determined by the couple with the larger electrochemical rate constant.

The potentials calculated from eq 13 are the maximum values for photogalvanic cells of this type. Substituting bulk (not surface) concentrations calculated under typical conditions into eq 13 (e.g., a ruthenium(III) concentration in the illuminated compartment of 4×10^{-6} M in 0.5 M H_2SO_4) gives an upper limit of 0.19 V which is reasonable in the light of the observed value of 0.14 V (Table III).[36,38]

Finally, changing the substituents on the polypyridine rings of the ruthenium complex affords the possibility of increasing the lifetime of the emitting state of the ruthenium(II) and/or lowering the reduction potential of the ruthenium(III), thereby changing the steady-state concentrations and increasing the efficiency of the cell. The quenching behavior and the steady-state characteristics of systems of this type are currently under investigation in this laboratory.

Acknowledgments. This research was supported by the U.S. Energy Research and Development Administration. Helpful assistance from Drs. S. M. Lin and D. Hsu is appreciated. We thank Drs. C. Creutz and S. Feldberg for helpful discussions.

References and Notes

(1) (a) H. D. Gafney and A. W. Adamson, *J. Am. Chem. Soc.*, **94**, 8238 (1972); (b) J. N. Demas and A. W. Adamson, *ibid.*, **95**, 5159 (1973).
(2) P. Natarajan and J. F. Endicott, *J. Phys. Chem.*, **77**, 971 (1973).
(3) P. Natarajan and J. F. Endicott, *J. Phys. Chem.*, **77**, 1823 (1973).
(4) M. Wrighton and J. Markham, *J. Phys. Chem.*, **77**, 3042 (1973).
(5) C. R. Bock, T. J. Meyer, and D. G. Whitten, *J. Am. Chem. Soc.*, **96**, 4710 (1974).
(6) G. Navon and N. Sutin, *Inorg. Chem.*, **13**, 2159 (1974).
(7) G. S. Laurence and V. Balzani, *Inorg. Chem.*, **13**, 2976 (1974).
(8) C. R. Bock, T. J. Meyer, and D. G. Whitten, *J. Am. Chem. Soc.*, **97**, 2909 (1975).
(9) C-T. Lin and N. Sutin, *J. Am. Chem. Soc.*, **97**, 3543 (1975).
(10) C. Creutz and N. Sutin, *Inorg. Chem.*, in press.
(11) (a) F. H. Burstall, F. P. Dwyer, and E. C. Gyarfas, *J. Chem. Soc.*, 953 (1950); (b) C. F. Liu, N. C. Liu, and J. C. Bailar, *Inorg. Chem.*, **3**, 1085 (1964).
(12) P. Pfeiffer and B. Werdelmann, *Z. Anorg. Allg. Chem.*, **263**, 31 (1950).
(13) J. R. Pladziewicz, T. J. Meyer, J. A. Broomhead, and H. Taube, *Inorg. Chem.*, **12**, 639 (1973).
(14) C. G. Hatchard and C. A. Parker, *Proc. R. Soc. London, Ser. A*, **235**, 518 (1956).
(15) (a) R. F. Chen, G. G. Vurek, and N. Alexander, *Science*, **156**, 949 (1967); (b) Y. Haas and G. Stein, *J. Phys. Chem.*, **75**, 3668 (1971); (c) J. N. Demas, E. W. Harris, C. M. Flynn, Jr., and D. Diemente, *J. Am. Chem. Soc.*, **97**, 3838 (1975).
(16) The shorter lifetime of the emitting state(s) of $Os(bpy)_3^{2+}$ relative to $Ru(bpy)_3^{2+}$ is of interest. Measurements at 77 K (ref 19) have shown that the shorter lifetime of $^*Os(bpy)_3^{2+}$ is primarily due to its much larger rate of nonradiative decay; its rate of radiative decay at low temperature is, in fact, slower than that of $^*Ru(bpy)_3^{2+}$. This result is somewhat surprising in view of the stronger spin–orbit coupling in the osmium complex and has been rationalized (ref 19) in terms of a possible higher degree of covalency in the osmium complexes, and the fact that all of the components of the triplet state may not be equally involved in the emission process (see also ref 20).
(17) Trifluoromethylsulfonic acid was used for these measurements since larger photogalvanic effects were observed in the presence of this acid than with hydrochloric or sulfuric acid, and the system was more stable than when perchloric acid was used.
(18) Note, however, that the bands in the spectrum of the osmium complex are shifted to higher energy relative to those of the corresponding iron complex, despite the greater ease of oxidation of the metal center in the osmium complex.
(19) J. N. Demas and G. A. Crosby, *J. Am. Chem. Soc.*, **93**, 2841 (1971).
(20) R. W. Harrigan, G. D. Hager, and G. A. Crosby, *Chem. Phys. Lett.*, **21**, 487 (1973).
(21) G. A. Crosby, K. W. Hipps, and W. H. Elfring, Jr., *J. Am. Chem. Soc.*, **96**, 629 (1974).
(22) E. F. Lytle and D. M. Hercules, *Photochem. Photobiol.*, **13**, 123 (1971).
(23) This estimate of $(E^\circ)^*$ is consistent with the value of -0.81 ± 0.02 V reported recently for the $Ru(bpy)_3^{3+}|{}^*Ru(bpy)_3^{2+}$ couple in acetonitrile containing 0.1 M tetra-*n*-propylammonium perchlorate (C. R. Bock, T. J. Meyer, and D. G. Whitten, *J. Am. Chem. Soc.*, **97**, 2909 (1975)). The agreement is good evidence for the assumption made above, and also earlier (ref 6), that the entropy difference between the ground and excited states of $Ru(bpy)_3^{2+}$ is small.
(24) The above procedure has also been used (ref 10) to estimate the potential of the $^*Ru(bpy)_3^{2+}|Ru(bpy)_3^{+}$ couple from the free energy change for reaction 6 and the $Ru(bpy)_3^{2+}|Ru(bpy)_3^{+}$ potential.
(25) F. P. Dwyer, N. A. Gibson, and E. C. Gyarfas, *J. Proc. R. Soc. N.S.W.*, **84**, 80 (1950).
(26) No direct evidence has been obtained whether the quenching of $^*Ru(bpy)_3^{2+}$ or $^*Os(bpy)_3^{2+}$ by molecular oxygen proceeds primarily by an energy- or an electron-transfer mechanism. The reported[27] formation of singlet oxygen in the quenching reactions could be accounted for in terms of an electron-transfer mechanism by postulating that the $M(bpy)_3^{3+}$ and O_2^- produced in the quenching rapidly react to form $M(bpy)_3^{2+}$ and $^1O_2$.
(27) (a) J. N. Demas, D. Diemente, and E. W. Harris, *J. Am. Chem. Soc.*, **95**,

6864 (1973); (b) J. N. Demas, E. W. Harris, C. M. Flynn, Jr., and D. Diemente, *ibid.*, **97**, 3838 (1975).
(28) B. M. Gordon, L. L. Williams, and N. Sutin, *J. Am. Chem. Soc.*, **83**, 2061 (1961).
(29) M. H. Ford-Smith and N. Sutin, *J. Am. Chem. Soc.*, **83**, 1830 (1961).
(30) E. K. Rideal and E. C. Williams, *J. Chem. Soc.*, **127**, 258 (1925).
(31) E. Rabinowitch, *J. Chem. Phys.*, **8**, 551 (1940).
(32) (a) R. Gomer, *Electrochim. Acta*, **20**, 13 (1975); (b) S. W. Feldberg, personal communication.
(33) Values of 0.42, 0.61, and 0.62 have been reported for the electrochemical transfer coefficient for the reduction $Fe^{3+} + e^- \rightleftharpoons Fe^{2+}$ at a Pt electrode in 1 *M* H_2SO_4 (ref 34). The electrochemical transfer coefficient for the reduction of $Ru(bpy)_3^{3+}$ has not been reported. There are theoretical grounds for expecting that electrochemical transfer coefficients will not, in general, differ greatly from 0.5 (ref 35).
(34) (a) H. Gerischer, *Z. Elektrochem.*, **54**, 366 (1950); (b) M. D. Wijnen and W. M. Smit, *Recueil*, **79**, 289 (1960).
(35) R. A. Marcus, *J. Phys. Chem.*, **67**, 853 (1963).
(36) The electrochemical rate constants (cm sec^{-1}) for the $Fe^{2+}|Fe^{3+}$ coupled are 7 × 10^{-3}, 1 *M* $HClO_4$, Hg electrode, 25° (ref 37a); 3 × 10^{-3}, 1 *M* H_2SO_4, Pt electrode (ref 34a); 5 × 10^{2}, 1 *M* H_2SO_4, Pt electrode (ref 34b). The electrochemical rate constant for the $Ru(bpy)_3^{2+}|Ru(bpy)_3^{3+}$ couple has not been reported although a value of 1.1 cm sec^{-1} has been published for the analogous iron complex in DMF at 25° (ref 37b). The latter value probably represents a lower limit (ref 37c). Based on the homogeneous exchange rates of the $Fe^{2+}|Fe^{3+}$ and $Ru(bpy)_3^{2+}|Ru(bpy)_3^{3+}$ couples, the electrochemical rate constant for the latter couple is expected to be $\geq 10^4$ times larger than the former (ref 35).
(37) (a) J. E. B. Randles and K. W. Somerton, *Trans. Faraday Soc.*, **48**, 937 (1952); (b) T. Saji, T. Yamada, and S. Aoyagui, *Bull. Chem. Soc. Jpn.*, **48**, 1641 (1975); (c) T. Saji, T. Yamada, and S. Aoyagui, *Electroanal. Chem. Interfacial Electrochem.*, **61**, 147 (1975).
(38) The difference between the surface and bulk concentrations will tend to be small when the individual fluxes are very small or when the homogeneous electron transfer rates (in the presence of light) are very large.

Kinetics of the Permanganate–Bromide Reaction at Low Reagent Concentrations

Samuel A. Lawani

Department of Chemistry, State University College, Buffalo, New York 14222 *(Received August 7, 1975)*

A study of the kinetics of the permanganate–bromide reaction at low reagent concentrations has been done at 25.1°C using a stopped-flow spectrophotometer. The monitoring was achieved by following the disappearance of permanganate, $MnO_4^- + 5Br^- + 8H^+ \rightarrow Mn^{2+} + \frac{5}{2}Br_2 + 4H_2O$, at 520 nm and the appearance of Br_3^-, $Br_2 + Br^- \rightleftharpoons Br_3^-$, at 267 nm. The reaction changes from first order to zero order with respect to permanganate as the reagent concentrations become lower; and the orders with respect to bromide and hydrogen ion concentrations are two and three, respectively. A mechanism which fits these findings is $2H^+ + Br^- + MnO_4^- \rightleftharpoons (H_2MnO_4Br)$ (K); $(H_2MnO_4Br) + H^+ + Br^- \rightarrow H_3MnO_4 + Br_2$ (k). The activation parameters for the rate constant, k_0, are $\Delta H^* = 1.4 \pm 0.1$ kcal/mol and $\Delta S^* = -19.9 \pm 0.4$ eu.

Introduction

The kinetics of the reaction between permanganate and bromide ions at high reagent (Br^- and H^+) concentrations was studied by Lawani and Sutter.[1] Their aim was to elucidate the mechanism of this redox reaction in acid medium. It was found that the results can be explained in terms of a set of coupled first-order reaction scheme:

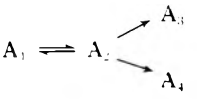

where A_1 is permanganate and the other A's are intermediates formed with MnO_4^- ion. However, at very low reagent concentrations this scheme no longer holds. Since the data obtained for the high reagent concentration region were extensive and complex to analyze, no attempt was made to pursue the very low concentration region. The purpose of the study presented here is to show how the electron-transfer mechanism changes from first to zero order with respect to $[MnO_4^-]$ in the latter region.

Experimental Section

The procedure, instruments, and chemicals used in this study are the same as described by Lawani and Sutter. The only difference is in the treatment of raw data. Photographs of the kinetic traces were read and, with the help of a computer program, the readings were converted to absorbances, D. Since $(D - D_\infty)$ would be negative at 267 nm where Br_3^-, MnO_4^-, and Br_2 absorb but positive at 520 nm where only MnO_4^- absorbs, the computer was instructed to plot absolute values of $(D - D_\infty)$ vs. time and take the slopes. Stoichiometric determinations[1] show that the reaction proceeds according to the equation

$$MnO_4^- + 5Br^- + 8H^+ \rightarrow Mn^{2+} + \tfrac{5}{2}Br_2 + 4H_2O$$

Results

It was previously reported[1] that at low bromide and hydrogen ion concentrations the first-order plots are concave down at the beginning, becoming linear after a length of time. As the concentrations become lower a stage is finally reached where only the last few points at the end of the plot lie on a straight line (see Figure 1). At this point one begins to question the validity of the first-order plot. A zero-order plot for the same set of data gives a straight line with only a few points falling off at the end as shown in Figure 2. The plots in Figures 1 and 2 are chosen because they illustrate the change from one order to another; but most of the data presented here comes from plots at even lower concentrations where most or all of the data obey the zero-order rate law. The slopes of the zero-order plots are designated as the observed rate constants, k_{obsd}.

A plot of k_{obsd} vs. $[Br^-]^2$ is linear with an intercept which

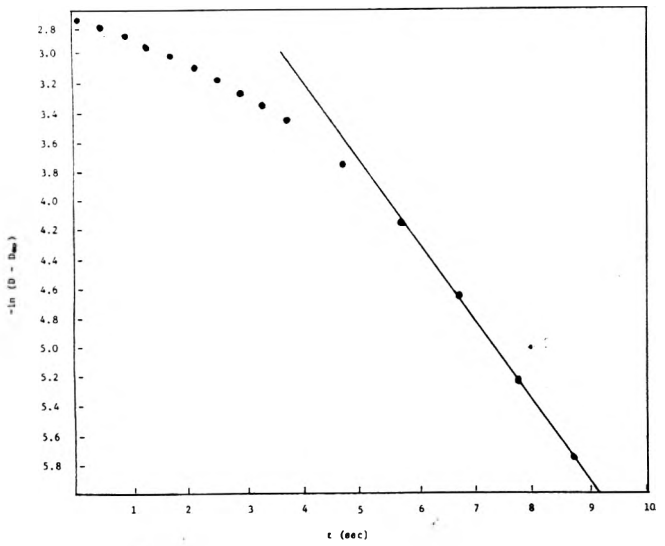

Figure 1. Concave down first-order plot: $[Br^-] = 4.00 \times 10^{-2}$ *M*; $[H^+] = 0.265$ *M*; $[MnO_4^-]_0 = 1.47 \times 10^{-5}$ *M*; temperature = 25.1°C; ionic strength, $I = 0.919$ *M*.

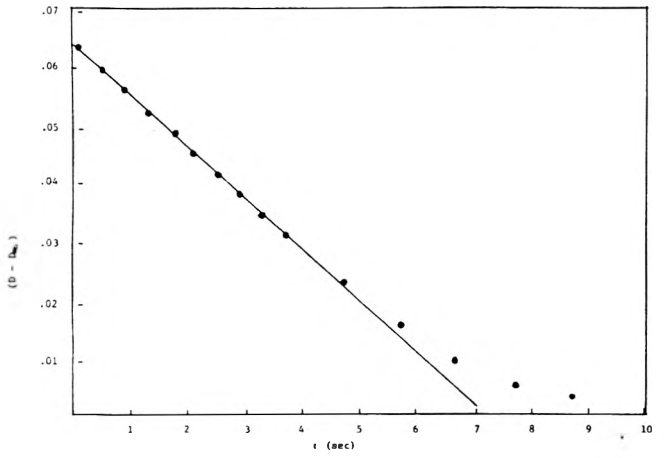

Figure 2. Zero order plot for the same data in Figure 1.

is approximately zero by the least-squares method. Table I shows the experimental data. All k_{obsd} values in this work are pseudo in $[Br^-]$ and $[H^+]$ which are in high excess compared to $[MnO_4^-]$. The hydrogen ion dependence is shown in Table II. A plot of k_{obsd} against $[H^+]^3$ is linear with an essentially zero intercept. The k_{obsd} with all concentration terms removed is represented as k_0. The value of k_0, calculated from $[Br^-]$ dependence, is $(2.35 \pm 0.02) \times 10^7\ M^{-5}$ sec^{-1} while a value of $(3.79 \pm 0.09) \times 10^7\ M^{-5}$ sec^{-1} is obtained from $[H^+]$ dependence. Each $[H^+]$ given here had to be calculated for several reasons. First, the second dissociation of sulfuric acid is not complete and secondly, K^+ ions from the KBr used as the reducing agent and the K_2SO_4 used to keep the ionic strength constant associate with SO_4^{2-} ions.[2] A combination of the Davies[3] equation and the work of Jenkins and Monk[2] was used to arrive at the $[H^+]$ values by the method of successive approximations. For this reason one cannot rely on these quantities as much as on bromide ion concentrations which were measured directly. This in turn means that the true rate constant, k_0, from $[Br^-]$ dependence should be more dependable.

The temperature dependence of the true rate constant (see Table IV) was used in a least-squares computer program which gave $\Delta H^* = 1.4 \pm 0.1$ kcal/mol and $\Delta S^* = -19.9 \pm 0.4$ eu.

TABLE I: Dependence of Observed Rate Constants on Bromide Ion Concentrations[a]

$[Br^-]$, *M*	$10^2 k_{obsd}$, *M* sec^{-1}	$[Br^-]$, *M*	$10^2 k_{obsd}$, *M* sec^{-1}
0.040	6.61	0.010	0.520
0.030	3.63	0.006	0.226
0.020	1.79	0.005	0.168

[a] $[H^+] = 0.265$ *M*; $[MnO_4^-]_0 = 9.25 \times 10^{-5}$ *M*; ionic strength, $I = 0.919$ *M*; temperature = 25.1°C.

TABLE II: Dependence of Observed Rate Constants on Hydrogen Ion Concentrations[a]

$[H_2SO_4]$, *M*	$[H^+]$, *M*	$10^2 k_{obsd}$, *M* sec^{-1}
0.10	0.132	4.24
0.08	0.106	2.50
0.06	0.079	1.11
0.04	0.053	0.623
0.02	0.027	0.225

[a] $[Br^-] = 0.10$ *M*; $[MnO_4^-]_0 = 4.63 \times 10^{-5}$ *M*; temperature = 25.1°C; $I = 0.919$ *M*.

Discussion

A mechanism which fits the observed behavior of this reaction is the following

$$2A + B + C \overset{K}{\rightleftharpoons} D \qquad (I)$$

$$D + A + B \overset{k}{\rightarrow} \text{products} \qquad (II)$$

where $A = H^+$, $B = Br^-$, and $C = MnO_4^-$. If step II is much slower than step I, the former may be neglected in calculating the concentration of D, which is given by

$$[D] = K[A]^2[B][C] \qquad (II')$$

In the early life of the reaction, approximately

$$[A] = [A]_0 - 2[D];\ [B] = [B]_0 - [D];\ [C] = [C]_0 - [D] \qquad (III)$$

where the zero subscript indicates initial concentration. Since $[C]_0 \ll [A]_0$ or $[B]_0$ one may use, as an approximation, the initial concentrations $[A]_0$ or $[B]_0$ instead of [A] or [B]. Under these conditions eq II′ becomes

$$[D] = K[A]_0^2[B]_0([C]_0 - [D])$$

Solving for [D] gives

$$[D] = \frac{K[A]_0^2[B]_0[C]_0}{1 + K[A]_0^2[B]_0}$$

Using this in step II of the mechanism the rate law becomes

$$-\frac{d[C]}{dt} = \frac{kK[A]_0^3[B]_0^2[C]_0}{1 + K[A]_0^2[B]_0}$$

Under the conditions of this work the product $[A]_0^2[B]_0$ ranges from 10^{-4} to 10^{-5} which suggests that $K[A]_0^2[B]_0$ may be negligible compared to unity. Hence the rate law becomes

$$-d[C]/dt = k_0[A]_0^3[B]_0^2[C]_0 = k_{obsd}$$

where $k_0 = kK$.

TABLE III: Dependence of Observed Rate Constants on Initial Permanganate Concentrations[a]

$[Br^-]$, M	$10^3 k_{obsd}$, M sec^{-1}	k_1, M^{-4} sec^{-1}	$[MnO_4^-]_0$, M	$10^{-7}k_0$, M^{-5} sec^{-1}
0.040	9.02	0.303	1.47×10^{-5}	2.06
0.040	99.7, 100	3.35, 3.39	1.49×10^{-4}	2.23, 2.26
0.020	2.37, 2.44	0.318, 0.328	1.47×10^{-5}	2.16, 2.23

[a] $[H^+] = 0.265$ M; ionic strength = 0.919 M; temperature = 25.1°C. Two values side by side indicate repeat runs.

TABLE IV: Temperature Dependence of the Observed and True Rate Constants[a]

Temp, °C	$10^2 k_{obsd}$	$10^{-7}k_0$
25.1	10.6	2.37
20.6	10.1	2.28
16.1	9.73	2.19
11.9	8.97	2.01

[a] $[MnO_4^-]_0 = 1.49 \times 10^{-4}$ M; $[H^+] = 0.265$ M; $[Br^-] = 0.040$ M; ionic strength = 0.919 M.

The zero-order plots being linear support this rate law. Furthermore, Table III in which both $[Br^-]$ and $[MnO_4^-]_0$ are varied lends more support to this rate equation. When the k_{obsd} have been stripped of their bromide and hydrogen ion dependence the resulting $k_0[C]_0$ values, designated as k_1, are in direct proportion to $[MnO_4^-]_0$. In terms of the actual reagents the mechanism is

$$2H^+ + Br^- + MnO_4^- \overset{K}{\rightleftharpoons} (H_2MnO_4Br)$$

$$(H_2MnO_4Br) + H^+ + Br^- \xrightarrow{k} H_3MnO_4 + Br_2$$

Equation III holds only in the early stages of the reaction and this accounts for some data points falling off at the end of the straight line in the zero-order plot. Neglecting this equation at the later stages, the mechanism in I and II above leads to a rate law which is first order in $[MnO_4^-]$. This is supported by Figure 1.

The mechanism proposed here involves a two-equivalent electron transfer step which is in agreement with some previous findings in permanganate redox reactions.[1,4,11] The rate law above is exactly the same as obtained for the MnO_4^-–Cl^- reaction[5] except that the rate did not depend on initial permanganate concentration. A two-electron transfer step was also suggested for that reaction. The value of ΔS^* for the present study indicates an entropy loss which may not be as big as one might expect since the mechanism shows that six reactant species combine to form only two product molecules. However, three hydrogen ions are involved in the mechanism, and according to Eigen[6] a proton has four water molecules attached to it as $H_9O_4^+$. When ions of opposite charges react the charges are neutralized and some, if not all, of the solvent molecules are released.[7] Although the bromide ion is not solvated[8] and will therefore have no solvent to release, the number of water molecules set free by the protons is enough to affect the overall entropy change appreciably.

The complex (H_2MnO_4Br) proposed here is not unreasonable because it is similar to $K_2OsO_4(OH)_2$ which has been isolated.[9] In the reactions between RuO_4^- and OH^- and ReO_4^- and OH^-, the intermediates $[RuO_4(OH)_2]^{3-}$ and $[ReO_4(OH)_2]^{3-}$, respectively, were proposed.[10] Permanganate, being similar to these oxyanions, would also be expected to coordinate other species in a similar manner.

A striking similarity in the permanganate–bromide and permanganate–cyanide[11] reactions is that each of them has two concentration regions, each region obeying a different rate law. In the MnO_4^-–CN^- reaction the rate law was found to be first order in both MnO_4^- and CN^- when their concentrations were low and the concentration of OH^- high. At high reagent concentrations and low $[OH^-]$, the rate was first order in $[MnO_4^-]$, second order in $[CN^-]$, and inverse first order in $[OH^-]$. The findings by Lawani and Sutter along with the present study show that at high reagent (Br^- and H^+) concentrations the rate law is first order in MnO_4^- but zero order in the same reactant at very low reagent concentrations. It is assumed that the reaction proceeds by two concurrent mechanisms, the predominant one being determined by the magnitudes of the bromide and hydrogen ion concentrations.

References and Notes

(1) S. A. Lawani and J. R. Sutter, *J. Phys. Chem.*, **77**, 1547 (1973).
(2) I. L. Jenkins and C. B. Monk, *J. Am. Chem. Soc.*, **72**, 2695 (1950).
(3) C. W. Davies, "Ion Association", Butterworths, Washington, D.C., 1962, p 39.
(4) L. J. Kirschenbaum and J. R. Sutter, *J. Phys. Chem.*, **70**, 3863 (1966).
(5) K. J. Liu, H. Lester, and N. C. Peterson, *Inorg. Chem.*, **5**, 2128 (1966).
(6) M. Eigen, *Proc. R. Soc. London, Ser. A*, **247**, 505 (1958).
(7) K. J. Laidler, "Chemical Kinetics", 2nd ed, McGraw-Hill, New York, N.Y., p 216.
(8) O. Ya. Samoilov, *Discuss. Faraday Soc.*, **24**, 141 (1957).
(9) F. Krauss and D. Wilken, *Z. Anorg. Chem.*, **145**, 151 (1925).
(10) A. Carrington and M. C. R. Symons, *J. Chem. Soc.*, 284 (1960).
(11) R. Stewart and van der Linden, *Can. J. Chem.*, **38**, 2237 (1960).

The Role of the Triplet State in the Photocoloration of the Dianthrones. A Reinvestigation

T. Bercovici, R. Korenstein, G. Fischer, and E. Fischer*

Department of Structural Chemistry, The Weizmann Institute of Science, Rehovot, Israel *(Received May 21, 1975)*

Flash-photolytic investigations show conclusively that photocoloration in the dianthrones, to form the B isomer, takes place via the triplet state of the starting isomer A. Supporting evidence is provided by triplet sensitization experiments, in which B is formed exclusively, under conditions where isomer C is the sole product of direct excitation of A.

In an earlier paper[1a] we provided detailed evidence for our conclusion that in dianthrone, I, and its derivatives the photocoloration to what is by now commonly called the "B" form passes through the triplet state of the starting form A:

$$A \xrightarrow{h\nu} {}^1A^* \longrightarrow {}^3A^* \longrightarrow D \longrightarrow B$$

(D is an unstable isomeric precursor of B). This conclusion was elaborated in a recent note,[1b] but contradicts earlier results by Huber and coworkers[3] who tried to correlate the triplet state and the formation of the photochromic isomer, in particular in triacetin solutions. According to Huber[3] and to a more recent paper by Gschwind and Wild,[2] most if not all the optical absorption in the visible region assigned to B, and arising from uv irradiation, *appears* virtually instantaneously, i.e., within the time resolution of the experimental setup (ca. 0.05 msec), while the triplet absorption *decays* at a much slower rate. No D was observed by these authors. They therefore concluded that B is formed directly from the excited singlet of A, parallel to the triplet:

$$A \xrightarrow{h\nu} {}^1A^* \begin{cases} \nearrow {}^3A^* \\ \searrow B \end{cases}$$

No clear-cut distinction between the colored B and C isomers was established by the above authors, though at sufficiently low temperatures little, if any, C is formed.[1a] The nature of B and C was established recently.[4]

In an effort to reconcile the results of both groups, and to find the possible reasons for the obvious discrepancies, we have now carried out additional flash experiments, using dilute solutions of the tetramethyl derivative II investigated by both groups, in three widely differing solvents: a mixture of aliphatic hydrocarbons (methylcyclohexane–2-methylpentane, 1:1), a mixture of alcohols (1-propanol–2-propanol, 3:2), and the highly viscous triacetin (glycerol triacetate). In addition, earlier[1b] sensitization experiments with the dimethyl derivative III, dissolved in methylene chloride, were extended, and carried out also with I and II.

As described earlier, the photoformation of D and B is controlled by the nature and the viscosity of the solvent medium in which A is dissolved. For each solvent a temperature T_1 exists at which practically no photocoloration is observed in flash photolysis, except that ascribed to the triplet $^3A^*$. (No disagreements exist regarding this point.) At a somewhat higher temperature T_2 the viscosity is sufficiently lower to allow formation of D, the precursor[1] of B. At this temperature the kinetics of the formation of D, and the subsequent spontaneous conversion D → B, can be followed flash photolytically. The photocyclization product "C", the formation of which is strongly temperature dependent,[1a] is formed to some extent at T_2 in triacetin, and not at all in the other two solvents. Since it is thermally stable at T_2, it gives rise to a permanent increase in absorption at its main peaks, in the range 410–500 nm, and at its minor peak, in the range 550–750 nm. At T_2, isomer B, the absorption of which covers the range 500–750 nm (cf. Figure 1) is the only stable photoproduct in 1P–2P and in MCH–2MP, and the major one in TA. Table I summarizes the values of T_1 and T_2 employed in the present study.

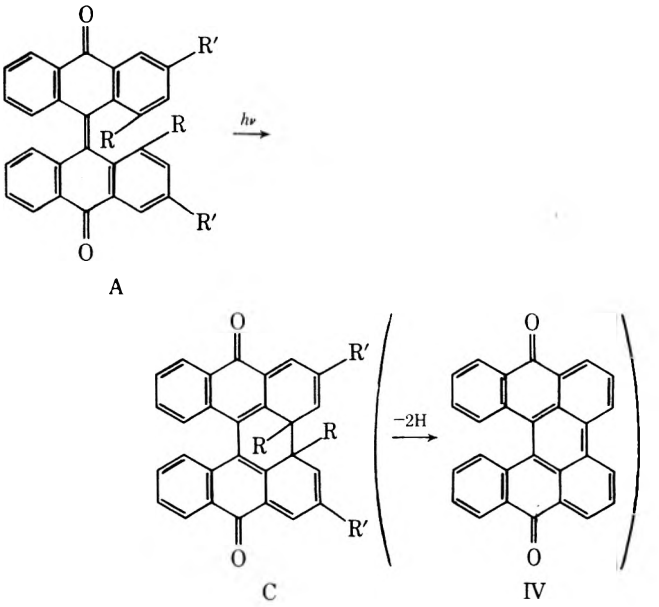

I: R = R′ = H; II: R = R′ = CH_3; III: R = CH_3; R′ = H

The kinetics of decay of the triplet $^3A^*$ and of formation and decay of D were followed, as before,[1] at 490 and 720 nm, respectively. (On the time scale of the present experiments the formation of the triplet $^3A^*$ is instantaneous.) With each solvent flash-photolytic experiments were carried out at two temperatures T_1 and T_2. Each kinetic curve was taken concurrently on two identical oscilloscopes operating at different time scales. In Figure 2 we present the results obtained with a 5×10^{-5} M solution of II in 1P–2P. The results in MCH–2MP closely parallel those in the propanol mixture at the corresponding temperatures. Figure 3 shows the observations in a similar solution in TA.

The results in the first two solvents can be summarized as follows (Figure 2). (a) At T_1 transient absorptions a and b appear "instantaneously" at both 490 and 720 nm, and

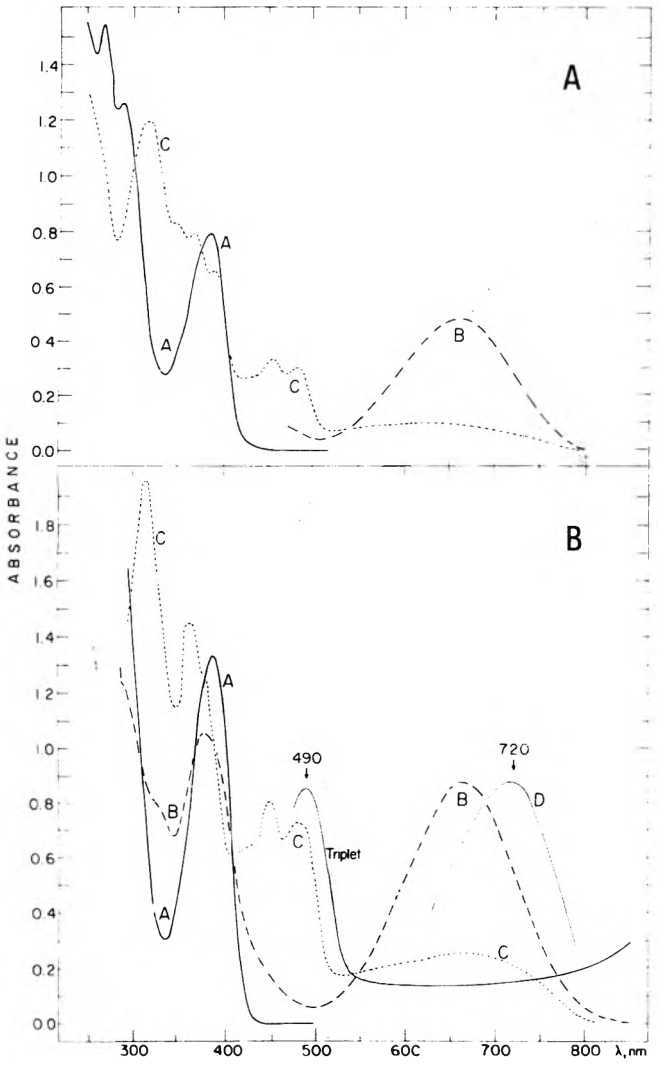

Figure 1. Absorption spectra of the various isomeric forms of compound II and III. The curves are named as detailed in text. (A) Compound III in CH_2Cl_2, at −70°. Curve C was obtained by 405-nm irradiation, and is completely reconverted into A by irradiation at 546 + 578 nm. Curve B was obtained by 436-nm irradiation of the same solution, to which biacetyl had been added to give a 0.1 *M* solution. (B) Compound II in triacetine. The absorption curves of D and of triplet A were obtained at −78° ($^3A^*$ by means of flash photolysis), B and C at −70°. Curve B resulted from 366-nm irradiation, followed by 546 + 578-nm irradiation to erase C, and describes a mixture of ca. 80% B and 20% A. Curve C was obtained by extrapolation,[1a] and describes the absorption calculated for the pure C isomer.

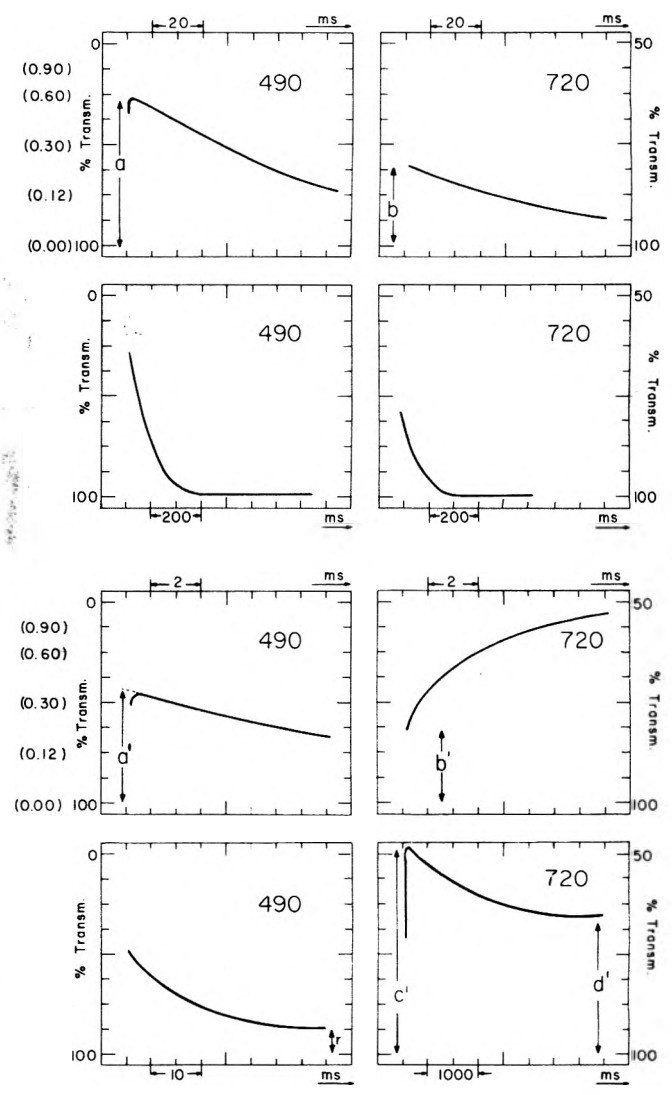

Figure 2. Oscilloscope traces obtained in flash-photolytic measurements of solutions of II in 1P–2P at −169 and −154°, at 490 and at 720 nm. The initial rise at 490 nm is higher at −169°, because in the experiment at −154° the solution had already been flashed several times, and a considerable part of A thereby converted into B. Wavelengths and time scales as indicated in each figure; upper part at −169°, lower part at −154°, at otherwise identical conditions. Optical density values are given in parentheses at the left-side vertical scale. The meaning of *a*, *b*, and *a'*–*d'* is explained in the text.

TABLE I: Values of T_1 and T_2 Employed with Various Solvents

Solvent[a]	MCH–2MP	1P–2P	TA
T_1, °C	−186	−169	−78
T_2, °C	−173	−154	−60

[a] MCH = methylcyclohexane, 2MP = 2-methylpentane, 1P = 1-propanol, 2P = 2-propanol, TA = glycerol triacetate, commonly known as triacetin.

decay to zero at identical rates at both wavelengths. (b) At T_2, an "instantaneous" increase b' in absorption at 720 nm is followed by a further slow increase up to c' and then a decrease to a stable value d'. b' is identical with b. At 490 nm, a transient absorption a' decays to a low final value r at a rate similar to that of the slow *increase* at 720 nm. The values for a, b, a', b', c', and d' in Figure 2, expressed as optical densities, were as follows: $a = 0.60$, $b = b' = 0.09$, $a' = 0.36$, $c' = 0.32$, $d' = 0.18$. As usual in such measurements, the oscilloscope trace measures percent absorption (100% − percent transmission) vs. time. It is therefore greatly distorted at low transmissions, as compared with the corresponding curve of optical density vs. time, in particular if the full-scale vertical deflection of the scope corresponds to the complete transmission range 0–100%. (Cf. left side scale of Figure 2, where optical density values are given in parentheses.)

We explain these results as follows. At T_1 the only transient is triplet $^3A^*$, which returns practically completely to ground-state A, because of the viscosity controlled energy barrier[1] separating it from the primary photoproduct D: A ← $^3A^*$ ↛ D. At T_2 this barrier is passed at a rate much beyond that of the return to the ground state, so that we ob-

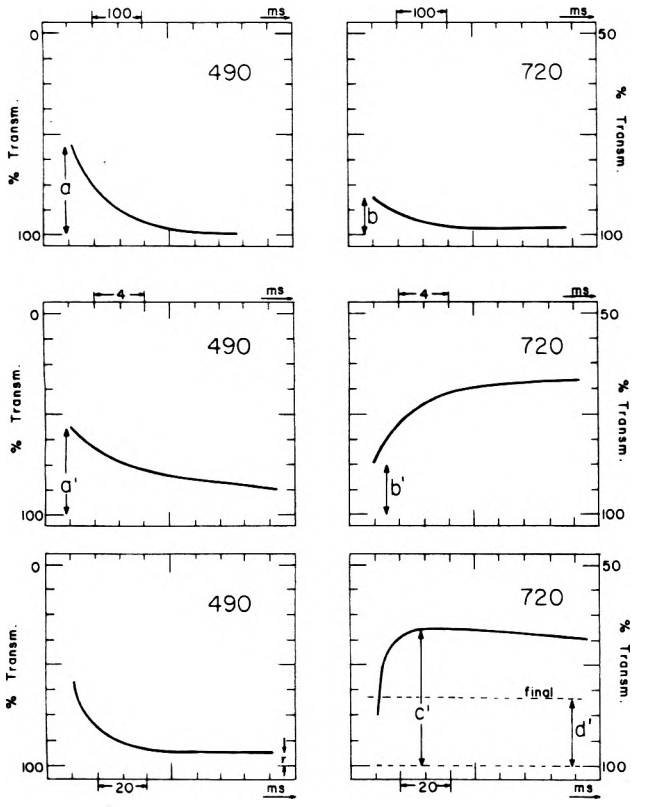

Figure 3. Oscilloscope traces obtained in flash-photolytic measurements of solutions of compound II in TA at −78° (upper half) and at −60° (lower half), at 490 and 720 nm, and with the timescales as indicated in each case.

serve in effect A ⇌ ^{3}A* → D. The instantaneous increase in absorption at 720 nm at T_2 is *solely* due to ^{3}A* which, on the time scale of our experimental set-up, is formed "instantaneously" from ^{1}A*. Since D absorbs at 720 nm much more strongly than ^{3}A*, the gradual formation of D from ^{3}A* is accompanied by an *increase* in absorption. At 490 nm ^{3}A* absorbs much more than D and therefore a *decrease* in absorption is observed, parallel to the increase at 720 nm. The formation of D is followed by its spontaneous conversion into B, which again is a viscosity controlled reaction.[1] Since at 720 nm B absorbs less than D, this conversion results in a *decrease* in absorption, down to that of B, which is stable at T_2. This is why the absorption at 720 nm passes through a peak value with time, depending on the rates of the spontaneous processes ^{3}A* → D and D → B. The absorption of ^{3}A* extends all the way from the peak at 490 nm to that at 890 nm, first described by Wild;[2] at 720 nm it is about one seventh that at 490 nm (0.09 and 0.60, respectively).

In TA solutions, Figure 3, the results at first sight do not appear as straightforward. In particular, not all of the initial absorption at 720 nm and −60° is accounted for by the absorption due to ^{3}A*, as observed at −78°. Expressing the results as optical densities, we have $a = 0.27$, $a' = 0.26$, $b = 0.040$, $b' = 0.061$, $c' = 0.19$, and $d' = 0.087$. Thus, out of an initial rise at 720 nm of $b' = 0.06$, only $b = 0.04$ can be attributed to the triplet ^{3}A*, while 0.02 is not accounted for. However, this is still only 2/19, i.e., about 10%, of the total absorbance c' assigned to D formed under these conditions. We note two experimental complications encountered with solutions in TA. First, TA is not a stable solvent, and we succeeded to obtain reproducible results only with freshly distilled solvent, using an efficient fractionating column at reduced pressure. Second, the cyclization product C which is formed to some extent at −60°, directly from the singlet excited ^{1}A*, could account for some of the initial absorption at 720 nm. (Cf. Figure 1, curve C.)

We therefore conclude that in the first two solvents D, and therefore indirectly B, is formed solely via ^{3}A*, while in TA this is the major pathway, and possibly the sole one. Of course, these conclusions hold strictly only for the temperatures T_2 at which our measurements were made. In the absence of conflicting evidence we may assume a similar mechanism at higher temperatures too, though in principle a singlet mechanism may open up at high temperatures.

It remains now to explain the discrepancy between the above results and those of the Zurich group, who found no evidence for the existence of the D isomer in triacetin, and no correlation between the photocoloration to B and the decay of triplet ^{3}A*. Two technical reasons might be responsible: the quality of the solvent TA, and the intensity of the flash. The difficulties with the solvent TA have been mentioned above, and indeed experiments carried out in Zurich with *our* solution proved the existence of D, by obtaining decay curves at 720 nm which pass through a maximum, basically similar to our Figure 3 (lower part).[5] As far as the flash intensity is concerned, we have recently described[6a] a case in which the course of secondary thermal reactions is affected by it. However, we believe that in the present case the major reason for what *looks* like a large discrepancy even with the same solution is actually the simple one elaborated above, i.e., the low sensitivity of the measurements at low optical transmissions. The flash intensities in Zurich were probably about five times higher than ours, even using our short cells, and therefore a'–d' there were mostly in the range below 40% transmission.

It seems advisable that one should always operate at the lowest flash intensities which are still compatible with the required experimental accuracy. In view of the ease with which transmission changes in the range between 100% and, e.g., 60%, can be measured accurately, there is normally no reason to employ flash intensities causing changes in transmission beyond this range.

To summarize, it seems that the reports of instantaneous photocoloration in TMD solutions are based on the two technical points mentioned above, and on the fact that the optical absorption of triplet ^{3}A* and of C extend all through the visible range. The "instantaneous" formation of C via a singlet mechanism, regarding which no disagreement exists may thus be responsible for observed differences between b and b′ in Figures 2 and 3.[6b]

We note that this is one of the few examples in which the sequence excited singlet → triplet → photoproduct can be followed by conventional flash photolysis, and the variation with viscosity of the rate of the second step can be measured.[1a]

So much for results with TMD. As mentioned before,[1] low-temperature flash experiments with dianthrone itself, I, and with a variety of its derivatives available to us, have shown that in all cases the triplet mechanism of photocoloration is either the sole or at least the predominant one at the temperatures of investigation. (In most cases B is formed directly from ^{3}A*, without evidence of D.)

Indirect support for the triplet mechanism is provided by sensitization experiments,[1b,7] with biacetyl serving as a triplet sensitizer. We have now used a similar system to obtain more direct support. As reported,[1a,8] the ratio between

the two colored photoproducts B and C of II and of III is a function of the solvent and the temperature. In solutions of III in methylene chloride, CH_2Cl_2, C is virtually the sole photoproduct.[1a] We could now show that nevertheless irradiation at 436 nm (where only biacetyl absorbs) of a solution of III and biacetyl in CH_2Cl_2 forms exclusively the B isomer. Since it is commonly accepted that the photocyclization product C is formed directly from the excited singlet $^1A^*$, we conclude that in this solvent intersystem crossing $^1A^* \rightarrow {}^3A^*$ is inefficient and $^1A^*$ disappears mainly by photocyclization and by fluorescence:

$$A \xleftarrow{F} {}^1A^* \longrightarrow C$$

However, once $^3A^*$ is formed via energy transfer, it is transformed into B in this solvent just as in others: $^3A^* \rightarrow B$.

Relevant experiments were carried out both flash photolytically at and below room temperature, and at −70° in the Cary 14 spectrophotometer. C was identified by its double peak at 460 and 480 nm and by its photoconversion back into A with light at 546 and 578 nm. Typical concentrations employed were: biacetyl, 10^{-1} *M* and III, 5×10^{-5} *M*. Figure 1a describes an experiment at −70°. Very similar results were obtained with CH_2Cl_2 solutions of II and of I. In the presence of biacetyl, irradiation produces B in both cases. In the absence of biacetyl the major photoproduct of II is its C isomer, while I is photooxidized to helianthrone, IV, via a C-like precursor observable only by flash methods.[9]

Experimental Section

The low-temperature techniques have been described before.[10] The copper block technique was employed throughout. In the flash-photolytic experiments we used cells made of rectangular cross-section Pyrex tubing (4 × 12 mm inside) with a light path of 20 mm along the direction of the measuring light beam.[11] The peak optical density of the solutions at the 390-nm peak was about 0.4 in the direction of the flash (4 mm), so that homogeneous irradiation was assured. In the regular flash experiments the light from the flash tubes was passed through Corning 3863 colored glass filters. In view of the Pyrex Dewar and cell this meant an effective wavelength range of irradiation between 330 and 400 nm. In the sensitization experiments the wavelength range 410–450 nm was transmitted by means of a suitable filter combination. The flash apparatus[12] consisted of two oxygen-filled 10-cm flash tubes operating in series at up to 20 kV with either one or two 1 μF capacitors. A 100-W, 12-V tungsten–iodine monitoring lamp was used with suitable light filters, a 500-mm Bausch and Lomb monochromator, a 9558 EMI photomultiplier, and Tektronix 564 storage oscilloscopes.

References and Notes

(1) (a) T. Bercovici, R. Korenstein, K. A. Muszkat, and E. Fischer, *Pure Appl. Chem.*, **24**, 531 (1970), where earlier papers are cited extensively; (b) T. Bercovici and E. Fischer, *Helv. Chim. Acta*, **56**, 1114 (1973).
(2) K. H. Gschwind and U. P. Wild, *Helv. Chim. Acta*, **56**, 809 (1973).
(3) J. R. Huber, U. Wild, and Hs. H. Günthard, *Helv. Chim. Acta*, **50**, 841 (1967).
(4) R. Korenstein, K. A. Muszkat, and Sh. Sharafi-Ozeri, *J. Am. Chem. Soc.*, **95**, 6177 (1973).
(5) U. Wild, private communication.
(6) (a) G. Fischer, E. Fischer, K. H. Grellmann, H. Linschitz, and A. Temizer, *J. Am. Chem. Soc.*, **96**, 6267 (1974); (b) Professor Wild has meanwhile agreed[5] that under the circumstances this summary reflects the feelings of both groups.
(7) H. H. Richtol, R. L. Strong, and L. J. Dombrowski, *Israel J. Chem.*, **12**, 791 (1974).
(8) G. Kortum, *Ber. Bunsenges. Phys. Chem.*, **78**, 391 (1974).
(9) R. Korenstein, unpublished results.
(10) E. Fischer, *Mol. Photochem.*, **2**, 99 (1970).
(11) E. Fischer, *Mol. Photochem.*, **6**, 111 (1974).
(12) T. Bercovici, R. Heiligman-Rim, and E. Fischer, *Mol. Photochem.*, **1**, 23 (1969).

Radiolysis of Cytosine in Dilute Neutral Aqueous Solution

George Gorin,* Nobuko Ohno, and L. M. Raff

Department of Chemistry, Oklahoma State University, Stillwater, Oklahoma 74074 *(Received April 18, 1975)*

Publication costs assisted by the National Science Foundation

Cytosine, 0.1–10 m*M*, has been radiolyzed at constant dose rates in 0.02 *M* phosphate buffer, pH 7. If the pH is then adjusted to 3, the absorption of the radiolysis products at 275 nm becomes negligible, and the radiochemical decomposition yield $G(-\text{cyt})$ can be calculated from the decrease in absorbance. In oxygen-saturated solutions it is described by the expression (D^* = dose in krad): $G(-\text{cyt}) = 3.3 - 0.024D^*$ (to at least 40% decomposition). The radiolysis products react with the radicals derived from the solvent about one fifth as fast as cytosine does. The radiolysis products have appreciable absorbance at <260 nm and pH 3, and at 266 nm and pH 7 or 11. The spectral characteristics of the predominant products resemble those of known dihydrocytosine derivatives. In solutions containing >1 m*M* cytosine and initially saturated with air, the oxygen is soon depleted; in absence of oxygen, different radiolysis products having a *higher* absorbance are formed.

Introduction[1]

This paper describes an investigation of the radiolysis of cytosine in dilute, neutral aqueous solution. For the most part, the systems studied were saturated with oxygen, but some experiments also were done in deoxygenated solutions. As we shall see, oxygen has a critical effect on the course of the radiolysis.

Cytosine is one of the four bases found in DNA. There is considerable evidence to indicate that the alteration of DNA by radiation plays an important part in the development of radiation injuries[2] and, for this reason, it is pertinent to investigate the effects of radiation on the constituent parts of DNA. In general, ionizing radiation is exceedingly harmful to living organisms and stringent precautions must be taken to minimize exposure.[3] However, on the other hand, controlled exposure to radiation has one important medical use; after surgical resection, it is the next most widely used means of treating cancer.[4] The mechanisms that underlie radiation injury are thus the subject of widespread and pressing interest.

A substantial amount of work has already been done on the radiolysis of cytosine, which has recently been reviewed by Infante et al.[5] Their paper should be consulted for details that will not be repeated here. More recently, two papers on the subject have been published by Polverelli and Teoule.[6] Selected results are summarized in Table I. This shows that the subject is very complicated, and that many questions have not yet been satisfactorily resolved. If the reported values of the radiochemical yield for decomposition $G(-\text{cyt})$[1] are correct, the composition of the solvent clearly has a critical effect on the radiolysis, and significant comparisons can only be made if the medium is kept constant, or appropriate adjustments are made.

It may be seen that the products are numerous and that some of the reported yields are discordant. However it is not clear, at this point, whether the discrepancies are due to inadequacies in the analytical determinations, or to real differences in the course and mechanism of the radiolysis, or to both.

It is not likely that any of the radiolysis products can substitute for cytosine in biological function. Thus it may be argued that, from the biological point of view, the destruction of cytosine is all that matters, and not whether it yields product P_1, or P_2, or a complex mixture $P_1 \ldots P_i$ (to be sure, some of these products may have biologically significant effects of their own; see, e.g., Polverelli et al.[15]). The present investigation was accordingly designed to concentrate on the precise determination of $G(-\text{cyt})$ in a medium of well-defined composition, and we deliberately avoided, as much as possible, the question of what products are formed.

Cytosine has an intense, characteristic spectrum in the ultraviolet, and measurement of the changes in that spectrum constitutes a convenient way of following the radiolysis. To interpret these changes properly it is, however, necessary to establish whether the spectra of the products overlap that of cytosine. The next section of the paper presents a theoretical treatment of the relationship between absorbance and radiolytic yield which is then applied to the interpretation of the experimental results.

Spectral Changes Due to Radiolysis

Let a substance S in solution be converted by radiation into a mixture of products $P_1 \ldots P_i$:

$$S + \ldots \longrightarrow \nu_1 P_1 + \ldots \nu_i P_i \qquad (1)$$

ν_i represents the amount of substance P_i, measured in moles, formed by the radiolysis of 1 mol of S, i.e., $\nu_i = G(P_i)/G(-S)$; ν_i is not a conventional stoichiometric coefficient, because, in general, it is not integral and, furthermore, it may vary with the dose D.

Let us first assume that the ν_i do not change with dose, i.e., G remains constant. It is convenient to define an "equivalent absorption coefficient" for the products by the expression

$$\epsilon_\Sigma^\lambda = \sum_i \nu_i \epsilon_i^\lambda \qquad (2)$$

where ϵ_i^λ is the molar absorption coefficient of the ith product at wavelength λ. If ϵ_Σ^λ is zero (or small enough to be negligible relative to the absorption coefficient of S, ϵ_S^λ) the absorbance remaining after a dose D is given by

$$A_D^\lambda = [S]\epsilon_S^\lambda = ([S]_0 - G(-S)E_v)\epsilon_S^\lambda \qquad (3)$$

TABLE I: Selected Studies of Cytosine Radiolysis[a]

Conditions	$G(-\text{cyt})$	Products[b]	Comments[c]	Ref
Degassed	0.9		Lowest yield reported in any conditions	7
pH 1, 0.01 *M* NaCl	8.8		Highest yield reported in any conditions	8
pH 5.2	2.15[c]		*G* determined spectrophotometrically[c]	9
pH 7.4, 0.01 *M* phosphate	3.4[c]		Same *G* in unbuffered medium	10
In air, no buffer		5-Hydroxycytosine (0.34) Uracil glycol (0.20) Cytosine glycol	Products from 10^{-3} *M* cyt after 150 krads[c]	11
Deoxygenated	1.8	5-Hydroxycytosine (0.46) Uracil (0.3) "Hydroxyhydrocytosine" (0.15) 5,6-Dihydroxycytosine (0.1)	From 0.01 *M* cyt, up to 50% decomposition	12
pH 3–4, deoxygenated, Cu(II) added	2.7	Cytosine glycols (2.28) 5-Hydroxycytosine (0.42)	From 0.01 *M* cyt, 0.002 *M* Cu	13
pH 7, deoxygenated		Dihydropyrimidines (<0.9)		14
Neutral	2.49[c]	$C_4H_7N_3O_2$ (0.61) Carboxyl ureides (0.21) 5,6-Dihydroxy-5,6-dihydrouracil (0.13) 5-Hydroxyhydantoin (0.10) Three additional products (0.15)[d]	From 10^{-3} *M* cyt after 37.5 krads; $G(-\text{cyt})$ from 10^{-4} *M* cyt after 3000 rads is 2.08, and *G* (products) are different	6

[a] For additional studies, see Infante et al.[5] [b] List of products may not be complete; original reference should be consulted for details (numbers in parentheses are *G* values for products). [c] See Discussion for further consideration of the subject. [d] Two more products have been reported in other papers.[15]

where E_v is the energy absorbed per unit volume.[16]

It follows from (3) and the assumptions stated above that A_D^λ decreases linearly with dose, and that the slope of the line equals $G(-\text{S})$:

$$G(-\text{S}) = (A_0^\lambda - A_D^\lambda)/E_v\epsilon_S^\lambda \quad (4)$$

If ϵ_Σ^λ is greater than zero, then eq 3 becomes

$$A_D^\lambda = [\text{S}]_D\epsilon_S^\lambda + ([\text{S}]_0 - [\text{S}]_D)\epsilon_\Sigma^\lambda = A_0^\lambda - G(-\text{S})E_v(\epsilon_S^\lambda - \epsilon_\Sigma^\lambda) \quad (5)$$

A_D^λ is still a linear function of dose, but $G(-\text{S})$ is now measured by

$$G(-\text{S}) = (A_0^\lambda - A_D^\lambda)/E_v(\epsilon_S^\lambda - \epsilon_\Sigma^\lambda) > (A_0^\lambda - A_D^\lambda)/E_v\epsilon_S^\lambda \quad (6)$$

Next, consider the absorbances at two different wavelengths, $\lambda = \alpha,\beta$. In general, the fractional change in absorbance will vary with wavelength. However, it may be observed in some cases that the fractional changes after a given *D* are the same, i.e.

$$(A_0^\alpha - A_D^\alpha)/A_0^\alpha = (A_0^\beta - A_D^\beta)/A_0^\beta \quad (7)$$

If so, with the appropriate substitutions one obtains

$$E_vG(-\text{S})(\epsilon_S^\alpha - \epsilon_\Sigma^\alpha)/[\text{S}]_0\epsilon_S^\alpha = E_vG(-\text{S})(\epsilon_S^\beta - \epsilon_\Sigma^\beta)/[\text{S}]_0\epsilon_S^\beta \quad (8)$$

and it follows that the following condition must hold:

$$\epsilon_\Sigma^\alpha/\epsilon_S^\alpha = \epsilon_\Sigma^\beta/\epsilon_S^\beta \quad (9)$$

This condition will of course be fulfilled if $\epsilon_\Sigma^\alpha = \epsilon_\Sigma^\beta = 0$. The alternative possibility, that ϵ_Σ^λ be > 0 and proportional to ϵ_S^λ at *all* the values of λ being considered, is extremely unlikely; it can almost certainly be discounted if, in the range considered, ϵ_S shows a well-defined maximum or other characteristic inflection(s). In other words, if it is found empirically that eq 7 holds for arbitrary α and β, one may conclude with near certainty that ϵ_Σ^λ is negligible.

Moreover it may be seen, by comparing eq 4 and 6, that the former always and unequivocally gives the *lower limit* to the value of *G*, i.e., if the presence of some absorbing product is overlooked, and ϵ_Σ is in fact not zero, the true *G* value will be greater than that given by eq 4.

The foregoing argument can be generalized to the case when *G* is not constant with dose. In that case, of course $\epsilon_\Sigma = f(D)$ and A_D^λ will not be a linear function of *D*. However, ϵ_Σ will have a definite value at any given dose, and eq 5–9 will hold for all λ *at that dose*.

Experimental Section

Materials. Two samples of cytosine were investigated, and both gave the same results; one sample, cytosine·H_2O, was from Schwarz Bioresearch, the other, cytosine·0.5H_2O, from Sigma Chemical. The sodium phosphates, of analytical-reagent grade, were obtained from Fisher Scientific.

All solutions were prepared with distilled water that had been passed through a deionizing resin, redistilled from alkaline permanganate, and finally distilled a third time. All the solutions to be irradiated contained 0.02 *M* phosphate, and their pH was 7 ± 0.05 (Beckman Model SS-2 pH meter); they were made up by diluting a 0.2 *M* stock solution that contained 10.76 g of $NaH_2PO_4 \cdot H_2O$ and 17.24 g of Na_2HPO_4 per liter.

Methods. Each irradiated sample had a volume of 9 ml and was contained in a 10-ml glass vial. The samples were irradiated in a Gammacell-200 cobalt-60 irradiator, equipped with the gas-inlet and sample-holder accessories (Atomic Energy of Canada). To minimize possible post-irradiation changes, the samples were examined as soon as possible, usually within 10–20 min. The measurements used to calculate $G(-\text{cyt})$ were corrected, if necessary, by extrapolation to zero time.

The dose rate, measured with the Fricke dosimeter, was between 2700 and 2000 rads min^{-1}. The calculation was based on $\epsilon(Fe^{3+}, 304\ nm)$ 2195 $M^{-1}\ cm^{-1}$, $G(Fe^{3+})$ 15.6.[17]

Oxygen Saturation or Removal. Oxygen was passed first into a pressure-regulating and ballast flask,[18] then through the Gammacell inlet tube, and finally through a thin glass capillary into the solution being irradiated. The ballast flask was a 500-ml Erlenmeyer that contained about 100 ml of water. The flask was fitted with an inlet and an outlet tube, as well as a gauge tube; the latter was placed vertically through the stopper so its lower end dipped below the surface of the water. Excess pressure in the flask was then indicated by the level of the water in the gauge tube. In this way the pressure could easily be adjusted to give the desired rate of flow through the solution being irradiated, 1–2 ml sec^{-1}.

To remove oxygen, helium was passed through the solution prior to irradiation. In this case, the sample vial was closed with a polyethylene cap, into which there had been drilled two small holes. The gas flow was regulated as described above, and it was maintained for 15 min at 0.3 ml sec^{-1}. The capillary was then withdrawn, the holes were immediately covered with Parafilm, and the vial was placed in the Gammacell.

Quantitative Absorbance Measurements. Cytosine solutions, initially 0.1 m*M*, were treated as follows; a 3.00-ml aliquot was added to 3.00 ml of HCl, of such concentration that the final pH was 3.0. In a similar way, a 3.00-ml aliquot of irradiated solution was adjusted to pH 11.0 by mixing it with 3.0 ml of NaOH. Cytosine solutions of 1 and 10 m*M* concentration were first diluted 10 or 100 times, respectively, with pH 7 buffer, and then treated as described above.

At pH 3 and 7, the spectra above 220 nm were determined both for the irradiated samples and the controls with a recording spectrophotometer (Cary Model 14); measurements at selected wavelengths, used in calculation of G, were made with a single-beam spectrophotometer (Beckman Model DU, fitted with a Gilford Model 22 photometer and light source). At pH 11, measurements were made at selected wavelengths, as needed. All measurements were made in 1-cm quartz cells.

Results

Spectrum of Cytosine. Cytosine is a weak base, with pK values of approximately 4.5 and 12.2.[5,19] At pH 3, therefore, cytosine exists predominantly as a protonated cation, at pH 7 and 11 as the un-ionized base; the loss of H^+ causes a shift in the maximum and decrease in its intensity. The following values were obtained in the present work (wavelengths are in nanometers, the molar absorption coefficients in $M^{-1}\ cm^{-1}$): in phosphate, pH 7, maximum 266 and 6400, minimum 247 and 4700; in HCl, pH 3, 275 and 10000, 238 and 1400; in NaOH, pH 11, 268 and 6300, 249 and 4600. These values are in satisfactory agreement with those reported in the literature.[19]

Spectra of Irradiated Solutions at pH 7. Figure 1 shows the family of curves obtained by irradiating initially 0.1 m*M* cytosine at pH 7 and measuring the spectrum without changing the pH. Although the absorbance at the maximum, 266 nm, decreases rapidly with dose, for curves B–E the absorbance below 250 nm increases with dose, and that around 252 nm remains nearly constant. Qualitatively this shows that ϵ_Σ^{252} is nearly equal to ϵ_{cyt}^{252} (ca. 4900), and that $\epsilon_\Sigma^{\lambda} > \epsilon_{cyt}^{\lambda}$ in the range λ 250–225 nm.

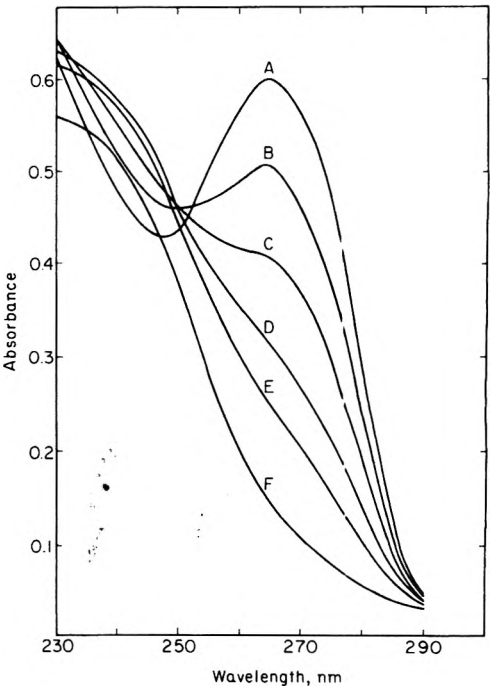

Figure 1. Spectra of cytosine solutions, initially 0.1 m*M*, after exposure to increasing doses, measured at pH 7. Doses in krads: A, zero; B, 6.7; C, 13.4; D, 20.1; E, 26.8; F, 40.2.

A plot of the absorbance at the maximum vs. dose, i.e., A_D^{266}/A_0^{266}, is shown in Figure 2, curve B. This line does not measure the fractional decrease in [cyt], as we shall see more clearly below. It is obvious from inspection of Figure 1 that plots of $A_D^{\lambda}/A_0^{\lambda}$ at λ 266–252 nm will have a rapidly decreasing slope, due to the fact that $\epsilon_\Sigma^{\lambda}$ is rising rapidly relative to ϵ_{cyt}^{λ} (cf. eq 5).

The products responsible for the absorbance at 220–250 nm are not completely stable. Figure 3 shows the post-irradiation changes taking place in a representative case at three selected wavelengths.

Spectra of Irradiated Solutions at pH 3. Figure 4 shows the family of curves obtained when the solutions which had been irradiated at pH 7 were adjusted to pH 3 prior to measuring the spectrum.

Numerical values of the ratios $A_D^{\lambda}/A_0^{\lambda}$ at 275 nm and at two other wavelengths, respectively 8 nm above and 9 nm below the maximum, are given in Table II. It may be seen that these values remain sensibly constant in the interval $A_D^{\lambda}/A_0^{\lambda} = 1–0.1$.

The significance of these results has been pointed out in a preceding section; one may conclude from them that ϵ_Σ^{275} (at pH 3) is negligible in comparison with ϵ_{cyt}^{λ} in the range λ 264–283 nm.

Values of A_D^{275}/A_0^{275} are plotted in Figure 2, curve A. The initial slope of this line is some 30% greater than that of curve B, and this measures the error made by neglecting ϵ_Σ^{266}. Its value can be calculated by solving eq 6 and 4 simultaneously, and the result is ca. 1900.

Calculation of $G(-cyt)$. Although curve A in Figure 2 is *nearly* straight to about 80% decomposition, the deviation of the best-fitting curve from linearity is appreciable. Since the data in Table II demonstrate that eq 4 applies, in initially 0.1 m*M* cytosine solutions, $G(-cyt)$ must be decreasing appreciably with dose.

The values of $G(-cyt)$ are shown in Figure 5. The points in this figure represent the average of four–six determina-

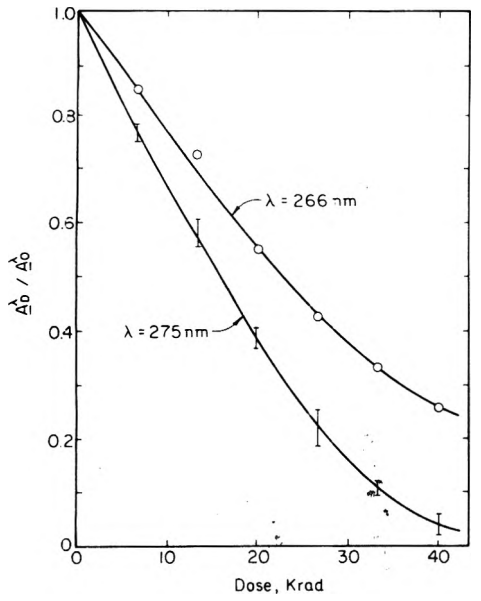

Figure 2. Fractional absorbance as a function of dose: (curve A) $A_D^{275}/A_0^{275} = [cyt]/[cyt]_0$, at pH 3; (curve B) A_D^{266}/A_0^{266}, at pH 7.

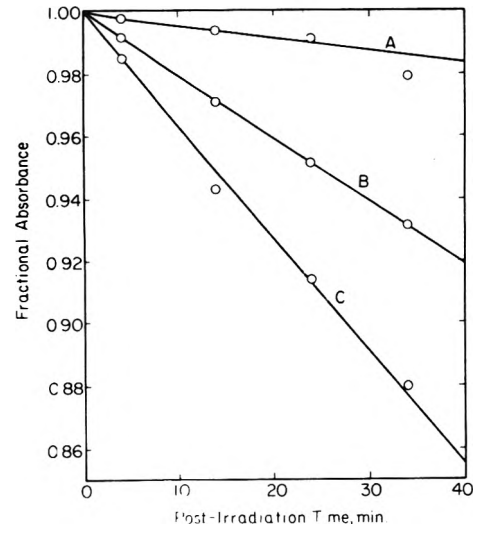

Figure 3. Changes in fractional absorbance occurring after irradiation in initially 0.1 m*M* in cytosine after exposure to 21 krads: A, at 220 nm; B, 232.5 nm; C, 248 nm.

TABLE II: Ratio of the Absorbance $A_D^{\lambda}/A_0^{\lambda}$ at pH 3

Wavelength, nm	Dose, krads				
	6.7	13.4	20.1	26.8	33.5
264	0.761	0.582	0.381	0.230	0.113
275	0.770	0.581	0.385	0.224	0.101
283	0.778	0.589	0.392	0.231	0.104

tions, and the bars indicate the extreme deviations. The line represents the least-squares fit of the data. It corresponds to the expression

$$G(-\text{cyt}) = G_0(-\text{cyt}) + bD = 3.35 - 0.024D^* \quad (10)$$

where G is in the usual units[1] and D^* is the dose *in krads*.

Measurements were also made in 1 and 10 m*M* cytosine. The results are summarized in Table III; i.e., the values of

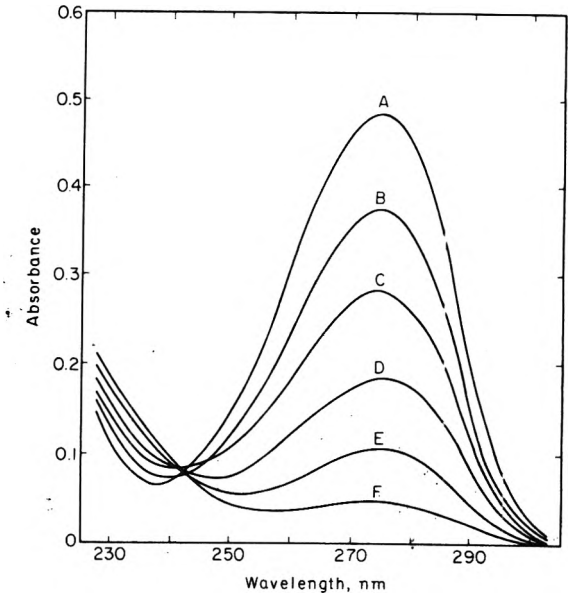

Figure 4. Spectra of cytosine solutions, initially 0.1 m*M*, after exposure to increasing doses, measured at pH 3. Doses in krads: A, zero; B, 6.7; C, 13.4; D, 20.1; E, 26.8; F, 40.2.

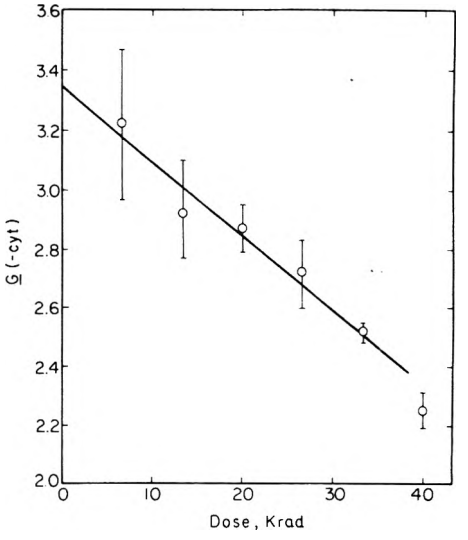

Figure 5. Decomposition yield of cytosine, for initially 0.1 m*M* cytosine, as a function of dose.

TABLE III: Values of G_0(cyt) and G(cyt)

Initial cytosine concn, m*M*	Oxygen concn	G_0 (−cyt)	G(−cyt) fraction decomposed 0.25	0.40
0.1	Satd by bubbling	3.35	3.16	3.03
1.0	Satd by bubbling	3.30	3.10	2.97
10	Satd by bubbling	3.23	3.17	3.12
1.0	Initially equilibrated with air	3.0	2.7	2.1

G_0(−cyt) are the same within experimental error and average 3.3 ± 0.1. Equation 10 adequately represents G in the range investigated, to 40% decomposition (radiolysis of the more concentrated solutions took proportionally larger doses, of course, and the irradiation was not continued beyond that point).

One may ascribe the decrease of G with dose to competition by the radiolysis products for the solvent radicals which are reacting with the cytosine. It may be estimated that the effective equivalent reactivity of the products is about one-fifth that of cytosine; that is why the cytosine decreases nearly in proportion to dose to beyond 50–60% decomposition.

Radiolysis in Deaerated Solutions. Effect of Oxygen Depletion. The solubility in water of oxygen at 1 atm pressure and 20°C is 1.3 mM; in air-equilibrated solutions [O_2] is 0.27 mM.[20] In our experiments the solvent contained 0.02 M phosphate and the temperature was 22–26°C; the effect of these factors on the solubility may be appreciable but cannot be large.

The results in Figure 6 show that the removal of oxygen from solution has a very great influence on the course of the radiolysis. Note that curve C was obtained after exposure to a greater dose than that represented by curve F in Figure 1, but that in the former case A_D^{275}/A_0^{275} is still about 0.6. Also note that curves B and C intersect A at about 295 nm; this means that ϵ_Σ^{295}, instead of being negligible, is equal to ϵ_{cyt}^{295}, ca. 1800.

These results indicate that the products obtained in absence of oxygen are qualitatively different from those obtained in oxygen-saturated solutions. This deduction can be made conclusively, without any independent knowledge of the identity of the products.

The rate of change of A^λ with dose is greatest at 275 nm, and from this it can be deduced that the ratio $\epsilon_\Sigma^{275}/\epsilon_{cyt}^{275}$ is smaller at that wavelength than at other values of λ; this should be expected, since ϵ_{cyt}^{275} is maximal. However the absolute value of ϵ_Σ^λ cannot be obtained from the present data, and hence $G(-cyt)$ cannot be calculated. We may, however, reasonably surmise that $\epsilon_\Sigma^{275} > 0$, and obtain from eq 6 the inequality $G(-cyt) > 1.4$.

If oxygen is present, but in limited quantity, we may expect results which are intermediate between those described above; the ratio cytosine/oxygen would of course be of determining importance. From the data given above it may be seen that for 0.1 mM cytosine the ratio is initially >10 in oxygen-saturated solutions, and about 3 in air-equilibrated ones. The last line of Table III gives the results obtained in an air-equilibrated solution; G_0 is only slightly smaller than in oxygen-saturated solutions, but (dA_D^{275}/dD) is substantially smaller.

In 1 and 10 mM cytosine solutions, the effect of oxygen depletion was of course much more marked. After irradiation for 10–20 min, dissolved oxygen was nearly exhausted, and the results approximated those obtained in deaerated solutions. The exact course of the radiolysis would of course depend on how rapidly oxygen was replenished by diffusion from the surface; probably the results would vary, to some extent, with the dose rate and the shape of the vessel.

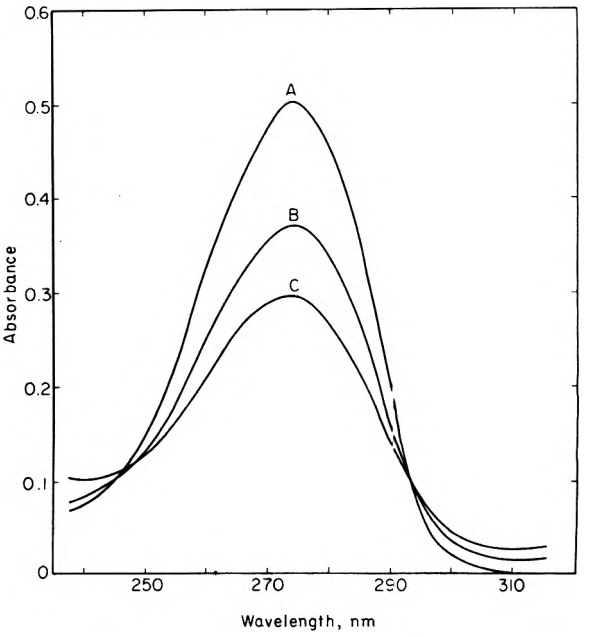

Figure 6. Spectra of cytosine solutions, initially 0.1 mM, after exposure to varying doses in deaerated, helium-saturated solution, measured at pH 3. Doses in krads: A, zero; B, 26.3; C, 53.6.

Discussion

Applications of Spectrophotometry to the Study of Radiolytic Reactions. The present study, as well as those cited previously, have demonstrated that the radiolysis of cytosine is a complex process; many products are formed and, moreover, their yields and even their identities depend critically on the composition of the system and other factors. Cytosine is by no means extreme in these respects, and many other biological substances must be even more complicated.

To minimize these difficulties it is important to find methods of study that are relatively easy to execute and that can provide a large number of fairly precise data. Spectrophotometry is such a technique.

Obviously it has limitations; it cannot be used if neither the starting materials nor the products have a measurable absorbance, and such cases do exist. However, they are not common, and there is a large scope for applications outside that domain.

In the preceding sections of this paper we have demonstrated how $G(-S)$ can be calculated directly from absorbance measurements if $\epsilon_S^\lambda \gg \epsilon_\Sigma^\lambda$. Nothing else need then be known about the identity and properties of the products.

Even more information can be obtained concerning the radiolysis process if at some other wavelengths ϵ_Σ^λ becomes comparable to, or greater than, ϵ_S^λ. This will be illustrated in the third part of this discussion.

If the absorbance of products overlaps that of the initial substance at all accessible wavelengths, then the value of $G(-S)$ cannot be obtained by spectrophotometry alone. This is the case for cytosine irradiated in the absence of air. As explained and exemplified above, one can, in such cases, obtain a lower limit to the value of G, but to obtain the true value one must have information about the absorbance of the products; this will be the subject of a subsequent paper.

The Value of $G(-cyt)$. Let us now discuss the values obtained in this work and by previous investigators. As we have seen, radiolysis is critically affected by the presence of oxygen, and therefore it is inappropriate to compare the results with those obtained in its absence. Moreover, we have shown that, if the oxygen concentration is not constantly replenished, near-anaerobic conditions may develop as the irradiation progresses. It is difficult to evaluate the extent to which this factor affected some of the previous investigations.

Since our experiments were all done at pH 7, we cannot comment on the effect of changing the pH. However, Barszcz and Shugar[10] have reported that the $G(-cyt)$ value

obtained at pH 7.4 was not significantly different from that in unbuffered solution, of pH approximately 6.5. The effect of changing the pH one or two units on either side of 7 is probably small, but larger changes likely would have an appreciable effect.

It is desirable to determine the G value at low doses, when the composition of the system has not been extensively changed by the radiolysis. However this poses a difficulty, inasmuch as $G(-\text{cyt})$ is determined by the *difference* between the initial concentration of solute and that remaining at dose D; relatively small uncertainties in the values of $[\text{cyt}]_D$ will then cause a much greater uncertainty in the value of $G(-\text{cyt})$. For example, if S is only 10% decomposed, an absolute error of 5% in [S] will cause an error of 50% in $G(-\text{S})$.

Scholes et al.[9] were the first to report a value of $G(-\text{cyt})$, 2.15, hence it is appropriate to consider their pioneering work before that of others. They state that their $G(-\text{cyt})$ value was calculated from $\Delta A/\Delta D$, and that they "checked" the result by paper chromatography; i.e., they imply that $\Delta[\text{cyt}]$, determined by this means, was the same as that calculated from ΔA. Their experimental procedure is not described in much detail, but it seems reasonable that the chromatographic determination of $\Delta[\text{cyt}]$ might be uncertain by a few percent. This would cause them to miss the absorbance due to the products, which we have demonstrated in this work. If we take our data for the absorbance at 266 nm and pH 7 and estimate a $G(-\text{cyt})$ value by drawing the "best" straight line through the first three points (Figure 2, curve A), we get a value of 2.3, in fair agreement with that reported in the original paper. In other words, our experimental results agree fairly well with those of Scholes et al; but we get a larger G value because we correct for the absorbance of products.

In view of the foregoing arguments, it is difficult to understand the results of Barszcz and Shugar. They also calculated $G(-\text{cyt})$ from $\Delta A/\Delta D$ without correcting for the absorbance of products, but they report $G(-\text{cyt})$ values averaging 3.4. Even though this value is in fair agreement with ours, the agreement is clearly fortuitous. Altogether, these reports show that the value of $G(-\text{cyt})$ is subject to a large uncertainty, and that care must be taken properly to estimate the latter.

With regard to the results by Polverelli and Teoule,[6] we must observe that their values were determined at doses so low that only a few percent of the cytosine would have been decomposed (3000 rads for 10^{-4} M solution, and 37.5 krads for 10^{-3} M solution). It is difficult to understand how the authors could obtain from the results $G(-\text{cyt})$ values to three significant figures. They comment that their result for 10^{-4} M solution, 2.08, is in good agreement with that of Scholes et al., and they dismiss the higher value obtained in 10^{-3} M solution, 2.49, as possibly "due to experimental errors." Our results indicate that both results are low and that the reported values of $G(-\text{cyt})$ must in fact be quite imprecise. It should however be recognized that the principal purpose of the cited paper was to determine products, and that the same strictures do not apply to that aspect of the work.

According to our results, the same $G(-\text{cyt})$ value is obtained for all three concentrations of cytosine, from 10^{-4} to 10^{-2} M. This is what one should expect if the cytosine reacts completely with the radicals formed by radiolysis of the solvent, and there is no change in the initial mechanism(s) of radiolysis. That fact, and the relatively good precision obtained, inspires confidence in the accuracy of the results.

If one wishes to determine $G(-\text{cyt})$ as accurately as possible, one should not assume, a priori, that the effect of products on $G(-\text{cyt})$ would be "negligible" for some arbitrarily chosen range of "low" doses. In our treatment of the data, we did not make such assumption, but calculated the curve which best fits *all* the data. As may be clearly seen in Figure 5, all values of $G(-\text{cyt})$ show a trend, and even for the lowest dose examined $G(-\text{cyt})$ is appreciably lower than the extrapolated value at zero dose, $G_0(-\text{cyt})$.

Some Aspects of the Radiolysis Mechanism. Let us now consider the value of $G(-\text{cyt})$ in the light of the mechanisms which are thought to occur in dilute aqueous solutions upon irradiation. It is generally agreed that the radiolysis of the water, if formulated in accordance with eq 1, may be represented as follows:[21,22a]

$$H_2O \longrightarrow 0.284(H_2O\cdot)^- + 0.284(OH\cdot) + 0.284H_3O^+ + 0.053(H\cdot) + 0.074H_2O_2 + 0.047H_2 \quad (11)$$

Cytosine reacts very rapidly with (OH·), the specific rate constant being $k_{12} = (2.5\text{–}4 \times 10^9\ M^{-1}\ \text{sec}^{-1})$:[5]

$$\text{cyt} + (OH\cdot) \rightarrow (\text{cyt OH}\cdot) \quad (12)$$

It may therefore be expected that all (OH·) will react in this way, even in the most dilute solutions studied. Cytosine also reacts very rapidly with the hydrated electron ($k_{13} = 7\text{–}13 \times 10^9$):[5]

$$\text{cyt} + (H_2O\cdot)^- \rightarrow (\text{cyt}\cdot)^- + H_2O \quad (13)$$

and somewhat more slowly with (H·) ($k_{14} = 10^8$ at pH 1):[5]

$$\text{cyt} + (H\cdot) \rightarrow (\text{cyt H}\cdot) \quad (14)$$

In oxygen-saturated solution, the situation is complicated by the fact that $(H_2O\cdot)^-$ and (H·) also react very rapidly with the oxygen:[22c]

$$(H_2O\cdot)^- + O_2 \rightarrow (O_2\cdot)^- + H_2O \qquad k_{15} = 2 \times 10^{10} \quad (15)$$

$$(H\cdot) + O_2 \rightarrow (HO_2\cdot) \quad k_{16} = 2 \times 10^{10} \quad (16)$$

On the basis of the above rates, it may be inferred that (H·) will be completely consumed by reaction with the oxygen. Reaction 13 should predominate over (15) in 10 mM cytosine solution, but the reverse should be true in 0.1 mM solution. In point of fact, $G(-\text{cyt})$ is not substantially different in the three cases. This suggests that reaction with the hydrated electron does not cause destruction of the cytosine; following (13), the electron would be transferred to oxygen:

$$(\text{cyt}\cdot)^- + O_2 \rightarrow \text{cyt} + (O_2\cdot)^- \quad (17)$$

(CytOH·) can react rapidly with oxygen:

$$(\text{cytOH}\cdot) + O_2 \rightarrow [\text{cyt(OH)}(O_2\cdot)] \quad (18)$$

Willson[23] has estimated that the rate constant for this reaction is $k_{18} = 2 \times 10^9$. Then $(\text{cyt(OH)}O_2\cdot)$ and $(O_2\cdot)^-$ will be the predominant intermediates present during the irradiation.

We may expect these intermediates to react in three ways. $(O_2\cdot)^-$ may disproportionate; this is a well known reaction ($k_{19} = 1.6 \times 10^7$):[22c]

$$2(O_2\cdot)^- + 2H_2O \rightarrow O_2 + 2OH^- + H_2O_2 \quad (19)$$

Secondly, the two radicals may react one with the other:

TABLE IV: Molar Absorption Coefficients of Some Pyrimidine Derivatives

Compound	pH	Wavelength, nm	ϵ, M^{-1} cm^{-1}	Ref
Cytosine	11	298	300	This work
		315	~0	
5,6-Dihydrocytosine	8	239 (max)	11300	26
Photohydrated 3-cytidylic acid	8.4	240 (max)	13700	27
	1.9	240	2000	
Uracil glycol	10	220 (max)		28
Uracil	11	285 (max)	5900	This work
		298	1300	This work
		315	0	This work
5-Hydroxycytosine	11	221 (max)		11
		273 (min)		11
		298	3000[a]	11
		317.5 (max)	4200	11

[a] Estimated.

$$[\mathrm{cyt(OH)O_2\cdot}] + (\mathrm{O_2\cdot})^- + \mathrm{H_2O} \rightarrow \mathrm{O_2} + \mathrm{cyt(OH)O_2H} + \mathrm{OH^-} \quad (20)$$

This reaction is, of course, analogous to (19). Finally, there could be disproportionation of the hydroxycytosineperoxyl radical. Little is known about such reactions but likely the molecule would be fragmented, giving urea, ammonia, and other small products:

$$2(\mathrm{C_4H_6N_3O_4\cdot}) + {}^{\prime}\mathrm{H_2O}\mathrm{H_2O} \rightarrow (\mathrm{CH_4N_2O}) + \mathrm{NH_3} + \ldots \quad (21)$$

It is pertinent to consider, in this connection, the work of Daniels and Schweibert,[24] although this was done largely at pH 2. At that pH, cytosine is in a different state of ionization, and $(\mathrm{H_2O\cdot})^-$ is undoubtedly consumed by reaction with $\mathrm{H_3O^+}$:[22d]

$$(\mathrm{H_2O\cdot})^- + \mathrm{H_3O^+} \rightarrow (\mathrm{H\cdot}) + 2\,\mathrm{H_2O} \qquad k_{22} = 2.3 \times 10^{10} \quad (22)$$

$G(-\mathrm{cyt})$ was nevertheless found to be 3.2–3.3, about the same as in the present work at pH 7, and this supports the inference that $(\mathrm{H_2O\cdot})^-$ does not cause the destruction of cytosine.

The cited authors obtained evidence for the formation of a peroxide, as represented in eq 20. This peroxide was rapidly converted to a nonperoxide product and $\mathrm{H_2O_2}$, and the rate of this reaction increased with pH so that no appreciable amount of peroxide would accumulate at pH 7. Although the nonperoxide product was not directly identified, it is plausible that this reaction pathway would lead to the cytosine and/or uracil glycols isolated by Ekert and Monier.[11]

From the stoichiometric point of view, if all of the cytosine were decomposed via reactions 12, 18, and 20 the decomposition yield would equal $G(\mathrm{OH\cdot})$, 2.7.[21] To rationalize the somewhat greater yield found in fact, one must accordingly postulate that some 20% of the cytosine reacts by some additional pathway; either one of the reactive intermediates must attack an additional molecule of cytosine, or $(\mathrm{cyt\cdot})^-$, formed in reaction 13, must undergo, to some extent, some reaction other than (17) to form a derivative product. A possibility is that the $(\mathrm{O_2H\cdot})$ radical would react directly with cytosine

$$(\mathrm{cyt}) + (\mathrm{O_2H\cdot}) \rightarrow (\mathrm{cytO_2H\cdot}) \quad (23)$$

and that the product would then react further, e.g., by disproportionation. Just the right amount of $(\mathrm{O_2H\cdot})$ is available from reactions 11, 15, 16, and 17 since $[G(\mathrm{H_2O\cdot}) + G(\mathrm{H\cdot})]$ is 0.34.[21] Because there is more than one possibility, the present results do not prove the occurrence of reaction 23, and it must be admitted that there is no precedent for postulating reaction between the relatively unreactive $(\mathrm{O_2H\cdot})$ and pyrimidine compounds.[25]

Further Characterization of the Products. As we have noted, if at some wavelength α, $\epsilon_\Sigma^\alpha = 0$, while at some other wavelength β, $\epsilon_\Sigma^\beta > 0$, the value of the latter can be calculated by solving eq 4 and 5 simultaneously. It may then be instructive to compare the results with what is known about the products from the work of Eckert and Monier[11] and of Polverelli and Teoule.[6]

Table IV reports selected spectral data for some of the substances that have been identified as products in the radiolysis of cytosine, or that may plausibly be products.

We see from this table that at pH 11 ϵ^λ for 5-hydroxycytosine and uracil are much larger than $\epsilon_{\mathrm{cyt}}^\lambda$ in the region λ 285–320 nm. In point of fact, the irradiated solutions, after adjustment to pH 11, showed negligible absorption at 317.5 nm, and the yield of 5-hydroxycytosine must therefore have been less than 3% (this would give $A = 0.010$ in 5×10^{-4} M solution. Similarly the low absorbance found at 290 nm allows us to exclude the formation of uracil.

Our deduction concerning uracil is in full agreement with the work of Polverelli and Teoule,[6] who found none of this product. With respect to 5-hydroxycytosine, on the other hand, our inference does not agree with the result of Eckert and Monier,[11] who found this compound to be a product of cytosine irradiated "under air". However it should be noted that 5-hydroxycytosine is a prominent product in the absence of oxygen,[12,13] and that in the conditions employed by Eckert and Monier (1 mM cytosine, 24 krads min^{-1}) the dissolved oxygen would soon have been exhausted.

As we have noted, at pH 7 ϵ_Σ is somewhat larger than ϵ_{cyt} in the region from 250 to 225 nm; moreover, ϵ_Σ around 250 nm decreases drastically when the pH is lowered from 7 to 3. We see from Table IV that photohydrated 3-cytidylic acid, the product derived by adding H and OH to the 5,6 double bond, has the requisite spectral properties, and we may expect that other dihydrocytosine derivatives would be similar. Our data, then, are consistent with the possibility that such derivatives be the main products of the radiolysis (G ca. 2).

According to Polverelli and Teoule,[6] a product or products having the formula $\mathrm{C_9H_7N_3O_4}$, i.e., oxidized derivatives of dihydrocytosine, are indeed the principal products ($G = 0.6$ out of a total $\Sigma G = 1.2$ for all identified products). However, in spite of the assiduous work by the investigators cited above, the products derived from about one-half of the cytosine still remain unidentified.

We do not wish to imply that the spectrophotometric measurements can in any way substitute for more direct ways of characterizing the products. However they can make a significant contribution to the problem by indicating the spectral characteristics of the products to be sought. Once the products have been isolated and their spectra determined, a comparison can be made between the values of ϵ_Σ^λ obtained, respectively, from eq 4 and 6 and from eq 2; this comparison would provide a check on the completeness of the products inventory.

Acknowledgments. The work described above was aided by a Biomedical Sciences Support Grant from the National Institutes of Health to the Research Foundation, Oklahoma State University, and by NSF Grant No. MPS 71-03499 and 75-18967 to L.M.R.

References and Notes

(1) All G values are in the units molecules $(100\ eV)^{-1}$.
(2) D. J. Kanazir, *Prog. Nucl. Acid Res. Mol. Biol.*, **9**, 117 (1969).
(3) A. P. Casarett, "Radiation Biology", Prentice-Hall, Englewood Cliffs, N.J., 1968.
(4) "End Results in Cancer, Report No. 4", L. M. Axtell, S. J. Cutler, and M. H. Myers, Ed., Department of Health, Education and Welfare, National Cancer Institute, 1972 (DHEW Publication NIH 72-272).
(5) G. A. Infante, E. J. Fendler, and J. H. Fendler, *Radiat. Res. Rev.*, **4**, 301 (1973).
(6) M. Polverelli and R. Teoule, *Z. Naturforsch. C*, **29**, 12, 16 (1974).
(7) C. A. Ponnamperuma, R. M. Lemmon, and M. Calvin, *Science*, **137**, 605 (1962).
(8) J. F. Ward and I. Kuo, *Int. J. Radiat. Biol.*, **15**, 293 (1969).
(9) G. Scholes, J. F. Ward, and J. Weiss, *J. Mol. Biol.*, **2**, 379 (1960).
(10) D. Barszcz and D. Shugar, *Acta Chim. Polon.*, **8**, 455 (1961).
(11) B. Ekert and R. Monier, *Nature (London)*, **188**, 309 (1960).
(12) M. N. Khattak and J. H. Green, *Int. J. Radiat. Biol.*, **11**, 131 (1966).
(13) J. Holian and W. M. Garrison, *Nature (London)*, **212**, 394 (1966).
(14) J. Holian and W. M. Garrison, *Nature (London)*, **221**, 57 (1969).
(15) M. Polverelli and R. Teoule, *C. R. Acad. Sci. Paris, Ser. C*, **277**, 747 (1973).
(16) Consistent units must of course be used; if ϵ is expressed, as usual, in $mmol^{-1}\ cm^2$ $(= M^{-1}\ cm^{-1})$, G is in molecules $(100\ eV)^{-1}$, and 1-cm cells are used for the absorbance measurements, one must multiply by the factor $(10^{-23}/6.02)$ mol molecule^{-1} and express E_v in (100 eV) dm^{-3}. If the density is 1 kg dm^{-3}, 1 rad = 6.242×10^{14} $(100\ eV)\ dm^{-3}$.
(17) "Radiation Dosimetry: X-Rays and Gamma Rays with Maximum Photon Energies Between 0.6 and 60 MeV" (ICRU Report No. 14), International Commission on Radiation Units and Measurements, Washington, D.C., 1969.
(18) C. A. Mannan, M. S. Thesis, Oklahoma State University, 1972.
(19) D. Shugar and J. J. Fox, *Biochim. Biophys. Acta*, **9**, 199 (1952).
(20) H. Stephen and T. Stephen, "Solubilities of Inorganic and Organic Compounds", Vol. 1, Pergamon Press, Oxford, 1963, part 2, pp 87 and 88; W. F. Linke, Ed., "Solubilities", Vol. II, American Chemical Society, Washington, D.C., 1965, p 1229.
(21) The values of ν are based on $G(OH\cdot) = G(H_2O\cdot)^- = 2.7$, $G(H\cdot) = 0.5$, $G(H_2O_2) = 0.7$, $G(H_2) = 0.45$. There is not complete agreement on the exact values, but the discrepancies are of no consequence for the present purpose (cf. ref 22a,b). We prefer to use the symbol $(H_2O\cdot)^-$ instead of e_{aq}^- to represent the hydrated electron, because with the former one can write formally balanced equations. The extent of hydration of the electron is, in fact, not known exactly, hence it would be more proper to write $[(H_2O)_{x}\cdot]^-$, but that is superfluous here.
(22) (a) E. J. Hart, *Radiat. Res. Rev.*, **3**, 285 (1972); (b) I. G. Draganic and Z. D. Draganic, "The Radiation Chemistry of Water", Academic Press, New York, N.Y., 1971, pp 123–168; (c) *ibid.*, pp 54–56; (d) *ibid.*, p 110.
(23) R. L. Willson, *Int. J. Radiat. Biol.*, **17**, 349 (1970).
(24) M. Daniels and S. C. Schweibert, *Biochim. Biophys. Acta*, **134**, 481 (1967).
(25) This has been pointed out by a reviewer, whose advice we acknowledge with thanks.
(26) B. M. Brown and M. J. E. Hewlins, *J. Chem. Soc. C*, 2050 (1968).
(27) H. E. Johns, J. C. LeBlanc, and K. B. Freeman, *J. Mol. Biol.*, **13**, 549 (1965).
(28) H. M. Kattak and J. H. Green, *Int. J. Radiat. Biol.*, **11**, 577 (1966).

Role of Crystal Imperfections in the Thermal Decomposition of Sodium Azide

V. Krishna Mohan and V. R. Pai Verneker*

Department of Inorganic and Physical Chemistry, Indian Institute of Science, Bangalore 560012, India *(Received February 3, 1975; Revised Manuscript Received August 19, 1975)*

The effects of dopants and pretreatment, mechanical and thermal, on the thermal decomposition of sodium azide have been investigated with a view to understanding the role of crystal imperfections in the decomposition. It has been observed that allovalent ions, Ba^{2+} and SO_4^{2-} ions, as well as precompression, sensitize the decomposition while preheating lowers the decomposition rate. The effects have been discussed in terms of the dependence of the decomposition rate upon the concentration of gross imperfections in the sodium azide lattice.

Introduction

The role of crystal imperfections in the thermal decomposition of solids has been stressed by several workers.[1-5] Boldyrev[3] has proposed a classification of reactions of thermal decomposition of solids. It has been shown that various types of macroscopic and microscopic defects have different effects depending upon the category of reactions. The role played by dislocations in thermal decomposition is well exemplified by the cases of calcite,[6] $NaBrO_3$,[7] α-$Pb(N_3)_2$,[7] and NH_4ClO_4.[8,9] Rajeshwar and Pai Verneker[4,5] have shown that prior mechanical and thermal treatment of ammonium perchlorate and alkali metal perchlorates results in enhanced decomposition rates. They have demonstrated that the increase in the density of the gross imperfections in the lattice upon prior treatment is responsible for the changes in the thermal reactivity of these materials.

Point defects also have been shown to play a significant role in thermal decomposition of solids.[10-12] The results of the numerous investigations[11,12] carried out on the thermal decomposition of the alkali and alkaline earth metal azides clearly establish that point defects play a vital role in ionic diffusion and electron transfer processes taking place during decomposition.

A survey of the work done on the thermal decomposition of sodium azide reveals that, though the decomposition of sodium azide has been the subject of a number of investigations,[13-18] the importance of crystal imperfections in the decomposition mechanism is not clearly understood. Most authors report a value of ~36 kcal mol^{-1} for the activation energy of decomposition. The rate-limiting step has been argued to be the thermal excitation of the electron of the azide ion to the conduction band. The fact that electron transfer reactions play an important role in thermal decomposition of sodium azide receives support from the observation of Jacobs and Kureishy[15] that Fe^{3+} ions, which could act as electron traps, sensitize the decomposition. However, Torkar[17] et al. from a study of the effect of allovalent cations and anions on the thermal decomposition of sodium azide arrived at the conclusion that the decomposition is diffusion controlled. Divalent cations have been found to enhance the decomposition rate. The sensitization was ascribed to an increase in the diffusion rate of sodium ions in Mn^{2+} doped NaN_3 samples. However, the effect of divalent anions could be seen to be concentration dependent; sodium azide doped with 0.01 mol % CO_3^{2-} ions decomposed at a slower rate than pure sodium azide while the opposite is true in the case of 0.1 and 1 mol % CO_3^{2-} ions doped samples. An altogether different type of observation has been reported by McGill[18] from a study on the influence of univalent cationic impurities on the thermal decomposition of sodium azide. Univalent ions, for example, K^+ and Cs^+ ions, having an ionic size larger than that of the host ion, decrease the induction period for decomposition. The author[18] speculates that this effect is due to an increase in the local strain energy on doping sodium azide with ions of greater size than the host cation.

It is, thus, evident from the above discussion that the present understanding of the exact manner in which dopants affect the decomposition kinetics of sodium azide is poor. Moreover, no investigation has been carried out to date to point out the role played by gross imperfections in the decomposition mechanism of sodium azide.

The present work was, therefore, carried out with a view to (i) study the effect of divalent cations and anions, and (ii) examine the effects of precompression and preheating on the thermal decomposition of sodium azide.

Experimental Section

Sodium azide used in the present investigation was supplied by Riedel, De Haen Ag Seelze, Hannover. All the samples were reprecipitated twice from double distilled water by acetone.

Doped materials were prepared by coprecipitation from an aqueous solution of sodium azide containing the desired concentration of the dopant. The dopants used were barium azide and sodium sulfate, both of Analar quality. The concentrations studied were 0.01 mol % (Ba^{2+} and SO_4^{2-} ions) and 0.05 mol % (Ba^{2+} ions). No attempt was made to determine the actual concentration of the dopant in the host lattice.

The effect of precompression on the thermal decomposition of sodium azide was studied by pelleting the samples at 200 and 300 kg/cm^2 in an uniaxial hydraulic press. After pelleting, the pellets were ground and then passed through sieves to obtain the desired particle size. Experiments on the precompressed samples were carried out on the same day to preclude the effects of ageing.

The kinetic studies of the thermal decomposition of NaN_3 samples were followed in the temperature range 240–300°C in a constant volume vacuum line with an initial pressure of 1×10^{-5} Torr. The pressure rise was measured using a McLeod gauge. All kinetic runs on the pure and doped materials were carried on samples having the particle size range 149–177 μm.

Infrared spectra of the sodium azide samples were taken on Carl-Zeiss UR 10 spectrophotometer.

Results

The isothermal decomposition of pure and doped sodium azide has been studied in the temperature range 240–300°C. Typical plots of the fractional decomposition, α, against the time, t, of heating are shown in Figure 1. The kinetic plots have been fitted to Avrami–Erofeev equation with $n = 2$. Table I gives the values of the rate constants for the thermal decomposition of pure and doped NaN_3. The activation energy values remain unchanged at 36 kcal mol^{-1} for both the samples. It could be seen from Table I that allovalent ions, both cationic and anionic, sensitize the decomposition.

The effect of precompression (at 200 and 300 kg/cm^2) and preheating (at 150°C for 1 hr) on the subsequent thermal decomposition of sodium azide has also been investigated in the same temperature range, i.e., 240–300°C. The values of the rate constants, at a representative temperature, for the thermal decomposition of the precompressed and preheated sodium azide samples are also given in Table I. It could be seen that precompression enhances the decomposition rate while preheating lowers it. The activation energy for the decomposition of precompressed NaN_3 was found to be the same as that for pure NaN_3.

Doped as well as precompressed (not shown in the figure) NaN_3 show a considerable broadening of the ir peaks. To illustrate the broadening effect a typical peak corresponding to the asymmetric stretching of the azide ion is displayed in Figure 2. The preheated samples exhibit a narrowing of the peaks.

Preliminary examination of the x-ray diffractograms, taken on a Phillips diffractometer, of precompressed sodium azide revealed a broadening of the diffraction peaks.

Discussion

The general form of the α–t curves obtained in the present work is similar to that observed by earlier workers. The present value of activation energy, 36 kcal mol^{-1}, is also in close agreement with the values reported in literature. Moreover, the activation energy for the thermal decomposition for pure, doped, and precompressed sodium azide is found to be the same. This indicates that the basic mechanism for decomposition remains unaltered in the case of these materials.

It is evident from the present work on the thermal decomposition of pure and doped sodium azide that the effect of doping the sodium azide lattice with allovalent ions is independent of the nature of the ion, as both anions and cations sensitize the decomposition. A consideration of the ionic radii of the foreign ions constituting the dopant materials, viz., Ba^{2+} ions and SO_4^{2-} ions, reveals that both the ions are larger than the host ions (ionic radii of Ba^{2+}, 1.35 Å; SO_4^{2-}, 2.4 Å; Na^+, 0.95 Å; N_3^-, 1.7 Å). As both the ions, Ba^{2+} and SO_4^{2-}, are larger than the ions constituting the host lattice, doping the sodium azide lattice with these ions results in an increased strain in the lattice. The number of gross defects would, therefore, increase as a consequence of

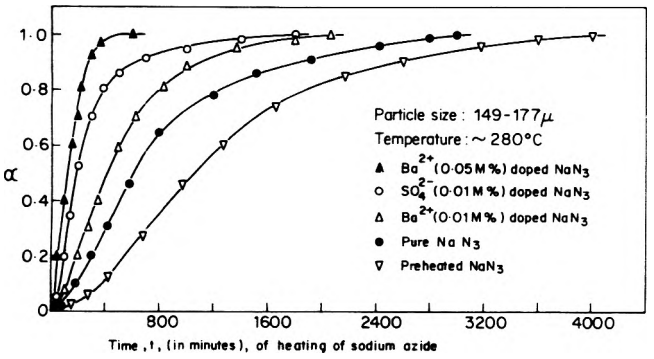

Figure 1. Plots of the fractional decomposition, α, vs. the time, t, (in min) of heating sodium azide.

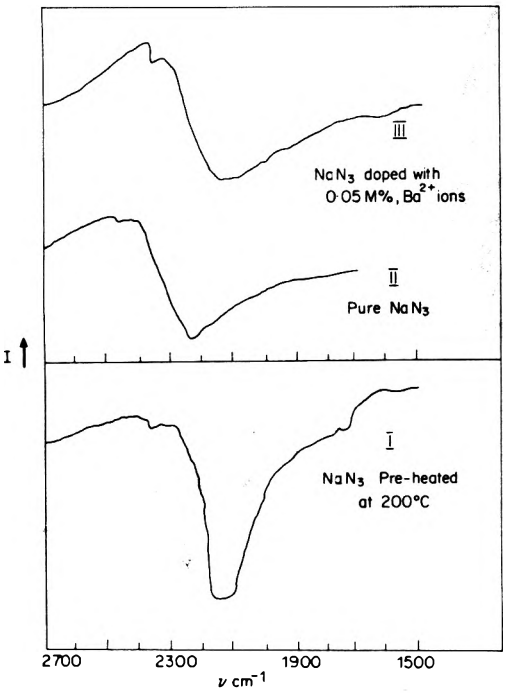

Figure 2. Infrared spectra of sodium azide samples.

TABLE I: Rate Constants for the Thermal Decomposition of Sodium Azide

Type of the sample	Rate constant k (min^{-1}) at 280°C
Preheated NaN_3	0.0008
Pure NaN_3	0.0015
NaN_3 doped with SO_4^{2-} ions (0.01 mol %)	0.0022
NaN_3 doped with Ba^{2+} ions (0.01 mol %)	0.0021
NaN_3 precompressed at 200 kg/cm²	0.0028
NaN_3 precompressed at 300 kg/cm²	0.0035
NaN_3 doped with Ba^{2+} ions (0.05 mol %)	0.0050

the increased strain and hence the decomposition would be sensitized. Ir spectra of the doped samples show that the absorption peaks of the azide ion undergo a considerable broadening on doping sodium azide. It has been established earlier[4,5] that broadening of ir peaks arises as a consequence of an increase in the concentration of gross imperfections in the lattice. Rajeshwar and Pai Verneker[4,5] have observed that precompression of ammonium perchlorate and alkali metal perchlorates results in a broadening of the perchlorate infrared absorption peaks along with a sensitization in their decomposition characteristics. From detailed x-ray diffraction studies they have concluded that the broadening arises as a consequence of an increase in the density of gross imperfections. A broadening of the ir absorption peaks, in the case of the doped sodium azide samples, would also imply an increase in the concentration of the gross defects in the lattice.

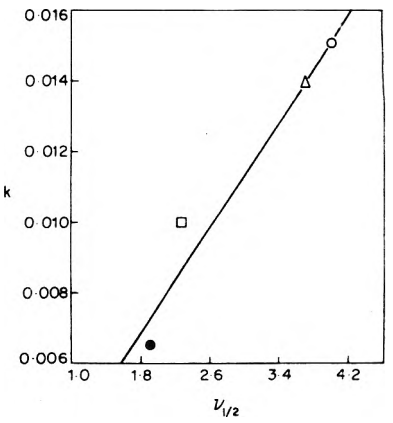

Figure 3. Plot of the rate constant, k (min^{-1}), for the thermal decomposition of sodium azide against, $\nu_{1/2}$, the band width of half absorption maxima: (●) preheated NaN_3; (□) pure NaN_3; (△) precompressed NaN_3; (○) NaN_3 doped with 0.05% Ba^{2+} ions.

Precompression of sodium azide has also been observed to have a sensitizing effect on the decomposition. Preliminary examination of the precompressed samples shows that precompression results in a broadening of the diffraction peaks. Keating and Krasner[19] have found a similar broadening on subjecting sodium azide to mechanical grinding. They have attributed this broadening to the production of strain in the lattice upon grinding. The ir spectrum of the precompressed sodium azide shows a broadening of the absorption peaks. These observations clearly indicate that precompression results in the production of gross imperfections within the lattice. The increase in the decomposition rate upon precompression can be attributed to the larger concentration of imperfections in the precompressed samples.

Further support for the dependence of the decomposition of sodium azide upon gross imperfections comes from the observation that the decomposition rate decreases when sodium azide is preheated at 150°C for 1 hr. No decomposition has been observed during the preheating period. Preheating of the samples might result in an annealing of the defects within the crystal. The ir spectrum of preheated sodium azide shows a sharpening of the absorption peaks (see Figure 2). The change in the thermal reactivity of sodium azide bears a direct relationship to the change in the broadening of the ir bands as is evident from Figure 3. The effect can be seen to be independent of the nature of the pretreatment.

The present studies, thus, clearly establish that the thermal decomposition of sodium azide is highly sensitive to the concentration of gross defects within the lattice. It is likely that point defects, especially anion vacancies, which act as electron traps, play a significant role in the decomposition mechanism but such effects are overshadowed by those produced due to gross imperfections.

References and Notes

(1) B. E. Bartlett, F. C. Tompkins, and D. A. Young, *Nature (London)*, **179**, 365 (1957).
(2) V. V. Boldyrev, "Metody izucheniya kinetiki termicheskogo vazlozheniya tvevdykh verschestv", Izd-Yo Tomskogo Gosuniversitela Tomsk, 1948, Chapter 1.
(3) V. V. Boldyrev, *Bull. Soc. Chim. Fr.*, 1054 (1969).
(4) K. Rajeshwar and V. R. Pai Verneker, *J. Phys. Chem. Solids*, in press.
(5) K. Rajeshwar and V. R. Pai Verneker, *J. Solid State Chem.*, in press.
(6) J. M. Thomas and G. D. Renshaw, *J. Chem. Soc.*, 2058 (1967); 2749 (1969).
(7) J. Jach, *J. Phys. Chem. Solids*, **24**, 63 (1963).
(8) P. J. Herley and P. W. Levy, *J. Chem. Phys.*, **49**, 1500 (1968).
(9) P. J. Herley and P. W. Levy, *J. Chem. Phys.*, **49**, 1493 (1968).
(10) J. N. Maycock and V. R. Pai Verneker, *Proc. R. Soc. London, Ser. A*, **307**, 303 (1968).
(11) P. Gray and T. C. Waddington, *Chem. Ind (London)*, 1555 (1955).
(12) P. Gray and T. C. Waddington, *Proc. R. Soc. London, Ser. A*, **235**, 106 (1956).
(13) W. Garner and D. J. B. Marke, *J. Chem. Soc.*, 657 (1936).
(14) E. A. Secco, *J. Phys. Chem. Solids*, **24**, 469 (1963).
(15) P. W. M. Jacobs and A. R. T. Kureishy, *J. Chem. Soc.*, 4718 (1964).
(16) R. F. Walker, *J. Phys. Chem. Solids.*, **29**, 985 (1968).
(17) K. Torkar, H. T. Spath, and G. W. Herzog, *Monatsh Chem.*, **98**, 298 (1967).
(18) W. J. McGill, *J. S. Afr. Chem. Inst.*, **22**, 143 (1969).
(19) D. T. Keating and S. Kranser, *J. Phys. Chem. Solids.*, **20**, 150 (1961).

Pulse Radiolytical Investigation of the Reversible Reaction of Biphenyl with the Solvated Electron in Liquid Ammonia

Farhataziz*[1] and Lewis M. Perkey

Radiation Laboratory,[2] University of Notre Dame, Notre Dame, Indiana 46556

(Received April 2, 1975; Revised Manuscript Received September 10, 1975)

Publication costs assisted by the U.S. Energy Research and Development Administration

From the measured solubility of biphenyl in liquid ammonia for the temperature range 21 to −15.5°, 9.4 kcal mol^{-1} for the heat of solution and 30 cal deg^{-1} mol^{-1} for the entropy of solution for a 1 *M* standard state are calculated. Nanosecond pulse radiolysis of biphenyl solutions in liquid ammonia show that the reaction of e_{am}^- with biphenyl produces the biphenyl anion and it is reversible. From the values of the equilibrium constant (the equilibrium concentration of the biphenyl anion divided by the initial concentration of biphenyl and the equilibrium concentration of e_{am}^-) at 21.6 and 10.5°, −20 kcal mol^{-1} for the heat of reaction and −44 cal deg^{-1} mol^{-1} for the entropy of reaction for a 1 *M* standard state are calculated. The specific rate of the reaction of e_{am}^- with biphenyl is equal to $1.24 \times 10^{(12\text{-}1600/2.3RT)}$ for the temperature range 21.6 to −75°. The extinction coefficient of the biphenyl anion at 0.403 μ, the wavelength of maximum absorption, is 3.1×10^4 M^{-1} cm^{-1} for the temperature range 23 to −76.5°. The calculated values of the standard heat of formation of e_{am}^- and the entropy of e_{am}^- for a 1 *M* standard state are −14 kcal mol^{-1} and 13 cal deg^{-1} mol^{-1}, respectively.

Introduction

The solvated electron in a mixture of methylamine and liquid ammonia reacts reversibly with benzene.[3] The equilibrium is interesting because in the reverse reaction an anion gives an electron to the solvent. Similar reversible reactions of the electron with CO_2 in isooctane, neopentane, and tetramethylsilane, and with biphenyl, B, in tetramethylsilane, have been reported.[4,5] In this communication, a study of the reversible reaction of e_{am}^- with B in liquid ammonia and various measured or calculated thermodynamic properties of species involved are reported.

Experimental Section

Biphenyl was obtained from Eastman Kodak. The purification of ammonia, and the vacuum line are described elsewhere.[6,7]

The vessel used for the determination of solubility of B in liquid ammonia is shown in Figure 1. The volume of the vessel up to any point between marks α and β is the sum of the previously determined volume up to the mark α and the computed volume of the length of precision bore capillary tube between mark α and the point of interest. After weighing a known amount of B in the vessel, it was attached to the vacuum line and evacuated. Such an amount of ammonia was condensed into the vessel, so that at the temperature of interest the saturated solution of B would fill the vessel to a point between marks α and β. The vessel was sealed off, allowed to warm to room temperature (~23°), and both portions were weighed to determine the weight of liquid ammonia in the vessel. By immersing the vessel in a bath (contained in a Dewar) of dissolved solid CO_2 in alcohol, the clear solution was cooled to crystallize out white needles of B. Except a tiny crystal of B, all B was redissolved by warming and shaking the vessel. The vessel was again immersed in a cold bath, and temperature was adjusted to give a preceptible growth of the tiny crystal of B. Most of the crystal was redissolved by warming and shaking the solution, and cooled again to a temperature a few tenths of a degree higher than previous crystal growth temperature. A fast crystal growth would indicate a repeat of above procedure at a higher temperature. The procedure was repeated till a temperature was found at which the

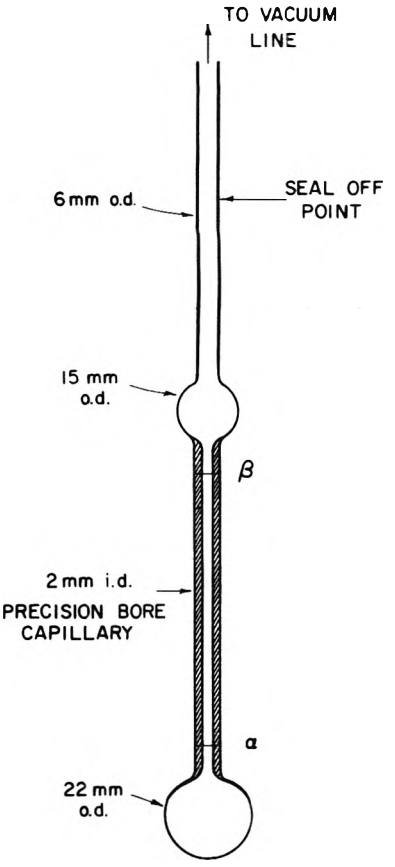

Figure 1. Pyrex glass vessel for solubility determination.

crystal would not grow for hours. However, a lowering of 0.2° in the temperature would give an effective growth of the crystal. For the temperature at which no crystal growth was observed, it was assumed that all B would dissolve in all liquid ammonia to give a saturated solution. The volume of the solution was determined as explained above. The solubility of B in liquid ammonia and the density of the saturated solutions were then calculated. Corrections for the vapor phase ammonia and volume change of the vessel at the lower temperature were made. The temperature of the cold bath was measured by a copper–constantan thermocouple and was read on a digital thermocouple thermometer (Model DS-100-T3 of Doric Scientific Corp.).

The irradiation cell and solution preparation are described elsewhere.[7] Because dilute solutions of B were difficult to prepare by direct weighing of the solute, a degassed known volume (maximum 50 μl at room temperature) of a methanolic solution of the required solute concentration was mixed with 1.56 g of degassed ammonia. The presence of methanol in solutions had no effect on the results; cf. Results section. For samples containing N_2O, 24 ml of N_2O at 23° and 1 atm was condensed in the irradiation cell and allowed to mix with 1.56 g of liquid ammonia; the cell was sealed to a final volume of ~5.5 ml. Assumption that all N_2O is dissolved gives a concentration of ~0.4 *M* at 23°.

The pulse-radiolysis system, split-beam technique, quartz Dewar for low temperature pulse radiolysis, and system for cooling irradiation samples are described elsewhere.[6-8] In the split-beam technique, the analyzing light beam after its passage through the irradiation cell (optical path length ~1 cm) and emergence from Linac room was split into two light beams by impinging it on a Balzer neutral-density filter at a 45° angle. The transmitted beam was focussed on the entrance slit of one monochromator and the reflected beam was focussed on the entrance slit of another monochromator. The technique permits a simultaneous study at two wavelengths of transient absorption signals. For study of the transient absorption spectrum, a selected wavelength of the reflected beam is used to monitor the dose per pulse delivered to the sample, and the wavelength of the transmitted beam is changed from pulse to pulse to obtain transient absorptions at various wavelengths. In study of kinetics of transients, the decay of the absorption signal at a properly selected wavelength for one species, and the growth of the absorption signal at another properly selected wavelength for another species can be investigated simultaneously by the split-beam technique.

The samples were irradiated with 5- or 10-nsec pulses of 10-MeV electrons from the Notre Dame Linac. Unless otherwise specified all concentrations given are for ~23°.

Results

Biphenyl Solubility. The solubility of B in liquid ammonia was determined at various temperatures. The results are summarized in Table I. For a 1 *M* standard state, the heat of solution, $\Delta H_1°$, and the entropy of solution, $\Delta S_1°$, are 9.4 kcal mol^{-1} and 30 cal deg^{-1} mol^{-1}, respectively. At 23°, from the density data for the various concentrations of B given in Table I and 0.606 g ml^{-1} density of liquid ammonia,[9a] a partial molar volume of B, $\bar{V}$(B), of 159 ml mol^{-1} is calculated, which gives 4 Å for radius of solvated B, B_{am}.

Transient Absorption Spectra. At 23° and for a wavelength range 0.31–0.75 μ, the transient absorption spectrum induced by an electron pulse in a 18 m*M* solution of B (no methanol) in liquid ammonia was measured by the split-beam technique.[7] To avoid any complication owing to excitation of B itself, a 0.3-μ cutoff filter was placed between the xenon lamp and the sample. The spectrum is shown in Figure 2 and is ascribed to biphenyl anion, B_{am}^-. For a 2 m*M* B solution, the transient absorption at all wavelengths was decreased by ~99% in the presence of ~0.4 *M* N_2O. For a 20 m*M* B solution, the measured transient absorption spectra at −50° for the wavelength range 0.35–0.45 μ, and at −25 and 0° for the wavelength range 0.39–0.42 μ, had peaks in agreement with the peak in the spectrum at 23° for the corresponding wavelengths. However, the shoulders at 0.390 and 0.375 μ in the spectrum were better resolved at −50° than at 23°. The wavelength for major peak in the spectrum shown in Figure 2 is invariant for temperature range 23 to −50° and it is assumed that its temperature invariance extends to the freezing point of ammonia.

For the temperatures and B concentrations in m*M* given in parentheses [23° (1 and 18); −0.9, −26.7 and −46.1° (10 and 20); and −76.5° (saturated >1)], the extinction coefficient of B_{am}^-, $\epsilon(B_{am}^-)$, at 0.403 μ, the wavelength of maximum absorption, was measured relative to the extinction coefficient of e_{am}^-, $\epsilon(e_{am}^-)$, at 1.73 μ at 23° and at 1.45 μ for other temperatures, respectively. The pertinent values of $\epsilon(e_{am}^-)$ were obtained from absorption spectra of e_{am}^- at different temperatures[8] and a maximum extinction coefficient 4.8×10^4 M^{-1} cm^{-1} of e_{am}^- at all temperatures.[10,11] The maximum $\epsilon(B_{am}^-)$ was the same for all solutions and all temperatures, and it was calculated to be 3.1×10^4 M^{-1} cm^{-1} for the temperature range 23 to −76.5°.

Reaction Kinetics. In experiments to measure specific rates, (i) the concentrations of reactants were adjusted for

TABLE I: Solubility of Biphenyl in Liquid Ammonia at Various Temperatures

Temp, °C	Saturated solution [B], m*M*	Saturated solution Density, g ml^{-1}	Density at 23°, g ml^{-1} [a]
21	437	0.660	0.657
8	210	0.638	0.617
6.5	193	0.640	0.617
4.2	171	0.641	0.613
−15.5	44.5	0.662	0.609

[a] Saturated solutions (with no solid phase) at lower temperatures were brought to 23°.

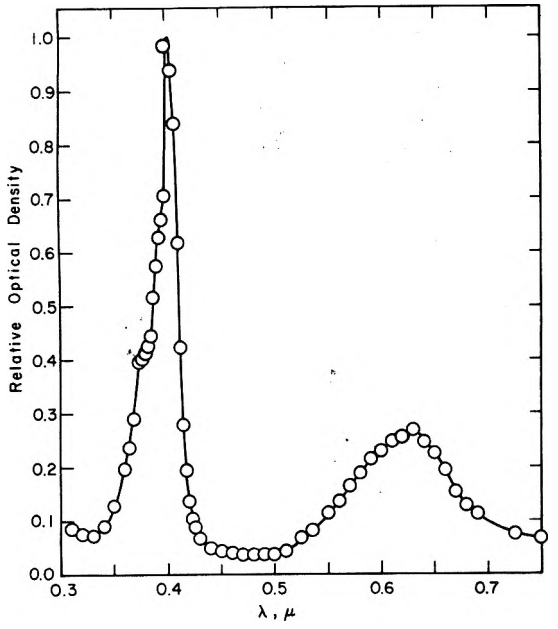

Figure 2. The absorption spectrum of the biphenyl anion in liquid ammonia at 23°.

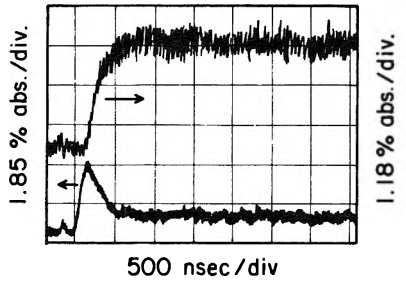

Figure 3. Transient absorption signals induced in a 62.3 μM solution of biphenyl (no methanol) in liquid ammonia at 21.6° by a 5-nsec electron pulse: decaying signal, e_{am}^- absorption at 1.75 μ; growing signal, biphenyl anion absorption at 0.403 μ.

pseudo-first-order kinetics and (ii) irradiation conditions were fixed such that the transient signal of e_{am}^- in neat ammonia showed negligible decay 1.5 μsec after the pulse.[7] The reaction of e_{am}^- with B_{am} was followed by recording either the growth of the absorption of B_{am}^- at 0.403 μ or the decay of the absorption of e_{am}^- at 1.75 μ at 21.6, 10.5, −2, and −26.3°, and at 1.4 μ at −44.6 and −75°. In some cases, the growth of the B_{am}^- absorption and decay of the e_{am}^- absorption were recorded simultaneously (cf. Figure 3). In one experiment at 23°, the decay of the e_{am}^- absorption was observed at 1.2, 1.3, 1.4, and 1.7 μ. At least four determination of reaction rates were made for each concentration of B_{am}. For temperatures ≥10.5°, the absorption signal of e_{am}^- decays to a plateau value greater than zero absorption (cf. Figure 3). This suggests that the reaction of e_{am}^- with B_{am} is reversible. For the reversible reaction

$$e_{am}^- + B_{am} \underset{k_2}{\overset{k_1}{\rightleftharpoons}} B_{am}^- \quad (1)$$

in which k_1 and k_2 are the specific rates of forward and reverse reactions, respectively, a standard kinetic treatment gives the following equations:

$$-\ln [A_t - A_\infty] = \{k_1[B_{am}]_0 + k_2\}t + C \quad (2)$$

$$-\ln [D_\infty - D_t] = \{k_1[B_{am}]_0 + k_2\}t + C \quad (3)$$

$$\frac{k_1[B_{am}]_0}{k_2} = \frac{D_\infty \epsilon(e_{am}^-)}{A_\infty \epsilon(B_{am}^-)} \quad (4)$$

In eq 2–4, A is optical density of e_{am}^-, D is the optical density of B_{am}^-, $[B_{am}]_0$ is initial concentration of B_{am}, t is the time, C is a constant, subscripts ∞ and t refer to at time ∞ (i.e., plateau value) and t respectively, and $\epsilon(e_{am}^-)$ and $\epsilon(B_{am}^-)$ are for the respective wavelengths of absorption measurements of e_{am}^- and B_{am}^-. At a given temperature, by analyzing the decay of e_{am}^- by eq 2 and the growth of B_{am}^- by eq 3 the values of $\{k_1[B_{am}]_0 + k_2\}$ were evaluated for various values of $[B_{am}]_0$; and subsequently from the slope and intercept of a linear plot (cf. Figure 4) of $\{k_1[B_{am}]_0 + k_2\}$ vs. $[B_{am}]_0$ values of k_1 and k_2 were obtained. The values of k_1/k_2 obtained at 21.6 and 10.5° are 7×10^4 and 29×10^4 M^{-1}, respectively. The values obtained for k_1 are given in Figure 5.

The presence or absence of methanol in a solution had no effect on the results. Similarly, the presence or absence of the 0.3-μ cutoff filter placed between the xenon lamp and the irradiation sample did not affect the results. A further confirmation of the kinetic analysis was provided by the fact that at 23° the observed decay of e_{am}^- absorption at 1.2, 1.3, 1.4, and 1.7 μ for a solution of B gave values of $\{k_1[B_{am}]_0 + k_2\}$ which were the same within experimental error. In a second approach, the plateau values of absorption signals of e_{am}^- and B_{am}^- obtained from simultaneous recording of decay of e_{am}^- and growth of B_{am}^- (cf. Figure 3) were analyzed with eq 4, in which appropriate values of $\epsilon(e_{am}^-)$ (obtained by the method described above) and $\epsilon(B_{am}^-)$ were used. For $[B_{am}^-]_0$ = 103.5, 82.8, 62.1, 41.4, and 21.6 μM, the average values of k_1/k_2 obtained are 9.6×10^4 and 33×10^4 M^{-1} at 21.6 and 10.5°, respectively. These values are in reasonable accord with the values determined above by use of eq 2 and 3. The mean of values of k_1/k_2 obtained by two methods are 8.3×10^4 and 31×10^4 M^{-1} at 21.6 and 10.5°, respectively, and thereby the calculated heat of reaction, $\Delta H_r°$, and the entropy of reaction, $\Delta S_r°$, are −20 kcal mol^{-1} and −44 cal deg^{-1} mol^{-1}, respectively.

For temperatures <10.5°, k_1 was evaluated from the decay of e_{am}^- and the growth of B_{am}^- by straightforward pseudo-first-order kinetics. The results shown in Figure 5 give $k_1 = 1.24 \times 10^{(12-1600/2.3RT)}$, in which R is the gas constant and T is absolute temperature.

Discussion

Absorption Spectrum of Biphenyl Anion. The transient absorption spectrum presented in Figure 2 for B solutions in liquid ammonia is attributed to B_{am}^- produced by the reaction of e_{am}^- with B_{am}. Such an assignment is supported

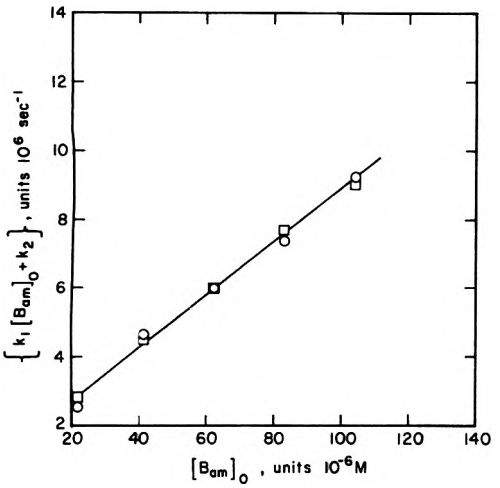

Figure 4. The plot of $\{k_1[B_{am}]_0 + k_2\}$ vs. $[B_{am}]_0$ at 21.6°: (O) e_{am}^- decay; (□) B_{am}^- growth. Each point is a mean of at least two observations.

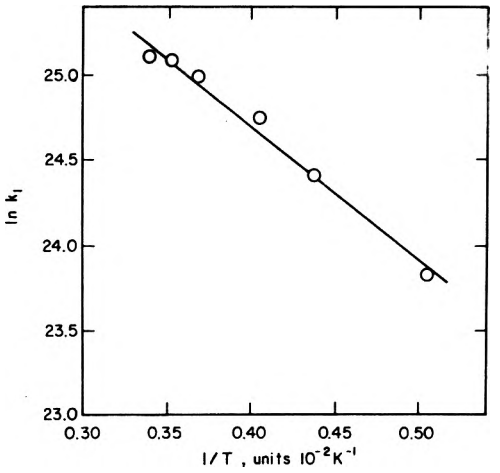

Figure 5. The plot of ln k_1 vs. $1/T$.

by the effect of N_2O on the transient absorption spectrum of 2 mM biphenyl solution. Furthermore, the rate at which the 0.403-μ absorption grows is equal to the rate at which e_{am}^- absorption decays (cf. Figure 3). The wavelengths for the peaks in the absorption spectrum in Figure 2 agree well with the wavelengths for the peaks in the absorption spectra of the biphenyl anion reported at room temperature in tetrahydrofuran,[12] water,[13] and ethylamine.[14] The absorption spectra of the biphenyl anion at 77 K in a glassy mixture of 3-methylpentane and 2-methyl-1-pentene[15] and at room temperature in ethanol[16] are also comparable with present results. In Table II, some characteristics of the major peak in absorption spectrum of the biphenyl anion are summarized for various solvents. The data indicate that the bandwidth at half-height and maximum extinction coefficient of the biphenyl anion are solvent dependent. Thus, it will be necessary to reexamine the yields of solvated electrons which were calculated in amines, deuterated ammonia, and ammonia on the basis that maximum extinction coefficient of the biphenyl anion is solvent independent.[14]

Reaction Kinetics. At 25°, for a reaction of e_{am}^- (diffusion coefficient of e_{am}^- is 4.88×10^{-4} cm^2 sec^{-1})[7] with a neutral molecule of 3.5-Å radius (crystal radius of B is 3.7 Å[18]), the calculated diffusion-controlled specific rate by the

TABLE II: Wavelength for Maximum Absorption, λ_{max}, Bandwidth at Half-Height, W, and Maximum Extinction Coefficient, ϵ_{max}, for the Absorption Spectrum of Biphenyl Anion in Various Solvents at Room Temperature[a]

Solvent	λ_{max}, nm	W, nm	ϵ_{max}, M^{-1} cm^{-1}	Ref
Water	405	38	2.6×10^4	13
Ammonia	403	28	3.1×10^4	Present work at 23°
Ethylamine	408	41		14
Tetrahydrofuran	400		3.8×10^4	17
Tetrahydrofuran	402	34	3.8×10^4	12

[a] Note Added in Proof. K. Sehested and E. J. Hart (*J. Phys. Chem.*, 79, 1639 (1975)) report a λ_{max} of 390 nm, W = 38 nm, and an ϵ_{max} of 1.9×10^4 M^{-1} cm^{-1} for the biphenyl anion in water at room temperature.

Smoluchowski–Debye equation[7] and its calculated activation energy from the viscosity of liquid ammonia for a temperature range −65 to 50°[9a,19] are 2.9×10^{11} M^{-1} sec^{-1} and 1.6 kcal mol^{-1}, respectively. Thus $k_1 = 8 \times 10^{10}$ M^{-1} sec^{-1} at 21.6° and its activation energy of 1.6 kcal mol^{-1} determined in present studies suggest that the reaction of e_{am}^- with B_{am} is probably diffusion controlled.

Partial Molar Volume of B_{am}. Combining 130 ml mol^{-1} volume of B in crystal[18] with $\bar{V}(B)$ = 159 ml mol^{-1} determined in present studies for B_{am} at 23°, a displacement of 29 ml of ammonia is calculated for dissolution of 1 mol of B at infinite dilution in liquid ammonia. For a heat of vaporization = 4.78 kcal mol^{-1} for liquid ammonia at 23°,[20] a displacement of 29 ml of ammonia requires 4.9 kcal, which is less than $\Delta H_l° = 9.4$ kcal mol^{-1}. Thus, dissolution of B in liquid ammonia must also cause other changes in the structure of ammonia.

Heats and Entropies. For discussion of standard thermodynamic properties, $\Delta H_f°(x_y)$ and $S°(x_y)$ refer to the heat of formation and entropy, respectively, of a species x in a state y. Gaseous electrons in the standard state have 1 atm fugacity, and the 1 M standard state refer to solvated species. All heats and entropies are in units of kcal mol^{-1} and cal deg^{-1} mol^{-1}, respectively, and are for 25°. Various values of heats and entropies of B are $\Delta H_f°(B_s) = 24.03$,[21] $\Delta H_f°(B_g) = 43.53$,[21] $S°(B_s) = 49.2$,[22] and $S°(B_g) = 92.2$,[23] in which subscripts s and g refer to solid and gaseous state, respectively. Temperature invariance up to 25° of values of $\Delta H_l°$, $\Delta S_l°$, $\Delta H_r°$, and $\Delta S_r°$ determined in present studies is assumed.

By combining $\Delta H_l°$ with $\Delta H_f°(B_s)$, and $\Delta S_l°$ with $S°(B_s)$ values of 33 and 79 are calculated for $\Delta H_f°(B_{am})$ and $S°(B_{am})$, respectively. For *zero energy assumption* (i.e., translational entropy of a neutral species for a 1 M standard state in gas and in solution is the same),[24] the comparison of $S°(B_{am}) = 79$ with the calculated value 85.8 of entropy of B_g for a 1 M standard state indicates a small decrease in internal entropy of B_g on dissolution.

The values of $\Delta H_r°$ and $\Delta S_r°$ on combination with values of $\Delta H_f°(B_{am})$ and $S°(B_{am})$ respectively give

$$\Delta H_f°(B_{am}^-) - \Delta H_f°(e_{am}^-) = 13 \quad (5)$$

$$S°(B_{am}^-) - S°(e_{am}^-) = 35 \quad (6)$$

Thus a knowledge of the values of $\Delta H_f°(B_{am}^-)$ and $S°(B_{am}^-)$ will give values of $\Delta H_f°(e_{am}^-)$ and $S°(e_{am}^-)$.

In liquid ammonia, the entropies of monovalent monoatomic ions,[25] $Z_{am}^{1\pm}$, with reference[26] to $S°(H_{am}^+) = -29$ can be represented by the empirical equation[27]

$$S°(Z_{am}^{1\pm}) = \frac{3}{2}R \ln F - \frac{12.3}{r} - 7.6 \qquad (7)$$

in which F is formula weight of $Z^{1\pm}$ and r is Pauling's estimated value of the univalent radius of the ion.[28] If B^- were monoatomic, then use of eq 7 with r = 3.7 Å (crystal radius of B^{18})[29] would give 4.1 for the empirical entropy of B_{am}^-, $S°(B_{am}^-)_{emp}$. For *zero energy assumption*,[24] $S°(B_{am}^-)_{emp} = S°(B_g)_{tr}^M + S_{el}°$, in which $S°(B_g)_{tr}^M$ is entropy of translation of B_g in a 1 M standard state and $S_{el}° = [S°(B_{am}^-) - S°(B_{am})]$ is electrostatic entropy. Combining 34.7, the value of $S°(B_g)_{tr}^M$ calculated from translational partition function, with 4.1 for $S°(B_{am}^-)_{emp}$, $S_{el}° = -31$ is calculated, which on subsequent combination with $S°(B_{am}) = 79$ gives $S°(B_{am}^-) = 48$. Substitution of 48 for $S°(B_{am}^-)$ in eq 6 gives $S°(e_{am}^-) = 13$, which compares well with 18, a value of $S°(e_{am}^-)$ obtained (for conditions in present investigations) from the calculated entropy of e_{am}^- by Lepoutre and Jortner.[30]

To a good first approximation, the heat of solution of a gaseous ion in a dielectric liquid can be calculated with the Born equation.[31] For a 3.7-Å radius of B^- [29] and 16.9 for the dielectric constant of liquid ammonia,[9b] such calculations give −46 for heat of solution of B_g^- in liquid ammonia. Use of this value with $\Delta H_f°(B_g) = 43.53$, $H°(e_g^-) = 1.5$,[30] and an electron affinity of B ~0,[32] gives $\Delta H_f°(B_{am}^-) = -1$ and thereby use of eq 5 gives $\Delta H_f°(e_{am}^-) = -14$. The value of $\Delta H_f°(e_{am}^-)$ given by Lepoutre and Jortner[30] converts to −21 for conditions in the present discussion. Considering the limitations involved in use of the Born equation, the agreement between two values is good.

Acknowledgments. The authors are grateful to Dr. W. P. Helman for his assistance in computer programming and to Dr. R. R. Hentz for his continuous guidance.

References and Notes

(1) On leave from the Pakistan Atomic Energy Commission.
(2) The Radiation Laboratory of the University of Notre Dame is operated under contract with the U.S. Energy Research and Development Administration. This is ERDA Document No. COO-38-990.
(3) R. K. Boddeker, G. Lang, and U. Schindewolf, *Angew. Chem., Int. Edit. Engl.*, **8**, 138 (1969).
(4) R. A. Holroyd, T. E. Gangwer, and A. O. Allen, *Chem. Phys. Lett.*, **31**, 520 (1975).
(5) J. M. Warman, M. P. De Haas, E. Zádor, and A. Hummel, *Chem. Phys. Lett.*, **35**, 383 (1975).
(6) Farhataziz, L. M. Perkey, and R. R. Hentz, *J. Chem. Phys.*, **60**, 4383 (1974).
(7) L. M. Perkey and Farhataziz, *Int. J. Radiat. Phys. Chem.*, in press.
(8) Farhataziz and L. M. Perkey, *J. Phys. Chem.*, 79, 1651 (1975).
(9) W. L. Jolly and C. J. Hallada in "Non-Aqueous Solvent Systems", T. C. Waddington, Ed., Academic Press, New York, N.Y., 1965: (a) p 4; (b) p 5.
(10) R. K. Quinn and J. J. Lagowski, *J. Phys. Chem.*, **73**, 2326 (1969).
(11) Farhataziz, L. M. Perkey, and R. R. Hentz, *J. Chem. Phys.*, **60**, 717 (1974).
(12) K. H. J. Buschow, J. Dieleman, and G. J. Hoijtink, *J. Chem. Phys.*, **42**, 1993 (1965).
(13) J. H. Fendler, H. A. Gillis, and N. V. Klassen, *J. Chem. Soc., Faraday Trans. 1*, **70**, 145 (1974).
(14) W. A. Seddon, J. W. Fletcher, F. C. Sopchyshyn, and J. Jevcak, *Can. J. Chem.*, 52, 3269 (1974).
(15) J. B. Sullivan and W. H. Hamill, *J. Chem. Phys.*, **44**, 2378 (1966).
(16) S. Arai and L. M. Dorfman, *J. Chem. Phys.*, **41**, 2190 (1964).
(17) P. Chang, R. V. Slates, and M. Szwarc, *J. Phys. Chem.*, **70**, 3180 (1966).
(18) W. B. Pearson, Ed., "Structure Reports", Vol. 26, N. V. A. Oosthoek's Uitgevers Mij, Utrecht, 1961, p 726.
(19) R. R. Dewald and J. H. Roberts, *J. Phys. Chem.*, **72**, 4224 (1968).
(20) R. C. Weast, Ed., "Handbook of Chemistry and Physics", 45th ed, Chemical Rubber Publishing Co., Cleveland, Ohio, 1964–1965, p E-13.
(21) J. D. Cox and G. Pilcher, Ed., "Thermochemistry of Organic and Organometallic Compounds", Academic Press, New York, N.Y., 1970, p 178.
(22) H. M. Huffman, G. S. Parks, and A. C. Daniels, *J. Am. Chem. Soc.*, **52**, 1547 (1930).
(23) R. S. Bradley and T. G. Cleasby, *J. Chem. Soc.*, 1690 (1953).
(24) R. M. Noyes, *J. Am. Chem. Soc.*, **84**, 513 (1962).
(25) W. M. Latimer and W. L. Jolly, *J. Am. Chem. Soc.*, **75**, 4147 (1953).
(26) C. M. Criss, R. P. Held, and E. Luksha, *J. Phys. Chem.*, **72**, 2970 (1968).
(27) The equation is based on an equation for aqueous solutions given by K. J. Laidler, *Can. J. Chem.*, **34**, 1107 (1956).
(28) L. Pauling, "The Nature of the Chemical Bond", 3rd ed, Cornell University Press, Ithaca, N.Y., 1960, p 514.
(29) Van der Waals radius of a neutral atom (ref 27, p 260) is approximately the same as univalent radius of monovalent anion of that atom (ref 27). Thus, the crystal radius of B is assumed equal to the univalent radius of B^-.
(30) G. Lepoutre and J. Jortner, *J. Phys. Chem.*, **76**, 683 (1972).
(31) E. A. Moelwyn-Hughes, "Physical Chemistry", 2nd ed, Pergamon Press, New York, N.Y., 1964, p 882.
(32) L. G. Christophorou and R. P. Blaunstein, *Chem. Phys. Lett.*, **12**, 173 (1971).

Thermodynamic Properties of the Molecular Complex $CuAlCl_4$

William C. Laughlin and N. W. Gregory*

Department of Chemistry, University of Washington, Seattle, Washington 98195 *(Received August 4, 1975)*

Publication costs assisted by the National Science Foundation

The vaporization of cuprous chloride is considerably enhanced in the temperature range 189–390° by the presence of aluminum chloride vapor. Evidence is presented to support the conclusion that the molecular species $CuAlCl_4$ is an important constituent of the vapor phase. Thermodynamic properties of this molecule have been derived from transpiration data. For the reaction $CuCl(s) + AlCl_3(g) \rightarrow CuAlCl_4(g)$, $\Delta H°_{640K} = -0.8$ kcal mol and $\Delta S°_{640K} = -2$ cal mol^{-1} deg^{-1}. The values $\Delta H°_{473K} = 34$ kcal mol and $\Delta S°_{473K} = 48$ cal mol^{-1} deg^{-1} are derived for the process $CuAlCl_4(s) = CuAlCl_4(g)$. The vapor phase complex does not show a strong absorption band in the wavelength range 200–600 nm, in contrast to Cu_3Cl_3.

Introduction

Relatively little is known about the cuprous chloride–aluminum chloride system. A melting point study by Kendall, Crittenden, and Miller[1] indicates the existence of only one solid state intermediate compound, $CuAlCl_4$, with a congruent melting point of 235°. The catalytic activity of $CuAlCl_4$ in the preparation of olefines has been a matter of considerable interest and has generated a substantial patent literature.[2,3] We have been interested in the nature of molecules formed in the vapor phase of such systems.[4–6] Cuprous halide vapor molecules have a strong absorption band in the region 200–250 nm and can be detected spectrophotometrically at relatively low concentrations.[7] In the present work we have demonstrated by transpiration experiments that the presence of aluminum chloride produces a considerable increase in the amount of copper in the vapor phase in equilibrium with cuprous chloride in the temperature range 180–390°. This is attributed to formation of $CuAlCl_4$ molecules and thermodynamic constants for this mixed metal dimer species have been derived. The vapor phase shows no new absorption band in the range 200–600 nm or appreciable enhancement of the characteristic cuprous chloride absorption. It is suggested that the vapor complex is fundamentally an ion pair, much like $NaAlCl_4$, rather than a molecule in which the bonding between copper and chlorine is similar to that in Cu_3Cl_3, the principal species in the saturated vapor of pure cuprous chloride in this temperature range.

Experimental Section

The experimental method used for the transpiration studies was basically that described by Richards.[8] Argon at ca. 1000 Torr and at flow rates between 9 and 72 cm^3 min^{-1} served as a carrier gas. The argon was made to flow either directly over $CuCl–AlCl_3$ mixtures or first over a solid sample of $AlCl_3$, heated in a compartment adjacent to the main reactor furnace to a temperature appropriate to introduce the desired partial pressure of aluminum chloride, and then over a sample of pure CuCl or over condensed mixtures of CuCl and $AlCl_3$. Partial pressures in the equilibrium vapor were deduced from the relative number of moles of Al, Cu, and Ar in the transported sample. Results showed no systematic dependence on flow rate in the indicated range. The amounts of aluminum and copper transported were determined by atomic absorption analysis[9] of material which condensed outside the reaction zone. The pressure of argon was measured manometrically; the number of moles of argon flowing through the reactor was determined by evaporating the sample of solid argon, collected in a liquid nitrogen cooled trap, into a calibrated volume and measuring the pressure of the gas at room temperature. Ideal gas behavior was assumed.

The CuCl sample was prepared by reaction of copper at 500° with chlorine; the latter was generated by thermal decomposition of $CuCl_2$, formed by vacuum dehydration of $CuCl_2·2H_2O$ (Baker Chemical, 99.1%). Samples of CuCl were subsequently sublimed under vacuum twice before being transferred into the transpiration reactor vessel. Aluminum trichloride was prepared by reaction of aluminum wire (Baker's Analyzed Reagent) and HCl (generated from Mallinckrodt Analytical Reagent NaCl and Allied Chemical 95.5–96.5% H_2SO_4). The product initially formed was resublimed twice under vacuum, with a sample finally collected in a side-arm extension of the transpiration apparatus where it could be introduced into the system by fracturing a Pyrex breakseal.

Results and Discussion

The transpiration data are summarized in Table I (see paragraph at end of text regarding supplementary material). In all experiments CuCl(s) was present as a separate solid phase. The contribution to the total number of moles of copper in the vapor phase expected from the vapor pressure of CuCl(s) was predicted from the data of Shelton.[10] Relative to the total collected this amount was negligible for the majority of runs but constituted as much as 85% in experiments in the high temperature range and in which the partial pressure of $AlCl_3$ was very low. The additional copper in the vapor was attributed to the presence of the mixed metal dimer $CuAlCl_4(g)$. The indicated number of moles of this species was subtracted from the total number of gram atoms of aluminum transported to give the number of gram atoms of aluminum in the form of the monomer and dimer of aluminum chloride. The relative amounts of $AlCl_3(g)$ and $Al_2Cl_6(g)$ were calculated using data from the JANAF Tables.[11] Partial pressures of the various components were calculated using Dalton's law, $P_i = X_iP_t$; P_t (the total pressure) and n_t (the total number of moles of gas) were taken as the values measured for argon, since $n_{Ar} \gg n_{Cu_3Cl_3} + n_{CuAlCl_4} + n_{AlCl_3} + n_{Al_2Cl_6}$.

Table I (supplementary material) includes several series of experiments in which CuCl(s) at a given temperature (very nearly the same if not identical) was allowed to equilibrate with various partial pressures of $AlCl_3$. It will be observed, for example, that around 640 K six experiments, in which the $AlCl_3$ pressures differ by factors as large as 70, were conducted. The amount of copper transported as the complex showed only a first power dependence on the $AlCl_3$ pressure which indicates that complex molecules containing more than one aluminum atom were not present at significant concentrations. A similar test of the number of copper atoms in the complex molecule was not feasible; however, in five experiments deposits of CuCl, the complex, and $AlCl_3$ appeared reasonably well separated and were analyzed separately. While the separation was not perfect the analysis generally confirmed the expected compositions. The material thought to be the complex gave Al/Cu ratios of 0.91, 0.97, 0.95, 0.94, and 0.98, respectively. The slight excess of copper over that expected for the formula $CuAlCl_4$ could be due to (a) the concomitant deposition of some CuCl with the complex, (b) a small amount of decomposition of $CuAlCl_4$ after condensation in the warm condensation region, losing $AlCl_3$, or (c) the deposition of small amounts of species such as Cu_2AlCl_5 or Cu_3AlCl_6. The observed ratios are close to unity, however, and we have assumed that the deviation was caused by (a) or (b) and hence that the principal vaporization reaction is

$$CuCl(s) + AlCl_3(g) = CuAlCl_4(g) \quad (1)$$

This conclusion also seems consistent with the reported composition of other similar complexes of aluminum chloride.[12,13] Alternatively, of course, (1) could be written with $\frac{1}{2}Al_2Cl_6(g)$, the dominant molecular form of aluminum chloride vapor at moderate to high pressures, as the reactant.

Equilibrium constants derived for (1) are shown in Table I (supplementary material) and are displayed graphically in Figure 1. At temperatures above 500 K, a liquid phase of unknown composition but presumed to be the complex was observed in the reactor along with CuCl(s) in several of the experiments. In the cases marked with an asterisk (Table I, supplementary material) the final equilibrium vapor mixture was generated by decomposition of this condensed complex, i.e. no aluminum chloride was introduced into the carrier gas before it entered the reaction zone. In the other experiments (in which a liquid phase may or may not have been present) equilibrium was approached by the reaction of an initial excess pressure of aluminum chloride with the copper chloride (i.e., (1) proceeding to the right). Values of K_1 in these two cases show good consistency.

A least-squares treatment based on an equation of the form $\log K_1 = AT^{-1} + B$ gave the line shown in Figure 1 with constants corresponding to an enthalpy change of -0.78 ± 0.06 kcal mol^{-1} and an entropy change of -2.0 ± 0.1 cal mol^{-1} deg^{-1} for the mean temperature of 560 K. The indicated uncertainties represent the least-squares analysis of the spread of the experimental data. Using JANAF values for the standard entropies and enthalpies of formation of CuCl(s) and $AlCl_3(g)$, our result leads to 113.7 cal mol^{-1} deg^{-1} and -172.8 kcal mol^{-1} for the standard entropy and enthalpy of formation, respectively, of $CuAlCl_4(g)$ at 560 K.

Information on the vibrational frequencies and the structure of the $CuAlCl_4$ molecule has not been found. We have used data for similar molecules to see if the experimentally derived value for the entropy is reasonable for such a molecule. The combined translational and rotational contribution is expected to be 77 cal mol^{-1} deg^{-1}, including a rotational contribution of 31.8 based on an assumed structure consisting of a tetrahedral $AlCl_4$ group with the copper atom bridging through coordination with two chlorine atoms (forming a planar $AlCl_2Cu$ ring) with overall symmetry C_{2v}. The bond distances were assumed the same as the mean values reported in a crystal structure study of $NaAlCl_4$.[14] From an analysis of the Raman spectrum of liquid $NaAlCl_4$, Balasubrahmanyam and Nanis[15] have assigned frequencies for the tetrachloroaluminate ion of 145(2), 183(3), 349, and 580(3) cm^{-1}. If these values are used for nine of the vibrational degrees of freedom for the $CuAlCl_4$ molecule, the remaining three degrees of freedom would have to contribute 13 cal mol^{-1} deg^{-1}, the equivalent of three frequencies of the order of 123 cm^{-1}, which appears generally reasonable.[16]

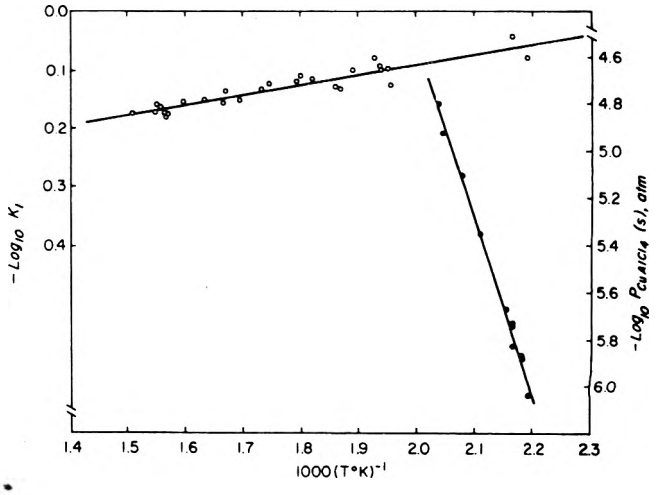

Figure 1. Temperature dependence of the equilibrium constant for reaction 1 (O, ordinate scale on left), and of the vapor pressure of $CuAlCl_4$ in equilibrium with its solid phase and CuCl(s) (●, ordinate scale on right).

An estimated value[11] of ΔC_p for (1) of -2.0 cal mol^{-1} deg^{-1} leads to a predicted heat of formation of $CuAlCl_4(g)$ of -173 kcal mol^{-1} and an absolute entropy of 95 cal mol^{-1} deg^{-1} at 25°.

In experiments below 500 K and with a sufficiently high partial pressure of aluminum chloride, the solid complex condensed in the reactor. In these cases the partial pressures of $CuAlCl_4$ reflect the saturation vapor pressure of the solid. Partial pressures of $AlCl_3$ were varied significantly above the saturation limit without observable effect on the apparent vapor pressure of the solid complex. The pressures of $AlCl_3$ generally remained above values expected for equilibrium with the excess of CuCl present and hence it appears that the solid complex formed a protective coating over the CuCl(s) crystals which prevented rapid equilibration through reaction 1. The P_{CuAlCl_4}/P_{AlCl_3} ratios (Table I, supplementary material) in parentheses are seen to be abnormally low. In two instances (marked with asterisks) $AlCl_3$ was not introduced into the carrier gas prior to its entry into the reactor and after substantial amount of the solid complex had been formed in earlier runs; then the solid complex, by decomposition, generated the aluminum chloride vapor found in the exit gas and the resulting data gave pressure ratios in good agreement with values of K_1 projected from the results at higher temperatures (see Figure 1).

The consistency of the derived sublimation vapor pressures at various aluminum chloride pressures suggests that the $CuAlCl_4$ solid phase remained at fixed composition. Data from the 11 runs in which $CuAlCl_4(s)$ was present are tabulated below the dotted line in Table I (supplementary material); the vapor pressure dependence on temperature is also shown in Figure 1. A least-squares treatment, assuming the simple vaporization reaction

$$CuAlCl_4(s) = CuAlCl_4(g) \quad (2)$$

led to a predicted enthalpy of 34.3 ± 1.0 kcal mol^{-1} and an entropy of 47.8 ± 2.4 cal mol^{-1} deg^{-1} for (2) at a mean temperature of 473 K. With an estimated ΔC_p of −6 cal mol^{-1} deg^{-1} for (2), a combination of results for (1) and (2) with JANAF values for CuCl(s) and $AlCl_3$ leads to a predicted standard enthalpy of formation of −208 ± 3 kcal mol^{-1} and an absolute entropy of 44.5 ± 4 cal mol^{-1} deg^{-1} for $CuAlCl_4(s)$ at 25°. The entropy value is not greatly different from the sum of the entropies of CuCl(s) and $AlCl_3(s)$, 47 cal mol^{-1} deg^{-1}, as generally expected for such complexes.

The temperature dependence of the saturation pressures of $CuAlCl_4(g)$ when a liquid phase is present along with CuCl(s) reflects not only the variation of the vapor pressure with temperature but also the effect of the change in solubility of CuCl in the liquid complex with temperature. While the calculated pressures of $CuAlCl_4$ above 500 K (Table I, supplementary material) do appear to converge, at a given temperature, on a limiting value presumed to characterize the saturated liquid, this upper limit could not be reliably fixed, i.e., one could not be certain in every case when a liquid phase was actually present, or if the liquid phase had reached saturation equilibrium with CuCl(s). Hence we have not attempted to calculate the properties of the liquid phase.

Acknowledgment. This work was supported by a grant from the National Science Foundation, GP 37033X.

Supplementary Material Available: Table I, experimental transpiration data (2 pages). Ordering information is available on any current masthead.

References and Notes

(1) J. Kendall, E. D. Crittenden, and H. K. Miller, *J. Am. Chem. Soc.*, **45**, 963 (1923).
(2) Eg. B. H. Johnson (Esso Research and Engineering Co.) U.S. Patent 3475347 (Cl. 252-429; Bolj) Oct 28, 1969.
(3) Eg. D. G. Walker (Tenneco Chemicals, Inc.) Ger. Offen. 2057162 (Cl.C Olgb) June 3, 1971.
(4) W. C. Laughlin and N. W. Gregory, *Inorg. Chem.*, **14**, 1263 (1975).
(5) W. C. Laughlin and N. W. Gregory, *Inorg. Chem.*, in press.
(6) C-F. Shieh and N. W. Gregory, *J. Phys. Chem.*, **79**, 828 (1975).
(7) D. L. Hilden and N. W. Gregory, *J. Phys. Chem.*, **76**, 1632 (1972).
(8) R. R. Richards and N. W. Gregory, *J. Phys. Chem.*, **68**, 3089 (1964).
(9) Perkin-Elmer Model 303.
(10) R. A. J. Shelton, *Trans. Faraday Soc.*, **57**, 2113 (1961).
(11) "JANAF Thermochemical Tables", Revised Edition, Thermal Laboratory, Dow Chemical Co., Midland Mich.
(12) G. I. Novikov and F. G. Gavryuchenkov, *Russ. Chem. Rev.*, **36**, No. 3, 156 (1967).
(13) C. R. Boston in "Advances in Molten Salt Chemistry", J. Braunstein, G. Manantov, and G. P. Smith, Ed., Plenum Press, New York, N.Y., 1971.
(14) N. C. Baenziger, *Acta Crystallogr.*, **4**, 216 (1951).
(15) K. Balasubrahmanyam and L. Nanis, *J. Chem. Phys.*, **42**, 676 (1965).
(16) L. Brewer, G. R. Somayajulu, and E. Brackett, *Chem. Rev.*, **63**, 111 (1963).

The Second Virial Coefficient of Nonpolar Substances

R. M. Gibbons

The British Gas Corporation, London Research Station, London SW6, England *(Received April 15, 1975)*

Publication costs assisted by The British Gas Corporation

Continued fractions have been developed for the second virial coefficient for the Barker Bobetic potential which contain, without significant error, all the thermodynamic information contained in the exact expression. Constants are obtained for the BB potential for Ne, Ar, Kr, and Xe. The general problem of obtaining approximate expressions for the results of statistical mechanical theories is discussed and compared with the analogous problem of using analytical mathematical functions on digital computers.

Introduction

Empirical correlations for the second virial coefficient, B, are still widely used today,[1-3] even though there are a number of intermolecular potentials which describe the second virial data for many substances better than any empirical correlation.[4-6] The reason for this is the complexity of the calculations to evaluate B from the intermolecular potentials, which precludes the use of these models for routine calculations of B. It is the purpose of this note to show how simplified expressions for the values of B calculated from intermolecular potentials may be obtained which are simple enough to use routinely. Since this is a general problem with all statistical mechanical theories, we start by discussing what is required of such simplified forms before discussing the application of the method to the calculation of B for the Barker Bobetic (BB) potential,[7] which was chosen as an example because it is one of the best potentials for argon which has yet been devised. We conclude with a short discussion of the application of the method to other statistical mechanical theories.

The integral for B for a realistic potential is typical of statistical mechanical theories of fluids in that the answer is provided as an intractable integral which can only be

evaluated by a numerical integration. It is this feature which makes all these theories so inconvenient to use. However, to use these theories it is not necessary to have the exact answer; in fact, such exact answers always contain far more information than is ever required. For example, exact answers provide exact information for all orders of derivatives for all values of the temperature and density including negative and complex values of these variables. (In practice the accuracy is limited to the round-off error of the computer even for exact answers.) Clearly, to use these theories to calculate thermodynamic properties, much of this information is not required, as we are normally only interested in the free energy, and its first few derivatives, over a restricted range of temperature, density, and composition. The initial problem then reduces to representing, sufficiently accurately, the results of numerical integrations in the statistical mechanical theories over a very restricted range of temperature, density, and composition.

This problem is in many ways analogous to that faced by computer manufacturers in representing mathematical functions for use on a computer. They solved that problem by developing expressions, normally continued fractions, which represented the function over a range of values with an error about equal to the round-off error of the computer. Similar techniques can be used for statistical mechanical theories as is shown below for B. While the best possible result is to develop an expression with an error equal to the round-off error of the computer, in many cases even this is not necessary. It is frequently sufficient that the errors in the calculated values, and the first few derivatives, be much less (say a factor of 10 less) than the errors in the experimental data; the errors in the calculated values will then not be significant in making comparisons with experimental data.

The problem then becomes one of obtaining such approximate forms. It is shown in the next section how this may be done for B for the Barker Bobetic potential using continued fractions obtained by standard methods from the *results* of numerical integrations of eq 1.

A Continued Fraction for B

The values of B for the BB potential are obtained from the following integral:

$$B = -2\pi N \int_0^\infty (e^{-u/kT} - 1)R^2\,dR \qquad (1)$$

where u is the BB potential. For the reduced temperature range of 0.5–20.0, this integral can be represented by the following continued fractions:

$$B^* = B_H^* + B_S^* \qquad (2)$$

where B^* is the reduced value of B, $B/(2\pi r_m^3/3)$,

$$B_H^* = e^{gT^*}(a_0 + a_1/T^* + a_2/T^{*2} + 1.0/T^{*3})/(b_0 + b_1/T^* + b_2/T^{*2})$$

$$B_S^* = \exp(f/T)(c_0 + c_1/T^* + c_2/T^{*2} + 1.0/T^{*3})/(T^*(d_0 + d_1 + d_2/T^* + d_3/T^{*2})) \qquad (3)$$

$a_0 = +916.14919$
$a_1 = 8555.2627$
$a_2 = +8101.6196$

$b_0 = 1914.8161$
$b_1 = 13230.40$
$b_2 = 11315.04$

$g = -0.008$

$c_0 = 58147.879$
$c_1 = +8618.2141$
$c_2 = 1468.565$

$d_0 = 35416.003$
$d_1 = 10895.233$
$d_2 = 1132.4217$

$f = 0.7$

TABLE I: Force Constants for the BB Potential

Substance	ϵ/k, K	r_{min}, nm,	rms error, $cm^3\ mol^{-1}$
Neon	42.00	0.3084	0.5
Argon	140.58	0.3777	2.6
Krypton	199.60	0.4004	3.8
Xenon	186.06	0.4468	0.4

where T^* is the reduced temperature, kT/ϵ, and ϵ and r_m are force constants for the BB potential as defined in ref 7. The root-mean-square errors for these expressions for B^*, $T^*\,dB^*/dT^*$, $T^{*2}\,d^2B^*/dT^{*2}$ are $<1.0 \times 10^{-3}$, $<2.0 \times 10^{-3}$, $<2.0 \times 10^{-3}$, respectively. (For argon at the critical point, these rms errors would mean errors of <0.1 $cm^3\ mol^{-1}$, <1.5 J mol^{-1}, and <0.02 J mol^{-1} K^{-1} in B, the enthalpy, and heat capacity, respectively.) These errors are much less than the experimental errors of the corresponding measured quantities and so can be ignored in making comparisons with experimental data. It may also be noted that these expressions can be extrapolated to reduced temperatures of 0.2 and 100.0 without introducing any large errors and are well behaved at infinite but not at zero temperatures.

Though the BB potential is based on data for argon, it can be extended to other substances by assuming that the potentials are conformable. This is the underlying idea of the corresponding states principle, and, while it may not be strictly true, it is sufficiently good to allow accurate calculation of thermodynamic properties. The results for values of B calculated from the BB potential for the inert gases shown in Table I illustrate this. The rms error values are small and are mostly due to the scatter in the data particularly at low temperatures, as was found for the same sets of data in ref 4 for a series expansion for B.

Discussion

These results show that such continued fractions can represent the classical integral for B over a reduced temperature range of 0.5–20.0 and can be used in its place, without introducing significant errors over the whole temperature range of interest. (For argon, $0.5 < T^* < 20$ corresponds to 75–3000 K.) The same approach can be used for any potential since the constants are obtained from the *results* of the numerical integrations for B. Since we have previously developed a series expansion for B,[4] it is worth pointing out why this representation is superior. The series expansion in ref 4 was almost as accurate for B as the continued fraction, but the errors in the derivatives of B obtained from the series expansion had errors about equal to the errors in the experimental data for specific heat, enthalpy, and Joule Thomson coefficients, whereas the errors in these quantities calculated from the continued fraction were much less. From the point of view of calculating thermodynamic properties, then, the continued fraction is a complete replacement for the classical integral for B calculated from the BB potential and yet is still as simple to use as an empirical equation.

It is pertinent to ask if continued fractions can be used in this way to avoid complex numerical integrations in other physical theories. It has been used successfully for the exponential integral functions[8,9] which occur in the BH theory with the Lennard-Jones potential. It seems possible that this technique can be used in many theories where the analytical answers are too unwieldy to be of practical use. It could provide a way of avoiding the complex numerical in-

tegrations which always occur in the answers for statistical mechanical theories using realistic potentials, and so make it possible for these theories to be used widely for routine calculations.

References and Notes

(1) J. P. O'Connell and J. M. Prausnitz, *Ind. Eng. Chem. Process Des. Dev.*, **6**, 245 (1967).
(2) K. S. Pitzer and R. F. Curl, *J. Am. Chem. Soc.*, **79**, 2369 (1957).
(3) C. Tsonopoulos, *AIChE J.*, **20**, 263 (1974).
(4) R. M. Gibbons, *Cryogenics*, **13**, 658 (1973).
(5) R. M. Gibbons, *Cryogenics*, **14**, 399 (1974).
(6) J. R. Johnson, and P. R. Eubank, *Ind. Eng. Chem., Fundam.*, **12**, 156 (1973).
(7) J. A. Barker and M. V. Bobetic, *Phys. Rev. B.*, **2**, 4176 (1970).
(8) R. M. Gibbons, *J. Chem. Soc., Faraday Trans.*, **71**, 301 (1975).
(9) R. M. Gibbons, *J. Chem. Soc., Faraday Trans.*, **71**, 353 (1975).

Association and Vapor Pressure Isotope Effect of Variously Deuterated Methanols in *n*-Hexane

H. Wolff,* O. Bauer, R. Götz, H. Landeck, O. Schiller, and L. Schimpf

Physikalisch-Chemisches Institut, Universität Heidelberg, 69 Heidelberg, West Germany *(Received July 19, 1974; Revised Manuscript Received July 14, 1975)*

Publication costs assisted by Physikalisch-Chemisches Institut, Universität Heidelberg

Activity coefficients have been determined for solutions of CH_3OH, CH_3OD, CD_3OH, and CD_3OD in *n*-hexane between 35 and 75°C from isothermal vapor pressure measurements. Using Wilson's equations for representing the activity coefficients, curves for the partial pressure ratios of the deuterioisomeric methanols do not show oscillating behavior as they do when using the Redlich–Kister type representation. In each case, Wilson's parameters, association constants, association energies, heats of vaporization, and excess Gibbs free energies suggest that the energy of the deuterium bond of the methanols is larger than that of their hydrogen bond. An association energy of about 5 kcal/mol is derived using Wilson's representation, while the value of 6–7 kcal/mol derived from the Redlich–Kister representation is too large. The ratios $p(CD_3OH)/p(CH_3OH)$ and $p(CD_3OD)/p(CH_3OD)$ are inverse (>1) in the whole concentration range, whereas $p(CH_3OD)/p(CH_3OH)$ and $p(CD_3OD)/p(CD_3OH)$ change from normal (<1) to inverse as the mole fraction goes to zero. Previous measurements on methylamines showed a similar behavior, except that the inversion point ($p/p' = 1$) occurs at a higher mole fraction. The pronounced difference is due to the weaker hydrogen bonding of the amino group compared to the hydroxyl group.

A. Introduction, Measurements, and Evaluation

The investigation of vapor pressure isotherms of binary mixtures from variously deuterated methyl-[1] or dimethylamines[2] and saturated hydrocarbons revealed characteristic differences in the association and the vapor pressure isotope effect of isomeric amines. The differences depended on whether the hydrogen-bonded group or the alkyl group was deuterated. So far, analogous investigations of the alcohols had only been made for CH_3OH and CH_3OD in solutions with *n*-hexane.[3] To consider in addition the methanols which are deuterated in the alkyl groups and to compare the results for the four variously deuterated compounds, the vapor pressure isotherms were also measured for solutions of CD_3OH and CD_3OD in *n*-hexane. In these investigations the preparation of the compounds and the pressure measurement method were the same as that described for the solutions of CH_3OH and CH_3OD. The 99.96 mol % product furnished by Fluka, Buchs, was used for *n*-hexane. CD_3OH and CD_3OD were products of E. Merck, Darmstadt, and C. Roth, Karlsruhe, being deuterated to about 99%.

In addition, the evaluation of the vapor pressure isotherms, which is basic to these investigations, so far followed the representation of the activity coefficients according to Redlich and Kister.[4] Denoting the activity coefficients of the two components of the mixture by f_1 and f_2, the mole fractions by x_1 and x_2, and the Redlich–Kister constants by A_{i-1} ($i = 2, 3 \ldots$), these equations are

$$f_1 = \exp\left\{x_2^2 \sum_{i=2}^{n} A_{i-1}(2x_1 - 1)^{i-3} \times (2[i-1]x_1 - 1)\right\} \quad (1a)$$

and

$$f_2 = \exp\left\{x_1^2 \sum_{i=2}^{n} A_{i-1}(1 - 2x_2)^{i-3} \times (1 - 2[i-1]x_2)\right\} \quad (1b)$$

To represent the activity coefficients of methanol solutions by means of these equations, it is necessary to take five to eleven Redlich–Kister constants instead of the usual three.[3] Denoting the partial pressures of a heavy and a light isomer in the same solvent at the same mole fraction by p and p' and the vapor pressures of the undiluted isomers by

P and P', the partial pressure quotients of two deuterioisomers are given by[1a]

$$p/p' = f_1P_1/f_1'P_1' \quad (2)$$

When using the activity coefficients from equations with five to eleven constants to calculate p/p' from eq 2, the resulting quotients as function of mole fraction oscillate.[3b] The amplitude and the frequency of the oscillations increase with growing number of the Redlich–Kister constants, as shown in Figure 1 for the quotients of CH_3OH and CH_3OD at the temperatures of 40 (nine–ten constants), 50 (eight constants), and 70°C (six constants). When plotting the calculated partial and total vapor pressures as well as their first and second derivatives with respect to the mole fraction, oscillations appear in the curves of the pressures, as is demonstrated for the system CH_3OH–*n*-hexane at 40°C in Figure 2. This led us to try the representation of the activity coefficients by Wilson's equations[5,6] requiring only two constants and by the NRTL equations developed by Renon and Prausnitz[7,8] requiring three constants.

The constants were determined by the least-squares fit developed by Barker[9] for obtaining constants in the Redlich–Kister equations. After transcription of that method to the Wilson or the NRTL equations, initial values of the constants were iterated fitting the measured pressures by

$$\bar{P} = x_1f_1R_1P_1 + x_2f_2R_2P_2 \quad (3)$$

where f_1 and f_2 were the activity coefficients of the respective equations and where the R's were gas imperfection factors determined as in ref 3a and 3b.

However, plotting the relative differences $\Delta P/P$ of the measured pressures P and the calculated pressures $\bar{P}$ vs. x_1 (Figure 3), $\Delta P/P$ from the NRTL equations was found to be two to three times larger than $\Delta P/P$ from Wilson's equations, especially at low concentrations. Therefore, only activity coefficients according to Wilson were used in the calculations, which were performed mainly for $x_1 \rightarrow 0$. Wilson's equations are[10]

$$f_1 = \frac{1}{x_1 + \Lambda_{12}x_2} \times \exp\left\{x_2\left(\frac{\Lambda_{12}}{x_1 + \Lambda_{12}x_2} - \frac{\Lambda_{21}}{\Lambda_{21}x_1 + x_2}\right)\right\} \quad (4a)$$

and

$$f_2 = \frac{1}{x_2 + \Lambda_{21}x_1} \times \exp\left\{-x_1\left(\frac{\Lambda_{12}}{x_1 + \Lambda_{12}x_2} - \frac{\Lambda_{21}}{\Lambda_{21}x_1 + x_2}\right)\right\} \quad (4b)$$

where

$$\Lambda_{12} = \frac{V_2}{V_1}\exp\left(-\frac{\lambda_{12} - \lambda_{11}}{RT}\right) \quad (5a)$$

and

$$\Lambda_{21} = \frac{V_1}{V_2}\exp\left(-\frac{\lambda_{12} - \lambda_{22}}{RT}\right) \quad (5b)$$

V_1 and V_2 denote the mole volumes of components 1 and 2 in the liquid state. $\lambda_{12} - \lambda_{11}$ and $\lambda_{12} - \lambda_{22}$ or the corresponding Λ_{12} and Λ_{21} represent the constants of Wilson's equations.

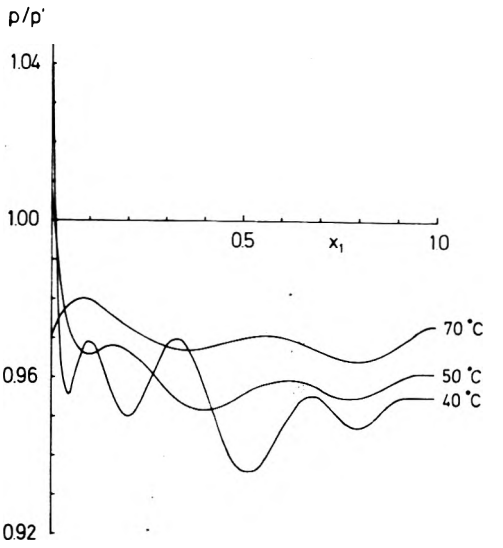

Figure 1. Partial pressure quotients of CH_3OD (p) and CH_3OH (p') as calculated from the Redlich–Kister equations with nine–ten constants (40°C), eight constants (50°C), and six constants (70°C). x_1 is the mole fraction of methanol.

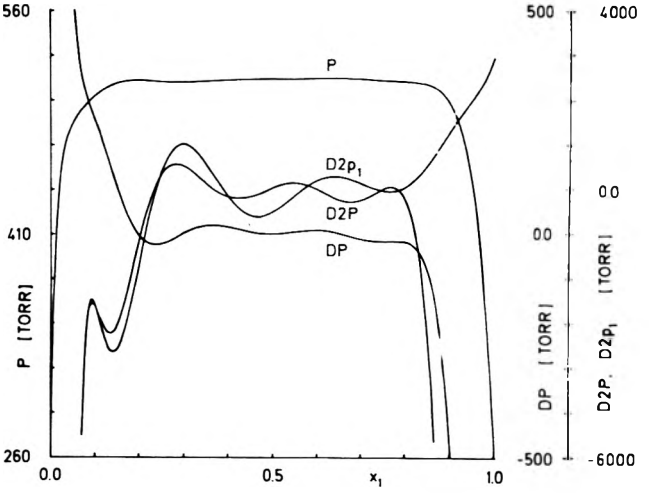

Figure 2. Pressures and their derivatives with respect to the mole fraction for CH_3OH–*n*-hexane at 40°C as calculated from the Redlich–Kister equations with nine constants; P = calculated total pressure; DP and D2P = first and second derivatives of P; D2p_1 = second derivative of the partial pressure of methanol. In the calculations the gas imperfection factors have been neglected. x_1 is the mole fraction of methanol.

B. Results and Discussion

1. *Measured Pressures, Activity Coefficients, and Results Derived from the Representation of the Activity Coefficients According to Wilson.* The pressures measured for mixtures of CD_3OH and CD_3OD with *n*-hexane are listed in Tables I and II. About 10 measurements out of 25–30 are chosen in the range $x_1 < 0.1$ to represent the vapor pressure function at small mole fractions more exactly than would be the case at an equidistant distribution of measured points. The Wilson constants derived from these measurements and the constants obtained for the systems with the remaining isomers, when using the measurements from ref 3a and 3b, are listed in Table III. Figure 4, showing the plots of $\Delta P/P$ vs. x_1 obtained from these constants for CH_3OH, CH_3OD, and CD_3OD in *n*-hexane, reveals the same magnitude of the relative deviations as Figure 3b.

TABLE I: Vapor Pressures of the System CD_3OH–*n*-Hexane in Torr[a]

x_1	+35°C	+40°C	+50°C	+60°C	+70°C	+75°C
0.0000	229.6	279.4	405.1	571.6	788.0	920.2
0.0108	334.3	400.8	558.6	755.6	1000.6	1146.9
0.0149	349.5	421.5	595.0	806.5	1064.4	1217.9
0.0277	376.2	457.1	663.2	922.8	1237.1	1418.4
0.0358	385.9	471.8	687.4	965.0	1307.4	1507.3
0.0509	397.8	487.6	716.1	1016.9	1397.8	1624.0
0.0552	399.2	489.7	720.5	1025.8	1413.7	1645.3
0.0689	404.6	497.1	733.8	1049.8	1456.9	1702.3
0.0785	407.5	500.9	740.9	1062.0	1478.8	1732.0
0.100	412.6	507.8	753.4	1084.4	1517.4	1782.6
0.121	414.5	510.5	759.0	1094.7	1536.0	1808.8
0.170	417.9	515.8	768.8	1113.5	1570.0	1852.8
0.208	419.0	517.5	773.6	1120.8	1584.0	1872.0
0.224	419.8	518.9	774.9	1124.1	1589.2	1879.4
0.284	420.2	519.3	777.1	1128.3	1598.7	1892.9
0.338	420.4	519.5	777.3	1130.1	1603.0	1899.4
0.405	420.5	519.9	777.8	1131.9	1606.4	1903.6
0.465	420.5	519.9	777.9	1132.1	1607.8	1905.8
0.550	420.7	520.0	778.1	1132.3	1607.8	1906.1
0.610	420.8	520.3	778.3	1132.4	1608.0	1906.4
0.671	420.6	520.0	777.9	1131.8	1606.0	1904.5
0.726	420.6	519.7	777.1	1129.8	1603.6	1901.4
0.757	420.5	519.3	776.3	1127.7	1600.5	1896.8
0.775	420.3	518.8	775.0	1126.4	1597.6	1893.6
0.809	419.2	517.2	773.1	1120.6	1588.7	1882.5
0.856	415.9	511.9	763.2	1106.9	1566.7	1855.3
0.907	401.2	494.1	734.3	1063.7	1504.3	1781.1
0.937	378.5	466.0	693.1	1005.0	1421.7	1683.7
0.956	353.9	436.2	650.7	945.8	1342.6	1593.2
0.987	269.5	336.1	511.0	757.4	1094.3	1309.9
1.000	211.0	266.9	419.0	637.2	942.0	1138.9

[a] x_1 is the mole fraction of CD_3OH in the liquid phase.

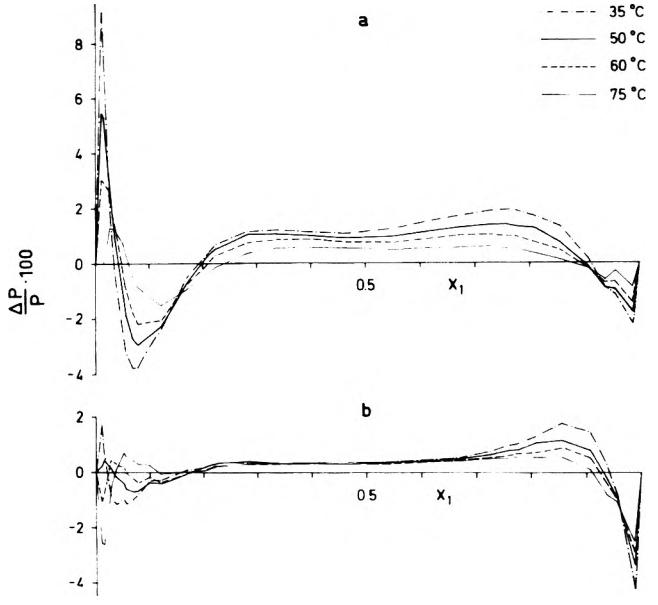

Figure 3. Relative differences $\Delta P/P$ of the measured and the calculated pressures as function of the mole fraction x_1 of the alcohol for CD_3OH–*n*-hexane at 35, 50, 60, and 75°C: (a) representation of the activity coefficients by means of the NRTI equations; (b) representation of the activity coefficients by Wilson's equations.

The systematic change with temperature and the similarity in the magnitude of the deviations prove these to be mainly due to the inadequacy of the representations. The differences are smallest at about 50°C, where ΔP is smaller than 1% in the whole range of mole fractions below $x_1 = 0.7$.

TABLE II: Vapor Pressures of the System CD_3OD–*n*-Hexane in Torr[a]

x_1	+35°C	+40°C	+50°C	+60°C	+70°C	+75°C
0.0000	229.5	279.3	404.6	570.9	788.2	920.1
0.0146	344.6	417.2	588.5	800.1	1057.5	1209.8
0.0187	355.5	431.7	616.4	846.4	1121.8	1281.6
0.0281	371.5	453.2	656.9	916.4	1229.6	1406.4
0.0306	374.4	457.1	664.2	932.0	1257.6	1448.7
0.0497	388.3	476.0	702.0	999.7	1375.6	1602.1
0.0594	391.0	480.2	710.2	1012.6	1401.5	1634.6
0.0691	396.2	487.3	716.8	1035.3	1442.0	1685.3
0.0794	398.8	490.9	729.3	1047.4	1461.5	1711.9
0.0965	402.9	496.0	738.0	1063.2	1491.0	1752.6
0.115	405.5	499.1	743.2	1073.0	1509.3	1777.3
0.120	405.7	500.2	745.1	1076.6	1516.6	1788.3
0.134	406.9	502.0	748.5	1084.2	1527.9	1802.8
0.146	409.1	502.7	750.5	1087.9	1536.7	1811.4
0.235	411.0	507.0	761.0	1104.7	1567.8	1852.7
0.248	411.2	507.2	761.1	1107.0	1570.5	1858.8
0.370	411.4	509.2	762.5	1110.9	1580.7	1874.2
0.485	411.7	509.3	762.6	1111.9	1581.5	1878.1
0.545	411.8	509.4	762.8	1111.9	1582.3	1878.6
0.604	412.2	509.7	762.8	1111.6	1582.5	1875.8
0.718	410.7	508.3	762.7	1110.6	1578.1	1871.8
0.867	405.9	498.5	743.0	1080.1	1529.8	1814.0
0.970	309.7	382.9	575.1	841.4	1201.4	1427.4
1.000	201.1	254.9	401.2	613.3	911.0	1103.1

[a] x_1 is the mole fraction of CD_3OD in the liquid phase.

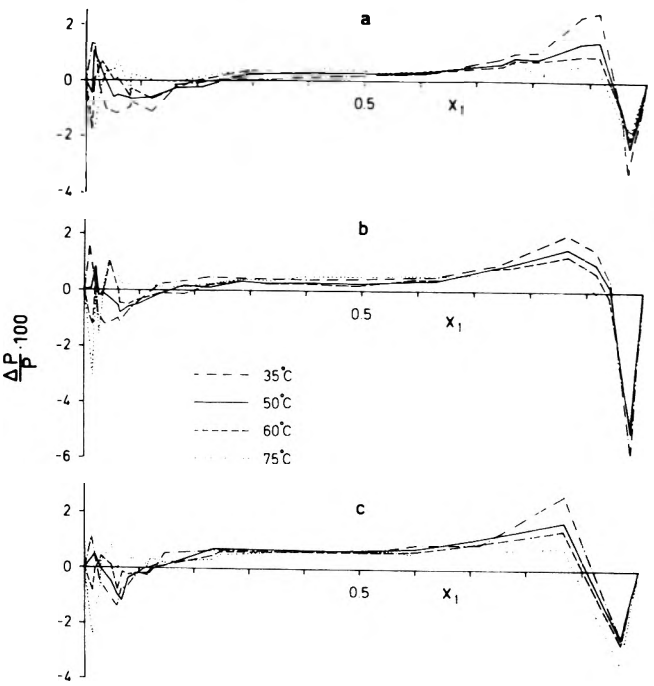

Figure 4. Relative differences $\Delta P/P$ of the measured and the calculated pressures as function of the mole fraction x_1 of the alcohol for CH_3OH–*n*-hexane (a). CH_3OD–*n*-hexane (b), and CD_3OD–*n*-hexane (c) at 35, 50, 60, and 75°C. The activity coefficients are represented by Wilson's equations.

The λ's can be conceived as energy parameters reflecting the interaction between the components of the mixture, with the suffixes 1 for methanol and 2 for *n*-hexane.[8,11,12] The parameters are negative by definition. The fact that $\lambda_{12} - \lambda_{11}$ is positive and about four times larger than $\lambda_{12} - \lambda_{22}$ is in agreement with the concept that the interaction between the methanol molecules is significantly larger than that between the hexane molecules, and also larger than

TABLE III: Wilson Parameters $\lambda_{12} - \lambda_{11}$ and $\lambda_{12} - \lambda_{22}$ of Binary Mixtures from Variously Deuterated Methanols (1) and *n*-Hexane (2)[a]

T, °C	$\lambda_{12} - \lambda_{11}$, cal/mol	(Λ_{12})	$\lambda_{12} - \lambda_{22}$, cal/mol	(Λ_{21})	$\lambda_{12} - \lambda_{11}$, cal/mol	(Λ_{12})	$\lambda_{12} - \lambda_{22}$, cal/mol	(Λ_{21})
	a. CH_3OH–*n*-Hexane				b. CH_3OD–*n*-Hexane			
35	2745	(0.0366_1)	772	(0.0875)	2806	(0.0331_3)	735	(0.0929)
40	2726	(0.0405_4)	759	(0.0912)	2774	(0.0375_1)	726	(0.0962)
50	2662	(0.0514_2)	720	(0.100_4)	2709	(0.0477_6)	688	(0.105_5)
60	2597	(0.0644_3)	690	(0.108_2)	2636	(0.0607_9)	658	(0.113_7)
70	2530	(0.0799_1)	659	(0.116_6)	2548	(0.0778_4)	635	(0.120_6)
75	2498	(0.0886_3)	651	(0.119_0)	2514	(0.0866_1)	629	(0.123_0)
	c. CD_3OH–*n*-Hexane				d. CD_3OD–*n*-Hexane			
35	2786	(0.0342_5)	810	(0.0823)	2799	(0.0335_3)	767	(0.0882)
40	2751	(0.0389_6)	798	(0.0857)	2777	(0.0373_6)	746	(0.0931)
50	2680	(0.0499_9)	765	(0.0936)	2713	(0.0474_8)	729	(0.0989)
60	2604	(0.0638_1)	736	(0.100_9)	2637	(0.0607_1)	707	(0.105_5)
70	2524	(0.0805_6)	712	(0.107_9)	2543	(0.0783_1)	693	(0.110_8)
75	2484	(0.0904_1)	700	(0.110_9)	2499	(0.0884_6)	689	(0.112_7)

[a] Values of Λ_{12} and Λ_{21} in parentheses.

TABLE IV: Wilson Parameters $\lambda_{12} - \lambda_{11}$ and $\lambda_{12} - \lambda_{22}$ of the Systems from Variously Deuterated Amines (1) and *n*-Hexane (2) Calculated from the Data in Ref 1, 2a, 13, and 14

	Nondeuterated associating group			Deuterated associating group		
T, °C	Amine	$\lambda_{12} - \lambda_{11}$, cal/mol	$\lambda_{12} - \lambda_{22}$, cal/mol	Amine	$\lambda_{12} - \lambda_{11}$, cal/mol	$\lambda_{12} - \lambda_{22}$, cal/mol
+20	CH_3NH_2	929	268	CH_3ND_2	973	263
+10		975	298		1015	307
0		1019	335		1058	359
−10		1067	376		1105	402
−20		1118	420		1160	453
−40		1227	569		1279	589
+20	CD_3NH_2	941	249	CD_3ND_2	972	268
+10		982	289		1019	311
0		1025	333		1060	341
−10		1068	384		1106	412
−20		1118	439		1159	483
−40		1229	558		1278	635
+20	$C_2H_5NH_2$	690	85	$C_2H_5ND_2$	729	81
−20		836	133		864	159
+20	$(CH_3)_2NH$	571	−47	$(CH_3)_2ND$	552	4
−20		670	55		696	61
+20	$(CD_3)_2NH$	526	6	$(CD_3)_2ND$	565	−13
−20		657	72		689	69

TABLE V: Activity Coefficients f_1 and f_2 of the Binary Mixtures from Variously Deuterated Methanols (1) and *n*-Hexane (2) at 50°C

Mole fraction MeOH	CH_3OH–*n*-hexane		CH_3OD–*n*-hexane		CD_3OH–*n*-hexane		CD_3OD–*n*-hexane	
	f_1	f_2	f_1	f_2	f_1	f_2	f_1	f_2
0	47.8_2	1	51.2_2	1	49.5_2	1	51.8_6	1
0.01	34.2_6	1.00_2	35.8_7	1.00_2	35.1_8	1.00_2	36.2_5	1.00_2
0.05	15.0_1	1.02_6	15.1_9	1.02_7	15.2_1	1.02_6	15.3_1	1.02_7
0.10	8.49_4	1.07_3	8.51_1	1.07_5	8.57_4	1.07_3	8.57_1	1.07_5
0.15	5.86_2	1.13_0	5.85_4	1.13_3	5.90_8	1.13_1	5.89_2	1.13_3
0.20	4.46_0	1.19_7	4.44_7	1.20_1	4.49_2	1.19_9	4.47_6	1.20_1
0.30	3.00_9	1.36_3	2.99_7	1.36_7	3.02_9	1.36_5	3.01_6	1.36_8
0.40	2.26_9	1.58_6	2.26_0	1.59_0	2.28_3	1.58_8	2.27_3	1.59_1
0.50	1.82_3	1.89_6	1.81_6	1.90_2	1.83_4	1.90_0	1.82_6	1.90_3
0.75	1.23_4	3.68_4	1.23_1	3.68_7	1.23_9	3.70_2	1.23_5	3.70_1
1	1	25.7_3	1	24.5_7	1	27.6_2	1	26.2_1

that between the hexane and the methanol molecules. The calculated values of $\lambda_{12} - \lambda_{11}$, about 1000 and about 2500 cal/mol for methylamine (Table IV) and methanol, respectively, demonstrate the larger hydrogen bond energy of the methanols compared to the methylamines.

However, the most conspicuous observation is that $\lambda_{12} - \lambda_{11}$ of the compounds deuterated in the associating group is greater than $\lambda_{12} - \lambda_{11}$ of the compounds in which this group is not deuterated. The same observation is made for *n*-hexane solutions of amines when using Wilson's con-

stants for representing their activity coefficients (Table IV). In accordance with the determination of somewhat greater activity coefficients for the respective compounds (Table V), therefore, the deuterium bond energy is somewhat greater than the hydrogen bond energy. (The larger values of the activity coefficients are observed only for sufficiently diluted solutions, since the values at the undiluted state are unity by definition.)

The relation

$$(\lambda_{12} - \lambda_{11})_{CD_3OH} - (\lambda_{12} - \lambda_{11})_{CH_3OH} = (\lambda_{12} - \lambda_{11})_{CD_3OD} - (\lambda_{12} - \lambda_{11})_{CH_3OD}$$

can be expected to hold at any temperature. A comparatively large deviation at 35°C reflects the errors due to the small vapor pressures. At higher temperatures the agreement is not quite as good as for the corresponding calculation with methylamines (Table IV). However minor differences prove the equation to be satisfied, thus attesting to the consistency of the data.

2. *Association Constants, Association Energies, and Vaporization Energies.* The calculation of association constants for methanols in solution with *n*-hexane is based on the assumption of equilibria of monomers with dimers, dimers with trimers, etc., permitting the equilibrium constants to be different if necessary. Adopting this model, the binary solutions can be assumed to behave ideally if regarded as mixtures consisting of the solvent and of various forms of the associating component. As shown by Prigogine et al.,[15] thus two expressions for the Gibbs energy of the system as a function of the chemical potentials are obtained. Viewing the mixture as a binary system of macroscopic components, the potentials depend on the activity coefficients and the stoichiometric mole fractions. Viewing the mixture as a multicomponent system, the potentials depend on the true mole fractions. Appropriate transformation and solution of the expressions for the Gibbs energy and of the relations for the various chemical potentials and for the stoichiometric and the true mole fractions yield the expression

$$\beta_1 = f_1/(f_2 \lim_{x_1 \to 0} f_1) \tag{6}$$

for the fraction of molecules of the associating component which exist as monomers. The fraction of molecules existing as i mers is[13]

$$\beta_i = i x_{(i)}/x_1 f_2 \tag{7}$$

where $x_{(i)}$ denotes the true mole fraction of the $i$mers. Inserting β_i from eq 7 in $\Sigma\beta_i = 1$ and multiplying the sum by $x_1 f_2$, one obtains

$$x_{(1)} + 2x_{(2)} + 3x_{(3)} + \ldots = x_1 f_2 \tag{8}$$

Taking into account the definitions of the equilibrium constants

$$K_{1,2}{}^x = x_{(2)}/x_{(1)}{}^2, \quad K_{2,3}{}^x = x_{(3)}/x_{(2)}x_{(1)}, \text{ etc.} \tag{9}$$

eq 10 results:

$$x_{(1)} + 2K_{1,2}{}^x x_{(1)}{}^2 + 3K_{1,2}{}^x K_{2,3}{}^x x_{(1)}{}^3 + \ldots = x_1 f_2 \tag{10}$$

For sufficiently large dilution the dimerization constant can be calculated as

$$K_{1,2}{}^x = \frac{1 - \beta_1}{2 x_1 f_2 \beta_1{}^2} \tag{11}$$

by omitting the terms containing $x_{(1)}{}^3$, $x_{(1)}{}^4$, ... and by applying eq 7. Analogously the trimerization constant follows as

$$K_{2,3}{}^x = \frac{\frac{1}{3} - \frac{1}{3}\beta_1 - \frac{2}{3}K_{1,2}{}^x x_1 f_2 \beta_1{}^2}{K_{1,2}{}^x x_1{}^2 f_2{}^2 \beta_1{}^3} \tag{12}$$

by omission of the terms with powers of $x_{(1)}$ higher than $x_{(1)}{}^3$.

To calculate the equilibrium constants directly from Wilson's constants, f_1 and f_2 may be taken from eq 4. From (4a) we find

$$\lim_{x_1 \to 0} f_1 = \frac{1}{\Lambda_{12}} \exp(1 - \Lambda_{21}) \tag{13}$$

Applying De L'Hospital's rule, we obtain from (11) for $x_1 \to 0$

$$K_{1,2}{}^x = \frac{2 - \Lambda_{12} - \Lambda_{12}\Lambda_{21}{}^2}{2\Lambda_{12}} \tag{14}$$

when taking eq 4, and eq 6 after inserting eq 13. Considering eq 4, 6, and 13, and applying De L'Hospital's rule twice, the trimerization constant follows as

$$K_{2,3}{}^x = 2K_{1,2}{}^x + \frac{(\Lambda_{21} - 1)^2(1 + 2\Lambda_{21})\Lambda_{12}{}^2 - 3(1 - \Lambda_{12})^2}{6K_{1,2}{}^x \Lambda_{12}{}^2} \tag{15}$$

The association constants calculated in this way are listed in Table V. Their values differ little from those obtained previously for CH_3OH and CH_3OD with the help of the Redlich–Kister equations.[3] In agreement with the values of $\lambda_{12} - \lambda_{11}$ as well as those of the activity coefficients, the constants indicate a somewhat enhanced association for the OD compounds compared to their OH analogues.

The dimerization energies, $\Delta U_{1,2}$, calculated from the association constants according to van't Hoff, are likewise shown in the table. Their values, ~5 kcal/mol, are smaller than those of 6–7 kcal/mol derived from the representations of f_1 and f_2 according to Redlich and Kister. The smaller values agree better with other results.[16] They are, therefore, preferable.

The values for the dimerization energy do not permit the unequivocal conclusion that the energy of the deuterium bond is larger than that of the hydrogen bond. However, the vaporization energy

$$\Delta U_v = RT^2 \frac{\mathrm{d} \ln P_1}{\mathrm{d}T} - RT \tag{16}$$

which is more reliably determined, supports this result (Table VI). ΔU_v does not depend on the special assumptions of the association model used for the calculation of the association constants and the association energies. Thus, even if the present model were shown to be incorrect, the larger energy of the deuterium bridge is demonstrated.

3. *Vapor Pressure Isotope Effect.* Previous authors[17-19] have determined, as a function of temperature, the vapor pressure isotope effect of the undiluted methanols, characterized by the ratio of the pressures p of the heavy and p' of the light compound. Figure 5 compares these ratios from our measurements to those of the corresponding methylamines.[1b] The inverse effect ($p/p' > 1$) of the pairs with the deuteration difference in the alkyl groups is significantly smaller ($p/p' = \sim 1.01$) than that of the methylamines ($p/p' = \sim 1.04$). The normal effect ($p/p' < 1$) of the pairs with the difference in the associating groups, however, is a little

TABLE VI: Association Constants $K_{1,2}{}^{x}$, $K_{2,3}{}^{x}$, $K_{1,2}{}^{c\,a}$ and Dimerization Energies $\Delta U_{1,2}$ of Variously Deuterated Methanols in Solution with *n*-Hexane, and Vaporization Energies ΔU_V of the Undiluted Methanols

Methanol	T, °C	$K_{1,2}{}^{x}$	$K_{1,2}{}^{c}\,M^{-1}$	$\Delta U_{1,2}$, cal/mol	$K_{2,3}{}^{x}$	ΔU_V, cal/mol
CH_3OH	35	26.8	3.58		40.7	
	40	24.2	3.25		36.8	
	50	18.9	2.58	−4930	28.9	8390
	60	15.0	2.08		23.0	
	70					8240
	75					
CH_3OD	35	29.7	3.96		45.0	
	40	26.2	3.52		39.7	
	50	20.4	2.79	−5130	31.2	8520
	60	15.9	2.21		24.4	
	70					8350
	75					
CD_3OH	35	28.7	3.83		43.5	
	40	25.2	3.38		38.3	
	50	19.5	2.66	−5250	29.8	8380
	60	15.2	2.10		23.3	
	70					8250
	75					
CD_3OD	35	29.3	3.91		44.5	
	40	26.3	3.53		39.9	
	50	20.6	2.80	−5150	31.3	8470
	60	16.0	2.21		24.5	
	70					8350
	75					

[a] $K_{1,2}{}^{c}$ represents the dimerization constant defined as a function of concentration, it results from $K_{1,2}{}^{x}$ by multiplying by the molar volume of the solvent.

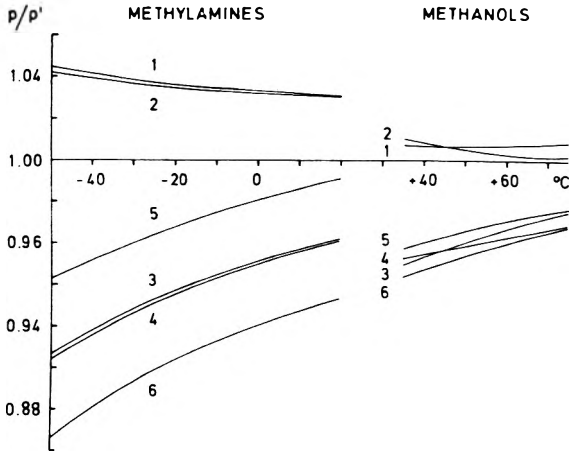

Figure 5. Vapor pressure quotients p/p' of undiluted methanols and methylamines as function of the temperature: (1) CD_3OH/CH_3OH and CD_3NH_2/CH_3NH_2, (2) CD_3OD/CH_3OD and CD_3ND_2/CH_3ND_2, (3) CH_3OD/CH_3OH and CH_3ND_2/CH_3NH_2, (4) CD_3OD/CD_3OH and CD_3ND_2/CD_3NH_2, (5) CD_3OD/CH_3OH and CD_3ND_2/CH_3NH_2, (6) CH_3OD/CD_3OH and CH_3ND_2/CD_3NH_2.

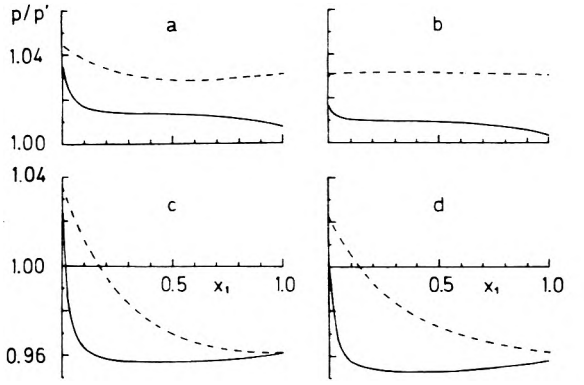

Figure 6. Partial pressure quotients p/p' of deuterioisomeric methanols in solutions with *n*-hexane at 50°C (——) and of deuteriosimeric methylamines in solutions with *n*-hexane at 20°C (- - - -) as function of the methanol or the methylamine mole fraction x_1: (a) CD_3OH/CH_3OH and CD_3NH_2/CH_3NH_2, (b) CD_3OD/CH_3OD and CD_3ND_2/CH_3ND_2, (c) CH_3OD/CH_3OH and CH_3ND_2/CH_3NH_2, (d) CD_3OD/CD_3OH and CD_3ND_2/CH_3ND_2.

greater than that of the amines. (At 40°C p/p' is found to be about 0.95 for CH_3OH/CH_3OD and CD_3OH/CD_3OD, while a value of about 0.96 is extrapolated for the amines.)

Figure 6, showing the concentration dependence of the ratios according to eq 2, proves in addition the inverse effect to be nearly concentration independent, while the normal effect changes into the inverse effect with dilution. The curves, based on Wilson type representations of the activity coefficients and thus without oscillatory behavior, clearly show this transition.

As seen in Figure 6c,d, by comparison of the curves for methanols (solid lines) to those of the amines (dotted lines), the transition from the normal to the inverse effect results only at high dilution. The same characteristic behavior follows from the plot of the total pressure differences $P' - P$ (Figure 7), showing the inversion ($P' - P = 0$) for *n*-hexane solutions of CH_3OH and CH_3OD at a methanol mole fraction $x_1 = 0.02$. For the corresponding amines the crossover occurs at $x_1 = 0.17$, even though the temperature is lower. (The maxima and minima shown by the curves at high mole fractions are due to the inadequacy of the representations in this range (cf. Figures 3b and 4). The differences were calculated from

$$P' - P = x_1R_1P_1'\Delta f_1 + x_2R_2P_2'\Delta f_2 + x_1R_1f_1'\Delta P_1 \quad (17)$$

where P' is the total pressure of the *n*-hexane solutions of CH_3OH or CH_3NH_2, while P is the total pressure of the

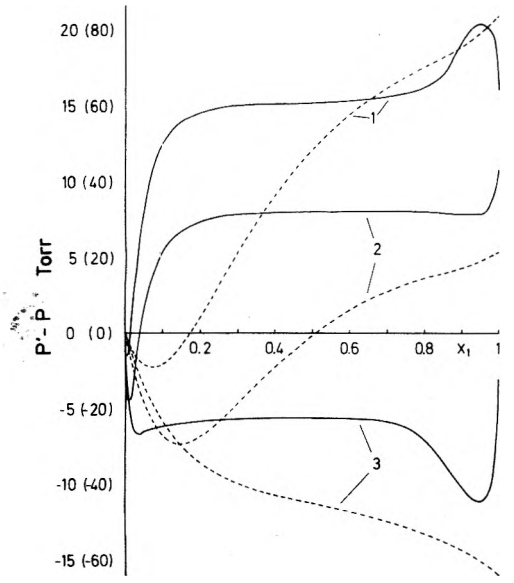

Figure 7. Total pressure differences $P' - P$ of mixtures of variously deuterated methanols and *n*-hexane at 50°C (solid lines, ordinate values without parentheses) and of mixtures of variously deuterated methylamines and *n*-hexane at 20°C (dotted lines, ordinate values within parentheses). P' refers to the mixtures of *n*-hexane and CH_3OH or CH_3NH_2. P refers to the mixtures of *n*-hexane and (1) CH_3OD or CH_3ND_2, (2) CD_3OD or CD_3ND_2, and (3) CD_3OH or CD_3NH_2. x_1 is the mole fraction of methanol or methylamine.

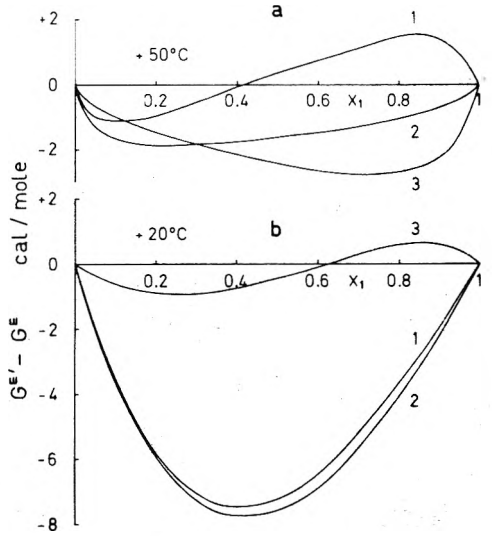

Figure 8. Differences $G^{E'} - G^E$ of the excess Gibbs free energies of mixtures of variously deuterated methanols and *n*-hexane at 50°C (a) and of mixtures of variously deuterated methylamines and *n*-hexane at 20°C (b). $G^{E'}$ refers to the mixtures of *n*-hexane and CH_3OH or CH_3NH_2. G^E refers to the mixtures of *n*-hexane and (1) CH_3OD or CH_3ND_2, (2) CD_3OD or CD_3ND_2, and (3) CD_3OH or CD_3NH_2. x_1 is the mole fraction of methanol or methylamine.

system with the deuterated compound. f_1' and f_2' are the activity coefficients of CH_3OH or CH_3NH_2 and of *n*-hexane, while Δf_1 and Δf_2 denote the differences of the activity coefficients for the two systems compared. P_1' and P_1 are the pressures of the pure isomers, ΔP_1 is the difference of these pressures, and P_2 is the pressure of pure *n*-hexane.)

According to the relation[20]

$$\frac{p}{p'} = \prod_{i=1}^{6} \left(\frac{u_{i(\mathrm{cond})}' \sinh (u_{i(\mathrm{cond})}/2)}{u_{i(\mathrm{cond})} \sinh (u_{i(\mathrm{cond})}'/2)} \right) \times \prod_{i=7}^{3N} \left(\frac{u_{i(\mathrm{cond})}' u_{i(\mathrm{gas})} \sinh (u_{i(\mathrm{gas})}'/2) \sinh (u_{i(\mathrm{cond})}/2)}{u_{i(\mathrm{cond})} u_{i(\mathrm{gas})}' \sinh (u_{i(\mathrm{gas})}/2) \sinh (u_{i(\mathrm{cond})}'/2)} \right) \quad (18)$$

($u_i = h\nu_i/kT$, ν_i = wavenumber of vibrations) the vapor pressure ratio depends on the shifts of the intermolecular (i = 1–6) and the intramolecular (i = 7–$3N$) vibrations with condensation or solvation. Shifts to lower wavenumbers increase while shifts to higher wavenumbers decrease the ratio. For the methylamine pairs with different methyl groups the occurrence of an inverse effect and the lack of a significant change of this inverse effect in the whole concentration range has been explained based on two assumptions: (1) the amino group vibrations, even those of the undiluted compounds, cancel in their influence on the ratio; (2) the influence of the red-shifted methyl group vibrations on the ratio is greater than that of the blue-shifted vibrations. For the methanols with different methyl groups because of the smallness of their inverse effect one is lead to the conclusion that the hydroxyl group vibrations do not cancel to the same extent.

The normal effect of the methylamine pairs with different amino groups has been interpreted assuming the following: the methyl group vibrations cancel in the ratio; the influence of the blue-shifted amino group vibrations (in particular of the hindered rotations or the torsions occurring with the association) is greater than the influence of the red-shifted amino group vibrations. For the normal effect of the methanols substantially the same explanation holds true with respect to the hydroxyl group vibrations, irrespective of the degree to which the methyl group vibrations of the alcohols cancel.

The change from the normal to the inverse effect results from the dissociation of the associated molecules into the monomers. This transition is accompanied by a reduction of the vibrational shifts. In particular the torsions of the hydroxyl groups, observed at 655 and 475 cm^{-1} for undiluted CH_3OH and CH_3OD, respectively,[21] are considerably lowered (to about 275 and 215 cm^{-1}, when considering the values for the torsions of the monomers in an argon matrix[22]). Thus the vibrations fall in the range where both the vibration of the deuterated and the vibration of the nondeuterated molecule are largely excited, and where, therefore, their influence on the ratio is significantly reduced. As a consequence of this the inverse effect of the red-shifted vibrations, though likewise reduced, predominates.

The appearance of the inversion only at high dilution conforms to the concept that the methanols form much stronger hydrogen bonds than the methylamines.

4. *Excess Gibbs Free Energies.* The maximum value of the excess Gibbs free energy has been calculated to about 200 cal/mol for mixtures of methanol and *n*-hexane at 50°C as well as for mixtures of methylamine and *n*-hexane at 20°C.[23] Figure 8 represents the differences of the excess Gibbs free energies calculated from

$$G^{E'} - G^E = RT \left(x_1 \ln \frac{f_1'}{f_1} + x_2 \ln \frac{f_2'}{f_2} \right) \quad (19)$$

where $G^{E'}$ refers to CH_3OH or CH_3NH_2 in *n*-hexane, while G^E refers to the system with the deuterated compound.

The values of $-(G^{E'} - G^E)$ are distinctly greater for the pairs with CH_3ND_2 and CD_3ND_2 (Figure 8b, curves 1 and 2) than for the pair with CD_3NH_2 (Figure 8b, curve 3). The greater values result from f_1 and f_2 being greater than f_1'

and f_2'. That means, the curves for $G^{E'} - G^E$ of the methylamine solutions reflect the somewhat enhanced association of the compounds deuterated in the associating groups.

The curves for the methanol solutions (Figure 8a) are more complicated, possibly in part due to the insufficiency of the data. However, at low concentrations, where $G^{E'} - G^E$ depends mainly on f_1 and f_1', the curves show the course observed for the methylamines in the whole concentration range. Considering the different hydrogen bond strengths of the hydroxyl and the amino groups, thus the results for the variously deuterated methanols conform again to the concepts on hydrogen bonding and vapor pressure isotope effect of the variously deuterated amines.

Acknowledgment. We gratefully acknowledge support of this work by the Deutsche Forschungsgemeinschaft, Bad Godesberg, by the Fonds der Chemie, Frankfurt, and by the BASF, Ludwigshafen.

References and Notes

(1) (a) H. Wolff and A. Hopfner, *Ber. Bunsenges. Phys. Chem.*, **69**, 710 (1965); (b) *ibid.*, **71**, 461 (1967).
(2) (a) H. Wolff and R. Würtz, *J. Phys. Chem.*, **74**, 1600 (1970); (b) *Z. Phys. Chem. (Frankfurt am Main)*, **67**, 115 (1969).
(3) (a) H. Wolff and H.-E. Hoppel, *Ber. Bunsenges. Phys. Chem.*, **72**, 710 (1968); (b) **72**, 722 (1968).
(4) O. Redlich and A. T. Kister, *Ind. Eng. Chem.*, **40**, 345 (1948).
(5) G. M. Wilson, *J. Am. Chem. Soc.*, **86**, 127 (1964).
(6) J. M. Prausnitz, *Oil Gas J.*, **8**, 61 (1969).
(7) H. Renon and J. M. Prausnitz, *Ind. Eng. Chem.*, **8**, 413 (1963).
(8) J. M. Prausnitz, "Molecular Thermodynamics of Fluid-Phase Equilibria", Prentice Hall, Englewood Cliffs, N.J., 1969.
(9) J. A. Barker, *Aust. J. Chem.*, **6**, 207 (1953).
(10) In Wilson's orginal paper[5] the constants are defined in a different way. However taking into account the relations

$$g_{2/1} - g_{11} = \lambda_{12} - \lambda_{11}$$

$$g_{1/2} - g_{22} = \lambda_{12} - \lambda_{22} \qquad [g_{1/2} = g_{2/1}]$$

$$A_{1/2} = 1 - \Lambda_{21}$$

and

$$A_{2/1} = 1 - \Lambda_{12}$$

eq 4 can be transformed in Wilson's orginal equations.
(11) H. Krug, D. Haberland, and H.-J. Bittrich, *Chem. Tech.*, **23**, 410 (1971).
(12) H. Krug, Dissertation Technichshe Hochschule fur Chemishe, "Carl Schorlemmer", Leuna-Merseburg, 1969.
(13) H. Wolff and A. Hopfner, *Ber. Bunsenges. Phys. Chem.*, **66**, 149 (1962).
(14) H. Wolff, A. Hopfner, and H.-M. Hopfner, *Ber. Bunsenges. Phys. Chem.*, **68**, 410 (1964).
(15) (a) I. Prigogine, V. Mathot, and A. Desmyter, *Bull. Soc. Chim. Belg.*, **58**, 547 (1949); (b) I. Prigogine and R. Defay, "Chemical Thermodynamics", Longmans, Green and Co., London, 1954, p 410.
(16) (a) G. C. Pimentel and A. L. McClellan, "The Hydrogen Bond", W. H. Freeman, San Francisco, Calif., 1960, Appendix B; (b) C. G. Savini, D. R. Winterhalter, and H. C. Van Ness, *J. Chem. Eng. Data*, **10**, 168, 171 (1965); (c) E. E. Tucker and E. D. Becker, *J. Phys. Chem.*, **77**, 1783 (1973); (d) W. A. P. Luck, *Discuss. Faraday Soc.*, **43**, 115 (1967).
(17) J. Beersman and J. C. Jungers, *Bull. Soc. Chim. Belg.*, **56**, 72 (1947).
(18) I. Kiss, G. Jákly, G. Jancsó, and H. Illy, *Acta Chim. Hung.*, **51**, 65 (1967).
(19) I. Rabinovich, "Influence of Isotopy on the Physicochemical Properties of Liquids", Consultants Bureau, New York, N.Y., 1970.
(20) J. Bigeleisen, *J. Chem. Phys.*, **34**, 1485 (1961).
(21) M. Falk and E. Whalley, *J. Chem. Phys.*, **34**, 1554 (1961).
(22) P. D. Mallinson and D. C. McKean, *Spectrochim. Acta, Part A*, **30**, 1133 (1974).
(23) H. Wolff, A. Hopfner, and H.-E. Hoppel, *Ber. Bunsenges. Phys. Chem.*, **71**, 151 (1967).

Volumetric and Isentropic Compressibility Behavior of Aqueous Amine Solutions. II

M. V. Kaulgud* and K. J. Patil

Department of Chemistry, Nagpur University, Nagpur-10, India *(Received November 11, 1974; Revised Manuscript Received September 25, 1975)*

Partial molal volumes ($\bar{V}_2$) and apparent molal compressibilities (ϕ_K) have been measured for the following amines and pyridine in aqueous solutions from density and sound velocity measurements at 20°C (or 25°C): *i*-$PrNH_2$, *i*-$BuNH_2$, *sec*-$BuNH_2$, *t*-$BuNH_2$, $1,2Pr(NH_2)_2$, $1,4Bu(NH_2)_2$, ethanolamine, pyrrolidine, piperidine, and morpholine. The limiting partial molal excess volumes ($\bar{V}_2^{0E}$) are in general negative and go through a minima with increasing concentration except for pyridine. The limiting apparent molal compressibilities (ϕ_K^0) are also found to be negative except for pyridine and *t*-$BuNH_2$. The magnitudes of $\bar{V}_2^{0E}$, ϕ_K^0, and the slopes of the $\bar{V}_2(x_2)$ and $\phi_K(x_2)$ curves are higher for solutes with more hydrophobic character and decrease on substitution of a second amino or hydroxy group. These results are consistent with the promotion of structure of the solvent. There appears to exist a one to one correspondence between the limiting volumes and compressibilities as well as the slopes of the concentration plots of the partial volume and apparent compressibility. The isomeric butyl amines however show higher slopes for the compressibility plots. Moreover, *t*-$BuNH_2$ exhibits the unique behavior of yielding a positive value for ϕ_K^0, a minimum in the $\phi_K(x_2)$ curve, and also a minimum value for $d\phi_K/dx_2$ in the isomeric series. These pecularities are believed to arise out of the unique way of dissolution of *t*-$BuNH_2$ in water, substitutional dissolution in very dilute solutions, and interstitial dissolution at higher concentrations.

Introduction

In the previous work,[1] the volumetric and compressibility behavior in dilute aqueous solutions of some straight chain mono- and dialkylamines was reported and the results discussed from the point of view of solute-solvent interactions. Of special interest was the observation that the apparent molal compressibility (ϕ_K) for some of the lower

TABLE I:

Solute	Concn range, m	$\bar{V}_2^0$, ml mol^{-1}	$\bar{V}_2^{0E}$, ml mol^{-1}	$d\bar{V}_2/dx_2$, ml mol^{-1}	$10^{10}\phi_K$, cm^2 dyn^{-1} mol^{-1}	$10^{10}(d\phi_K/dx_2)$, cm^2 dyn^{-1} mol^{-1}
$EtNH_2$	0.5–18	58.0	−8.0	−69	−2.5	200
n-$PrNH_2$	0.37–5.5	74.0	−8.5	−159	−9.5	357
i-$PrNH_2$	0.4–5.9	75.5	−10.3	−165	−12.0	324
n-$BuNH_2$	0.3–3.6	88.8	−10.1	−163	−16.0	1150
i-$BuNH_2$	0.4–3.9	89.5	−11.6	−180	−18.0	1000
sec-$BuNH_2$	0.25–3	89.1	−11.7	−240	−18.0	832
$tert$-$BuNH_2$	0.06–5	92.4 93.0[b]	−12.2	−362	+10.0	735
$(Et)_2NH$	0.25–8.6	90.8	−12.1	−153	−10.0	416
$Et(NH_2)_2$	2.5–40.0	62.1	−5.0	−39	−6.5	45
$1,2Pr(NH_2)_2$	1.6–18.8	78.1	−7.0	−48	−4.5	85
$1,4Bu(NH_2)_2$	1.1–17.6	92.5		−30	−6.0	100
$Et(OH)NH_2$	1.9–41.0	58.8	−1.2	−15	+3.5	20
Pyrrolidine[a]	1.9–8.9	77.0[b] 77.8[c]	−5.8	−112[b] −137[c]	−3.5	217
Piperidine[a]	0.5–8.0	92.4[b] 92.5[c]	−6.8	−154[b] −267[c]	−12.0	545
Morpholine[a]	1.7–22.5	82.7	−4.7	−30	+4.0	66
Pyridine[a]	1.0–24.4	77.0 77.7[d]	−4.1		+6.2 +2.2[d]	190

[a] These solutes are studied at 25°C, while the rest of the data are at 20°C. [b] Data obtained after applying the hydrolysis correction. [c] These values are taken from ref 5. [d] From ref 7.

amines exhibited a minimum in the $\phi_K(x_2)$ curves. This fact was used to support the concept of substitutional dissolution[2] for these amines and an interstitial mode of dissolution for others which did not show a minimum in the $\phi_K(x_2)$ curves. Slopes of the $\phi_K(x_2)$ curves also exhibited significant differences for related compounds.

The effect of chain branching in monofunctional mixed solutes as well as the effect of substitution of a second hydrophilic interacting center on the solution properties of alcohols, ethers, cyclic ethers, and cyclic amines have been studied extensively and relevant information has been summarized lucidly.[2,3] The highly symmetrical t-BuOH, for instance, shows maximum enthalpy and entropy effects and has also a maximum value for $\Delta\theta_{str}$, the structural contribution to the rise in the temperature of maximum density of water (TMD). This has been interpreted in terms of maximum solvent structure stabilization caused by dissolved solute molecules. Similar extensive information on enthalpy and entropy effects in branch chain amines, diamines, and cyclic amines is lacking. Also, no information is yet available on the volumetric and compressibility behavior of these compounds in dilute aqueous solutions. In the present paper sound velocity and density of dilute aqueous solutions of the following compounds have been obtained experimentally and the results analyzed: i-$PrNH_2$, i-$BuNH_2$, sec-$BuNH_2$, t-$BuNH_2$, $1,2Pr(NH_2)_2$, $1,4Bu(NH_2)_2$, ethanolamine, pyrrolidine, piperidine, morpholine, and pyridine.

Experimental and Results

i-$BuNH_2$ (Fluka-Purum), sec-$BuNH_2$ (Fluka-Purum), t-$BuNH_2$ (Fluka-Pract), ethanolamine (Fluka-Purum), morpholine (BDH), pyrrolidine (Merck), and piperidine (Riedel-de-Haen) were dried over potassium hydroxide pellets for at least 48 hr, distilled twice, and the middle fractions were collected. 1,2-Propanediamine (Fluka-Pract), 1,4-butanediamine (Merck), and isopropylamine (70% in water) were used directly. All solutions were prepared fresh before measurements with double distilled water by weighing in glass stoppered flasks.

Sound velocity (U) and compressibility (β) for the amines handled in this work show[4] a maximum in U and a minimum in β at a concentration which is governed by the geometry and chain length of the solute.

Densities at constant temperatures (20 or 25°C) were measured with a calibrated 10-ml density bottle suspended in a thermostat held at constant temperature (±0.02°C) for over 1 hr. The densities are considered to be accurate to ±5 units in the fifth decimal place.

Partial molal volumes ($\bar{V}_2$) of the amines were calculated from the density data by first calculating the apparent molal volumes (ϕ_V) given by the expression

$$\phi_V = \frac{1000(d_0 - d)}{cd_0} + \frac{M_2}{d_0} \quad (1)$$

(where the symbols have their usual meanings) and then converting the ϕ_V into $\bar{V}_2$ using the equation

$$\bar{V}_2 = \phi_V + m\left[\frac{d\phi_V}{dm}\right] \quad (2)$$

where m is the molality. The slopes ($d\phi_V/dm$) were evaluated by drawing tangents by the mirror method. $\bar{V}_2^0$'s, the limiting partial molal volumes, were evaluated by extrapolating $\bar{V}_2$ to zero concentration. However, for most of the amines (except pyridine, morpholine, and ethanolamine) the pK_a values are around 10.5–11.2. Hence strictly speaking corrections for the hydrolysis of the amines should be applied as done by Cabani et al.,[5] in order to obtain true $\bar{V}_2^0$'s for the unhydrolyzed amine molecules. The concentration range handled in this work is not too low and the $\bar{V}_2^0$'s have been evaluated to indicate trends rather than to yield precise values. In view of this, the correction procedure turned out to be meaningful only in the case of pyrrolidine and piperidine, in which cases inspite of the relatively high concentrations our $\bar{V}_2^0$ values show good agreement with those reported by Cabani et al.[5] (cf. Table I). Of the

other amines corrections applied[6] in the case of t-$BuNH_2$ (where the corrections were found to be necessary on account of the low concentrations handled) caused an increase of 0.6 ml in $\bar{V}_2^0$ (cf. Table I and Figure 4), which is of the order of accuracy (±0.5 ml) claimed for the $\bar{V}_2^0$ values. Hence it was not thought necessary in the purview of this paper to correct for hydrolysis for the rest of the amines. $\bar{V}_2^0$'s for all the amines except pyrrolidine and piperidine were hence obtained by smooth extrapolations. The discrepancy in the limiting volume for pyridine obtained by us (77.0 ml mol^{-1}) and that of Conway et al.[7] (77.7 ml mol^{-1}) is believed to arise from extrapolation done from higher concentrations.

Figures 1–3 show the variation of $\bar{V}_2$ with mole percent amine. For pyrrolidine, piperidine, and t-$BuNH_2$ the appropriate function $\phi^*/(1-\alpha)$ has been plotted against $(1-\alpha)c_B^0$ (cf. eq 4 in ref 5) in Figure 4.

The apparent molal compressibility (ϕ_K) were calculated from the expression:

$$\phi_K = \frac{1000(\beta - \beta_0)}{c} + \beta_0\phi_V \qquad (3)$$

where β and β_0 are the adiabatic compressibilities of the solution and pure solvent, respectively, and c is the concentration in molarity. Estimated uncertainties in ϕ_K are about $\pm 1 \times 10^{-10}$ cm^2 dyn^{-1} at the lowest concentration. For t-$BuNH_2$ where the measurements were extended to very low concentrations, these are higher as shown in Figure 5. Figures 5 and 6 show the variations of ϕ_K with mole percent amine for all the compounds handled in this work. The limiting values of ϕ_K^0 have been obtained by smooth extrapolations.

In Table I we have collected values of $\bar{V}_2^0$, $\bar{V}_2^{0E}$, slopes of the $\bar{V}_2(x_2)$ curves ($d\bar{V}_2/dx_2$) (hereafter abbreviated as h'), ϕ_K^0 values as obtained above, and the corresponding slopes ($d\phi_K/dx_2$) (hereafter abbreviated as k'). For the sake of comparison the corresponding parameters for n-$PrNH_2$, n-$BuNH_2$, $EtNH_2$, $(Et)_2NH$, and $Et(NH_2)_2$ reported earlier[1] have also been included in the table. The slope values are taken to indicate trends and no claim is made regarding their absolute values.

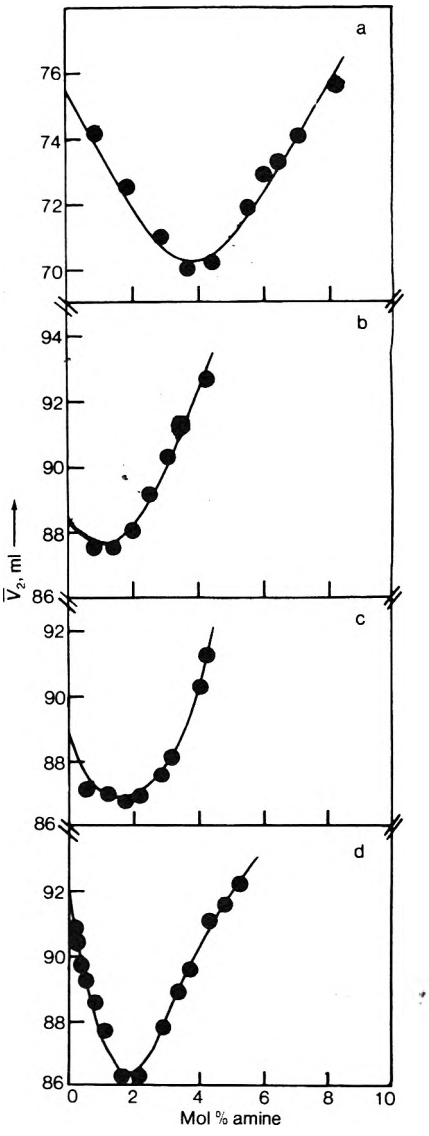

Figure 1. Partial molal volume vs. mole percent amine at 20°C for aqueous solutions of (a) isopropylamine, (b) isobutylamine, (c) *sec*-butylamine, and (d) *tert*-butylamine.

Discussions

The excess partial molal volumes $\bar{V}_2^E$ are all negative and go through a minima with increasing concentration except for pyridine. In an isomeric series the concentration at the minimum in $\bar{V}_2$ is least for the symmetrical isomer. The magnitude of the limiting partial molal excess volume $\bar{V}_2^{0E}$ is least for the straight chain isomer and highest for the highly symmetrical isomer (cf. n-$BuNH_2$ and t-$BuNH_2$). Introduction of an additional amino (or hydroxy) group, i.e., on making the molecule more hydrophilic, brings about a reduction in the magnitude of $\bar{V}_2^{0E}$ (cf. n-$PrNH_2$ and $1,2Pr(NH_2)_2$; $EtNH_2$ and $Et(NH_2)_2$; as also $Et(OH)NH_2$. The ϕ_K^0 values in general are negative and become more negative with increasing chain length and/or hydrophobic character. This is also true for the cyclic amines pyrrolidine and piperidine. It appears that chain branching leads to more negative values for ϕ_K^0 (cf. the isomeric butylamines). However, additional experimental evidence is needed before this statement can be generalized. The case of t-$BuNH_2$ showing a minimum in the $\phi_K(x_2)$ curve and hence yielding a positive ϕ_K^C is unique and deserves special mention (see below).

These and the earlier observations[1] regarding the volumetric behavior of straight chain and branch chain amines are similar to those of the corresponding alcohols.[3] It is thus reasonable to conclude that similar structural promotion for solvent water molecules must be occurring in dilute solutions of amines as well. The negative ϕ_K^0 values corroborate these conclusions in as much as they reflect the loss in the structural compressibility of water on account of the solute induced order in the solvent. Even pyrrolidine and piperidine showing negative ϕ_K^0 and appreciable loss of volume in solution must be looked upon as causing a reinforcement in solvent structure. However, in view of the opposite trends in the entropy and enthalpy of hydration, namely, $T\Delta S_h^\circ \lesssim \Delta H_h^\circ$ for cyclic amines[11] and $T\Delta S_h^\circ > \Delta H_h^\circ$ for straight chain monofunctional solutes, one is forced to conclude that structure promotion in these two classes of compounds must be taking place in different ways. Introduction of a second amino or hydroxy group leads to a simultaneous decrease in both $\bar{V}_2^{0E}$ and ϕ_K^0 indicating loss of the structure-promoting ability (cf. diamines and ethanolamine). These interrelations can possibly be better demonstrated on a plot of $\bar{V}_2^{0E}$ vs. ϕ_K^0 (Figure 7).

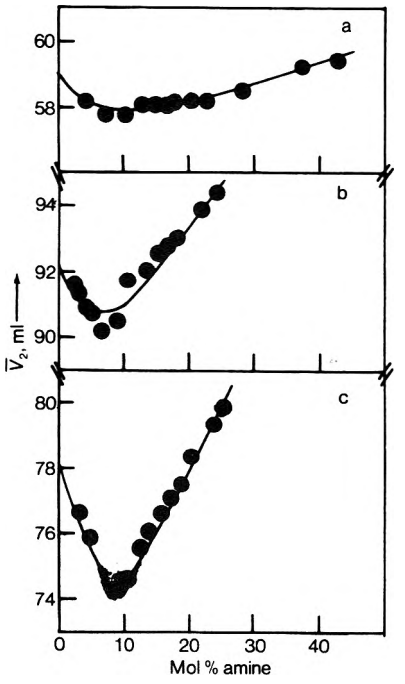

Figure 2. Partial molal volume vs. mole percent of amine at 20°C for aqueous solutions of (a) ethanolamine, (b) 1,2-propanediamine, and (c) 1,4-butanediamine.

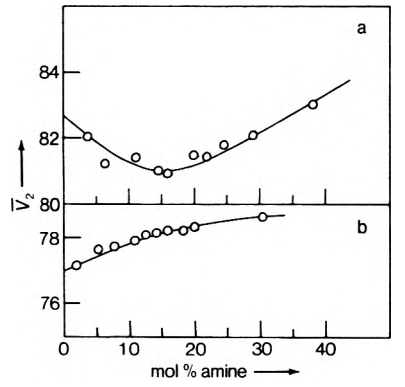

Figure 3. Partial molal volume vs. mole percent for aqueous solutions of (a) morpholine and (b) pyridine at 25°C.

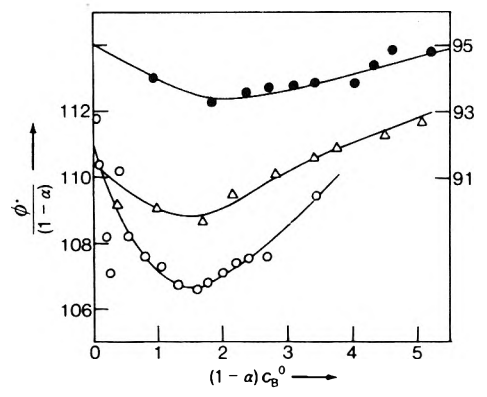

Figure 4. The function $\phi^*/(1-\alpha)$ ml mol^{-1} as a function of $(1-\alpha)c_B^0$ for *tert*-butylamine (O, 20°C), piperidine (Δ, 25°C), and pyrrolidine (●, 25°C) (right-hand scale).

All points seem to group around the straight line drawn. Highly hydrophilic and weak structure forming solutes seem to cluster at the lower end of this line whereas hydrophobic structure forming solutes occupy positions at the upper end. The only exception seems to be t-$BuNH_2$ which falls way below the line, thus stressing its unique character once again (see below).

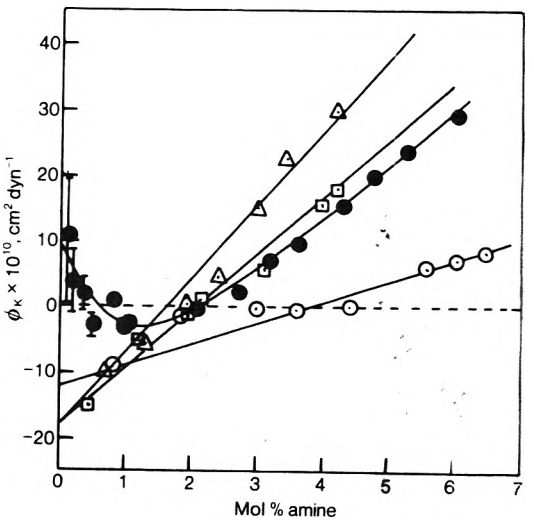

Figure 5. Apparent molal compressibility at 20°C vs. mole percent of amine for the aqueous solutions of isopropylamine (O), isobutylamine (Δ), *sec*-butylamine (□), and *tert*-butylamine (●).

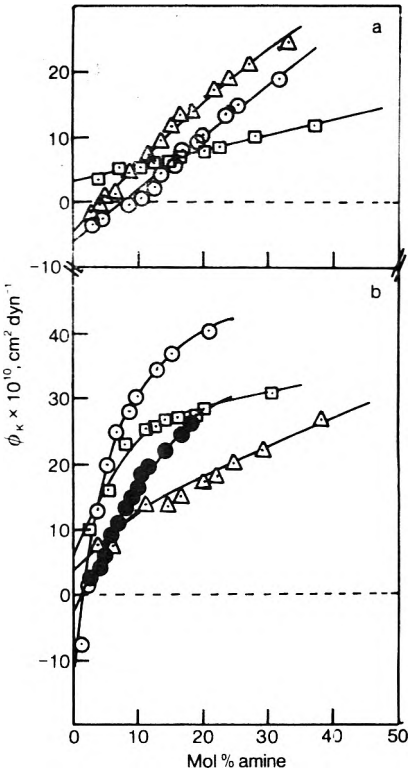

Figure 6. Apparent molal compressibility vs. mole percent amine for the aqueous solutions of (a) 1,2-propanediamine (Δ), 1,4-butanediamine (O), and ethanolamine (□) at 20°C and (b) pyrrolidine (●), piperidine (O), morpholine (Δ), and pyridine (□) at 25°C.

Slopes of the partial volume–concentration plots h' (= $d\bar{V}_2/dx_2$) and the apparent compressibility–concentration plots k' (= $d\phi_K/dx_2$) for all the compounds including earlier results[1] have been plotted in Figure 8 and show some significant trends. Both of these parameters show a monotonous almost linear dependence from $MeNH_2$ to $PrNH_2$.

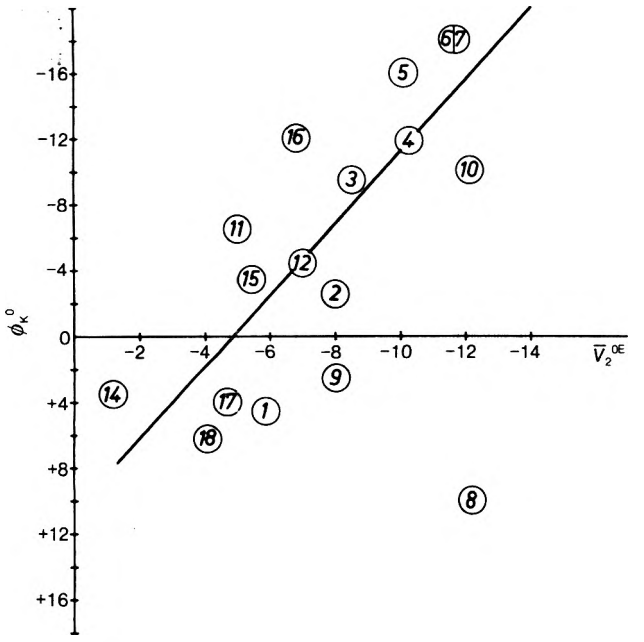

Figure 7. (1) $MeNH_2$, (2) $EtNH_2$, (3) n-$PrNH_2$, (4) i-$PrNH_2$, (5) n-$BuNH_2$, (6) i-$BuNH_2$, (7) sec-$BuNH_2$, (8) t-$BuNH_2$, (9) $(Me)_2NH$, (10) $(Et)_2NH$, (11) $Et(NH_2)_2$, (12) $1,2Pr(NH_2)_2$, (13) $1,4Bu(NH_2)_2$, (14) $Et(OH)NH_2$, (15) pyrrolidine, (16) piperidine, (17) morpholine, (18) pyridine.

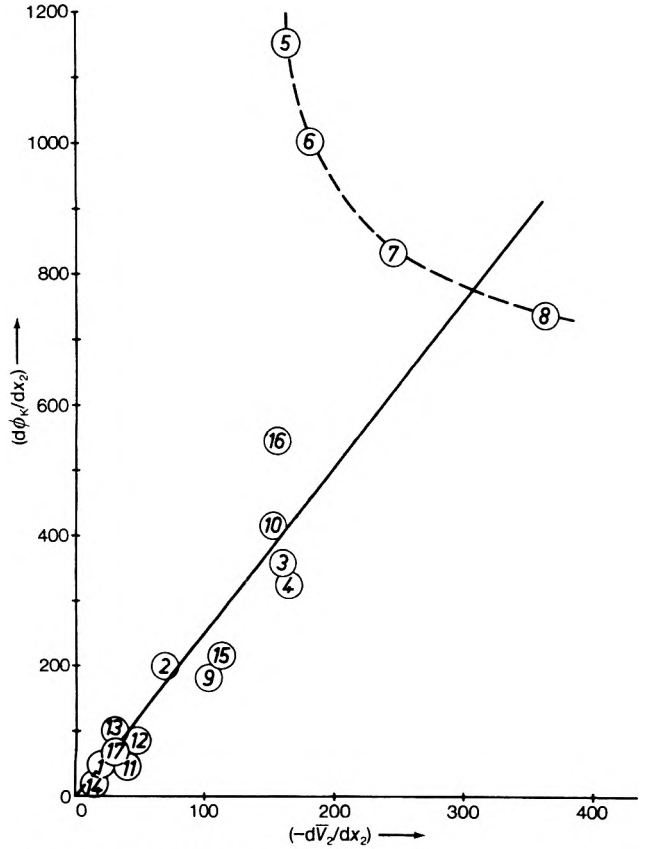

Figure 8. See caption to Figure 7.

Substitution of a second polar group causes a simultaneous decrease in both these parameters (cf. $PrNH_2$ and $1,2Pr(NH_2)_2$; $EtNH_2$ and $Et(NH_2)_2$; $EtNH_2$ and $Et(OH)NH_2$ etc). Even cyclic amines, diamines, and dialkylamines fit into this interrelationship, the points lying near this line. Pyrrolidine and diethylamine lie considerably apart, thus corroborating the earlier statement regarding the stabilizing influence being exerted in a different way. Slopes for piperidine are greater than for pyrrolidine in conformity with the viewpoint that increase in the number of the hydrophobic centers leads to enhanced structural effects. The highly hydrophilic ethanolamine shows very small values for h' and k'. As in Figure 7, one can see here too that weak structure forming solutes occupy positions at the lower left end of the graph, being followed successively by strong structure formers as one proceeds along the *line*. There appears to exist a one to one correspondence between the solute–solute interactions and their effects on the slopes of the partial volume and compressibility.

The isomeric butylamines however seem to behave entirely differently. In the first place the k' values are considerably larger while h' appears to show a normal trend. Secondly, t-$BuNH_2$ surprisingly shows the smallest value for k', though one would have anticipated the highest value in the isomeric series for the following reasons: (a) maximum value for h' suggesting strongest solute–solute interaction[8,9] and hence maximum ordering of the solvent structure; (b) maximum loss in volume on dissolution, indicating least disturbance of the existing order; and finally (c) highest value for the viscosity B coefficient[10] in the isomeric series indicating the extent of tightly bound cosphere water. The observed reversal in the trend of k' as against the expected trend, $n <$ iso $<$ sec $<$ tert, strongly suggests a basic differences in the mode of interaction of the isomeric butylamines with the surrounding water cage structure. As is well known, t-$BuNH_2$ forms a unique clathrate hydrate in which the amine molecule is free to rotate inside the cage whereas normally the polar end of the solute is known to become anchored into the surrounding solvent cage.

Mention must be finally made of one more uniqueness of t-$BuNH_2$ of showing a minimum in the $\phi_K(x_2)$ curve. Just as a minimum in the $\bar{V}_2^E(x_2)$ curves is taken as an indication of different modes of solute–solvent interaction before and after the minimum, similarly a minimum in ϕ_K must also arise out of different modes of dissolution before and after.

A positive value of 10 units of ϕ_K^0 for t-$BuNH_2$ indicates that the introduction of the first molecules in water must be leading to an incipient structural breakdown of water. This might be due to the displacement of the "framework" [2] water molecules into the "interstices" [2] and occupation of the amine molecules at the framework sites. Such a mode of "substitutional" dissolution (as was also proposed for methyl- and dimethylamine[1]) apparently persists upto the minimum in ϕ_K (0.7–1 mol %). The monotonous increase in ϕ_K thereafter resembles the $\phi_K(x_2)$ curves for other amines. The limiting partial molal excess volume $\bar{V}_2^{0E}$, which is negative for all the butylamines, does not however enable such a distinction, because it denotes the net volume loss due to the accommodation of the amine molecules in cavities, whether already present or created by displacement of network water molecules into the interstices.

It can be said in conclusion that whereas the lower members of amines, diamines, dialkylamines, and also cyclic amines seem to fit well into a scheme of interdependence of volumetric and compressibility parameters, the higher members beginning with butylamines show marked departures. Before an exact meaning can be attached to these ob-

servations, more extensive measurements at still lower concentrations are desirable.

Acknowledgments. The authors are thankful to Professor R. H. Sahasrabudhey for his keen interest in this work and are also grateful to the referees for their helpful comments. Financial assistance to one of us (K.J.P.) rendered by the University Grants Commission, India, is also gratefully acknowledged.

References and Notes

(1) M. V. Kaulgud and K. J. Patil, *J. Phys. Chem.*, **78**, 714 (1974).
(2) F. Franks and D. J. G. Ives, *Quart. Rev. Chem. Soc.*, **20**, 1 (1966).
(3) F. Franks, "Water, a Comprehensive Treatise", Vol. 2, Plenum Press, New York, N.Y., 1973, Chapters 1 and 5.
(4) (a) M. V. Kaulgud and K. J. Patil, *Acustica*, **28**, 130 (1973); (b) *Ind. J. Pure Appl. Phys.*, **13**, 322 (1975).
(5) S. Cabani, G. Conti, and L. Lepori, *J. Phys. Chem.*, **76**, 1338 (1972).
(6) For the *tert*-butylamine–water system, the hydrolysis correction was applied at 20°C, through the equation: $\phi^* = \phi_V^{obsd} - \alpha(1.782\sqrt{\alpha c_B^0} + \phi^0_{BH^+OH^-})$. The α values were calculated by taking $pK_a = 10.788$. The term $\phi^0_{BH^+OH^-}$ was calculated by employing the values $\phi^0_{Na^+Cl^-} = 16.10$ ml mol^{-1} and $\phi^0_{Na^+OH^-} = -6.4$ ml mol^{-1} (taken from the compilation made by F. J. Millero in "Structure and Transport Processes in Water and Aqueous Solutions", R. A. Horne, Ed., Wiley-Interscience, New York, N.Y., 1971 Chapter 15). $\phi^0_{BH^+Cl^-}$ was determined experimentally. The hydrochloride of *t*-$BuNH_2$ (99.96% based on chloride estimation) was prepared and the densities measured at 20 ± 0.001°C in the concentration range 0.025–0.2 *M* by means of a 25-ml density bottle. Linear extrapolations to infinite dilution of the ϕ_V values yielded $\phi^0_{V\,BH^+Cl^-} = 103.5 \pm 0.8$ ml mol^{-1}.
(7) B. E. Conway and L. H. Laliberte in "Hydrogen-Bonded Solvent Systems", A. K. Covington and P. Jones, Ed., p 139.
(8) F. Franks, M. A. J. Quickenden, D. S. Reid, and B. Watson, *Trans. Faraday Soc.*, **66**, 583 (1970).
(9) F. Franks and M. A. J. Quickenden, *Chem. Commun.*, 388 (1968).
(10) R. I. Patel, K. J. Patil, and M. V. Kaulgud, *Z. Phys. Chem.*, (*Frankfurt am Main*), **86**, 67 (1973).
(11) S. Cabani, G. Conti, and L. Lepori, *Trans. Faraday Soc.*, **67**, 1943 (1971).

A Classical Test of the Entropy Production Function. Compatibility with Kinetic Laws and Local Equilibrium

J. W. Chasteen[1] and R. H. Spitzer*

School of Materials Engineering, Purdue University, West Lafayette, Indiana 47907 *(Received June 4, 1975)*

Publication costs assisted by the National Science Foundation

An expression for irreversible entropy production is developed for constant volume systems which are capable of heat and mass transfer. The expression is derived in two forms, one of which does not include an assumption of local equilibrium. When accepted mathematical forms of pertinent fluxes are substituted into the expression in either of its forms, the results properly display positive values for non-steady-state systems and correctly reduce to accepted forms for the entropy production at the steady state. The expression is thus in accord with known behavior regardless of whether local equilibrium is an adequate description of real kinetic processes. The entropy production function is shown to be consonant with classical thermodynamics by integrating it in space and time for two systems which are construed to proceed from one well-defined equilibrium state to another. The results of these integrations are identical with changes in entropy as calculated by techniques of classical thermodynamics. In order to perform the integrations, assumptions of not only specific forms for the pertinent fluxes but also of local equilibrium are necessary. Since the integrals yield accurate results even though infinite gradients are sometimes experienced, there are evidently connections between the assumptions of local equilibrium and accepted kinetic laws. This relationship is explored in order to clarify the role played by local equilibrium in irreversible thermodynamics. The time–space integrals of the reduced entropy production expression are shown to be analytically independent of kinetic parameters and a case is made for the instantaneous validity of the entropy production expression.

Several investigators[2-7] have deduced an expression for the local time rate of creation of entropy. In all cases, the authors assume local existence of thermodynamic properties, local conservation of energy, and local conservation of mass. Another feature which is common to all macroscopic theories of irreversible processes is the assumption of equilibrium locally at all points and times in nonequilibrium systems. This last assumption is the one which is most suspect. Its rationalization is discussed at some length by some of the investigators[4-7] who assert that the assumption is best justified by the validity of conclusions drawn from irreversible thermodynamics. The discussions caution that erroneous conclusions ar likely when considering systems that are at some point and time experiencing steep thermodynamic gradients.[6]

In order to clarify the role played by the local equilibrium assumption, in the present work, an entropy production expression is first derived without the imposition of local equilibrium. This expression properly displays positive values for nonequilibrium systems and correctly reduces to the accepted value for steady-state entropy production.

To develop a calculable expression for instantaneous

values of entropy production for nonstationary states, the local equilibrium assumption is hypothesized and the result is tested in a simple, but stringent way, i.e., by integration.

When a well-defined thermodynamic system proceeds between two well-defined equilibrium states, the net entropy change of the universe due to such a process is ascertainable by methods of classical thermodynamics. That change, which is precisely known, should be calculable by integrating the entropy production expression over the volume of the system and over all time.

Such calculations are done for two different transport systems. The results of the calculations demonstrate that, when properly integrated, for simple systems, the entropy production expression is consonant with classical thermodynamics. The calculations furthermore demonstrate that, although real systems may not behave in accord with local equilibrium, such an assumption leads to no erroneous conclusions, even when steep thermodynamic gradients exist at some points along the real path.

1. The Entropy Production Expression

The following development is limited to a constant volume system in which the spontaneous processes are heat and mass transfer. At each point, and at every instant of time within such a system, the laws of conservation of energy and mass may be stated as

$$\partial u/\partial t = -\vec{\nabla} \cdot \vec{J}_E \tag{1.1}$$

$$\partial c_i/\partial t = -\vec{\nabla} \cdot \vec{J}_i \tag{1.2}$$

where u is the time and position dependent energy per unit volume, c_i is the concentration of species i, and $\vec{J}_E$ and $\vec{J}_i$ are local fluxes of energy and mass, respectively.

Entropy is a nonconserved quantity for which a continuity equation may be written

$$\partial s/\partial t = -\vec{\nabla} \cdot \vec{J}_s + \dot{\eta} \tag{1.3}$$

where $\dot{\eta} \geq 0$ is the local entropy production per unit volume, s is the time–position dependent entropy per unit volume, and $\vec{J}_s$ is the local entropy flux which, for a constant volume system, is defined by the relation

$$\vec{J}_s = \frac{\vec{J}_q}{T} = \frac{(\vec{J}_E - \sum \mu_i \vec{J}_i)}{T} \tag{1.4}$$

where μ_i, T, and $\vec{J}_q$ are the local chemical potential, absolute temperature, and flux of heat, respectively.

Substitution of eq 1.4 into 1.3, solution for $\dot{\eta}$, and rearrangement through use of vector identities, results in

$$\dot{\eta} = \vec{J}_E \cdot \vec{\nabla}\left(\frac{1}{T}\right) - (\sum \mu_i \vec{J}_i) \cdot \vec{\nabla}\left(\frac{1}{T}\right) - \frac{1}{T}\sum \vec{J}_i \cdot \vec{\nabla}\mu_i + \frac{\partial s}{\partial T} + \frac{1}{T}\vec{\nabla} \cdot \vec{J}_E - \frac{1}{T}\sum \mu_i \vec{\nabla} \cdot \vec{J}_i \tag{1.5}$$

Substitution of eq 1.1 and 1.2 into the last two terms of (1.5) and reassertion of (1.4) over the first two terms yields

$$\dot{\eta} = \vec{J}_q \cdot \vec{\nabla}\left(\frac{1}{T}\right) - \frac{1}{T}\sum \vec{J}_i \cdot \vec{\nabla}\mu_i + \left(\frac{\partial s}{\partial t} - \frac{1}{T}\frac{\partial u}{\partial t} + \frac{1}{T}\sum \mu_i \frac{\partial c_i}{\partial t}\right) \tag{1.6}$$

The bracketed term is by definition equal to zero for points within systems which have relaxed to a steady-state configuration, but is also hypothesized to be zero for nonsteady-state systems by assuming that the combined statement of the first and second laws for reversible processes at constant volume applies locally to the nonequilibrium system:

$$du = T\,ds + \sum \mu_i\,dc_i \tag{1.7}$$

Incorporation of this assumption into eq 1.6 results in the following expression for the local entropy production

$$\dot{\eta} = -\frac{1}{T^2}\vec{J}_q \cdot \vec{\nabla}T - \frac{1}{T}\sum \vec{J}_i \cdot \vec{\nabla}\mu_i \tag{1.8}$$

2. Case Studies

The following case studies will demonstrate the consistency which exists between classical thermodynamics and the entropy production expression.

The case studies take the following format: first, a system process between two fully defined equilibrium states is defined; second, the net entropy increase in the system and its isolated surroundings is calculated by methods of classical thermodynamics. Next, the entropy production expression is properly integrated in space and time. Finally the net entropy change calculated by the integration is compared with the classical result.

In order to integrate the entropy production expression, it is necessary to assume that the mathematical expressions for the pertinent fluxes are known.

Heat Transfer. The system consists of an infinite flat plate of pure solid and of thickness L. The faces are maintained at constant and equal temperatures, T_2, by contact with isothermal surroundings. The system is initially at a uniform temperature T_1, and spontaneously proceeds to T_2 at constant volume. The combination of the system and its surroundings constitutes an isolated system. The net entropy change due to relaxation between equilibrium states is

$$\Delta S = \Delta S_{sys} + \Delta S_{surr}$$

and is calculated along reversible paths which connect the initial and final equilibrium states of system and surroundings.

$$\Delta S = \int_I^{II} dS_{sys} + \int_I^{II} dS_{surr}$$

The combined statement of the first and second laws for closed systems on reversible paths at constant volume is

$$dE_{sys} = T_{sys}\,dS_{sys} = \rho C_v\,dT_{sys}$$

$$dE_{surr} = T_{surr}\,dS_{surr} = T_2\,dS_{surr} = -dE_{sys}$$

Thus

$$\Delta S = \rho C_v \int_V \int_{T_1}^{T_2} \left(\frac{1}{T} - \frac{1}{T_2}\right) dT\,dV$$

where ρC_v (the constant volume heat capacity per unit volume) is assumed independent of temperature. Therefore

$$\Delta S = \rho A L C_v \left[\ln\left(\frac{T_2}{T_1}\right) - \frac{(T_2 - T_1)}{T_2}\right] \tag{2.1}$$

where A is any chosen area of the infinite flat plate.

Since, $\vec{J}_i = 0$, the entropy production expression (1.8) becomes

$$\dot{\eta} = -\frac{1}{T^2}\vec{J}_q \cdot \vec{\nabla}T \tag{2.2}$$

where T is the local absolute temperature at any time and $\vec{J}_q$ is the local flux of heat. Integration of (2.2) between equilibrium states should yield the classical expression (2.1). Thus

$$\Delta S = -\int_0^\infty \int_V \frac{1}{T^2} \vec{J}_q \cdot \vec{\nabla} T \, dV \, dt \tag{2.3}$$

The volume integral above is over the volume of the system, i.e., the infinite flat plate because, by definition, the temperature gradients in the surroundings are identically zero.

Rearrangement of (2.2) by vector identities results in

$$-\frac{1}{T^2} \vec{J}_q \cdot \vec{\nabla} T = \vec{J}_q \cdot \vec{\nabla} \left(\frac{1}{T}\right) = \vec{\nabla} \cdot \left(\frac{\vec{J}_q}{T}\right) - \frac{1}{T} \vec{\nabla} \cdot \vec{J}_q \tag{2.4}$$

Also, since heat energy is conserved

$$\vec{\nabla} \cdot \vec{J}_q = -\rho C_v \left(\frac{\partial T}{\partial t}\right)_x \tag{2.5}$$

and, by the divergence theorem

$$\int_V \vec{\nabla} \cdot \frac{\vec{J}_q}{T} \, dV = \int_\Gamma \frac{\vec{J}_q}{T} \cdot \hat{n} \, da \tag{2.6}$$

where Γ is the surface bounding the system, $\hat{n}$ is the unit outward normal to that surface, and da is the differential area identified with $\hat{n}$.

When (2.4), (2.5), and (2.6) are incorporated into (2.3), the expression for the change in entropy for an area A of the flat plate becomes

$$\Delta S = A \int_0^\infty \left[\frac{J_q}{T}\bigg|_L - \frac{J_q}{T}\bigg|_0\right] dt + \rho C_v A \int_0^L \int_0^\infty \frac{1}{T} \left(\frac{\partial T}{\partial t}\right)_x dt \, dx \tag{2.7}$$

The second term of ΔS becomes

$$\rho C_v A \int_0^L \int_{T_1}^{T_2} d(\ln T) \, dx = \rho C_v A L \ln \left(\frac{T_2}{T_1}\right) \tag{2.8}$$

In order to evaluate the first term of (2.7), a precise expression for the heat flux must be known. Thus Fourier's law for heat conduction will be considered applicable, i.e.

$$\vec{J}_q = -\kappa \vec{\nabla} T \tag{2.9}$$

where κ is the thermal conductivity and, for simplicity, will be considered independent of temperature. Equations 2.5 and 2.9 along with the boundary conditions for the system define the time-temperature-position path traversed by the system as it proceeds to the final equilibrium state. The temperature is given by[8]

$$T(x,t) = T_2 - 4(T_2 - T_1) \sum_{n=1}^{\infty} \frac{1}{(2n-1)\pi} \times \sin\left[\frac{(2n-1)\pi x}{L}\right] \exp\left[\frac{-\kappa}{\rho C_v}\left[\frac{(2n-1)\pi}{L}\right]^2 t\right] \tag{2.10}$$

and thus, by (2.9), the heat flux is given by

$$J_q = \frac{4\kappa(T_2 - T_1)}{L} \sum_{n=1}^{\infty} \cos\left[\frac{(2n-1)\pi x}{L}\right] \times \exp\left[\frac{-\kappa}{\rho C_v}\left[\frac{(2n-1)\pi}{L}\right]^2 t\right] \tag{2.11}$$

Substitution of (2.11) into the first term of (2.7) with boundary temperatures held constant at T_2 yields

$$A \int_0^\infty \left[\frac{J_q}{T}\bigg|_L - \frac{J_q}{T}\bigg|_0\right] dt = \rho C_v A L \left(\frac{T_2 - T_1}{T_2}\right) \left(\frac{8}{\pi^2}\right) \times \sum_{n=1}^{\infty} \frac{\exp\left[-\frac{\kappa}{\rho C_v}\left(\frac{(2n-1)\pi}{L}\right)^2 t\right]}{(2n-1)^2}\Bigg|_0^\infty \tag{2.12}$$

Since

$$\sum_{n=1}^{\infty} \frac{1}{(2n-1)^2} = \frac{\pi^2}{8}$$

completion of the integration indicated in (2.12) results in the following value for the first term of (2.7):

$$A \int_0^\infty \left[\frac{J_q}{T}\bigg|_L - \frac{J_q}{T}\bigg|_0\right] dt = -\rho C_v A L \left(\frac{T_2 - T_1}{T_2}\right) \tag{2.13}$$

Substitution of (2.8) and (2.13) into (2.7) results in

$$\Delta S = \rho A L C_v \left[\ln\left(\frac{T_2}{T_1}\right) - \frac{(T_2 - T_1)}{T_2}\right] \tag{2.14}$$

which is the same expression as (2.1), the entropy increase as calculated by classical thermodynamics.

Mass Transfer (Diffusion). The system consists of an infinite flat plate of a two-component ideal solid solution. The plate is of thickness L and is constrained at constant temperature, pressure, and molar quantity. The two components are identified as species $i = 1, 2$. The faces are maintained at constant and equal chemical potentials (μ_i^{II}) by contact with reservoirs of constant T, P, and composition. The system is initially at equilibrium at uniform chemical potential μ_i^{I}, specified by T, P, and an initial mole fraction N_i^{I}. It proceeds spontaneously to μ_i^{II} and a corresponding N_i^{II} at constant T and P.

Since the system and its reservoirs constitute an isolated system, the net entropy change due to relaxation between the two equilibrium states is

$$\Delta S = \Delta S_{sys} + \Delta S_{surr}$$

Also, since the change in volume upon mixing an ideal solution from pure components is zero, the process takes place at constant volume.

The combined statement of the first and second laws for open systems at constant volume defines reversible paths for system and surroundings, i.e.,

$$dE^\alpha = T \, dS^\alpha + \sum \mu_i^\alpha \, dn_i^\alpha$$

$$dE^\beta = T \, dS^\beta + \sum \mu_i^\beta \, dn_i^\beta = -dE^\alpha$$

where α and β imply system and surroundings, respectively.

Thus

$$\Delta S = \int_I^{II} dS^\alpha + \int_I^{II} dS^\beta = -\frac{1}{T}\left\{\int_I^{II} \sum \mu_i^\alpha \, dn_i^\alpha + \int_I^{II} \sum \mu_i^\beta \, dn_i^\beta\right| \tag{2.15}$$

It follows from the definition of the system that (a) μ_i^β = constant, (b) n_T^α = total number of moles in the system = constant, (c) $dn_T^\alpha = 0$, and (d) $dn_i^\beta = -dn_i^\alpha = -n_T^\alpha \, dN_i^\alpha$ where N_i^α = the mole fraction of i in α (the system). Also

$$\sum \mu_i^\alpha \, dN_i^\alpha = \sum d(\mu_i^\alpha N_i^\alpha) - \sum N_i^\alpha \, d\mu_i^\alpha$$

where $\sum N_i^\alpha \, d\mu_i^\alpha = 0$ by virtue of the Gibbs–Duhem relation. Therefore

$$\Delta S = \frac{n_T{}^{\alpha}}{T}\left[-\sum \int_{\mathrm{I}}^{\mathrm{I}} \mathrm{d}(\mu_i{}^{\alpha} N_i{}^{\alpha}) + \sum \mu_i{}^{\beta} \int_{\mathrm{I}}^{\mathrm{II}} \mathrm{d}N_i{}^{\alpha}\right] \quad (2.16)$$

Also, by definition, $\mu_i{}^{\beta} = \mu_i{}^{\alpha,\mathrm{II}} = \mu_i{}^{\mathrm{II}}$ = the chemical potential of component i in the system at state II. Therefore

$$\Delta S = \frac{n_T}{T}\left[N_2{}^{\mathrm{I}}(\mu_2{}^{\mathrm{I}} - \mu_2{}^{\mathrm{II}}) + N_1{}^{\mathrm{I}}(\mu_1{}^{\mathrm{I}} - \mu_1{}^{\mathrm{II}})\right] \quad (2.17)$$

All quantities in (2.17) refer to the system where the subscripts index a component and the superscript a thermodynamic state.

The chemical potential of a component in an ideal solution is

$$\mu_i = \mu_i{}^{0} + RT \ln N_i$$

Also $n_T = AL/\upsilon$ where A is some chosen area of the flat plate and υ is the molar volume of the solid solution.

Substitution of the above observations into (2.17) results in

$$\Delta S = \frac{ALR}{\upsilon}\left[N_2{}^{\mathrm{I}} \ln\left(\frac{N_2{}^{\mathrm{I}}}{N_2{}^{\mathrm{II}}}\right) + N_1{}^{\mathrm{I}} \ln\left(\frac{N_1{}^{\mathrm{I}}}{N_1{}^{\mathrm{II}}}\right)\right] \quad (2.18)$$

or, when expressed in terms of a single component

$$\Delta S = \frac{ALR}{\upsilon}\left|N_1{}^{\mathrm{I}} \ln\left[\frac{N_1{}^{\mathrm{I}}(1 - N_1{}^{\mathrm{II}})}{N_1{}^{\mathrm{II}}(1 - N_1{}^{\mathrm{I}})}\right] + \ln\left(\frac{1 - N_1{}^{\mathrm{I}}}{1 - N_1{}^{\mathrm{II}}}\right)\right| \quad (2.19)$$

When the change in states of the system takes place by isothermal mass diffusion, $\vec{\nabla}T = 0$, and the entropy production expression (1.8) becomes

$$\dot{\eta} = -\frac{1}{T}\sum_1^2 \vec{J}_i \cdot \vec{\nabla}\mu_i \quad (2.20)$$

where μ_i is the local chemical potential of species i and $\vec{J}_i$ is its local flux. If (2.20) is a valid expression, then integration between equilibrium states should yield the classical result (2.19). Thus

$$\Delta S = -\int_0^{\infty}\int_V \frac{1}{T}\sum_1^2 \vec{J}_i \cdot \vec{\nabla}\mu_i \, \mathrm{d}V \, \mathrm{d}t \quad (2.21)$$

but, since T is constant

$$\frac{\vec{J}_i}{T} \cdot \vec{\nabla}\mu_i = \frac{1}{T}\vec{\nabla} \cdot (\mu_i \vec{J}_i) - \frac{\mu_i}{T}\vec{\nabla} \cdot \vec{J}_i$$

therefore

$$\frac{1}{T}\sum_1^2 \vec{J}_i \cdot \vec{\nabla}\mu_i = \frac{1}{T}\vec{\nabla} \cdot (\mu_1 \vec{J}_1 + \mu_2 \vec{J}_2) - \frac{\mu_1}{T}\vec{\nabla} \cdot \vec{J}_1 - \frac{\mu_2}{T}\vec{\nabla} \cdot \vec{J}_2$$

Also, since the molar volume is constant, when the dimensions of J are taken to be moles/unit area/unit time

$$\vec{J}_2 = -\vec{J}_1$$

and

$$\frac{1}{T}\sum_1^2 \vec{J}_i \cdot \vec{\nabla}\mu_i = \frac{1}{T}\vec{\nabla} \cdot (\mu_1 - \mu_2)\vec{J}_1 - \frac{1}{T}(\mu_1 - \mu_2)\vec{\nabla} \cdot \vec{J}_1 \quad (2.22)$$

(2.22) causes (2.21) to become

$$\Delta S = -\int_0^{\infty}\int_V \frac{1}{T}\vec{\nabla} \cdot (\mu_1 - \mu_2)\vec{J}_1 \, \mathrm{d}V \, \mathrm{d}t + \int_0^{\infty}\int_V \frac{1}{T}(\mu_1 - \mu_2)\vec{\nabla} \cdot \vec{J}_1 \, \mathrm{d}V \, \mathrm{d}t \quad (2.23)$$

The divergence expression in the integrand of the second term for a constant molar volume system is

$$\vec{\nabla} \cdot \vec{J}_1 = -\frac{1}{\upsilon}\left(\frac{\partial N_1}{\partial t}\right)_x \quad (2.24)$$

and, for ideal binary solutions

$$\frac{(\mu_1 - \mu_2)}{T} = \frac{(\mu_1{}^{0} - \mu_2{}^{0})}{T} + R \ln\left(\frac{N_1}{1 - N_1}\right) \quad (2.25)$$

Upon substitution of (2.24) and (2.25) into (2.23) and inversion of the order of integration, the second term becomes

$$\int_0^{\infty}\int_V \frac{\mu_1 - \mu_2}{T}\vec{\nabla} \cdot \vec{J}_1 \, \mathrm{d}V \, \mathrm{d}t =$$

$$-\frac{1}{\upsilon}\int_V\int_0^{\infty}\left[\frac{\mu_1{}^{0} - \mu_2{}^{0}}{T} + R \ln\left(\frac{N_1}{1 - N_1}\right)\right]\left(\frac{\partial N_1}{\partial t}\right)_x \mathrm{d}t \, \mathrm{d}V =$$

$$-\frac{A}{\upsilon}\int_0^{L}\int_{N_1{}^{\mathrm{I}}}^{N_1{}^{\mathrm{II}}}\left[\frac{\mu_1{}^{0} - \mu_2{}^{0}}{T} + R \ln\left(\frac{N_1}{1 - N_1}\right)\right]\mathrm{d}N_1 \, \mathrm{d}x$$

Completion of the integration reduces this term to

$$-\frac{AL}{\upsilon}\left(\frac{\mu_1{}^{0} - \mu_2{}^{0}}{T}\right)(N_1{}^{\mathrm{II}} - N_1{}^{\mathrm{I}}) - \frac{AL}{\upsilon}R\left[N_1{}^{\mathrm{II}} \ln\left(\frac{N_1{}^{\mathrm{II}}}{1 - N_1{}^{\mathrm{II}}}\right) - N_1{}^{\mathrm{I}} \ln\left(\frac{N_1{}^{\mathrm{I}}}{1 - N_1{}^{\mathrm{I}}}\right) - \ln\left(\frac{1 - N_1{}^{\mathrm{I}}}{1 - N_1{}^{\mathrm{II}}}\right)\right] \quad (2.26)$$

Consider now the first term of (2.23). By application of the divergence theorem and recognition that the system is a flat plate undergoing unidirectional diffusion, the first term becomes

$$-\int_0^{\infty}\int_{\Gamma}\frac{(\mu_1 - \mu_2)}{T}\vec{J}_1 \cdot \hat{n} \, \mathrm{d}a \, \mathrm{d}t =$$

$$-A\int_0^{\infty}\left\{\left(\frac{(\mu_1 - \mu_2)}{T}J_1\right|_L - \left(\frac{(\mu_1 - \mu_2)}{T}J_1\right|_0\right\}\mathrm{d}t \quad (2.27)$$

but $(\mu_1 - \mu_2)/T$ is the same at both boundaries and is given by

$$\left.\frac{\mu_1 - \mu_2}{T}\right|_{0,L} = \frac{\mu_1{}^{0} - \mu_2{}^{0}}{T} + R \ln\left(\frac{N_1{}^{\mathrm{II}}}{1 - N_1{}^{\mathrm{II}}}\right) \quad (2.28)$$

Combination of (2.28) and (2.27) reduces the first term of (2.23) to

$$-A\left[\frac{\mu_1{}^{0} - \mu_2{}^{0}}{T} + R \ln\left(\frac{N_1{}^{\mathrm{II}}}{1 - N_1{}^{\mathrm{II}}}\right)\right] \times \int_0^{\infty}(J_1|_L - J_1|_0)\,\mathrm{d}t \quad (2.29)$$

Completion of the analysis of (2.29) requires a precise knowledge of the mass flux. Thus Fick's law for mass diffusion will be considered applicable i.e.

$$\vec{J}_1 = -D_1\vec{\nabla}c_1 \quad (2.30)$$

where D_1 is the concentration independent mass diffusivity of species 1.

Equations 2.30, 1.2, and the boundary conditions for the system define the time–concentration–position path traversed by the system during its procession between equilibrium states I and II. The concentration is given by[8]

$$c_1(x,t) = c_1^{II} - 4(c_1^{II} - c_1^{I}) \sum_{n=1}^{\infty} \frac{1}{(2n-1)\pi} \times \sin\left[\frac{(2n-1)\pi x}{L}\right] \exp\left\{-D_1\left[\frac{(2n-1)\pi}{L}\right]^2 t\right\} \quad (2.31)$$

By virtue of (2.30), J_1 is given by

$$J_1 = \frac{4D_1(c_1^{II} - c_1^{I})}{L} \sum_{n=1}^{\infty} \cos\left[\frac{(2n-1)\pi x}{L}\right] \times \exp\left\{-D_1\left[\frac{(2n-1)\pi}{L}\right]^2 t\right\} \quad (2.32)$$

Use of the above to define the integrand of (2.29) causes (2.29) to become

$$-AL(c_1^{II} - c_1^{I})\left[\frac{(\mu_1^0 - \mu_2^0)}{T} + R\ln\left(\frac{N_1^{II}}{1-N_1^{II}}\right)\right]\left(\frac{8}{\pi^2}\right) \times \sum_{n=1}^{\infty} \frac{\exp\left\{-D_1\left[\frac{(2n-1)\pi}{L}\right]^2 t\right\}}{(2n-1)^2}\Bigg|_0^{\infty}$$

Since

$$c_1^{II} - c_1^{I} = \frac{1}{v}(N_1^{II} - N_1^{I}) \quad \text{and} \quad \sum_{1}^{\infty} \frac{1}{(2n-1)^2} = \frac{\pi^2}{8}$$

(2.29), the first term of (2.23), becomes

$$\frac{AL}{v}\left[\frac{(\mu_1^0 - \mu_2^0)}{T}(N_1^{II} - N_1^{I})\right] + \frac{AL}{v}R\left[N_1^{II}\ln\left(\frac{N_1^{II}}{1-N_1^{II}}\right) - N_1^{I}\ln\left(\frac{N_1^{II}}{1-N_1^{II}}\right)\right] \quad (2.33)$$

Finally, ΔS as defined by the entropy production expression, is just the sum of (2.26) and (2.33) and

$$\Delta S = \frac{AL}{v}R\left|N_1^{I}\ln\left[\frac{N_1^{I}(1-N_1^{II})}{N_1^{II}(1-N_1^{I})}\right] + \ln\left(\frac{1-N_1^{I}}{1-N_1^{II}}\right)\right| \quad (2.34)$$

which, by comparison with (2.19), is again seen to be the same as the entropy change calculated by methods of classical thermodynamics.

3. Dependence of Entropy Production on Kinetic Parameters

The foregoing case studies have resulted in calculations of net entropy changes between equilibrium states by integration of the entropy production expression. The final expressions were independent of any assumed kinetic parameters as, of course, they must be for consistency with classical thermodynamics. Thus the entropy production expression has been shown to be an effective tool for calculating changes in entropy between equilibrium states. If an entropy state can be unambiguously assigned to all points at all times then its time rate of change may also be assigned and the summation property of entropy makes it possible to calculate changes between any two arbitrary times. In order to calculate such changes, it is necessary only to accept that, since the entropy production expression is valid over all time, it is equally valid between any two arbitrary times. This hypothesis is considered in the Discussion.

The following discussion will show that the total entropy change between equivalent dimensionless, but arbitrary, times is independent of kinetic parameters.

Heat Transfer (Thermal Conductivity). Equations 2.3 and 2.9 give the increase in entropy between any two arbitrary times t_1 and t_2

$$\Delta S(t_1,t_2) = \kappa \int_{t_1}^{t_2}\int_V \frac{1}{T^2}|\vec{\nabla}T|^2\,dV\,dt \quad (3.1)$$

which, for the system under consideration

$$\Delta S(t_1,t_2) = A\kappa \int_{t_1}^{t_2}\int_0^L \frac{1}{T^2}\left(\frac{\partial T}{\partial x}\right)_t^2 dx\,dt \quad (3.2)$$

where T is given by (2.10) and $(\partial T/\partial x)_t$ is readily deduced from (2.11).

Upon introduction of the dimensionless variables

$$\theta = \kappa t/\rho C_v L^2 \qquad \chi = x/L \quad (3.3)$$

into (3.2), the entropy change becomes

$$\Delta S(t_1,t_2) = \Delta S(\theta_1,\theta_2) = \rho C_v AL \int_{\theta_1}^{\theta_2}\int_0^1 \frac{1}{T^2}\left(\frac{\partial T}{\partial \chi}\right)_\theta^2 d\chi\,d\theta \quad (3.4)$$

The above expression is independent of the thermal conductivity except that it is contained in the θ limits.

Two observations are now possible: (1) if $t_1 = 0$ and $t_2 = \infty$ then, regardless of the thermal conductivity, $\theta_1 = 0$ and $\theta_2 = \infty$. Therefore the total entropy produced during relaxation between two equilibrium states is analytically independent of the thermal conductivity and dependent only on the thermodynamic parameters, as it should be. (2) The change in entropy between any two dimensionless times is a function only of thermodynamic variables.

Mass Diffusion. Upon reference to (2.20) and (2.30), the increase in entropy between any two arbitrary times, t_1 and t_2, due to mass diffusion of the type defined in the previous section, is given by

$$\Delta S(t_1,t_2) = \int_{t_1}^{t_2}\int_V \left(\sum_1^2 D_i\vec{\nabla}c_i \cdot \frac{\vec{\nabla}_{Ti}}{T}\right) dV\,dt \quad (3.5)$$

The assumptions of ideality and constant molar volume lead to

$$\frac{\vec{\nabla}\mu_i}{T} = \frac{R}{N_i}\vec{\nabla}N_i = \frac{R}{c_i}\vec{\nabla}c_i$$

and, since $\vec{J}_1 = -\vec{J}_2$, $D_1\vec{\nabla}c_1 = -D_2\vec{\nabla}c_2$, and $c_2 = \rho - c_1$, $\vec{\nabla}c_2 = -\vec{\nabla}c_1$ and thus $D_1 = D_2$.

Incorporation of the above observations into (3.5) and assertion of unidirectional diffusion as the mode of transport causes the entropy change to become

$$\Delta S(t_1,t_2) = \rho RDA \int_{t_1}^{t_2}\int_0^L \frac{1}{c_1(\rho - c_1)}\left(\frac{\partial c_1}{\partial x}\right)_t^2 dx\,dt \quad (3.6)$$

where c_1 is given by (2.31) and $D(\partial c/\partial x)$ is given by (2.32).

It is possible to convert the integrand of (3.6) to dimensionless form by defining

$$\phi = Dt/L^2 \qquad \chi = x/L \quad (3.7)$$

When (3.7) are incorporated into (3.6) the entropy change becomes

$$\Delta S(t_1, t_2) = \Delta S(\phi_1, \phi_2) =$$

$$\rho ALR \int_{\phi_1}^{\phi_2} \int_0^1 \frac{1}{[c(\rho - c)]} \left(\frac{\partial c}{\partial \chi}\right)_\phi^2 d\chi \, d\phi \quad (3.8)$$

The above expression is seen to be independent of the mass diffusivity except that it is contained in the ϕ limits.

Two observations similar to those for heat transfer may now be made. (1) If $t_1 = 0$ and $t_2 = \infty$, then $\phi_1 = 0$ and $\phi_2 = \infty$. Therefore the total entropy produced by relaxation between two equilibrium states by mass diffusion is analytically independent of the mass diffusivity and dependent only on thermodynamic parameters. (2) The change in entropy between any two dimensionless times (ϕ) is dependent only on thermodynamic parameters.

4. Discussion

The entropy production expression (1.6) which resulted from the assumptions and attitudes as outlined in the introductory sections is, for clarity, reproduced here:

$$\dot{\eta} = \vec{J}_q \cdot \vec{\nabla}\left(\frac{1}{T}\right) - \frac{1}{T}\sum \vec{J}_i \cdot \vec{\nabla}\mu_i + \left(\frac{\partial s}{\partial t} - \frac{1}{T}\frac{\partial u}{\partial t} + \frac{1}{T}\sum \mu_i \frac{\partial c_i}{\partial t}\right) \quad (4.1)$$

The development of this expression was based upon two assumptions of conservation, a mathematical statement of continuity, and a definition. The two assumptions of conservation were that energy and mass are at all times locally conserved (1.1 and 1.2). Since the second law states that entropy is not conserved, it was only possible to construct a continuity expression (1.3) involving its local time derivative and its flux. The $\dot{\eta}$ term of the continuity expression is taken to be the local entropy production. In order to deduce a testable expression for $\dot{\eta}$, the entropy flux $\vec{J}_s$ was then defined in terms of other, less ambiguous, fluxes (1.4).

Since experience dictates that assumptions of conservation of energy and mass are highly plausible and one can certainly write a continuity equation for any defined parameter, the only cogent question involves whether the $\dot{\eta}$ which balances the continuity equation is actually the local rate of creation of entropy. Since entropy and its time derivative exist, whether $\dot{\eta}$ is entropy production rests entirely upon whether the entropy flux is properly defined. But such a definition cannot be directly tested.

The investigation then most fruitfully turns to the question of whether the entropy production expression ($\dot{\eta}$ of 4.1) is in mathematical accord with known behavior. Such investigation begins by assuming that, since Fourier's law of heat conduction (2.9) and Fick's law of mass diffusion (2.30) are experimentally verifiable, these laws are applicable to entropy production. Incorporation of these laws and the definition of chemical potential into (4.1) yields

$$\dot{\eta} = \frac{\kappa}{T^2}|\vec{\nabla}T|^2 + R\sum \frac{D_i}{c_i}|\vec{\nabla}c_i|^2 + \left(\frac{\partial s}{\partial t} - \frac{1}{T}\frac{\partial u}{\partial t} + \frac{1}{T}\sum \mu_i \frac{\partial c_i}{\partial t}\right) \quad (4.2)$$

Now the second law states that

$$dS \geq \delta q/T$$

Thus the combined statement of the first and second laws for a constant volume element is, in general

$$du \leq T\,ds + \sum \mu_i\, dc_i$$

It is then possible to state that, in general

$$\frac{\partial s}{\partial t} - \frac{1}{T}\frac{\partial u}{\partial t} + \frac{1}{T}\sum \mu_i \frac{\partial c_i}{\partial t} \geq 0 \quad (4.3)$$

The first two terms of (4.2) are positive or zero and the bracketed term, which is identical with (4.3), is positive or zero, and, therefore

$$\dot{\eta} \geq 0$$

which, of course, it must be. It is of interest to note that this necessity is met by only assuming the validity of testable kinetic laws. No assertion of local equilibrium has been necessary.

As a second query, if $\dot{\eta}$ of (4.1) is to be entropy production, it must also be consonant with accepted expressions for that quantity when a system is in a stationary thermodynamic state. Since "stationary state" is defined to be that state wherein the time derivatives of all thermodynamic state variables vanish, for such a state, the bracketed term in the entropy production expression vanishes. Thus, for simple heat conduction, the entropy production expression reduces to

$$\dot{\eta} = \vec{J}_q \cdot \vec{\nabla}\left(\frac{1}{T}\right) = \vec{\nabla} \cdot \left(\frac{\vec{J}_q}{T}\right) - \frac{1}{T}\vec{\nabla} \cdot \vec{J}_q$$

At stationary state, the divergence of the heat flux is identically zero. Consider now an infinite flat plate of thickness L the faces of which are maintained at temperatures T_1 and T_2, assume Fourier's law to be applicable, and note that the overall entropy production, $\dot{S}_{irr}$, is the volume integral of $\dot{\eta}$. Thus the steady state entropy production is

$$\dot{S}_{irr} = A \int_0^L \dot{\eta}\, dx = \frac{A\kappa}{L}\frac{(T_2 - T_1)^2}{T_1 T_2}$$

The above expression is a plausible result[2] and an accepted expression for the steady-state entropy production of such a system.[9] It is here again noteworthy that the above result was achieved only by assuming the validity of a testable kinetic law and that, once again, no assertion of local equilibrium has been necessary.

A similar result is deducible for simple mass diffusion but such a development yields no new information.

In this report, a new and more stringent test of the entropy production expression has been conducted through the following reasoning. If $\dot{\eta}$ of (4.1) is the local rate of creation of entropy, not only must it always be positive and reduce to the proper steady-state expression for that quantity but it must also reflect the change in entropy of an isolated system by virtue of its integral in time, *i.e.*, between equilibrium states. Since such an entropy change is readily and separately calculable by techniques of classical thermodynamics, it was possible to test this property of the entropy production expression. Such tests were conducted, with positive results, in the text of this report.

The applicability of testable kinetic laws was assumed and, also, it was finally necessary to assume local equilibrium, i.e., that the bracketed term of (4.1) vanishes for all times and at all positions. It was strictly only necessary to assume that the integral of the bracketed term of (4.1) between equilibrium states vanishes but, by virtue of (4.3), such can be the case only if the term vanishes identically. The entropy production expression which was actually tested by integration between equilibrium states was that of (1.8) which, for clarity, is reproduced here:

$$\dot{\eta} = -\frac{1}{T^2}\vec{J}_q \cdot \vec{\nabla}T - \frac{1}{T}\sum \vec{J}_i \cdot \vec{\nabla}\mu_i \qquad (4.4)$$

Thus, because of the positive results of the integral tests, one of only two possibilities must prevail; namely, either (1) local equilibrium and accepted linear kinetic laws accurately describe such nonequilibrium systems at all positions and times or (2) at some positions and/or some times both fail. The failure of one at any point and time demands a failure of the other at some point and time because the integrals of the bracketed term of (4.1) and the terms involving fluxes must be precisely compensatory. Although simultaneous failure seems probable, the integral tests cannot establish the time or locations of the compensatory failures. Whatever be the case, however, adoption of the combined assumption of local equilibrium and linear kinetic laws led to the proper change in the entropy of systems between equilibrium states.

Several investigators[4,6,7] have expressed doubt concerning the accuracy of the assumption of local equilibrium in systems which are widely displaced from equilibrium and thus forced to sustain large thermodynamic gradients. The systems investigated here experienced infinite gradients at their surfaces for times approaching zero (see 2.10 and 2.31) and yet the combined assumptions of local equilibrium and linear kinetic laws at these times and positions led to precisely accurate results. Thus the combined assumptions of local equilibrium and linear kinetic laws have considerable utility even when applied to highly nonequilibrium systems in which their individual applicability might be questionable.

It thus seems probable that local equilibrium accurately describes all points at all times whereat the linear kinetic laws are accurate and experimentally verifiable. Furthermore, when and if one assumption fails, the other fails simultaneously in an entirely compensatory manner. This assertion of simultaneous and compensatory failure then implies that $\dot{\eta}$ of (4.1) is pointwise and timewise the rate of creation of entropy and that it may be properly calculated by applying the assumption of local equilibrium and known laws of kinetics. There is thus merit in an investigation of the volume integral of the reduced form of $\dot{\eta}$ (4.4) which incorporates the assumption of local equilibrium and the applicability of accepted laws of kinetics. Such an investigation will be the subject of a later report.

Acknowledgment. This work was supported, in part, by the Purdue University School of Materials Engineering and, in part, by the Advanced Research Projects Agency (IDL Program DAHC-0213) and the National Science Foundation (MRL Program DMR 72-03018).

References and Notes

(1) This work taken in part from the thesis of J. W. Chasteen to be submitted to Purdue University in partial fulfillment of the requirements for the degree of Doctor of Philosophy.
(2) G. N. Lewis and M. Randall, "Thermodynamics", 2nd ed, revised, K. S. Pitzer and L. Brewer, Ed., McGraw-Hill, New York, N.Y., 1961, pp 453–454.
(3) A. Sommerfeld, "Thermodynamics and Statistical Mechanics", Academic Press, New York, N.Y., 1956, p 154.
(4) D. D. Fitts, "Nonequilibrium Thermodynamics", McGraw-Hill, New York, N.Y., 1962, p 23.
(5) S. R. deGroot and P. Mazur, "Non-Equilibrium Thermodynamics", Interscience, New York, N.Y., 1962, p 23.
(6) I. Gyarmati, "Non-Equilibrium Thermodynamics", Springer-Verlag, New York, N.Y., 1970, pp 66–74.
(7) K. G. Denbigh, "The Thermodynamics of the Steady State", Methuen, London, 1951, p 58.
(8) H. S. Carslaw and J. C. Jaeger, "Conduction of Heat in Solids", 2nd ed, Clarendon Press, Oxford, 1959, Chapter III.
(9) J. W. Cahn and W. W. Mullins in "Decomposition of Austenite by Diffusional Processes", V. F. Zackay and H. I. Aaronson, Ed., Interscience, New York, N.Y., 1962, p 123.

Desorption of Oxygen from the Silver (110) Surface[1]

G. Rovida

Istituto di Chimica Fisica, Università di Firenze, Italy *(Received July 21, 1975)*

Publication costs assisted by Snamprogetti

The kinetics of oxygen desorption, from a silver single crystal with the main faces parallel to the (110) plane, was studied in a LEED–Auger apparatus. On the basis of the thermal desorption spectrum, obtained at maximum oxygen coverage, the process appears to be second order, with an activation energy of about 40 kcal/mol. The same activation energy was derived from the rate of decomposition of the (2 × 1) superstructure which is observed with LEED on the (110) face at maximum coverage. The results indicate that at high coverages oxygen desorbs directly from an immobile layer, so that the desorption process can be considered as the decomposition of a two-dimensional oxide. At lower oxygen coverages, at which other ordered two-dimensional phases are observed with the LEED, oxygen becomes mobile above 150°C and desorbs at temperatures slightly lower than those observed for high coverages.

1. Introduction

The kinetics of oxygen desorption from silver polycrystalline samples has recently been studied by Kollen and Czanderna[2a] and Czanderna, Chen, and Biegen.[2b] These authors found two types of desorption: one occurring below 100°C and attributed to a molecular adsorbed species; the other observed above 180°C and attributed to dissociatively adsorbed oxygen. The latter form was considered to be mobile at the temperature of desorption.

Previous work conducted in this laboratory with low-energy electron diffraction (LEED)–Auger techniques and thermal desorption on the chemisorption of oxygen on the low index faces of silver[4,5] showed that, under the experimental conditions employed, only the second type of oxygen adsorption is observed, which has been considered to be the dissociated form. This oxygen, at least on the (111) and (110) faces, forms ordered surface phases at maximum coverage (reached at pressures higher than 10^{-3} Torr), which are stable up to the temperatures of rapid oxygen desorption. The desorption spectra showed a peak with maximum at about 280°C. This temperature is higher than that reported for maximum desorption rate by Kollen and Czanderna[2a] (230–250°C, depending on the initial coverage). It must, however, be considered that a much lower heating rate was used by these authors. Taking this into account, the desorption process was considered to be essentially the same.

Since it is difficult to use samples bounded by only one crystal face, the desorption spectra obtained from single crystals cannot be interpreted on the basis of a unique geometry. If, however, the oriented face of the sample is a large fraction of the geometrical area, the desorption process on this face might dominate the observed kinetics.

The data obtained from the LEED diagram, on the other hand, concern only the crystal plane corresponding to the oriented face of the single crystal observed, so that this technique is highly specific for studying adsorption or desorption phenomena occurring on sites of uniform and well-known geometry.

As mentioned above, previous LEED studies showed that, on the (110)[5] as well as on the (111) silver surface,[4] the ordered layer formed by oxygen chemisorption at maximum coverage disappears at the same temperatures at which rapid desorption is observed. This can be interpreted by two mechanisms. The first is that the ordered surface phase (which can be considered as a two-dimensional oxide) collapses at temperatures very near to that of desorption giving a mobile layer from which the recombination of atoms and the desorption occur. The second is that the ordered phase remains stable and that oxygen desorbs directly from the immobile layer.

The aim of the present work was to give more specific support for the interpretation of the mechanism of oxygen desorption from the silver surface by comparing thermal desorption results with more specific data obtained with LEED on a single crystal face. The (110) face was preferred because a well-ordered (2 × 1) superstructure is formed at full coverage upon oxygen chemisorption.[5] This surface phase gives very strong extra beams, whose intensities are easier to measure in comparison with the (4 × 4) superstructure found on the (111) face. Moreover, other (n × 1) structures were observed on the (110) face at lower coverages with a different thermal stability. On the (100) face, strong faceting was found upon oxygen adsorption on some samples,[3] while on others, with a better prepared surface, the faceting was much less important; no strong chemisorption was observed on the (100) domains, giving ordered surface phases.[6]

2. Experimental Section

The experimental conditions were described and discussed elsewhere,[4,5] so that they will be only briefly reviewed here.

A standard three-grid LEED system was employed, in which the residual pressure was usually of the order of 10^{-9} Torr or less. Auger spectra were obtained using the LEED grids as an analyzer, and an auxiliary electron gun at glancing incidence. A quadrupole mass spectrometer was used to analyze the gas composition.

The sample was a silver single crystal disk (6 N purity) about 2 mm thick, with the two faces of about 8 mm diameter, cut parallel to the (110) plane within 1°. After the final chemical treatment, the sample surface was cleaned in the LEED system either by ion bombardment or by heating in oxygen, both treatments being followed by heating in the

ultrahigh vacuum. No significant difference in the surface properties was observed after the two treatments.

The exposures to oxygen (pressures higher than 10^{-3} Torr were found to be necessary to saturate completely the silver surface in a few minutes) were performed by enclosing the sample in a special isolation valve, in which oxygen could be introduced at the desired pressure and pumped off by an auxiliary gas manifold. In the manifold, a residual pressure of 10^{-8} Torr could be maintained under pumping. Without pumping, the residual pressure could rise up to the 10^{-5} range, and experimental evidence showed that the residual gas pressure did not rise significantly during admission of oxygen.

The desorption spectra were obtained in the LEED chamber by rapidly raising the temperature of the sample in the ultrahigh vacuum and following the oxygen pressure with the mass spectrometer. The sample temperature was measured by a Pt—Pt–Rh thermocouple welded to the clamping support very near to the sample. The temperature reading was usually accurate to within ±2°C: this was the interval of the automatic regulation during heating at constant temperature. During rapidly increasing temperatures, a nearly constant difference between the sample temperature and that measured by the thermocouple could arise, but a rough estimation showed that the difference should not have exceeded 20°C at the highest heating rates employed. Significant differences in the temperature of different parts in the sample were not expected because of the high thermal conductivity of silver.

3. Results and Discussion

The starting condition of the sample surface for studying the desorption was usually obtained by exposing the sample to 10^{-1} Torr of oxygen at 150°C for 5 min in the isolation valve. After pumping the oxygen while cooling the sample and reexposing the latter again to the ultrahigh vacuum, the LEED diagram indicates the formation of the well-ordered (2 × 1) superstructure, whose structure and stability were studied in a previous work.[5] This two-dimensional phase seems to correspond to the maximum oxygen coverage on the (110) silver surface. When the sample covered by this superstructure is heated, the mass spectrometer indicates only one desorption peak, with a maximum at about 280°C, like that reported in Figure 1. No significant desorption of oxygen below 100°C was observed, even if the sample was allowed to cool to room temperature in an oxygen atmosphere.

Taking into account the higher heating rate, the observed desorption temperature is in agreement with that attributed by Kollen and Czanderna[2a] to the oxygen which is adsorbed on the silver surface in the dissociated form. In order to show that the same desorption process is occurring, an analysis of the desorption kinetics has been made on the basis of the peak profile.

In the apparatus used, experiments were conducted in order to ascertain that the pumping speed for oxygen was constant in the pressure range observed during the desorption. The results showed that, although the pumping speed is not very reproducible after long periods, it is sufficiently independent of the pressure and constant for a series of experiments conducted for short time intervals. Thus, it can be assumed that during the desorption the oxygen pressure variation is related to the desorption rate, $-dN/dt$, by the equation:

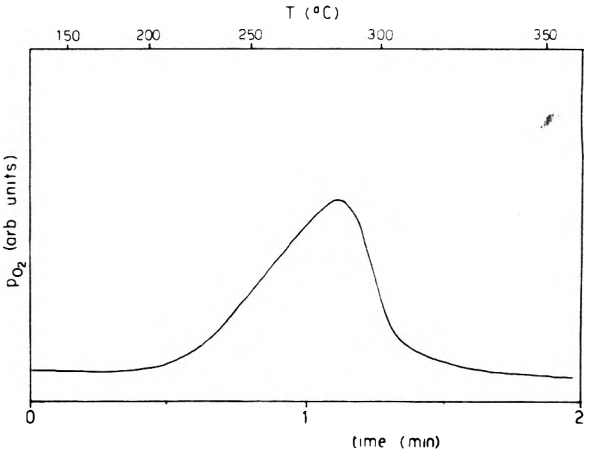

Figure 1. Thermal desorption spectrum of oxygen after exposure of the sample to 10^{-1} Torr oxygen at 150°C for 5 min.

$$-\frac{dN}{dt} = \frac{V}{AkT_0}\left[\frac{dp}{dt} + \frac{S}{V}(p - p_0)\right] \quad (1)$$

where p_0 is the background pressure of oxygen, S is the pumping speed of the system for oxygen, V the volume, T_0 the temperature of the system, and A the sample surface. Measurements of the S/V ratio gave a value of about 8 sec^{-1} for the system. Since in the desorption spectrum, as that reported in Figure 1, the maximum value of dp/dt is less than 5% with respect to the term $S/V(p - p_0)$, the first term can be neglected, so that the increase of the oxygen pressure is directly proportional to the desorption rate to a good approximation, and the area under the desorption peak is directly proportional to the amount of oxygen desorbed.

It is assumed, following Kollen and Czanderna,[2a] that the desorption rate can be described by the relation

$$-\frac{d\theta}{dt} = \nu_n e^{-E/RT}\theta^n \quad (2)$$

where θ is the oxygen fractional coverage, ν_n a frequency factor, n the order of the process, and E the activation energy. This relation should hold if the desorption is a simple process. In this case, ν_n and E are independent of θ and can be derived by analyzing the experimental data for $n = 1$ or $n = 2$. If the rate of temperature variation as function of time is known, the kinetics parameters can be evaluated using integrated forms of eq 2. In the present case, the rate cannot be reduced to a simple form, so that another analysis of the experimental data will be applied.

Combining eq 1, with the term dp/dt neglected, and eq 2 we obtain

$$\Delta p = p - p_0 = K_n e^{-E/RT}\theta^n$$

where K_n is a constant whose value is difficult to estimate for the system considered, with sufficient accuracy. This equation, however, allows the value of E to be determined, if a value of n is found for which the equation is verified.

The fractional coverage θ can be evaluated at each point of the desorption peak by a graphical integration, assuming that the total area of the peak corresponds to $\theta = 1$. An Arrhenius plot of the ratio $\Delta p/\theta^n$ should then give a straight line for the correct value of n. This is shown in Figure 2, in which the data obtained from the peak of Figure 1 are reported for first and second order plots. The experimental points cover a range of θ from about 0.1 to 0.9. The second-

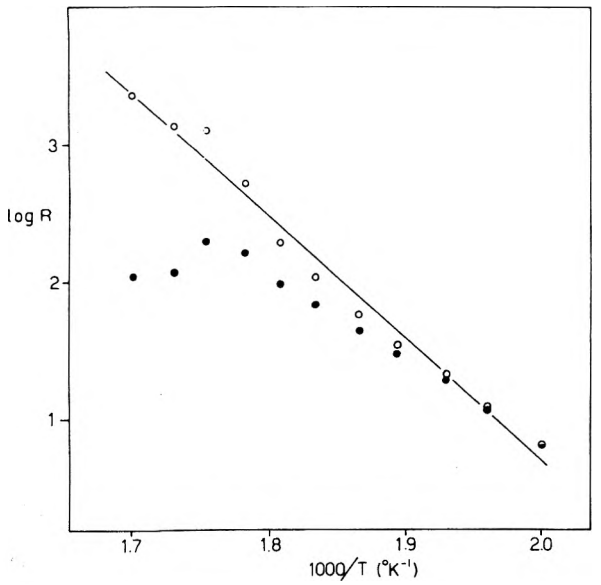

Figure 2. Arrhenius plot of the quantity $R = \Delta p/\theta^n$, obtained from the desorption peak of Figure 1: ●, $n = 1$; ○, $n = 2$.

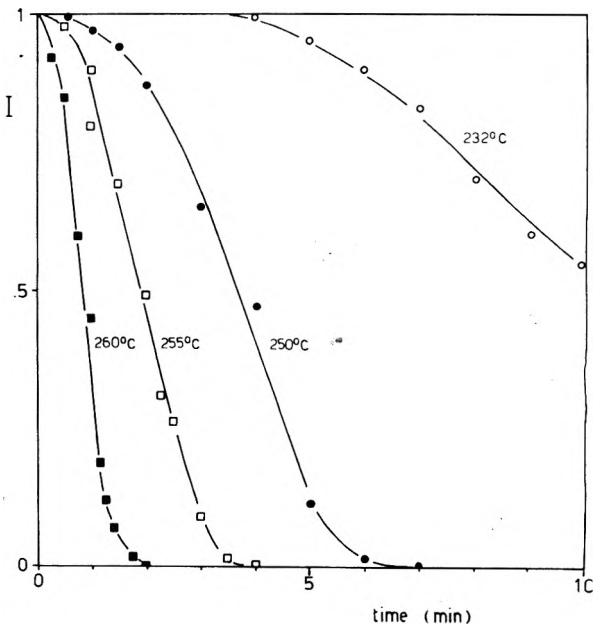

Figure 3. Ag(110) (2 × 1) O superstructure. Plot of normalized intensity vs. time for the (1/2, 0) beam (47 eV), at constant temperatures.

order analysis gives the best result, in agreement with the more accurate study of Kollen and Czanderna.[2a]

The activation energy derived by the straight line (with the least-squares method) is 40.3 ± 4.1 kcal/mol. Different runs gave values differing by no more than 2 kcal/mol. The value of E obtained is in satisfactory agreement with the value of 34.5 ± 3.5, obtained from thermal desorption data, and with 41.8 ± 3.5, obtained from isothermal desorption data, as reported in ref 2a.

Although the frequency factor was not evaluated in the present analysis, the result confirms that the desorption process observed is fundamentally the same as that studied by Kollen and Czanderna on a polycrystalline sample.

As mentioned in section 1, however, the desorption spectrum cannot be considered characteristic of the desorption mechanism from the (110) domains only, although about ⅔ of the geometrical area of the sample could be considered in principle as (110) faces.

On the (110) domains, LEED indicates that the (2 × 1) O superstructure maintains a good long-range order up to the temperature at which oxygen desorbs. The decomposition of the (2 × 1) phase has thus been followed by measuring the intensity of a diffracted beam, characteristic of this superstructure. In Figure 3, a series of curves is reported, which shows the variation of the intensity of the (1/2, 0) beam as function of time, during heating the sample at constant temperatures. The intensity for each curve was normalized to the initial value measured at the corresponding temperature, after the background intensity was subtracted. In this way the difference in intensity between the curves, due to the Debye–Waller effect, should in principle be eliminated. Since the (1/2, 0) beam is characteristic of the (2 × 1) phase, it can be assumed that its intensity is a unique function of the fraction of the surface covered by the ordered domains. If the mechanism of destruction of this phase is the same in the temperature range considered, equal intensity for different curves in Figure 3 should correspond to equal fractional coverage. For a simple desorption process, the integrated form of the kinetic equation may be considered to be of the form $f(\theta,\theta_0) = Kt$, where f is a function depending on the order of the process, θ_0 is the initial fractional coverage, and K is the temperature-dependent rate constant. Thus, for a given process, runs made at constant temperatures, in which θ is recorded as function of time, starting with the same θ_0, allow relative values of the constant K to be determined by measuring the time necessary to obtain the same fractional coverage. For the curves of Figure 3, this corresponds to the time necessary to reach the same relative intensity.

In Figure 4a, the time necessary to reach the half-value of the intensity at seven different temperatures is reported in an Arrhenius plot, from which an activation energy of 41.7 kcal/mol can be derived.

In Figure 3, it can be seen that all the curves show an almost linear portion which, for $t = 0$, extrapolates to about the same point, so that the slope of this portion may be considered to be a measure of the rate constant of the process. The slopes, derived with the least-squares method, are reported in the Arrhenius plot of Figure 4b, which gives a better fit to a straight line. From this, an activation energy of 39.6 kcal/mol is obtained.

Thus, the value of the activation energy for the destruction of the (2 × 1) O surface phase is the same as that derived from the desorption spectra, within the limits of error. This strongly indicates that the destruction of the (2 × 1) phase is the rate-determining step of the whole desorption mechanism. That is, if this superstructure is formed by atomic oxygen, the atoms desorb directly from the immobile layer by recombination to molecules. In this case, an oxygen atom must recombine with a nearest neighbor in order to form an activated complex from which the O_2 molecule desorbs.

The desorption with recombination in an immobile adsorption layer has been treated.[9] If each atom has z nearest neighbors, the equation for the desorption rate is

$$-\frac{d\theta}{dt} = \frac{K(z-1)^2}{z(z-\theta)}\theta^2$$

In the model proposed for the (2 × 1) O superstructure, which is considered as a two-dimensional oxide with a distorted hexagonal packing, each oxygen atom has six oxygen

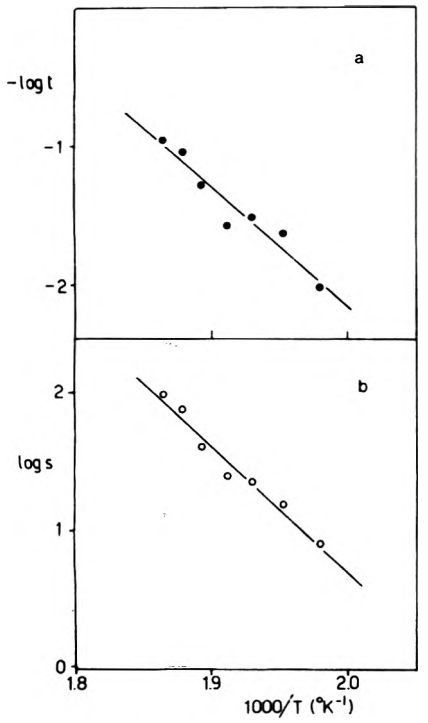

Figure 4. Arrhenius plot of the time necessary to observe the half-value (a) and of the slope of the linear portion (b) in the curves of *I* vs. time, for the (1/2, 0) beam.

neighbors at about the same distance. This high value of z approaches the above equation to that for a simple second-order law, in agreement with the order indicated by the desorption spectra.

The same mechanism would also be valid for the desorption of oxygen from the silver (111) surface. On this surface, oxygen forms a two-dimensional oxide which is interpretable on the basis of an hexagonal packing, probably similar to that found on the (110) face. The superstructure found on the (111) face is also observed up to the temperature of oxygen desorption.

The decomposition of the surface layer can be considered as that of a two-dimensional oxide. In a previous paper,[4] it was pointed out that the observed activation energy for the desorption of oxygen from the silver surface is very close to that reported by Allen[8] for the decomposition of bulk silver oxide.

The above mechanism is different from that proposed by Kollen and Czanderna.[2a] These authors, on the basis of the value of the preexponential factors, concluded that oxygen atoms recombine from a mobile adsorption layer, forming an activated complex with greater mobility. Czanderna[9] considered that atomic oxygen becomes mobile above 100°C on the silver surface. Sandler and Durigon,[10] on the basis of isotope exchange experiments, concluded that the adsorbed oxygen atoms become mobile at about 160°C.

The present results indicate that the adsorption layer formed on the (110) face at full coverage, which can be considered as a two-dimensional oxide, maintains a rigid structure up to the temperature of desorption, and that oxygen desorbs from an immobile layer.

However, on the (110) face, oxygen forms other ordered two-dimensional phases at lower coverages, characterized by ($n \times 1$) periodicity, with $n > 2$.[5] These phases seem to correspond to a much lower content of oxygen and to have a different type of structures with respect to the (2 × 1) superstructure. They also have a different thermal stability, since they are reversibly disordered at about 150°C; the formation of streaks in the LEED pattern along the [1$\bar{1}$0] direction accompanying the disordering, indicates that oxygen becomes mobile at this temperature along the trough present on the (110) face in this direction. The low coverage structures can be obtained by partial desorption of oxygen from the (2 × 1) superstructure and allowing the adsorbed atoms to rearrange in a new ordered phase by heating at temperatures just lower than that of desorption. In fact, when the (2 × 1) structure is partially destroyed by rapidly desorbing some oxygen, the low coverage ($n \times 1$) structures are not immediately observed after cooling. It is necessary to heat at about 150°C for several minutes, in order to transform the residual disordered (2 × 1) into a well-ordered (3 × 1) or (4 × 1) superstructure.

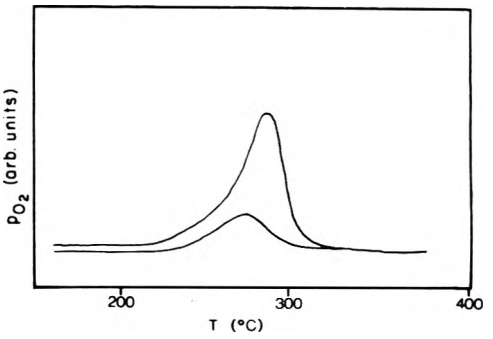

Figure 5. Thermal desorption spectra observed when the sample is covered by the (2 × 1) O superstructure (maximum coverage; upper curve) and by the (3 × 1) O superstructure (lower curve).

When the surface is covered by these phases, oxygen is observed to desorb at temperatures slightly lower than that at which it desorbs from the maximum coverage structure. In Figure 5, two desorption spectra are reported: one obtained at full coverage of the surface; the other after about ⅔ of the initial oxygen was previously desorbed, leaving the surface covered mainly by the (3 × 1) superstructure with small residual domains of the (2 × 1). The sample, in the latter conditions, gives a desorption peak with a maximum at a temperature lower by about 15°C. This is in contrast with the behavior expected for a second-order desorption, for which the maximum in the desorption rate should be observed at increasing temperatures with decreasing coverage, as indeed observed by Kollen and Czanderna.[2a] These authors, by desorbing oxygen from a coverage about ⅓ of the maximum coverage, found an increase of 24°C in the temperature of the maximum desorption rate.

The present results indicate that, at lower coverages, oxygen desorbs from the (110) face with a different mechanism, which, if the order is unchanged, should be characterized by a lower activation energy or higher preexponential factors. In particular, at low coverages oxygen becomes mobile before desorbing, in agreement with the previous results of other authors.[9,10]

It may be concluded that, starting the desorption from the full coverage, if the heating rate is sufficiently high, the desorption kinetics are probably dominated by the decomposition of the immobile layer (corresponding to the (2 × 1) superstructure for the (110) silver surface). If the heating rate is low, a rearrangement of the adsorbed oxygen may gradually change the mechanism to that of a desorption from a mobile layer.

Although these results have been obtained on a single

crystal face, they can probably be generalized to indicate that the mechanism of desorption of oxygen from the silver surface may not only depend on the crystal face, but also on the coverage. Correspondingly, different parameters in the desorption kinetics should be found. Significant variations at least in the preexponential factor of the rate constant are expected, due to the different degrees of freedom of the surface atoms. Further work on single crystal faces, with a precise evaluation of the desorption kinetics parameters at different coverages, should significantly improve the understanding of the states of oxygen chemisorbed on the silver surface.

References and Notes

(1) Work supported by Snamprogetti, under Contract No. A/1-34305.
(2) (a) W. Kollen and A. W. Czanderna, *J. Colloid. Interface Sci.*, **38**, 152 (1972); (b) A. W. Czanderna, S. C. Chen, and J. R. Biegen, *J. Catal.*, **33**, 163 (1974).
(3) G. Rovida, F. Pratesi, M. Maglietta, and E. Ferroni, *J. Vac. Sci. Technol.*, **9**, 796 (1972).
(4) G. Rovida, F. Pratesi, M. Maglietta, and E. Ferroni, *Surf. Sci.*, **43**, 230 (1974).
(5) G. Rovida and F. Pratesi, *Surface Sci.*, in press.
(6) G. Rovida and F. Pratesi, unpublished results.
(7) B. M. W. Trapnell, "Chemisorption", Butterworths, London, 1955.
(8) J. A. Allen, *Aust. J. Chem.*, **13**, 431 (1960).
(9) A. W. Czanderna, *J. Phys. Chem.*, **68**, 2765 (1964).
(10) L. Sandler and D. D. Durigon, *J. Phys. Chem.*, **69**, 4201 (1965).

Thermodynamic Parameters for Acid Dissociation of Trihaloacetaldehyde Hydrates

Joseph L. Kurz* and Michael A. Stein

Department of Chemistry, Washington University, St. Louis, Missouri 63130 *(Received July 10, 1975)*

Publication costs assisted by the National Science Foundation

The temperature dependence of pK_a has been measured spectrophotometrically for *p*-cresol (used as indicator), fluoral hydrate, and chloral hydrate. Parameters for acid dissociation at 25° in aqueous solution are (given in order are pK_a, $\Delta H°$ in kcal mol^{-1}, $\Delta S°$ in cal deg^{-1} mol^{-1}, and $\Delta C_p°$ in cal deg^{-1} mol^{-1}): *p*-$CH_3C_6H_4OH$, 10.26_7, 5.74, -27.7_3, and −35; $CF_3CH(OH)_2$, 10.24_9, 6.69, -24.4_7, and −37; $CCl_3CH(OH)_2$, 10.07, 7.1, −22.2, and $\Delta C_p°$ not determined. The values of $\Delta S°$ for the aldehyde hydrates are in the range expected for dissociations of uncharged acids in aqueous solution; thus the CX_3 substituent in these acids does *not* lead to anomalous (near zero) values of $\Delta S°$ such as are observed for dissociation of the structurally similar trihaloacetic acids. The origin of that anomaly therefore must lie in some interaction which involves the $-CO_2H$ and/or $-CO_2^-$ groups and which cannot occur when those groups are replaced by $-CH(OH)_2$ and $-CH(OH)O^-$.

Introduction

It is known that $\Delta S° \sim 0$ for the dissociations of trifluoro- and trichloroacetic acids in aqueous solution.[1,2] Comparison of the thermodynamic parameters for the dissociation of these trihaloacetic acids to those for the dissociations of unsubstituted carboxylic acids shows that the acid-strengthening effect of the CX_3 group is almost entirely manifested as a change in $\Delta S°$; $\Delta H°$ is near zero for the dissociations of both sets of acids. These trihalo acids (and to a lesser extent, the dihaloacetic acids) are thus among the very small number of acids which disobey the commonly accepted generalization[3] that all ionizations of uncharged acids in aqueous solution have standard entropy changes near −22 cal deg^{-1} mol^{-1}. In contrast, $\Delta C_p°$ for trichloroacetic acid dissociation is "normal" (ca. −40 cal deg^{-1} mol^{-1}).

In order to interpret the values of $\Delta S^{\ddagger}$ and $\Delta C_p^{\ddagger}$ for water-catalyzed trihaloacetate ester hydrolyses (which have been under study in these laboratories),[4] it is necessary to know how general these anomalous effects of trihalomethyl substituents may be. In particular, it would be useful to know the effect of a CX_3 group on $\Delta S°$ and $\Delta C_p°$ for acid dissociation of the tetrahedral intermediates, $CX_3C(OH)_2OR$, in those hydrolyses. Since the thermodynamic parameters for dissociation of such unstable intermediates are not amenable to direct measurement, the structurally similar trihaloacetaldehyde hydrates, $CX_3C(OH)_2H$, were chosen as model acids.

Experimental Section

Materials. The ethyl hemiacetal of fluoral (PCR) was purified by distillation through a Nester/Faust spinning band column; the central fraction was collected over a 0.1° range at ca. 99° and atmospheric pressure. Solutions of fluoral hydrate were prepared by dropping the purified hemiacetal into a stirred solution of phosphorus pentoxide in sulfuric acid,[5] passing the resulting gas through a column of phosphorus pentoxide on glass beads, and absorbing the fluoral in H_2O or D_2O. No impurities could be detected by PMR either in the purified hemiacetal or in the fluoral hydrate solutions.

Borax was National Bureau of Standards pH standard (sample 187a). Chloral (Fisher), *p*-cresol (Aldrich Gold Label 99+%), and other reagents were found to be sufficiently pure and were used without further purification. Ordinary distilled water was freed from CO_2 and ionic impurities by passage through a mixed-bed ion-exchange column (Barnstead 0808).

Measurements Using Borax and Fluoral Hydrate Buffers. Fluoral hydrate buffers were prepared from the aqueous fluoral hydrate solution and carbonate-free standard KOH solutions. The ionic strength was varied by changing the amount of KOH; no additional salts were added. Fluoral hydrate/conjugate base ratios of ca. 2, 1, and 0.5 were used and the resulting three pK_a values for each constant ionic strength were averaged. Borax buffers were prepared according to the instructions accompanying the NBS Borax.

To each optical cell was added 3.00 ml of a buffer and 20.0 μl of 0.092 *M* *p*-cresol in water. Solutions of perchloric acid and carbonate-free KOH were used in place of the buffer in measurements of the optical densities arising from un-ionized *p*-cresol and from the corresponding conjugate base. The silica stoppers were sealed into the 10-mm absorbtion cells with the minimum sufficient amount of silicone grease to prevent drifts in optical density resulting from evaporation losses at the higher temperatures. After each cell was filled and stoppered, its optical density was measured first at 25.0° and then at the other temperatures; frequent remeasurements at 25.0° were made during the sequence of temperatures to ensure that no significant change in the optical density at 25.0° had taken place. The occurrence of such changes thwarted attempts to measure pK_a values at temperatures higher than 55°. The blank (i.e., no *p*-cresol) optical density of each cell–solution combination was measured at different temperatures by the same procedure.

Optical densities were measured at 295.5 nm with a Cary 16K spectrophotometer and were reproducible within ±0.001 over the range (up to 1.8) observed in these measurements. Temperatures were monitored with a thermistor in an absorbtion cell; the resolution of the resistance bridge was sufficient to detect temperature changes as small as 0.01° at all temperatures used in these measurements. The maximum possible error in the measured temperatures is estimated to be 0.1°. Since the temperature dependence of the pK_a of the indicator (*p*-cresol) is quite close to those of the buffer acids (boric acid and fluoral hydrate), the sensitivities of the observed optical densities to changes in temperature were small; for all solutions, an error of 0.1° would cause an error in the observed optical density which was less than 0.0003.

Measurements Using Chloral Hydrate Buffers. The conjugate base of chloral hydrate decomposes in aqueous solution. At the higher temperatures, that decomposition is sufficiently rapid to cause a significant drift in the optical density of *p*-cresol in a chloral hydrate buffer. Therefore at each temperature individual cells containing *p*-cresol and chloral hydrate were brought to temperature equilibrium in the cell compartment of the spectrophotometer; KOH solution (60 μl of 1.000 *F*) was then added, the solution mixed without removing the cell from the thermostatted holder, and the optical density recorded as a function of time. The recorder trace was extrapolated back to the time of mixing to obtain the correct optical density. Other aspects of the procedure were as described for fluoral hydrate buffers. The extrapolated optical densities were less reproducible than those of the stable fluoral hydrate buffers, and at temperatures above 55° the extrapolated values were too uncertain to be useful.

Calculations of pK_a. The value of pK_a for *p*-cresol at each temperature was calculated from the observed optical densities of solutions of *p*-cresol in NBS borax buffer (OD), 0.1 *F* $HClO_4$ (OD_A), and 0.25 *F* KOH (OD_B) using eq 1. The value of the pH in eq 1 was taken as the value cited in the NBS certificate minus a correction for the change in pH resulting from partial reaction of the buffer with the added *p*-cresol. The extent of that reaction was calculated from the observed optical density and the resulting correction was always ≤0.004 pH units.

$$pK_a = pH + \log \frac{OD_B - OD}{OD - OD_A} - \log y_- \qquad (1)$$

In using eq 1, the value of y_-, the molar activity coefficient of the anionic conjugate base of *p*-cresol, was assumed to be given by the Davies equation[6] in the form of eq 2 where *I* is the ionic strength and *A* is the Debye–Hückle limiting slope at the temperature of the measurement.

$$\log y_- = \frac{-A\sqrt{I}}{1 + \sqrt{I}} + 0.15I \qquad (2)$$

An apparent value of pK_a for fluoral or chloral hydrate in each fluoral or chloral buffer at each temperature was calculated from eq 3 in which $(pK_a)_{cresol}$ is the smoothed

$$pK_a = (pK_a)_{cresol} + \log \frac{[HA]}{[A^-]} - \log \frac{OD_B - OD}{OD - OD_A} \qquad (3)$$

value of the pK_a for *p*-cresol at that temperature (calculated from eq 4 and the *A*, *B*, *C* parameters in Table I). The acid/base buffer ratio, $[HA]/[A^-]$, in eq 3 was calculated from the amounts of fluoral or chloral hydrate and of KOH used to prepare the buffer and includes corrections for partial reaction of $CX_3CH(OH)O^-$ with the added cresol (as for the borax buffer) and with water (to give OH^- + $CX_3CH(OH)_2$). The latter correction was computed from pK_a for $CX_3CH(OH)_2$ and pK_w. The total correction was always <0.05 pH units.

Results and Discussion

The pK_a of *p*-cresol was measured at each of six temperatures equally spaced between 5 and 55° inclusive; the observed values were fitted by least-squares to the Everett and Wynne-Jones equation[7] in the form of eq 4. At each of

$$-pK_a = A/T + B \log T + C \qquad (4)$$

the same temperatures, apparent values of pK_a for fluoral hydrate were measured at ionic strengths of 0.01, 0.02, and 0.04, and the apparent pK_a of chloral hydrate was measured at $I = 0.02$. The apparent pK_a values for fluoral hydrate were extrapolated linearly[8] to zero ionic strength and the extrapolated values were fitted to eq 4 by least-squares. Table I lists the *A*, *B*, *C* parameters for the three acids along with the corresponding values of pK_a (25°), $\Delta H°$ (25°), $\Delta S°$ (25°), and $\Delta C_p°$ (assumed temperature independent). The relationships between these values and the *A*, *B*, *C* parameters are given by eq 4–7 in which *R* is the gas constant.

$$\Delta H° = R(BT - A \ln 10) \qquad (5)$$

$$\Delta S° = R[C \ln 10 + B(1 + \ln T)] \qquad (6)$$

$$\Delta C_p° = RB \qquad (7)$$

For *p*-cresol and fluoral hydrate the standard deviation of the observed pK_a values from the smoothed values calculated from eq 4 is ca. ±0.001; for chloral hydrate that standard deviation is near ±0.01. Those observed and cal-

TABLE I: Parameters for Acid Dissociation[a,b]

	A^c	B^c	C^c	$pK_a{}^d$ (25°)	$\Delta H°$ (25°),[e] kcal mol^{-1}	$\Delta S°$ (25°),[f] cal deg^{-1} mol^{-1}	$\Delta C_p°$,[g] cal deg^{-1} mol^{-1}
p-Cresol	−3523.18 ± 145.954	−17.5206 ± 1.11366	44.9032 ± 3.24583	10.267	5.74 ± 0.02	−27.73 ± 0.07	−35 ± 2
	(−4627.25 ± 542.913)[h]	(−26.4764 ± 4.25404)[h]	(70.7572 ± 12.3481)[h]	(10.277)[h]	(5.49 ± 0.06)[h]	(−28.6 ± 0.2)[h]	(−53 ± 8)[h]
$CF_3CH(OH)_2$	−3872.72 ± 147.449	−18.6246 ± 1.12507	48.8253 ± 3.27907	10.249	6.69 ± 0.02	−24.47 ± 0.07	−37 ± 2
				(10.22)[i]			
$CCl_3CH(OH)_2$	−477.354 ± 1077.13	8.36196 ± 8.21873	−29.1644 ± 23.9540	10.07	7.1 ± 0.1	−22.2 ± 0.5	*k*
				(10.04)[j]			

[a] From pK_a measurements over the temperature range, 5–55°; molar standard state; dilute aqueous reference state. [b] The indicated uncertainties are standard deviations. [c] From eq 4. [d] Smoothed values from *A*, *B*, *C*, and eq 4. [e] From eq 5. [f] From eq 6. [g] From eq 7; assumed temperature independent. [h] Recalculated from data in D. T. Y. Chen and K. J. Laidler, *Trans. Faraday Soc.*, 58, 480 (1962). [i] R. Stewart and M. Mocek, *Can. J. Chem.*, 41, 1160 (1963). [j] R. P. Bell and D. P. Onwood, *Trans. Faraday Soc.*, 58, 1557 (1962). [k] The pK_a values are not sufficiently precise to give a meaningful value of ΔC_p for $Cl_3CCH(OH)_2$.

culated pK_a values along with the error correlation matrices[9] for the *A*, *B*, *C* parameters are given in microfilm. The standard deviations for $\Delta H°$, $\Delta S°$, and $\Delta C_p°$ in Table I are calculated from the standard deviations of *A*, *B*, and *C* together with the error correlation coefficients. No standard deviations for the pK_a values are cited in the table, since a significant contribution to the uncertainty in pK_a is likely to come from the approximation inherent in the use of the Davies equation. (Vide infra.)

Equation 3 is based on the assumption that y_{HA}/y_{A^-} has the same value at any fixed value of I independently of whether "HA" is *p*-cresol, fluoral hydrate, or chloral hydrate. Extrapolation to zero ionic strength of the pK_a for fluoral hydrate replaces that assumption with the assumption in eq 1 and 2 that log y_- is correctly given by the Davies equation when "HA" is *p*-cresol and the solvent is 0.01 *m* Borax (for which I = 0.02). Comparison of predictions from the Davies equation to observed mean activity coefficients for 1:1 electrolytes suggests that errors in the pK_a values in Table I which arise from this assumption should be much less than 0.01, but may well be comparable to or larger than the experimental scatter (cited above as ±0.001).

Since such errors in log y_- should be approximately temperature independent, it is probable that their contributions to the total uncertainties in $\Delta H°$, $\Delta S°$, and $\Delta C_p°$ are not conspicuously larger than the standard deviations of those parameters given in Table I. This expectation is in accord with the observation that the values of $\Delta H°$, $\Delta S°$, and $\Delta C_p°$ for fluoral hydrate vary over ranges of only ca. 0.04 kcal mol^{-1}, 0.3 cal deg^{-1} mol^{-1}, and 4 cal deg^{-1} mol^{-1}, respectively, when they are calculated directly from apparent pK_a values at I = 0.01, 0.02, and 0.04 instead of from the extrapolated pK_a values. The entries for this work in Table I are also in good agreement with previously reported values where such exist.

In conclusion, inspection of the entries in Table I reveals that $\Delta S°$ and $\Delta C_p°$ for the ionization of $CX_3CH(OH)_2$ have "normal" values. That is, their values are in the range commonly observed for ionizations of uncharged acids (e.g., phenols and halogen-free carboxylic acids). The anomalous values of $\Delta S°$ for the ionization of polyhaloacetic acids[1,2] thus appear to arise from some interaction which specifically involves the $-CO_2H$ (and/or $-CO_2^-$) group. Whatever that interaction is, it does not occur when the carboxyl group is replaced by the structurally similar $-CH(OH)_2$ group. Perhaps this difference is a consequence of the possibility of stabilization of the $RCH(OH)O^-$ anion by intramolecular hydrogen bonding[10] in place of the hydrogen bonding to solvent which is required for a RCO_2^- anion. Such a difference in solvent–anion interaction might well lead to a significant change in the effects of the ideomorphic solvent structure which has been suggested[1] to be present in the neighborhood of halocarbon substituents.

Acknowledgment. The authors gratefully acknowledge support of this work by the National Science Foundation (GP-38915X).

Supplementary Material Available: the supplement contains error correlation matrices and tables of observed and smoothed (via eq 4) pK_a values (2 pages). Ordering information is given on any current masthead.

References and Notes

(1) J. L. Kurz and J. M. Farrar, *J. Am. Chem. Soc.*, **91**, 6057 (1969).
(2) J. Jordan, *Rec. Chem. Prog.*, **19**, 193 (1958).
(3) K. S. Pitzer, *J. Am. Chem. Soc.*, **59**, 2365 (1937).
(4) J. L. Kurz and G. J. Ehrhardt, *J. Am. Chem. Soc.*, **97**, 2259 (1975).
(5) M. Braid, H. Iserson, and F. E. Lawler, *J. Am. Chem. Soc.*, **76**, 4027 (1954).
(6) C. W. Davies, "Ion Association", Butterworths, London, 1962, p 41.
(7) D. H. Everett and W. F. K. Wynne-Jones, *Trans. Faraday Soc.*, **35**, 1380 (1939).
(8) The total variation of the apparent pK_a's through the range $0 < I < 0.04$ was ca. 0.02 at each temperature and, as expected, was linear within the experimental scatter.
(9) A. A. Clifford, "Multivariate Error Analysis", Wiley, New York, N.Y., 1973.
(10) W. J. Middleton and R. V. Lindsey, Jr., *J. Am. Chem. Soc.*, **86**, 4948 (1964).

Interaction of *p*-Nitrosalicylic Acid and Ethylenediamine in Mixed Solvents. A Proton Donor–Acceptor Equilibrium

S. P. Moulik,* S. Ray,

Department of Chemistry, Jadavpur University, Calcutta 700032, India

and A. R. Das

Department of Physical Chemistry, Indian Association for the Cultivation of Science, Calcutta 700032, India

(Received June 25, 1974; Revised Manuscript Received June 23, 1975)

The proton transfer complex of *p*-nitrosalicylic acid with ethylenediamine has been studied in mixed solvents with a view toward understanding the electrostatic and specific effects of protic and aprotic solvents. The equilibrium constants have been determined and the thermodynamic parameters, $\Delta G°$, $\Delta H°$, and $\Delta S°$, evaluated in several solvent systems. It has been observed that the solvent polarity fails to be a proper guide of complex formation. The formation can be appreciably arrested by the addition of a high polar solvent such as formamide.

Introduction

A phenolic acid usually releases proton from the –OH group in a polar medium depending on the pK of the compound. In doing so, the anion exhibits a characteristic absorption band whose intensity can be a convenient measure of its dissociation. In a medium of low polarity electrostatic factors reduce the above ionization; in such a medium a withdrawing agent (an amine) is necessary for favorable release of the proton. The released proton is preferentially transferred to the base and a proton transfer complex or hydrogen bonded ion pair is formed. When the acid is not that weak, some of the released hydrogen ions may be accepted by the polar solvent molecules (of course in a less preferential manner than the added base), thus making the whole transfer process complex.[1] Besides, specific solvation, solute–solvent interaction, and solvent structural effects may also influence the ionization process.[1,2]

Since in a solvent medium the electrostatic or solvent polarity effect on the proton transfer to a base is complicated by the additional acceptance of the protons by the solvent molecules, a condition is, therefore, needed to reduce the second process to a minimum for the understanding of the first. Under normal conditions, *p*-nitrosalicylic acid has been observed to satisfy this by not releasing its phenolic proton even into pure water when a base is absent. An orderly measure of the electrostatic effects on the proton donor–acceptor equilibrium of it with an amine (ethylenediamine) is expected in mixed solvent media. Results of such investigations using 12 nonaqueous solvents are reported in what follows. Such an investigation can be important for the basic understanding of the hydrogen bonded interactions between the acid and the basic groups in proteins responsible for various biological activities.

Experimental Section

Materials and Method. *p*-Nitrosalicylic acid of Eastman Organic Chemicals, mp 227–228°C, was recrystallized twice from conductivity water, and its melting point was checked for purity. All the solvents used were either E. Merck pro analysi or BDH AnalaR grades. They were further purified prior to use by standard chemical and physical treatments. The sample of urea (BDH, AnalaR) was used without further purification. Aqueous solutions were prepared using double distilled conductivity water (specific conductance = 1.5×10^{-6} mho cm^{-1} at 30°C).

Spectral measurements were taken in a Beckman DU spectrophotometer using 1-cm matched silica cells. The prepared samples were placed in a temperature controlled thermostatic bath (working in the deviation range of ±0.2°C) for a period of 1 hr, and the absorbances were measured in the spectrophotometer having arrangements for circulating the water of the bath around the cell compartment. Two types of experiments were performed. In the first, *p*-nitrosalicylic acid samples of a fixed concentration were mixed with increasing amounts of ethylenediamine in a fixed solvent composition by placing equal amounts of the proton donor in different containers, and adjusting the final composition by the required addition of

the amine and the solvent. The absorbances of each of these solutions were then measured over a wide range of wavelengths. In the second set of measurements, the concentrations of the proton donor and the acceptor were kept constant, and the solvent compositions were varied over a wide range. The absorbances of these solutions were measured at the characteristic wavelength of the complex, which is 414 nm in the present case.

Results

Spectra of p-Nitrosalicylic Acid. As long as the phenolic proton is unreleased, the spectra of the acid in water and in nonaqueous solvents, viz., alcohols, acetone, dioxane, etc., are all almost alike with a broad band at 320 nm, falling sharply in the visible direction (practically zero absorbance for a 4.03×10^{-5} M acid at 400 nm). In the presence of increasing concentrations of the diamine a characteristic band appears at 414 nm, and sharpens with a concomitant decrease of the 320-nm band of the undissociated acid. This is a general tendency of a proton transfer process in which one form changes into another with a noteworthy occurrence of an isosbestic point[1] (the isosbestic point in the present system is at 355 nm).

Equilibrium Constant of the Complex. To understand the thermodynamics of the process, determination of the equilibrium constant of the complex is obvious. This was done in the following way. For the reaction

$$\underset{\text{donor}}{AH} + \underset{\text{acceptor}}{B} \overset{K}{\rightleftharpoons} \underset{\text{complex}}{A^-\ldots H^+B} \qquad (1)$$

$$K = [C_c]/[C_a - C_c][C_b - C_c] \qquad (2)$$

where $[C_a - C_c]$, $[C_b - C_c]$, and $[C_c]$ are the equilibrium concentrations of the donor acid, the acceptor base, and the 1:1 complex, respectively. The concentration of the free base (equilibrium concentration) can seldom be determined. This was avoided by the use of large excess of the base, and eq 2 then becomes

$$K = [C_c]/[C_a - C_c][C_b] \qquad (3)$$

Now the measured absorbance is

$$A = \epsilon_c[C_c] + \epsilon_a[C_a - C_c] \qquad (4)$$

where ϵ_c and ϵ_a are the extinction coefficients of the complex and the proton donor, respectively (the concentration of the amine is assumed zero, which is a reality).

Combining eq 3 and 4 we have

$$[C_a]/\{A - \epsilon_a[C_a]\} = 1/\{\epsilon_c - \epsilon_a\} + 1/K\{\epsilon_c - \epsilon_a\}[C_b] \qquad (5)$$

Equation 5 can be further reduced to

$$[C_a]/A = 1/\epsilon_c + 1/K\epsilon_c[C_b] \qquad (6)$$

selecting a wavelength at which only the complex absorbs but the proton donor does not (in the present case the complex only absorbs at 414 nm and above). In all the measurements the concentrations of the base were kept nearly 100 times more than the p-nitrosalicylic acid and eq 6 was used to evaluate ϵ_c and K from the intercepts and the slopes, respectively. Representative least-squares plots are illustrated in Figure 1, and the comprehensive results are given in Table I with appropriate standard deviations. The very close fitting of the data to straight lines supports the presence of 1:1 complex formation. Chances of higher order complexes were, however, not truly zero.[1] The formation of

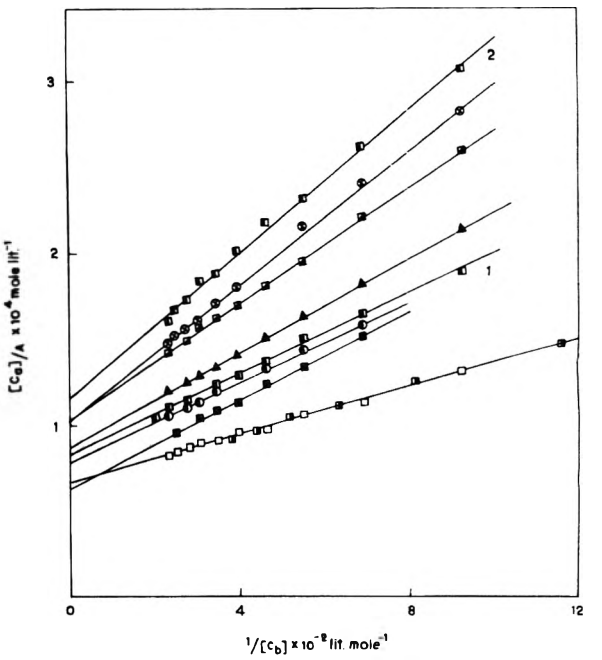

Figure 1. Graphical determination of equilibrium constants of the complex in various mixed solvent media: (□, ◨) water, open and half-closed points represent duplicate experiments; (■) urea, 37.25 wt %; (◐) ethylene glycol, 14.24 wt %; (◧) methanol, 8.01 wt % (line 1), 16.46 wt % (line 2); (▲) ethanol, 9.66 wt %; (◪) 1-propanol, 9.83 wt %; (⊗) 2-propanol, 12.15 wt %.

the complex was maximum in pure water, decreased with the addition of nonaqueous solvents, and was appreciably low in the presence of small concentrations of acetone and dioxane. The protic solvents behaved differently than the aprotic ones.

Dependence of K on Solvent Polarity. The dielectric constants reported in Table I were taken from the work of Akerlof.[3] Whenever direct data were not available, a method of interpolation was adopted. Those on dimethylformamide and formamide were taken from the work of Rohdewald and Moldner,[4] and that of aqueous urea solutions were taken from the data of Wyman[5] computed by Kundu and Majumdar.[6] Dielectric constants of aqueous mixtures of acetonitrile are not available in the literature, therefore, the effects of this solvent could not be brought into the general line.

To test the requirements of Coulomb's law, a plot of log K against D^{-1} was made for the hydroxylic solvents; the dependence was not linear (Figure 2). An apparent conclusion is that solvent effects other than electrostatic are present. In this figure, the 30° set is seen to be above the 55° set. It was observed that use of increased concentrations of p-nitrosalicylic acid yielded higher K values. This may then explain the increased K values observed for the 30° set which contained appreciably higher concentration of the proton donor. The altered activities of all the species at higher concentration of the donor probably made the equilibrium constant more for the 30° set than the 55° set. For a comfortable comparison a detailed knowledge of the activities of all the species is required. A sharp distinction among the mixed solvents appear in that the dipolar aprotic solvents (acetone and DMF) reduced the equilibrium constant more than the protic ones.

Effect of Temperature. The effects of temperature on complex formation in various solvent media were studied

TABLE I: Physicochemical Properties of the Complex in Various Environments[a]

Solvent	$\epsilon_C \times 10^{-3}$, M^{-1} cm^{-1}	D	$K \times 10^{-2}$, M^{-1}	$-\Delta G°$, kcal mol^{-1}
Water	15.06 ± 0.16	76.7	9.60 ± 0.04	4.14 ± 0.003
Glycol–water (14.24)	12.79 ± 0.38	72.5	6.80 ± 0.09	3.93 ± 0.008
Methanol–water (8.01)	12.17 ± 0.90	73.4	7.03 ± 0.07	3.95 ± 0.006
Methanol–water (16.46)	8.67 ± 0.16	69.3	5.52 ± 0.001	3.80 ± 0.003
Methanol–water (25.21)	5.59 ± 0.17	65.2	3.44 ± 0.02	3.52 ± 0.004
Ethanol–water (9.66)	11.61 ± 0.10	71.4	6.30 ± 0.02	3.88 ± 0.002
Acetone–water (3.96)	11.93 ± 0.43	74.4	5.24 ± 0.02	3.77 ± 0.002
1-Propanol–water (9.83)	9.77 ± 0.10	70.0	6.10 ± 0.02	3.86 ± 0.002
2-Propanol–water (12.15)	9.91 ± 0.15	68.2	4.98 ± 0.14	3.74 ± 0.02
2-Methyl-2-propanol–water (12.06)	11.61 ± 0.55	66.7	3.91 ± 0.03	3.60 ± 0.005
Dioxane–water (2.05)	23.31 ± 2.36	74.2	1.70 ± 0.09	3.09 ± 0.03
Urea–water (37.25)	15.85 ± 0.38	92.9	5.01 ± 0.001	3.75 ± 0.003

[a] Weight percent of the first named compound in parentheses. Temperature 30 ± 0.2°C. Transition energy at 414 nm = 70.2 kcal mol^{-1}. Donor concentration = 5.16×10^{-4} *M*.

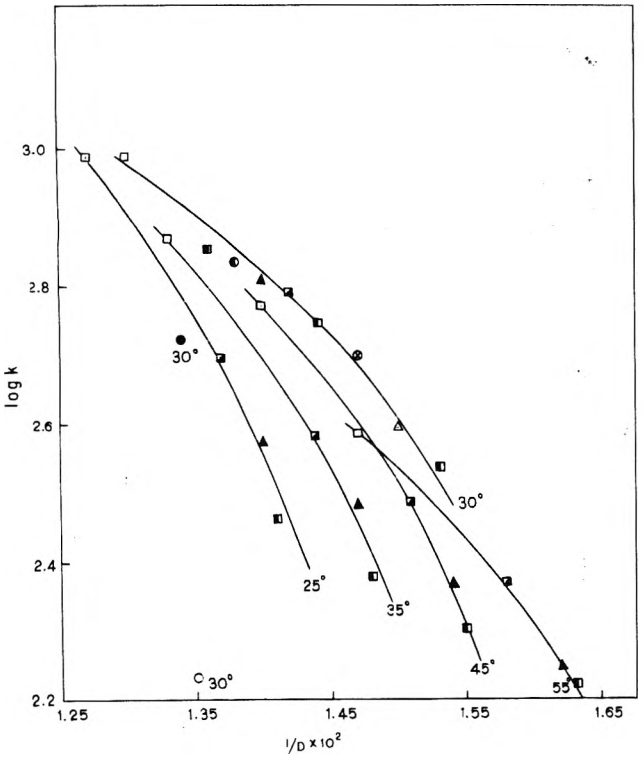

Figure 2. Effect of solvent polarity on complex formation. Dependence of *K* on dielectric constants of solvent mixtures at five different temperatures: for 25, 35, 45, and 55° sets: (□) water, (◪) 1-propanol (8.2 wt %), (▲) ethanol (12.15 wt %), (◧) methanol (16.46 wt %); for 30° set: (□) water, (◧) methanol (8.01, 16.46, and 25.21 wt %), (◐) ethylene glycol (14.24 wt %), (▲) ethanol (9.66 wt %), (◪) 1-propanol (9.83 wt %), (⊗) 2-propanol (12.15 wt %), (△) 2-methyl-2-propanol (12.06 wt %), (◐) acetone (3.96 wt %), (○) dioxane (2.05 wt %).

to evaluate the standard enthalpy and entropy changes. The reaction was spectrophotometrically studied at four different temperatures at 10° intervals in the range 25–55°C. The equilibrium constants were determined applying eq 6, and log *K* vs. T^{-1} plots were made to obtain $\Delta H°$ from the slopes. The thermodynamic parameters obtained at 25°C are given in Table II. The standard states of the reactants were considered to be the hypothetical states of ideal solutions of unit molarity. As stated above the concentration effects of the proton donor on the derived *K* values were checked. Extrapolation of these values to zero

TABLE II: Solvent Controlled Thermodynamic Parameters of the Complex at 25°C[a]

Solvent	$-\Delta G°$, kcal mol^{-1}	$-\Delta H°$, kcal mol^{-1}	$-\Delta S°$, cal mol^{-1} deg^{-1}
Water	4.07 ± 0.02	6.11 ± 0.085	6.84 ± 0.30
Methanol–water (16.46)	3.36 ± 0.006	3.72 ± 0.200	1.22 ± 0.64
Ethanol–water (12.15)	3.51 ± 0.010	4.99 ± 0.153	4.97 ± 0.48
Propanol–water (8.20)	3.67 ± 0.007	4.88 ± 0.085	4.06 ± 0.31

[a] Weight percent of the first named compound in parentheses. Donor concentration = 5.16×10^{-5} *M*.

donor concentration in water and in 16.46% methanol showed a 5% decrease of the reported *K* values at 5.16×10^{-5} *M* donor concentration.

The effect of temperature may also be considered to be equivalent to the electrostatic effect, since the dielectric constant of the solvent changes (usually decreases) with increasing temperature. Plots of log *K* vs. D^{-1} for the working temperatures for several mixed solvent systems are presented in Figure 3. For each solvent system a good linear variation was observed. The slopes of these lines were, on the other hand, different. The scope of specific solvent effects was further supported.

Detailed Solvent Effects. For an understanding of the solvent effects in detail, identical experimental conditions were maintained, where to the aqueous samples having a fixed *p*-nitrosalicylic acid (3.26×10^{-4} *M*) and ethylenediamine (0.424 *M*) concentration, varied proportions of nonaqueous solvents were added, and the absorbances were measured at 414 nm. The fixed concentrations of the donor and the acceptor could thus give a direct estimate of the extent of the complex on a comparative basis of the solvent polarities and compositions. The results are elaborated in Figure 4. It is seen that at constant mole fraction, the efficiencies of the solvents are in the following order: dioxane < acetone < 2-methyl-2-propanol ≈ dimethylformamide < 2-propanol < 1-propanol < ethanol < acetonitrile < methanol < glycol < urea. In this comparison formamide behaves rather peculiarly. The general trend of the solvent effects is almost in the order of increasing dielectric constant having notable variations with acetone, DMF, and FA. These findings encouraged us to measure the results at iso-

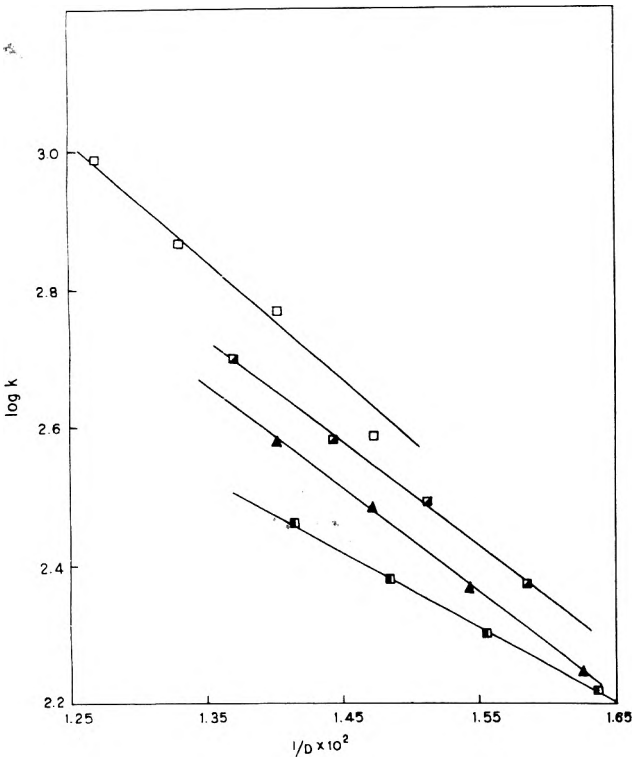

Figure 3. Effect of solvent polarity on complex formation. Dependence of K on temperature induced dielectric constant for the solvent media recorded in F gure 2 for the sets at 25, 35, 45, and 55°.

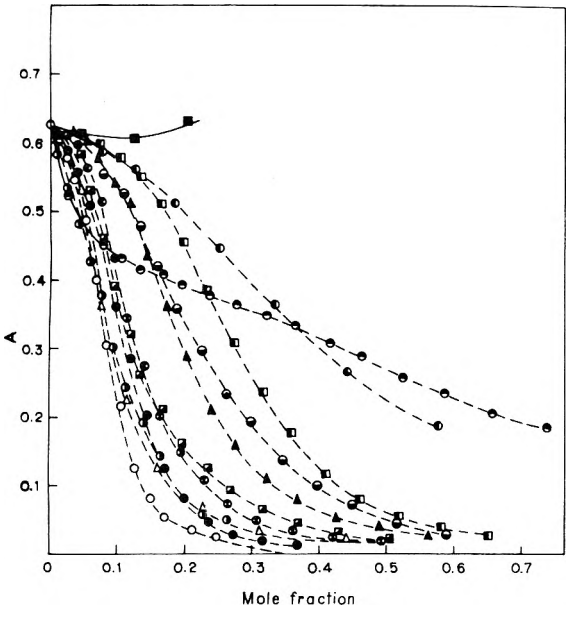

Figure 4. Influence of solvent compositions on the absorbance of the complex at fixed donor and acceptor concentrations of 3.26 × 10^{-5} and 0.424 M, respectively: (■) urea, (◐) ethylene glycol, (◧) methanol, (◓) formamide, (◒) acetonitrile, (▲) ethanol, (⊗) 2-propanol, (◪) 1-propanol, (●) acetone, (◑) dimethylformamide, (△) 2-methyl-2-propanol, (O) dioxane.

dielectric conditions. In Figure 5, absorbances are plotted against the dielectric constants for several of the solvents. It is seen that the order of efficiency is the reverse. Specific solvent effects other than electrostatic is further supported.

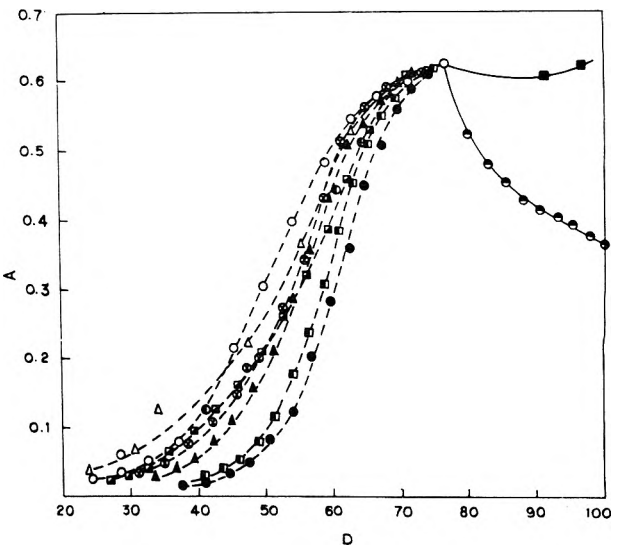

Figure 5. Absorbances of Figure 4 plotted against the dielectric constants of the media with their corresponding signs.

Discussion

The high stability of p-nitrosalicylic acid in releasing its phenolic hydrogen (pK = 10.37)[8] in the absence of a strong proton-withdrawing agent can be reconciled through the formation of intramolecular hydrogen bonding. In the presence of the diamine this bond is weakened owing to a greater pull, and the released proton is lodged on the amine via a hydrogen bonded ion pair formation.[1,9] This ion pair formation can be expected to depend on the polarity of the medium. That this electrostatic effect is not independent of the type of the solvents is evidenced from the nonlinear variation of log K with D^{-1} when various mixed solvents are compared (Figure 2). On the other hand, linear variation of log K with D^{-1} for a fixed solvent composition at different temperatures warrants electrostatic effects to be a proper guide (Figure 3). In this context importance of a threshold polarity of the medium for the proton transfer complex should be recognized.[1,2,10]

A comparison of the added nonaqueous solvents on the basis of mole fraction shows that the order of complexation follows the polarity order of these solvents. This is not manifested when the comparison is made at isodielectric conditions (Figures 4 and 5). It is anticipated that the complex becomes stabilized through solvation by the water molecules.[11] This is supported by the fact of more complex formation in water–dioxane medium than in water–methanol medium at isodielectric conditions, since more water molecules are needed in the former than in the latter to yield equidielectric states. The same principle holds for other solvent systems. With this end in view, log A values at 0.1, 0.2, 0.25, and 0.4 mole fractions have been plotted against D^{-1} for many solvent systems in Figure 6 (log A values have been used to give a comparative basis with log K, A being directly proportional to K). Recognizing the probable uncertainties in the measurements the correlation is noteworthy. The necessity of water molecules for the stabilization of the complex by solvation may further be indicated by the maximum $-\Delta S°$ and $-\Delta H°$ values[12,13] in this medium (Table II). A sound comparison of thermodynamic parameters given in this table is restricted for want of a single reference state for different solvent systems.

The results given in Figure 6 further show that the protic

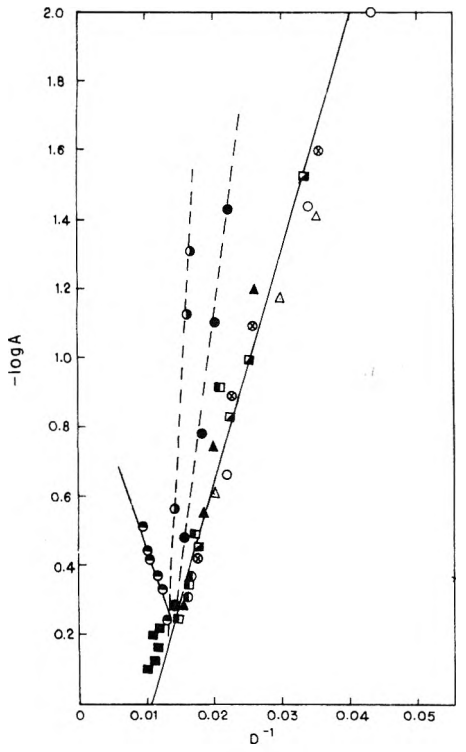

Figure 6. Dependence of $-\log A$ on D^{-1} at isomole fractions, 0.1, 0.2, 0.25, and 0.4, computed from the results incorporated in Figure 4.

solvents behave differently than the aprotic cases; the individual aprotic solvents are seen to have their own specificities. In this regard the pronounced effect of formamide at low concentrations is a special feature. At high concentrations it is less effective than either methanol or glycol (see Figure 4). All these results adjudicate a complex analysis when aprotic solvents are used. Further experiments are needed for a meaningful dissection.

Acknowledgment. The authors extend their thanks to Professor M. N. Das, Head of the Physical Chemistry Section, for laboratory facilities.

References and Notes

(1) S. P. Moulik, A. K. Chatterjee, and K. K. Sen Gupta, *Spectrochim. Acta, Sect. A*, **29**, 365 (1973).
(2) S. P. Moulik, A. K. Chatterjee, and K. K. Sen Gupta, *Ind. J. Chem.*, **12**, 92 (1974).
(3) G. Akerlof, *J. Am. Chem. Soc.*, **54**, 4125 (1932).
(4) P. Rohdewald and M. Moldner, *J. Phys. Chem.*, **77**, 373 (1973).
(5) J. Wyman, Jr., *J. Am. Chem. Soc.*, **55**, 4116 (1933).
(6) K. K. Kundu and K. Majumdar, *J. Chem. Soc., Faraday Trans. 1*, **69**, 806 (1973).
(7) E. H. Lane, S. D. Christian, and J. D. Childs, *J. Am. Chem. Soc.*, **96**, 38 (1974).
(8) J. L. Ernst and J. Manashi, *Trans. Faraday Soc.*, **59**, 230 (1963).
(9) J. W. Smith, *J. Chim. Phys.*, **58**, 182 (1964).
(10) R. M. Scott and S. N. Vinogradov, *J. Phys. Chem.*, 73, 1890 (1969).
(11) S. N. Vinogradov, R. A. Hudson, and R. M. Scott, *Biochim. Biophys. Acta*, **214**, 6 (1970).
(12) G. C. Pimentel and A. L. McClellan, "The Hydrogen Bond", W. H. Freeman, San Francisco, Calif., 1960.
(13) E. M. Arnett, E. J. Mitchell, and T. S. S. R. Murty, *J. Am. Chem. Soc.*, **96**, 3875 (1974).

Limitations Concerning Use of Manganese(II) Selective Broadening in Nuclear Magnetic Resonance Spectroscopy for Determination of Ligand Binding Sites

William G. Espersen and R. Bruce Martin*

Chemistry Department, University of Virginia, Charlottesville, Virginia 22901 *(Received July 31, 1975)*

Publication costs assisted by the National Science Foundation

From comparison of proton and carbon-13 spin–lattice and transverse relaxation times in the presence of Mn(II), it is concluded that in many cases the dipolar term is not the dominant contributor to line broadening. Hence selective broadening experiments to determine the site of Mn(II) binding to small ligands based on an r^{-6} dependence between Mn(II) and the affected nucleus are not generally applicable. Binding sites and distances may be estimated from selective T_1 measurements, but in this case it must be established that the predominant dipolar interaction contributing to relaxation is that between the paramagnetic ion and the affected nucleus and that other, closer interactions from unpaired spin density on the ligand do not contribute importantly.

Sites of Mn(II) binding to molecules such as nucleic acid bases, nucleosides and their phosphates, histidine and derivatives, and other amino acids and peptides have often been characterized by selective broadening of resonance lines in nuclear magnetic resonance spectroscopy due to hydrogen and carbon-13 atoms that are near to the presumed metal ion binding site. It is the purpose of this paper to assess the validity of selective broadening results with Mn(II) on a variety of small ligands. Previously we have shown that there are severe limitations to use of selec-

tive broadening with Cu(II);[1,2] this paper reports a parallel study with Mn(II).

Implicit in identification of metal ion binding sites by selective broadening experiments are two assumptions. In the first, the paramagnetic ion induced line broadening which is proportional to the inverse transverse relaxation time in the presence of paramagnetic ion, T_{2P}^{-1}, is given only by the first term in parentheses in eq 1 so that the fast exchange limit applies.[2-4]

$$T_{2P}^{-1} = pq(T_{2M}^{-1} + \tau_M \Delta\omega_M^2) \quad (1)$$

In eq 1, p is the ratio of molar concentrations of paramagnetic ion to ligand (typically 10^{-2} or less), q is the average number of ligands bound in an identical way, T_{2M} is the transverse relaxation time of the bound ligand, τ_M is the mean lifetime of a ligand bound to the metal ion, and $\Delta\omega_M$ is the chemical shift between bound and unbound ligand resonances. When the second term in eq 1 is dominant, the intermediate exchange limit applies and the information required from T_{2M}^{-1} is lost. For other restrictions involved in eq 1 see ref 2-4.

In the second assumption, the inverse transverse relaxation time for a nucleus on the bound ligand is given only by the first or dipolar term in eq 2, while the second or scalar term is negligible.[2-4]

$$T_{2M}^{-1} = 7a\tau_c r^{-6} + bA^2\tau_e \quad (2)$$

In eq 2, $a = \gamma_I^2 g^2 \beta^2 S(S+1)/15$, τ_c is the correlation time modulating the dipolar interaction, r is the distance between the paramagnetic ion and the measured nucleus, $b = S(S+1)/3\hbar^2$, A is the scalar or hyperfine coupling constant, which is generally different for each ligand nucleus, and τ_e is the correlation time modulating the scalar interactions. Only when the first or dipolar term of eq 2 dominates does the r^{-6} dependence appear and furnish the basis for stating that lines from nuclei nearest to the paramagnetic ion are most broadened.

In order for a selective broadening experiment to designate the site of paramagnetic metal ion binding to a ligand, only the first terms of both eq 1 and 2 should be dominant. Not only must the fast exchange limit apply, but the dipolar term should exceed the scalar term. A test for dominance of these two terms is to compare the value of T_{2P}^{-1} determined from line broadening to the spin-lattice relaxation time due to the paramagnetic ion, T_{1P}^{-1}, obtained from pulsed NMR experiments. There is no intermediate exchange region for T_{1P}^{-1}, and the scalar term is almost always negligible so that

$$T_{1P}^{-1} = pqT_{1M}^{-1} = pq6a\tau_c r^{-6} \quad (3)$$

Combination of the first terms of eq 1 and 2 with eq 3 yields

$$T_{1P}/T_{2P} = 7/6 = 1.17 \quad (4)$$

Equation 4 is valid only for predominance of the dipolar term in the fast exchange limit. Values greater than 7/6 for the ratio of eq 4 indicate that the fast exchange limit of eq 1 is not attained and/or that the dipolar term of eq 2 is not predominant. In the fast exchange limit, 50% dipolar and 50% scalar contributions to T_{2M}^{-1} yields $T_{1P}/T_{2P} = 7/3 = 2.33$. Thus ratios greater than 2.33 indicate that the dipolar term is no longer the dominant contributor to paramagnetic ion induced line broadening.[1,2] A 2:1 dipolar to scalar contribution yields $T_{1P}/T_{2P} = 7/4 = 1.75$. Hence, the ratio need not be much greater than 1.17 for the scalar term in eq 2 to be significant.

The main paramagnetic metal ion considered in this paper is Mn(II). For complexes of Mn(II) the inverse scalar correlation time is nearly equal to the inverse electron spin relaxation time, $\tau_e^{-1} \simeq \tau_s^{-1} \simeq 10^8$ sec^{-1}. Since the ligands studied were small, the inverse dipolar correlation time is nearly that of the inverse rotational correlation time of the complex $\tau_c^{-1} \simeq \tau_R^{-1} \simeq 10^{10}$ sec^{-1}.

Experimental Section

High quality commercial ligands were prepared in D_2O solvent at concentrations of 0.1–0.5 M for the proton and 2 M for the carbon-13 experiments. Carboxylic acid ligands were about 75% ionized, amine ligands about half-neutralized, and amino acid ligands had their amine half-neutralized. Magnetic resonance experiments were performed at 23.5 kG on a JEOL PFT-100P/EC 100 FT-NMR spectrometer. Relaxation times in presence of paramagnetic ion were calculated from

$$T_{1P}^{-1} = (T_{1P}^{-1})_{Mn} - (T_{1P}^{-1})_0$$

where the terms on the right are the inverse spin–lattice relaxation times with and without Mn(II), respectively, and

$$T_{2P}^{-1} = \pi(W_{Mn} - W_0)$$

where W_{Mn} and W_0 are the full line width in Hz at half-height with and without Mn(II), respectively. T_1 values were measured accurately (±10%) with a 180°–τ–90° pulse sequence and calculated by an external least-squares fit program. Linear first-order plots indicated exponential decays. Other details have already been supplied elsewhere.[2] When T_{1P}/T_{2P} is near 7/6, the ratio may be difficult to determine accurately due to the lack of significant broadening.

Results

Table I lists inverse spin–lattice and transverse relaxation times for hydrogen and carbon-13 nuclei determined for each nucleus on a single solution for a series of ligands in the presence of Mn(II). Representative $[Mn^{2+}]/[ligand]$ ratios for a single experiment are also presented, but experiments were performed over a range of Mn(II) concentrations. Ratios of T_{1P}^{-1} or T_{2P}^{-1} to $[Mn^{2+}]/[ligand]$ reveal the sensitivity of the two inverse relaxation times to Mn(II) concentration. Thus, for a specified amount of Mn(II), lesser broadening (T_{2P}^{-1}) occurs for the unidentate carboxylates than for the other ligands in Table I.

Imidazole was studied with four paramagnetic divalent first row transition metal ions and the results are shown in Table II. In addition to the T_{1P}/T_{2P} ratios for each metal ion for protons and carbon-13, T_{1P}^{-1} and the scalar coupling constant, A, are tabulated for the ratio of the nucleus at the 2 position to the average of the two nuclei at the 4 and 5 positions. The scalar coupling constant ratios were evaluated by assuming the fast exchange limit in eq 1 and combining with eq 2 and 3 to obtain

$$T_{2P}^{-1} = 7T_{1P}^{-1}/6 + pqbA^2\tau_e$$

from which A ratios may be calculated.

Discussion

More than half the ligands of Table I exhibit T_{1P}/T_{2P} values greater than 2.3, indicating that the dipolar term of

TABLE I: Spin–Lattice and Transverse Relaxation Times in Presence of Mn(II)

Ligand		$10^4[Mn^{2+}]/[ligand]$	T_{1P}^{-1}, sec^{-1}	T_{2P}^{-1}, sec^{-1}	T_{1P}/T_{2P}
		Protons			
Acetate		15	4.4	13.1	3.0
Chloroacetate		22	4.9	11.6	2.4
Malonate		1.5	4.5	16.5	3.7
Succinate		24	21	34	1.6
1,2-Diaminoethane		7.1	6.0	39	6.5
Glycinate		5.8	27	45	1.7
Sarcosinate	CH_2	2.8	5.4	21	3.9
	CH_3		5.7	33	5.8
N,N-Dimethylglycinate	CH_2	3.6	13.7	18.3	1.3
	CH_3		15.1	34	2.3
L-Methionine	CH	0.8	7.7		
	SCH_2		1.8	7.9	4.4
	CH_3		0.17		
	CH_3	6.4	1.5	2.9	1.9
S-Methyl-L-cysteine	CH	1.1	11.5		
	CH_2		4.8		
	CH_3		0.74	4.3	5.8
Glycylglycinate	CH_2COO^-	5.1	4.2	7.9	1.9
	CH_2NH_2		13.5	21	1.6
Imidazole	H2	3.0	6.3	16.5	2.6
	H4, H5		3.4	15.8	4.6
5′-AMP	H8	1.2	18.2	24	1.3
	H2	3.6	6.5	9.8	1.5
		Carbon-13			
Glycinate	CH_2	4.5	8.9	11.0	1.2
	COO^-	0.7	1.0	4.7	4.7
Imidazole	C2	0.09	0.35	37	106
	C4, C5		0.16	22	140

TABLE II: Ratios of Relaxation Times for Imidazole in Presence of Metal Ions

Metal ion	T_{1P}/T_{2P} H2	T_{1P}/T_{2P} H4, H5	T_{1P}^{-1} H2/H4, H5	A H2/H4, H5
Mn(II)	2.6	4.6	1.8	0.88
Co(II)	6.0	17	1.9	0.77
Ni(II)	4.2	9.2	2.0	0.88
Cu(II)	21	48	1.7	0.85
	C2	C4, C5	C2/C4, C5	C2/C4, C5
Mn(II)	106	140	2.1	1.28
Cu(II)	500	460	1.4	1.25

eq 2 contributes less than 50% to the broadening of proton lines. Therefore, the use of selective broadening by Mn(II) to ascertain the site of ligand binding is subject to severe limitations, as the r^{-6} term is only a minor contributor to broadening in most cases. In only one-third of the cases in Table I does the dipolar term contribute 2/3 to broadening. Since the requisite frequency and temperature dependent studies have not been performed, it is uncertain whether the limitation on greater dipolar contributions is due to the intermediate exchange second term of eq 1 or the scalar term of eq 2, but it is more likely to be the latter in most cases. Whatever the reason, the fact that the dipolar term is seldom a predominant contributor to broadening renders suspect arguments of Mn(II) site binding dependent upon the dipolar r^{-6} dependence between the paramagnetic ion and the affected nuclei.

Compared to the proton T_{1P}/T_{2P} values found for Cu(II),[1,2] those for Mn(II) are similar for carboxylate ligands and much lower for amine donors. The scalar contribution to broadening is much greater for aliphatic amines bound to Cu(II) than to Mn(II). With adenosine monophosphate (AMP) the interaction with Mn(II) is mainly dipolar while that with Cu(II) is predominantly scalar. A greater proportion of Mn(II) than Cu(II) will be at the phosphate rather than the adenine, however.

Since eq 3 for T_{1P}^{-1} does not contain intermediate exchange or scalar terms, determination of the spin–lattice relaxation time should allow derivation of distance information as $r^6 \sim T_{1P}$. The sixth root of ratios of T_{1P} of two nuclei in the same complex should relate relative distances of these two nuclei to the paramagnetic metal ion in selective T_1 experiments. Nearly identical T_{1P} values for the two kinds of protons in both sarcosinate and dimethylglycinate indicate Mn(II) binding at the amino group. From the T_{1P}^{-1} values in Table I for L-methionine, the methyl protons are 1.5 and 1.9 times as far from the Mn(II) as the SCH_2 and CH protons, respectively. For *S*-methyl-L-cysteine the methyl protons are 1.4 and 1.6 times as far from the Mn(II) as the CH_2 and CH protons, respectively. Allowing for conformational mobility in the side chain, these results indicate that, at these high ligand to Mn(II) ratios, the ligands chelate to the Mn(II) as substituted glycinates with the ether sulfurs unbound. For the case of Cu(II) the same conclusion was reached for methionine, but for *S*-methylcysteine it was suggested that a weak interaction may occur with the ether sulfur while Cu(II) is chelated at the glycinate locus.[2]

For C-13, the T_{1P}/T_{2P} ratio of 1.24 for the CH_2 carbon of glycinate suggests a nearly wholly dipolar interaction. For imidazole the T_{1P}/T_{2P} ratios are $\geq$100 for both carbons, suggesting predominant scalar interactions in this system. Selective broadening experiments designed to locate the Mn(II) binding sites by C-13 NMR in aromatic ligands such as imidazole derivatives and nucleic acids are suspect since the broadening does not depend on r^{-6}. Since the hy-

perfine constants vary for each carbon, the scalar interactions are apt to vary at each carbon about the ring. Even larger T_{1P}/T_{2P} ratios are found for Cu(II) and the carbons of glycinate and imidazole.[2]

The T_{1P}/T_{2P} ratios for complexes of imidazole with several metal ions reported in Table II indicate that the dipolar term is never dominant. It has been established that the main contributor to the high ratio for protons for Cu(II) is the scalar term of eq 2.[2] The ratios of the scalar coupling constants are quite constant for H2/H4, H5 for Mn(II), Ni(II), and Cu(II). This result suggests that unpaired spin densities are distributed in similar ratios about the imidazole ring for each of the three metal ions. A constant ratio is also obtained for C2/C4, C5 for Mn(II), and Cu(II). This ratio is different than that found for protons since the scalar coupling constants are generally different for different nuclei.

In contrast to the constancy of the scalar coupling constant ratios for imidazole complexes of Mn, Ni, and Cu ions in Table II, the T_{1P}^{-1} ratios are not constant for either the proton or carbon-13 nuclei. Constant nucleus 2/nuclei 4, 5 ratios are expected if the only dipolar interaction is that between the paramagnetic metal ion and the affected nucleus. Small differences in imidazole–metal ion bond lengths[5] are unable to account for the discrepancies and it is unlikely that other differences in geometry would do so. Rather, the lack of constancy of the T_{1P}^{-1} ratios lends further support to the suggestion that additional dipolar terms are important.[2] As was pointed out for Cu(II) and imidazole, a small amount of unpaired spin density at C5 is much closer to H5 than is the large unpaired spin density on the Cu(II) bound at N3. As a result of the strong r^{-6} dependence, the small amount of unpaired spin density at C5 is likely to be the major contributor to relaxation at H5. This kind of occurrence should also apply to other paramagnetic metal ion complexes.

Selective broadening is severely compromised because the dipolar term makes only a minority contribution to broadening in many cases. Selective T_1 experiments according to eq 3 may enable the requisite distance information to be determined. However, if selective T_1 arguments are employed to estimate distances, it must be established that the predominant dipolar interaction contributing to relaxation is that between the paramagnetic ion and affected nucleus as other more local interactions from unpaired spin density on the ligand may contribute importantly to relaxation and result in significant errors.[6]

References and Notes

(1) W. G. Espersen, W. C. Hutton, S. T. Chow, and R. B. Martin, *J. Am. Chem. Soc.*, **96**, 8111 (1974).
(2) W. G. Espersen and R. B. Martin, *J. Am. Chem. Soc.*, in press.
(3) T. J. Swift and R. E. Connick, *J. Chem. Phys.*, **37**, 307 (1962); **41**, 2553 (1964).
(4) R. A. Dwek, R. J. P. Williams, and A. V. Xavier in "Metal Ions in Biological Systems", Vol. 4, H. Sigel, Ed., Marcel Dekker New York, N.Y., 1974, Chapter 3.
(5) R. J. Sundberg and R. B. Martin, *Chem. Rev.*, **74**, 471 (1974).
(6) This research was supported by two grants from the National Science Foundation, one from the molecular biology section and the other from the chemistry section for the purchase of the NMR instrument.

Optical Activity of d–d Transitions in Copper(II) Complexes of Amino Acids, Dipeptides, and Tripeptides. Dynamical Coupling Model

R. W. Strickland and F. S. Richardson*

Department of Chemistry, University of Virginia, Charlottesville, Virginia 22901 *(Received July 17, 1975)*

Publication costs assisted by the Petroleum Research Fund

The chiroptical properties associated with the d–d transitions in dissymmetric Cu^{2+}–amino acid, –dipeptide, and –tripeptide complexes are calculated on a theoretical model based on an independent systems representation of the electronic structure in these complexes. The metal ion and fragments within the ligand environment are treated as independent subsystems to zeroth order in the model and interactions between these subsystems are then treated by perturbation techniques. Wave functions for the d–d excited states of the Cu^{2+} ion are calculated to second order in perturbation theory. Rotatory strength expressions for the d–d transitions are developed to first, second, and third order in perturbation coefficients and these expressions are used in carrying out calculations. In evaluating the interaction energies between subsystems in our model we retain only the dynamical coupling terms resulting from the correlation of electron motion on the interacting groups. Static coupling mechanisms are not admitted into the model. The dynamical coupling terms are assumed to arise from electric quadrupole (metal)–electric dipole (ligand), electric hexadecapole (metal)–electric dipole (ligand), and electric dipole (ligand)–electric dipole (ligand) interactions between transition densities localized on the various subsystems. The rotatory strengths calculated for the Cu^{2+} d–d transitions are correlated with various structural features of the complexes studied and possible spectra–structure relationships are discussed.

I. Introduction

A considerable number of studies on the chiroptical properties of complexes formed between transition metal ions and amino acid, dipeptide, and tripeptide ligands have been reported in the literature.[1,2] These studies are of special interest for developing chiroptical spectroscopy as a probe of the structural characteristics of metal ion binding

sites in complex biomolecular systems. The spectra–structure relationships discovered for the model metal ion–amino acid, –dipeptide, and –tripeptide systems are expected to be at least qualitatively applicable to spectra–structure correlations in metalloenzymes and metal–protein complexes.

Several of the studies on the chiroptical properties of metal ion–amino acid and –peptide systems have led to the formulation of empirically based spectra–structure relationships which are remarkably successful in correlating the data obtained on various series of similar systems. Additionally, in a few instances these relationships have been interpreted directly in terms of extant theoretical models of molecular optical activity.[1] Of special note is the "hexadecant sector rule" proposed and applied by Martin and coworkers[1] in interpreting the circular dichroism (CD) spectra of a large number of metal ion–amino acid and –peptide complexes. This sector rule derives directly from the one-electron, static coupling model of molecular optical activity as described by Schellman[3] and as elaborated upon by Mason[4,5] and by Richardson.[6,7] Most of the attention in developing spectra–structure relationships for chiral transition metal complexes has been placed on the CD spectra associated with the metal ion d–d transitions. These transitions generally fall within an easily accessible region of the spectrum, generally exhibit relatively large dissymmetry factors ($\Delta\epsilon/\epsilon$), and are more readily amenable to theoretical analysis than are the less well characterized metal–ligand charge-transfer and ligand–ligand transitions.

Despite the widely acknowledged utility and the apparent reliability of the spectra–structure relationships proposed for chiral metal ion–amino acid and –peptide complexes, a detailed theoretical examination of the optical activity exhibited by the d–d transitions in these systems has not yet been reported. Such an examination is of interest not only for supplying a theoretical foundation for spectra interpretation but also for investigating and testing the current theories of optical activity in chiral transition metal complexes. The theory of optical activity in transition metal complexes has been studied intensively over the past 15 years, but a fully satisfactory theory or model capable of providing widely applicable and reliable spectra–structure correlations has not yet emerged. The metal ion–amino acid and –peptide complexes provide excellent model systems for testing and investigating the current theories.

Chirality in transition metal complexes is generally attributed to one or more of the following structural features: (1) chiral distortions within the metal ion–donor atom cluster ("inherent dissymmetry" within the d–d chromophore); (2) chiral distributions of chelate rings about the metal ion ("configurational dissymmetry"); (3) chiral conformations of chelate rings ("conformational dissymmetry"); and (4) asymmetric centers within the ligands (including, in some cases, asymmetric donor atoms). Most theoretical analyses and sector rule applications have focused on the latter three sources of chirality, although the possible importance of inherent dissymmetry within the metal ion–donor atom cluster of six-coordinate Co^{3+} and Cr^{3+} complexes has also been examined in several recent studies.[8–10]

In the present study we are concerned with the optical activity of the d–d transitions in Cu^{2+}–amino acid and –peptide complexes. Crystal structure data[1,11] reveal that the Cu^{2+}–donor atom cluster in these systems is approximately symmetrical (achiral) and that the chelate rings are not dissymmetrically distributed about the metal ion. The d–d optical activity of these systems must arise, then, from conformational dissymmetry within the chelate rings and (or) from vicinal interactions between the metal ion and asymmetric centers in the ligand environment. In the present study we shall neglect both configurational dissymmetry and inherent dissymmetry (within the metal ion–donor atom cluster) as sources of optical activity. It is highly likely that there exists considerable (or, at least, nonnegligible) inherent dissymmetry within the metal ion–donor ion clusters characteristic of metal binding sites in many biological macromolecules. The influence of this type of chiral distortion upon Cu^{2+} d–d optical activity will be presented in a separate report.[12]

We employ an independent systems model in this study to calculate the d–d rotatory strengths of various Cu^{2+}–amino acid, –dipeptide, and –tripeptide complexes. The application of this type of model in calculating molecular optical activity has been elaborated upon by several workers and the details of the method will not be discussed here.[3–10,13–15] Of special relevance to the calculations reported here are the work of Höhn and Weigang[13] and of Mason and co-workers.[4,5] We calculate the purely *electronic* contributions to the d–d rotatory strengths and ignore possible effects arising from vibronic interactions. Neglect of vibronic interactions precludes quantitative prediction of CD spectra since for many of the systems studied here rather substantial pseudo-Jahn–Teller (PJT) interactions are expected between the nearly degenerate (in some cases) d–d excited states. The possible influence of PJT interactions on the chiroptical spectra of systems with nearly degenerate electronic states has been examined elsewhere.[16–18] In these previous studies it was concluded that such interactions do not invalidate spectra–structure relationships based on "net" rotatory strengths associated with the interacting states. The role of the Herzberg–Teller (HT) vibronic coupling mechanism in determining CD spectral features has been investigated in some detail by Weigang and co-workers. However, the influence of HT type vibronic interactions on the chiroptical spectra of coordination compounds has not been subjected to thorough study. Neglect of vibronic interactions in the present study should have little effect on the qualitative or semiquantitative aspects of spectra–structure correlation; it does, however, preclude detailed spectra prediction.

II. Theory

A. *Basic Model.* Within the approximations of the independent systems model we partition the metal complexes into three parts: (A) an idealized ML_4Z_2 metal ion (M)–donor atom (L or Z) cluster (including all metal electrons and σ-ligating electrons) with exact D_{4h} symmetry; (B) the π-electron systems of the donor atoms or groups; and (C) the nondonor atoms or groups of the complex. In the metal ion–amino acid and –peptide complexes of interest here the Z donor atoms lie along the C_4 symmetry axis of the ML_4Z_2 cluster, and the (B) subsystems include the amide and/or carboxylate ligand moieties. The electronic Hamiltonian of the overall system is partitioned as follows

$$H = h_A + h_B + h_C + V_A + V_{AB} + V_{AC} + V_{BC} \quad (1)$$

where h_A, h_B, and h_C represent zeroth-order electronic Hamiltonian operators for the (A), (B), and (C) subsystems, respectively, V_A represents a local distortion poten-

tial within the ML_4Z_2 cluster to accommodate deviations from strict D_{4h} symmetry, and V_{AB}, V_{AC}, and V_{BC} are pairwise interaction potentials operative among the three subsystems of the complex.

Adopting a perturbation approach we rewrite eq 1 as

$$H = h_A + h_B + h_C + V = H^0 + V \tag{2}$$

where the operator, $V = V_A + V_{AB} + V_{AC} + V_{BC}$, is treated as a perturbation on the eigenstates of the operator, $H^0 = h_A + h_B + h_C$. To zeroth order, the electronic states of the system are written as

$$\psi^0_{\alpha\beta\gamma} = |A_\alpha B_\beta C_\gamma\rangle$$

where A_α, B_β, and C_γ are eigenfunctions of h_A, h_B, and h_C, respectively. The ground state is designated by ψ^0_{000}, an excited state localized on ML_4Z_2 is denoted by $\psi^0_{\alpha 00}$, an excited π state localized on a (B) subsystem is represented by $\psi^0_{0\beta 0}$, and an excited state localized on a (C) subsystem is given by $\psi^0_{00\gamma}$. To first order in perturbation theory, the electronic wave function for an excited state ($\alpha 00$) is given by

$$\psi_{\alpha 00} = \psi^0_{\alpha 00} + \sum_{\alpha' \neq \alpha} \langle\psi^0_{\alpha' 00}|V|\psi^0_{\alpha 00}\rangle \psi^0_{\alpha' 00}/\Delta E^0_{\alpha\alpha'} + \sum_{\beta} \langle\psi^0_{0\beta 0}|V|\psi^0_{\alpha 00}\rangle \psi^0_{0\beta 0}/\Delta E^0_{\alpha\beta} + \sum_{\gamma} \langle\psi^0_{00\gamma}|V|\psi^0_{\alpha 00}\rangle \psi^0_{00\gamma}/\Delta E^0_{\alpha} \tag{3}$$

where ΔE^0_{ij} represents the energy difference between zeroth-order states i and j. Doubly excited configurational states are excluded from the expansion given in eq 3.

Equation 3 for the first-order wave functions is correct only if we neglect exchange interactions between the electronic distributions of the three subsystems (A), (B), and (C). This formulation allows for dynamical excitation (energy) exchange interactions and for static Coulombic interactions between the subsystems, but it excludes charge exchange (or charge-transfer) interactions. In the systems of interest in the present study, charge-transfer (CT) between the (B) subsystems and the ML_4Z_2 cluster may be of significant importance in determining the spectroscopic properties of electronic transitions primarily localized within the ML_4Z_2 chromophore. To include these specific CT processes we relax the independent systems approximation, include CT states in our basis set of zeroth-order states, introduce an electron-exchange term into V_{AB}, and add an interaction term V_{CD} to V which represents the interaction between subsystems (C) and the CT states of the composite group D = AB. Now, in addition to the excited states $|A_\alpha B_0 C_0\rangle$, $|A_0 B_\beta C_0\rangle$, and $|A_0 B_0 C_\gamma\rangle$, we also have CT states of the type $|A_\delta B_\delta C_0\rangle = |D_\delta C_0\rangle$, in which an electron has been transferred out of a configuration on (A) and into one on (B) or vice versa. Equation 3 can now be rewritten as

$$\psi_{\alpha 00} = \psi^0_{\alpha 00} + \sum_{\alpha' \neq \alpha} \langle\psi^0_{\alpha' 00}|V|\psi^0_{\alpha 00}\rangle \psi^0_{\alpha 00}/\Delta E^0_{\alpha\alpha'} + \sum_{\beta} \langle\psi^0_{0\beta 0}|V|\psi^0_{\alpha 00}\rangle \psi^0_{0\beta 0}/\Delta E^0_{\alpha\beta} + \sum_{\gamma} \langle\psi^0_{00\gamma}|V|\psi^0_{\alpha 00}\rangle \psi^0_{00\gamma}/\Delta E^0_{\alpha} + \sum_{\delta} \langle\psi^0_{\delta 0}|V|\psi^0_{\alpha 00}\rangle \psi^0_{\delta 0}/\Delta E^0_{\alpha\delta} \tag{4}$$

In the present study we set the ground state wave function of H equal to the lowest eigenstate of H^0 (that is, $\psi_{000} = \psi^0_{(000)}$). The excited states, however, were expressed to *second order* in the basis ($\psi^0_{\alpha 00}$, $\psi^0_{0\beta 0}$, $\psi^0_{00\gamma}$, $\psi^0_{\delta 0}$). The electric and magnetic dipole transition moments associated with transitions (000) → ($\alpha 00$) were expressed to second order (in perturbation coefficients), and the electronic rotatory strengths

$$R_{000,\alpha 00} = \mathrm{Im}\,\langle\psi_{000}|\hat{\mu}|\psi_{\alpha 00}\rangle \cdot \langle\psi_{\alpha 00}|\hat{m}|\psi_{000}\rangle \tag{5}$$

were also expressed to second order.

B. *Interaction Matrix Elements.* Assuming exact D_{4h} symmetry for the ML_4Z_2 cluster and neglecting V_A, the following interaction matrix elements appear in our second-order expressions for the $\psi_{\alpha 00}$ wave functions:

$$V_{\alpha\alpha'} = \langle\psi^0_{\alpha 00}|V_{AB} + V_{AC}|\psi^0_{\alpha' 00}\rangle \tag{6a}$$

$$V_{\alpha\beta} = \langle\psi^0_{\alpha 00}|V_{AB}|\psi^0_{0\beta 0}\rangle \tag{6b}$$

$$V_{\alpha\gamma} = \langle\psi^0_{\alpha 00}|V_{AC}|\psi^0_{00\gamma}\rangle \tag{6c}$$

$$V_{\beta\gamma} = \langle\psi^0_{0\beta 0}|V_{BC}|\psi^0_{00\gamma}\rangle \tag{6d}$$

$$V_{\alpha\delta} = \langle\psi^0_{\alpha 00}|V_{AB}|\psi^0_{\delta 0}\rangle \tag{6e}$$

$$V_{\beta\delta} = \langle\psi^0_{0\beta 0}|V_{AB}|\psi^0_{\delta 0}\rangle \tag{6f}$$

$$V_{\gamma\delta} = \langle\psi^0_{00\gamma}|V_{CD}|\psi^0_{\delta 0}\rangle \tag{6g}$$

The interaction term, $V_{\alpha\alpha'}$, arises from "static" coupling between the chromophore (A) and the ligand subsystems (B) and (C). That is, this term reflects the interaction between static ground state charge distributions on (B) and (C) with transition densities ($\psi^0_{\alpha 00}\psi^0_{\alpha' 00}$) localized on the ML_4Z_2 chromophore. The static, one-electron theory of optical activity in metal complexes is based upon this type of interaction[4-9] and the sector (or regional) rules most commonly used in interpreting the CD spectra of chiral coordination compounds derive from this type of interaction.[1,2] This term should indeed dominate or contribute significantly in those cases where the ligand groups which confer chirality upon the complex are charged or are highly polar. In those cases where the chirality derives from ligand groups which are uncharged and nonpolar, one may expect the $V_{\alpha\alpha'}$ type interaction to be of considerably lesser importance in determining the optical activity of transitions localized on ML_4Z_2.

The interaction terms (6b–e) arise from "dynamical" couplings between transition densities localized on two different subsystems of the complex. For example, $V_{\alpha\beta}$ represents the electrostatic energy of interaction between a transition density ($\psi^0_{\alpha 00}\psi^0_{000}$) localized on (A) and a transition density ($\psi^0_{0\beta 0}\psi^0_{000}$) localized on (B). These terms contribute to the so-called dynamical coupling (DC) mechanism of molecular optical activity. The static coupling (SC) term (6a) involves the dynamical behavior of just one electron; the rest of the electrons in the system are assumed to provide an average, or static, field in which the "one electron" must move. The dynamical coupling terms, on the other hand, arise from the correlated motions of two or more electrons located in different subsystems of the complex.[13] In the present study we consider only the dynamical coupling terms in calculating the rotatory strengths of transitions localized on ML_4Z_2.

In calculating the DC terms (6b–e), we restrict the ($\psi^0_{\alpha 00}$) basis set to d–d states of the ML_4Z_2 cluster and represent the (B) and (C) subsystems as spatial arrays of electric-dipole oscillators. That is, the basis states ($\psi^0_{0\beta 0}$) and ($\psi^0_{00\gamma}$) are chosen so that the transitions (000) → ($0\beta 0$) and (000) → (00γ) are electric dipole allowed and are localized within the (B) and (C) subsystems, respectively. The d–d transi-

tions are represented as electric quadrupole and electric hexadecapole oscillators. The terms (6b) and (6c), then, have the following components: (6b) electric quadrupole (A)–electric dipole (B) + electric hexadecapole (A)–electric dipole (B) interactions; (6c) electric quadrupole (A)–electric dipole (C) + electric hexadecapole (A)–electric dipole (C) interactions. The charge-transfer transitions (000) → (δ0) are represented as electric dipole oscillators localized within the composite (AB) = (D) group.

On our model the (000) → (α00) transitions are electric dipole forbidden by parity. However, certain transitions within this set may be magnetic dipole allowed. On the other hand, the transitions (000) → ($0\beta0$), (000) → (00γ), and (000) → (δ0) were selected to be pure electric dipole transitions. Consequently, nonvanishing values of $R_{000,\alpha00}$ arise entirely from coupling of the magnetic dipole oscillators on (A) with electric dipole oscillators located in the (B), (C), or (D) subsystems. This mechanism for generating optical activity within the independent systems model (modified in the present case to include CT interactions) corresponds to what Schellman has termed the μ·m coupling mechanism for magnetic dipole allowed–electric dipole forbidden transitions.[15]

C. *Rotatory Strengths.* Given the model and approximations discussed in sections IIA and IIB, the rotatory strength of a transition (000) → (α00) may be expressed as

$$R_{000,\alpha00} = \mathrm{Im}\,(\boldsymbol{P}_{000,\alpha00} \cdot \boldsymbol{M}_{\alpha00,000}) \tag{7}$$

where

$$\boldsymbol{P}_{000,\alpha00} = \sum_{\beta}[V_{\alpha\beta} + \sum_{\gamma} V_{\alpha\gamma}V_{\gamma\beta}/\Delta E^0_{\alpha\gamma} + \sum_{\delta} V_{\alpha\delta}V_{\delta\beta}/\Delta E^0_{\alpha\delta}]\boldsymbol{P}^0_{0\beta}/\Delta E^0_{\alpha\beta} + \sum_{\gamma}[V_{\alpha\gamma} + \sum_{\beta} V_{\alpha\beta}V_{\beta\gamma}/\Delta E^0_{\alpha\beta} + \sum_{\delta} V_{\alpha\delta}V_{\delta\gamma}/\Delta E^0_{\alpha\delta}]\boldsymbol{P}^0_{0\gamma}/\Delta E^0_{\alpha\gamma} + \sum_{\delta}[V_{\alpha\delta} + \sum_{\gamma} V_{\alpha\gamma}V_{\gamma\delta}/\Delta E^0_{\alpha\gamma} + \sum_{\beta} V_{\alpha\beta}V_{\beta\delta}/\Delta E^0_{\alpha\beta}]\boldsymbol{P}^0_{0\delta}/\Delta E^0_{\alpha\delta} \tag{8}$$

and

$$\boldsymbol{M}_{\alpha00,000} = \boldsymbol{M}^0_{\alpha0} + \sum_{\alpha'\neq\alpha}\left[\sum_{\beta} V_{\alpha\beta}V_{\beta\alpha'}/\Delta E^0_{\alpha\beta} + \sum_{\gamma} V_{\alpha\gamma}V_{\gamma\alpha'}/\Delta E^0_{\alpha\gamma} + \sum_{\delta} V_{\alpha\delta}V_{\delta\alpha'}/\Delta E^0_{\alpha\delta}\right]\boldsymbol{M}^0_{\alpha'0}/\Delta E^0_{\alpha\alpha'} \tag{9}$$

The symbols $\boldsymbol{P}^0$ and $\boldsymbol{M}^0$ refer, respectively, to zeroth-order electric and magnetic dipole transition moments associated with local transitions within the subsystems (A_α, B_β, C_γ, and D_δ). Note that the perturbed electric dipole transition moment $\boldsymbol{P}_{000,\alpha00}$ includes only first- and second-order terms since $\boldsymbol{P}^0_{0\alpha} = 0$ for all α (pure d–d states). Also note that the perturbed magnetic dipole transition moment $\boldsymbol{M}_{\alpha00,00}$ includes only zeroth and second order terms since in our model, $\boldsymbol{M}^0_{\beta0} = \boldsymbol{M}^0_{\gamma0} = \boldsymbol{M}^0_{\delta0} = 0$, for all β, γ, and δ. That is, magnetic dipole oscillators in the ligand environment are not admitted into our model; all perturbing oscillators are electric dipole oscillators.

Combining eq 7 and 8 and inserting them into eq 7 leads to first, second, third, and fourth order terms in the resulting rotatory strength expression. However, the expression is complete only to second order since the wave functions were developed only to second order. In computing $R_{000,\alpha00}$ we neglected all terms higher than third order in the perturbation matrix elements.

III. Structures

A. *Amino Acid Complexes.* The following bis amino acid complexes were studied: (1) *cis*- and *trans*-[Cu(*S*-Ala)$_2$], where Ala = alaninato ligand; (2) *cis*- and *trans*-[Cu(*S*-Pro)$_2$], where Pro = prolinato ligand; (3) *cis*- and *trans*-[Cu(*N*-CH_3-*S*-Ala)$_2$], where *N*-CH_3-*S*-Ala = *N*-methyl-*S*-alaninato ligand; and, (4) *cis*- and *trans*-[Cu(*N*-CH_3-*S*-Pro)$_2$], where *N*-CH_3-*S*-Pro = *N*-methyl-*S*-prolinato ligand.

The structure parameters for the chelate rings in the bis alanine complexes were adapted from crystal structure data on bis(glycinato)copper(II) monohydrate.[11] In both the cis and trans isomers each nonplaner chelate ring has the same chirality and the two chelate rings are related by a C_2 operation (about a C_2 axis perpendicular to the CuN_2O_2 coordination cluster in the trans isomer and about a C_2 axis lying in the plane of the CuN_2O_2 cluster in the cis isomer). Methyl groups were attached to the α-carbon atom of each glycinato ligand to generate the alaninato complexes. Calculations were carried out on structures in which the α-methyl substituents were disposed axial to the chelate rings and equatorial to the chelate rings.

The structure parameters for the bis proline complexes were generated from the crystal structure data reported for bis(DL-prolinato)copper(II) dihydrate.[11] The conformational geometry of the chelate ring formed by the L(*S*) configurational isomer of the prolinato ligand was adopted in the systems we examined. Both the cis and trans isomers of [Cu(*S*-Pro)$_2$] have exact C_2 point group symmetry.

The *cis*- and *trans*-[Cu(*N*-CH_3-*S*-Ala)$_2$] structures were generated by substituting a methyl group for a hydrogen atom on the amino group of each alaninato ligand of the bis alanine complexes. In the structures examined in this study, the *N*-methyl groups were disposed trans to the α-methyl groups. This trans arrangement of methyl substituents (on the amino nitrogen atom and the α-carbon atom of a single chelate ring) is sterically favored over the cis arrangement.

The *cis*- and *trans*-[Cu(*N*-CH_3-*S*-Pro)$_2$] structures were generated by substituting a methyl group for a hydrogen atom on the nitrogen atom of the pyrrolidine ring in each prolinato ligand.

B. *Dipeptide Complexes.* Three Cu^{2+}–dipeptide complexes were studied. These are (1) [Cu(AG)(H_2O)], where AG = *S*-alanylglycinato ligand; (2) [Cu(GA)(H_2O)], where GA = glycyl-*S*-alaninato ligand; and, (3) [Cu(AA)(H_2O)], where AA = *S*-alanyl-*S*-alaninato ligand. The structure parameters for the chelate rings in these systems were adapted from those reported for crystalline glycylglycinatocopper(II) trihydrate (obtained from x-ray diffraction data).[11] The AG, GA, and AA ligands each function as a tridentate chelate system via an amino group donor, a deprotonated peptide nitrogen donor, and a carboxyl group donor. The CuN_2O_2 (one oxygen atom from a water molecule) cluster forms a slightly distorted square. The chelate ring formed by the carboxyl and peptide groups is assumed to be exactly planer in our model structures, whereas the chelate ring formed by the peptide nitrogen and the terminal amino group is assumed to be flexible. Nonplaner conformations of the NH_2-terminal ring were generated by locating the C_α atom above or below the plane defined by the CuN_2O_2 coordination cluster. Nonplaner distortions of this ring also

moved the carbonyl oxygen atom out of the CuN_2O_2 plane and removed the plane of symmetry through the Cu–NH_2 group. The disposition of the C_α atom above (or below) the CuN_2O_2 plane also determines whether the α-methyl substituent is axial (or equatorial) to the chelate ring in the AG and AA complexes.

C. *Tripeptide Complexes.* Seven Cu^{2+}–tripeptide complexes were examined in this study. These are (1) $[Cu(AGG)]^-$, where AGG = *S*-alanylglycylglycinato ligand; (2) $[Cu(GAG)]^-$, where GAG = glycyl-*S*-alanylglycinato ligand; (3) $[Cu(GGA)]^-$, where GGA = glycylglycyl-*S*-alaninato ligand; (4) $[Cu(AAG)]^-$, where AAG = *S*-alanyl-*S*-alanylglycinato ligand; (5) $[Cu(AGA)]^-$, where AGA = *S*-alanylglycyl-*S*-alaninato ligand; (6) $[Cu(GAA)]^-$, where GAA = glycyl-*S*-alanyl-*S*-alaninato ligand; and (7) $[Cu(AAA)]^-$, where AAA = *S*-alanyl-*S*-alanyl-*S*-alaninato ligand. Each of these ligands functions as a tetradentate chelate system in which the amino group, the two deprotonated peptide nitrogen atoms, and the carboxyl group coordinate to the Cu^{2+} ion. The CuN_3O coordination cluster in these complexes is nearly square-planer. In our model systems, we assume that the two chelate rings involving the two peptide nitrogens and the carboxyl oxygen as donor atoms are exactly planer, and that the third chelate ring in which the terminal-NH_2 group is a donor can be either planer or nonplaner. Nonplanarity in the NH_2-terminal ring was generated by displacing the C_α atom away from the CuN_3O plane and allowing the carbonyl oxygen atom to also be distorted from this plane.

IV. Calculations and Results

A. *Amino Acid Complexes.* To carry out calculations based on the model described in section II the following input parameters are required: (1) energies of the d–d excited states (relative to the ground electronic state); (2) magnetic dipole transition moments of the various d–d transitions; (3) electric quadrupole and electric hexadecapole matrix elements connecting all the metal ion d–d states; (4) locations of the electric dipole oscillators representing various parts of the ligand environment; (5) magnitudes and polarizations of the electric dipole transition integrals associated with the perturbing oscillators; (6) energies of the perturbing oscillators; (7) energies and electric dipole transition integrals of the low-lying ligand → metal charge-transfer transitions.

For the bis alaninato complexes, the perturbing oscillators of the (B) subsystem were chosen to be associated with $\pi \rightarrow \pi^*$ transitions localized on the two carboxylate moieties of each complex. Just two such oscillators were chosen for each complex and these were assumed to have identical properties. Their energy was taken to be 55000 cm^{-1} and their magnitude was 3.0 D. They were positioned at the centers of the C=O carbonyl bonds and were assumed to be polarized along these bonds. Four C_γ type oscillators were assigned to each alaninato ligand, two associated with $\sigma \rightarrow \sigma^*$ transitions within the two N–H fragments of the amino group, one associated with a $\sigma \rightarrow \sigma^*$ transition in the C_α–H fragment, and one associated with a $\sigma \rightarrow \sigma^*$ transition within the C_α–CH_3 fragment. These oscillators were positioned at bond midpoints (N–H, C_α–H, and C_α–C) and each was assumed to be polarized along the appropriate bond axis. The energies and electric dipole moments associated with the corresponding transitions were assigned as follows: (1) N–H oscillators, E_γ = 70000 cm^{-1} and μ_γ = 2.0 D; (2) C_α–H oscillator, E_γ = 70000 cm^{-1} and μ_γ = 1.0 D; (3) C_α–CH_3 oscillator, E_γ = 65000 cm^{-1} and μ_γ = 1.5 D. Four D_δ oscillators were assigned to each bis alaninato complex. Two of these oscillators were polarized along the two Cu–O bond axes and were positioned at the midpoints of the Cu–O bonds. The energies and electric dipole moments of these D_δ oscillators were chosen to be E_δ = 35000 cm^{-1} and μ_δ = 2.0 D, respectively. The other two D_δ oscillators were positioned at the midpoints of the two Cu–N bonds and were directed along these bonds. The energies and dipole moments of these oscillators were chosen to be 40000 cm^{-1} and 2.0 D, respectively. Each of the perturbing oscillators, B_α, C_γ, and D_δ, was treated as a *point* dipole.

The electric quadrupole and electric hexadecapole matrix elements between the Cu^{2+} 3d orbitals were each calculated in the *point* multipole approximation and the double ζ 3d radial functions of Richardson et al.[19] were employed in calculating the necessary $\langle r^2 \rangle$ and $\langle r^4 \rangle$ radial integrals. The relative energies of the d–d excited states were taken to be different for the cis and trans isomers of $[Cu(S\text{-}Ala)_2]$. The relative ordering of the 3d orbitals in the trans complex was assumed to be[12] $3d_{x^2-y^2} > 3d_{z^2} > 3d_{xy} > 3d_{xz} > 3d_{yz}$ (the carboxyl oxygen donor atoms lying along the *x* axis). The relative ordering of the 3d orbitals in the cis complex was assumed to be[12] $3d_{x^2-y^2} > 3d_{z^2} > 3d_{xy} > 3d_{xz} = 3d_{yz}$. The d–d transition energies were as follows

	Trans	Cis
$3d_{x^2-y^2} \leftarrow 3d_{z^2}$	14000 cm^{-1}	14000 cm^{-1}
$\leftarrow 3d_{xy}$	15000 cm^{-1}	15000 cm^{-1}
$\leftarrow 3d_{xz}$	15500 cm^{-1}	16500 cm^{-1}
$\leftarrow 3d_{yz}$	18000 cm^{-1}	16500 cm^{-1}

The calculations and selection of the input parameters listed above are rather crude and approximate. The approximations and assumptions inherent in these selections of input parameters may seriously influence the *absolute* magnitudes of the computed chiroptical properties. However, the *relative* magnitudes and signs of the computed d–d rotatory strengths are expected to yield qualitatively correct and reliable spectra–structure correlations. In the present study we are most interested in qualitative spectra–structure relationships.

The parameter sets chosen for calculations on the bis *N*-methyl-*S*-alaninato complexes are identical with those employed for the bis *S*-alaninato complexes except that one N–H oscillator on each ligand is replaced with a N–CH_3 oscillator (E_γ = 70000 cm^{-1}, μ_γ = 2.5 D).

The bis *S*-prolinato and bis *N*-methyl-*S*-prolinato complexes were treated in exactly the same way as the bis *S*-alaninato and bis *N*-methyl-*S*-alaninato complexes except for the number of C_γ oscillators in the ligand environment. For each prolinato ligand, we added two $\sigma \rightarrow \sigma^*$ (C–C) C_γ type oscillators and a $\sigma \rightarrow \sigma^*$ (N–C) C_γ type oscillator to represent the pyrrolidine ring system. The C–C oscillators were assigned an energy of 65000 cm^{-1} and a dipole moment of 1.5 D; the N–C oscillator was assigned an energy of 70000 cm^{-1} and a dipole moment of 2.5 D. Each of these oscillators was assumed to be oriented along the corresponding bond axis and each was positioned at the appropriate bond midpoint and treated as a point dipole.

The d–d rotatory strengths calculated to second order on the model described in section II are listed in Table I for the eight bis amino acid complexes examined in this study.

B. *Dipeptide Complexes.* The same kinds of input parameters are required to carry out calculations on the di-

TABLE I: Computed d–d Rotatory Strengths for Amino Acid Complexes

Complex	$R(10^{-40}$ cgs) $(z^2) \rightarrow (x^2-y^2)$	$(xy) \rightarrow (x^2-y^2)$	$(xz) \rightarrow (x^2-y^2)$	$(yz) \rightarrow (x^2-y^2)$	Net[a]
trans-[Cu(*S*-Ala)$_2$][b]	0.70	−3.37	−4.69	2.17	−5.19
trans-[Cu(*S*-Ala)$_2$][c]	0.22	−3.19	−3.19	2.19	−4.69
cis-[Cu(*S*-Ala)$_2$][b]	0.96	−5.44	4.18	−2.22	−2.52
cis-[Cu(*S*-Ala)$_2$][c]	0.40	−4.11	4.20	−2.01	−1.52
trans-[Cu(*N*-CH_3-*S*-Ala)$_2$][b]	1.46	−10.88	−6.27	6.34	−9.35
trans-[Cu(*N*-CH_3-*S*-Ala)$_2$][c]	1.21	−8.41	−5.02	4.85	−7.37
cis-[Cu(*N*-CH_3-*S*-Ala)$_2$][b]	1.11	−6.82	−7.01	6.91	−5.81
cis-[Cu(*N*-CH_3-*S*-Ala)$_2$][c]	0.70	−5.46	−6.01	6.13	−4.64
trans-[Cu(*S*-Pro)$_2$]	0.95	9.68	18.64	−6.44	22.83
cis-[Cu(*S*-Pro)$_2$]	−0.91	−5.44	4.55	3.66	1.86
trans-[Cu(*N*-CH_3-*S*-Pro)$_2$]	0.78	−8.49	−9.91	4.92	−12.70
cis-[Cu(*N*-CH_3-*S*-Pro)$_2$]	0.11	−10.66	−11.77	8.44	−13.88

[a] Algebraic sum of d–d rotatory strengths. [b] Methyl substituents axial to chelate rings. [c] Methyl substituents equatorial to chelate rings.

TABLE II:

Complex	$R(10^{-40}$ cgs) $(z^2) \rightarrow (x^2-y^2)$	$(xy) \rightarrow (x^2-y^2)$	$(yz) \rightarrow (x^2-y^2)$	$(xz) \rightarrow (x^2-y^2)$	Net[a]
[Cu(AG)(H_2O)], P	0.41	−3.48	−2.95	−0.14	−6.16
NP_a	0.98	−3.64	−3.14	−0.95	−6.75
NP_e	0.12	−3.06	−2.74	0.54	−5.14
[Cu(GA)(H_2O)], P	0.11	−8.18	−4.14	−1.15	−13.36
NP_a	0.13	−8.28	−4.19	−1.28	−13.62
NP_e	0.10	−8.12	−4.06	−1.12	−13.20
[Cu(AA)(H_2O)], P	0.52	−11.66	−7.09	−1.29	−19.52
NP_a	1.11	−11.92	−7.33	−2.23	−20.37
NP_e	0.22	−11.18	−6.80	−0.58	−18.34

[a] Algebraic sum of d–d rotatory strengths.

peptide complexes as were required for the calculations performed on the amino acid complexes. However, the B_β, C_γ, and D_δ oscillator selections differ slightly for the dipeptide systems. Two B_β type oscillators were chosen for the dipeptides, one associated with a π–π^* excitation localized on the amide moiety and the other associated with a π–π^* excitation localized on the carboxylate moiety. The amide B_β oscillator was positioned at the midpoint of a line connecting the nitrogen (peptide) and oxygen atoms of the amide group and was directed along this line. The energy and dipole moment of this oscillator were assigned values of 60000 cm^{-1} and μ_β = 3.5 D, respectively. The carboxyl B_β oscillator was directed along the carbonyl C=O bond and was positioned at the midpoint of this bond. It was assigned an energy of 55000 cm^{-1} and a dipole moment of 3.0 D.

Four D_δ oscillators were employed in the dipeptide calculations. Their identities and properties are (1) Cu–N (amino group), E_δ = 40000 cm^{-1}, μ_δ = 2.0 D (along bond axis), located at bond midpoint; (2) Cu–N (peptide), E_δ = 30000 cm^{-1}, μ_δ = 2.0 D (along bond axis), located at bond midpoint; (3) Cu–O (carboxyl), E_δ = 35000 cm^{-1}, μ_δ = 2.0 D (along bond axis), located at bond midpoint; (4) Cu–O (water), E_δ 40000 cm^{-1}, μ_δ = 1.5 D (along bond axis), located at bond midpoint. The C_γ oscillators were chosen to be associated with $\sigma \rightarrow \sigma^*$ transitions localized in the C_α–H, C_α–CH_3, and N–H fragments of the overall dipeptide system. The properties of these oscillators were chosen to be identical with those selected for the amino acid complexes. All dipole oscillators in the B, C, and D subsystems were treated in the point dipole approximation.

The relative ordering of the 3d orbitals in the Cu^{2+}–dipeptide complexes was taken to be $3d_{x^2-y^2} > 3d_{z^2} > 3d_{xy} > 3d_{yz} > 3d_{xz}$ (with the peptide nitrogen and water oxygen atoms along the y axis and the amino nitrogen and carboxyl oxygen atoms along the x axis).

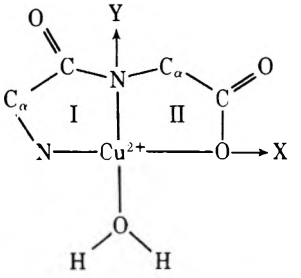

The d–d transition energies were assigned as $3d_{x^2-y^2} \leftarrow 3d_{z^2}$ (14000 cm^{-1}), $3d_{xy}$ (15500 cm^{-1}), $3d_{yz}$ (16000 cm^{-1}), $3d_{xz}$ (16500 cm^{-1}). All other properties associated with the Cu^{2+} 3d orbitals were calculated in the same way as was described for the amino acid complexes.

Three different conformational isomers of the NH_2-terminal chelate ring were considered, one planar and two nonplaner. The two nonplaner conformations are chiral and bear an enantiomeric relationship to each other. They are generated by distorting the C_α atom above or below the CuN_2O_2 plane. This distortion of the C_α atom also leads to a distortion in the NH_2 group and a distortion of the carbonyl oxygen atom out of the CuN_2O_2 plane. The Cu, N (peptide), C (carbonyl), and N (amino) atoms of the chelate ring remain coplaner. If C_α is methyl substituted (as in the

AG and AA complexes), then the nonplaner conformations lead to the methyl substituent being either axial or equatorial to the chelate ring. We shall refer to the three ring conformations as P (planer), NP_a (nonplaner with methyl substituent axial), and NP_e (nonplaner with methyl substituent equatorial).

The d–d rotatory strengths computed for the Cu^{2+}–dipeptide complexes are listed in Table II. Note that the rotatory strength values for $[Cu(AA)(H_2O)]$ are equal to the sums of the rotatory strengths calculated for the corresponding transitions in $[Cu(AG)(H_2O)]$ and $[Cu(GA)(H_2O)]$. That is, the contribution made to the d–d rotatory strengths by the α-methyl substituents are exactly additive on our model. Our basic model does not allow for three-way interactions which include two C_γ oscillators. That is, C_γ–$C_{\gamma'}$ interactions are neglected. We extended the model to include such interactions and performed a series of calculations in which the two α-CH_3 groups in the (AA) complex were assumed to interact via dispersion forces. The interaction energies were found to be very small and to have a negligible effect on the d–d rotatory strengths.

C. *Tripeptide Complexes.* The input parameters selected for the tripeptide calculations are similar to those described for the dipeptide case.

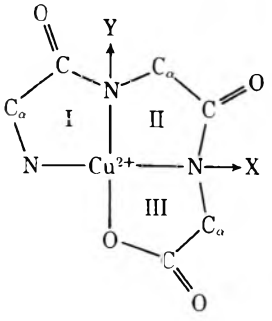

The two B_β oscillators associated with the two amide moieties were assigned identical properties (with values equal to those for the dipeptide case). The C_γ oscillators associated with the α-carbon substituents on the three chelate rings were also assigned indentical properties. The carboxyl and amino groups were treated in exactly the same way as for the dipeptide complexes, and all properties associated with the metal 3d orbitals or d–d electronic states were chosen as described for the dipeptides.

Four D_δ oscillators were selected for the tripeptide calculations. They are characterized as follows: (1) Cu–N (amino group), E_δ = 40000 cm^{-1}, μ_δ = 2.0 D (along bond axis), located at bond midpoint; (2) two Cu–N (peptide) oscillators, E_δ = 30000 cm^{-1}, μ_δ = 2.0 D (along bond axes), located at the midpoints of the two Cu–N (peptide) bonds in the tripeptide system; (3) Cu–O (carboxyl), E_δ = 35000 cm^{-1}, μ_δ = 2.0 D (along bond axis), located at bond midpoint. Nonplanarity in the NH_2-terminal ring (I) was introduced in the same way as was described for the dipeptide systems.

The d–d rotatory strengths computed for the Cu^{2+}–tripeptide complexes are listed in Table III. Again, interactions between oscillators within a particular subsystem (for example, C_γ–$C_{\gamma'}$ interactions) were excluded in our model so that contributions from individual oscillators of the same subsystem are strictly additive. Therefore, the rotatory strengths computed for $[Cu(AAA)]^-$ are just sums of those computed for $[Cu(AGG)]^-$ + $[Cu(GAG)]^-$ + $[Cu(GGA)]^-$, for example.

D. *General Comments on Calculations.* The approximations inherent in the calculations performed here are rather crude. However, the *qualitative* nature of the results appear not to be particularly sensitive to the choice of parameter sets except as they relate to the geometrical or stereochemical disposition of the perturbing oscillators. That is, the signs and relative magnitudes of the computed rotatory strengths appear to be determined largely by the relative positions of perturbing oscillators in the ligand environment rather than by the intrinsic spectroscopic properties of the interacting subsystems. Oscillator properties were chosen on the basis of empirical spectroscopic data available for the various perturbing groups and for the known charge-transfer transitions occurring in the near-ultraviolet spectra of Cu^{2+} complexes. Calculations were performed in which the parameter sets were varied (using values falling within "reasonable" ranges) and the qualitative aspects of the results were not altered significantly. The *absolute* values of the computed rotatory strengths were found to be somewhat sensitive to the input parameters, however.

In calculating the electric quadrupole and electric hexadecapole matrix elements between d–d states it was necessary to evaluate the radial integrals $\langle r^2 \rangle_{dd}$ and $\langle r^4 \rangle_{dd}$. For the results displayed in Tables I–III values of $\langle r^2 \rangle_{dd}$ = 0.5614 Å and $\langle r^4 \rangle_{dd}$ = 1.4594 Å were used. Variations of 0–30% in these values did not significantly alter the computed rotatory strengths. Several calculations were carried out in which the point dipole approximation for the perturbing oscillators was relaxed and, instead, the dipole oscillators were replaced by distributions of monopoles. This change in representation did not affect the qualitative aspects of the results, although the magnitudes of the computed rotatory strengths did change slightly. Inclusion of ligand quadrupole oscillators (associated with carbonyl n $\rightarrow \pi^*$ transitions) and the addition of out-of-plane polarized dipole oscillators on the carbonyl oxygens did not influence the calculated results by any significant amount.

Rotatory strength calculations with and without second- and third-order contributions included and with and without hexadecapole–dipole interaction terms included differ quite significantly. The $d_{x^2-y^2} \leftarrow d_{z^2}$ transition is both magnetic dipole forbidden and electric dipole forbidden to zeroth order. It gains a nonvanishing electric dipole component by a first-order perturbation process and a nonvanishing magnetic dipole component by a second-order mechanism in our model. Its rotatory strength appears, therefore, only in third-order terms and is computed to be quite small (relative to the values computed for the other d–d transitions). The $d_{x^2-y^2} \leftarrow d_{xy}$ transition is magnetic dipole allowed to zeroth order, but it gains electric dipole character only by coupling to the ligand environment through electric hexadecapole–electric dipole interactions, since it is electric quadrupole forbidden. Contrary to the frequently stated assumption that the $d_{x^2-y^2} \leftarrow d_{xy}$ transition should have the largest rotatory strength (and provides the dominant component in the d–d CD spectrum of chiral pseudotetragonal complexes), our calculations indicate that the rotatory strengths of the $d_{x^2-y^2} \leftarrow d_{xy}$, d_{xz}, and d_{yz} transitions are comparable in magnitude. This result was also obtained in calculations based on a molecular orbital model for computing electronic rotatory strengths.[12] A large zeroth order magnetic dipole transition moment does not ensure a large rotatory strength for a transition unless an effective mechanism exists whereby the transition can acquire an electric dipole component which is collinear with the magnetic di-

TABLE III: Computed d–d Rotatory Strengths for Tripeptide Complexes

Complex	$R(10^{-40}$ cgs) $(z^2) \rightarrow (x^2-y^2)$	$(xy) \rightarrow (x^2-y^2)$	$(yz) \rightarrow (x^2-y^2)$	$(xz) \rightarrow (x^2-y^2)$	Net[a]
[Cu(AGG)]$^-$, P	−0.26	−5.07	−4.11	−1.57	−11.00
NP_a	−0.38	−5.46	−4.52	−1.62	−11.98
NP_e	0.14	−4.46	−3.84	−1.41	−9.57
[Cu(GAG)]$^-$, P	0.16	−8.88	−6.92	−3.14	−18.78
NP_a	0.07	−8.92	−7.44	−3.22	−19.51
NP_e	0.28	−8.74	−5.99	−3.01	−17.46
[Cu(GGA)]$^-$, P	0.29	−8.44	−6.11	−1.11	−15.37
NP_a	0.30	−8.47	−6.15	−1.24	−15.56
NP_e	0.24	−8.41	−5.98	−1.01	−15.16
[Cu(AAG)]$^-$, P	−0.10	−13.95	−11.03	−4.71	−29.78
NP_a	−0.31	−14.38	−11.96	−4.84	−31.49
NP_e	0.42	−13.20	−9.83	−4.42	−27.03
[Cu(AGA)]$^-$, P	0.03	−13.51	−10.22	−2.68	−26.37
NP_a	−0.08	−13.93	−10.67	−2.86	−27.54
NP_e	0.40	−12.87	−9.82	−2.42	−24.73
[Cu(GAA)]$^-$, P	0.45	−17.32	−13.03	−4.25	−34.15
NP_a	0.37	−17.39	−13.59	−4.46	−35.07
NP_e	0.52	−17.15	−11.97	−4.02	−32.62
[Cu(AAA)]$^-$, P	0.19	−22.39	−17.14	−5.82	−45.15
NP_a	−0.01	−22.85	−18.11	−6.08	−47.05
NP_e	0.66	−21.61	−15.81	−5.43	−42.19

[a] Algebraic sum of d–d rotatory strengths.

TABLE IV: Summary of Experimental Data Reported for $\Delta\epsilon_{max}$ in the d–d Transition Region for Cu^{2+} Complexes in Solution

Complex	$\Delta\epsilon_{max}$ (λ_{max})	Solvent	Ref
[Cu(*S*-Ala)$_2$][a]	0.008 (769) −0.075 (619)	H_2O	2
[Cu(*S*-Ala)$_2$][a]	0.025 (800) −0.096 (595)	DMSO–H_2O	2
[Cu(*S*-Pro)$_2$][a]	0.255 (644) −0.072 (518)	H_2O	2
[Cu(*S*-Pro)$_2$][a]	0.265 (647) −0.065 (532)	DMSO–H_2O	2
[Cu(*S*-Ala)$_2$][b]	0.02 (730) −0.09 (625)	H_2O	20
[Cu(*S*-Pro)$_2$][b]	0.30 (665) −0.07 (525)	H_2O	20
[Cu(*N*-CH_3-*S*-Ala)$_2$][b]	0.003 (784) −0.080 (656) 0.018 (560) 0.015 (510)	H_2O	20
[Cu(*N*-CH_3-*S*-Pro)$_2$][b]	−0.25 (622)	H_2O	20
[Cu(GA)(H_2O)][c]	−0.35 (~650)	H_2O	21
[Cu(AG)(H_2O)][c]	−0.11 (~650)	H_2O	21
[Cu(AA)(H_2O)][c]	−0.47 (~650)	H_2O	21
[Cu(AGG)][c]	−0.17 (~560)	H_2O	1
[Cu(GAG)][c]	−0.69 (~560)	H_2O	1
[Cu(GGA)][c]	−0.42 (~560)	H_2O	1
[Cu(AAA)][c]	−1.19 (~560)	H_2O	1

[a] Isolated complexes dissolved in solvent. CD measurements performed at 20°C. [b] Complexes prepared by mixing ligands and metal ion in 2:1 molar ratio and titrating with standard base until endpoint is reached. CD measurements performed at 25°C. [c] Isolated complexes dissolved in solvent. CD measurements performed at ~25°C.

pole. For the $d_{x^2-y^2} \leftarrow d_{xy}$ transition in our model, this mechanism is provided by an electric hexadecapole–electric dipole (metal–ligand) interaction which is generally quite weak.

The $d_{x^2-y^2} \leftarrow d_{xz}$ and d_{yz} transitions are both magnetic dipole allowed and electric quadrupole allowed to zeroth order and they couple to the ligand oscillators via quadrupole–dipole and hexadecapole–dipole interactions. These transitions exhibit substantial first-order rotatory strength according to our independent systems/perturbation model.

V. Discussion

The theoretically calculated results given in Tables I–III can be readily correlated with experimental data on the chiroptical properties of Cu^{2+}–amino acid, –dipeptide, and –tripeptide complexes. A summary of the experimental data reported for $\Delta\epsilon_{max}$ (λ_{max}) in the d–d transition region is given in Table IV for a number of the Cu^{2+} complexes studied here. The CD spectra reported for these systems generally cannot be clearly resolved into components which

can be further assigned to individual d–d transitions. In some cases, however, two and possibly three component bands are discernible. The CD spectrum of [Cu(*S*-Ala)$_2$] in solution exhibits two extrema in the visible–near-infrared region, an intense negative band centered in the 590–620-nm region and a weak positive band near ~730 nm. The absorption spectrum of this complex exhibits a broad band with a maximum ($\epsilon \sim 60$) at about 620 nm. These results correlate qualitatively with the rotatory strengths calculated for the trans isomer of [Cu(*S*-Ala)$_2$] if we assume that the $3d_{x^2-y^2} \leftarrow 3d_{xy}$, $3d_{xz}$, and $3d_{yz}$ transitions are nearly degenerate and remain unresolved in the CD spectrum. It is likely that the $3d_{xz}$ and $3d_{yz}$ levels are strongly mixed via pseudo-Jahn–Teller interactions within the complex and that the *net* rotatory strength associated with transitions to these levels will determine the sign of the observable CD.

We note that chelate ring conformation has only a minor effect on the computed d–d rotatory strengths of [Cu(*S*-Ala)$_2$], and that vicinal effects due to the α-methyl groups apparently dominate the signs and magnitudes of the rotatory strengths. This result is in agreement with results previously obtained from molecular orbital calculations of d–d rotatory strengths in Cu^{2+}–amino acid complexes.[12] However, in contrast to results previously obtained from the molecular orbital calculations,[12] the present calculations predict like signs for the net d–d rotatory strengths of cis and trans isomers of [Cu(*S*-Ala)$_2$]. The lability of Cu^{2+}–amino acid complexes in solution preclude preparing pure cis or pure trans isomers and it is expected that, at least for alanine, both isomers are present in solution media.

Our calculated results for the *N*-methyl-substituted alanine complexes predict that these systems should exhibit CD spectra which are qualitatively similar to those observed for the unsubstituted alanine complexes. With respect to *net* d–d rotatory strength this is in agreement with experimental observation.[20] The [Cu(*N*-CH$_3$-*S*-Ala)$_2$] complex in solution is reported to show a very weak positive ($\Delta\epsilon \sim 0.003$) CD band at ~784 nm, a relatively strong ($\Delta\epsilon \sim -0.080$) negative CD band at ~656 nm, and two rather weak ($\Delta\epsilon \sim 0.018$–$0.015$) positive CD bands at ~560 and ~510 nm.[20] The single absorption maximum occurs at ~612 nm ($\epsilon \sim 80$). A detailed analysis of the CD spectrum again would require explicit consideration of possible vibronic effects.

It is well known that the bis complexes of *S*-proline with Cu^{2+} exhibit CD spectra which are dramatically different from the CD spectra of most other Cu^{2+}–amino acid complexes.[1,20-22] [Cu(*S*-Pro)$_2$] yields an intense ($\Delta\epsilon \sim 0.33$) positive CD band near 665 nm and a weak ($\Delta\epsilon \sim 0.07$) negative band near 525 nm in aqueous solution.[21] On the other hand, [Cu(*N*-CH$_3$-*S*-Pro)$_2$] exhibits a single negative CD band ($\Delta\epsilon \sim -0.18$) near 620 nm.[20] The absorption maxima appear at 612 (unsubstituted proline complex) and 620 nm (*N*-methyl-substituted proline complex).[21] Our calculated results are in qualitative agreement with these observations assuming that the trans isomers are preferred over the cis isomers in solution.

Our calculated results for the Cu^{2+}–dipeptide complexes show that α-methyl substitution on the COO^--terminal chelate ring has a substantially larger influence on d–d rotatory strengths than does α-methyl substitution on the NH_2-terminal chelate ring. This result is in agreement with experimental observation.[1,21] On our model this must be attributed to significantly different methyl–peptide–metal and methyl–carboxyl–metal three-way interactions for the two differenct α-methyl substituent groups, rather than to conformational equilibria in the NH_2-terminal ring. That is, metal–methyl interactions *through* the peptide and carboxyl B_β chromophores are significantly greater for the α-methyl group on the COO^--terminal chelate ring than for the α-methyl group on the NH_2-terminal group. Discrimination between the two α-methyl substituents with respect to their *relative* contributions to d–d rotatory strengths appears only in the second- and third-order terms of our model.

The relative magnitudes computed for the d–d rotatory strengths of [Cu(AGG)]$^-$, [Cu(GAG)]$^-$, and [Cu(GGA)]$^-$ are also in substantial agreement with experimental observation.[1,21] As was the case for the dipeptide complexes, differences in d–d rotatory strength contributions from the α-methyl substituents on the various chelate rings arise from different methyl–peptide–metal and methyl–carboxyl–metal three-way interactions. Again, conformational flexibility in the NH_2-terminal chelate ring cannot account for the relatively small d–d rotatory strengths calculated for the [Cu(AGG)]$^-$ system. The second- and third-order terms retained in eq 7 lead to the discrimination of [Cu(AGG)]$^-$, [Cu(GAG)]$^-$, and [Cu(GGA)]$^-$ d–d rotatory strength magnitudes.

To first order in our dynamical coupling model the $3d_{x^2-y^2} \leftarrow 3d_{xy}$, $3d_{xz}$, and $3d_{yz}$ transitions acquire rotatory strength via an electric hexacapole–electric dipole coupling mechanism. The first-order rotatory strength expressions involve metal d–d magnetic dipole transition moments, electric dipole transition moments associated with ligand (perturber group) transitions, and hexadecapole (metal)–dipole (ligand) interaction matrix elements. To first order, the $3d_{x^2-y^2} \leftarrow 3d_{z^2}$ transition remains optically inactive. Unlike the first-order static coupling model, the first-order dynamical coupling model does not lead to simple sector rule expressions.[1,5-7] If we simplified the physical aspects of our first-order dynamical coupling model so that the perturbing groups were treated as centers of isotropic polarizability, then a set of rather simple sector rules are obtained. These sector rules are

$$3d_{x^2-y^2} \leftarrow 3d_{xy} \qquad -XYZ(X^2 - Y^2)$$

$$3d_{x^2-y^2} \leftarrow 3d_{xz} + 3d_{yz} \qquad XYZ(X^2 - Y^2)$$

where (X, Y, Z) are perturber coordinates referred to a coordinate origin located on the metal ion. These rules suggest that the sign of the *net* rotatory strength of the $3d_{x^2-y^2} \leftarrow 3d_{xz} + 3d_{yz}$ transitions should obey the so-called "hexadecant" rule.[1,5]

Treating the perturbing groups as centers of isotropic polarizability is, of course, incompatible with our model since we consider the perturbers to be *oriented* dipole oscillators. Treating the perturbing groups to be centers of anisotropic polarizability would come closer to our model, and in this case the resulting sector rules would again be quite complex.[5,13]

To second and third order in our model the quadrupole–dipole interaction terms become important. Furthermore, the $3d_{x^2-y^2} \leftarrow 3d_{z^2}$ transition acquires rotatory strength in third order. In no case do the calculated results indicate that first-order terms alone make the dominant contributions to the net d–d rotatory strength or to the overall d–d rotatory strength pattern. In our model it is essential that the higher order terms be retained in calculating the rotatory strengths.

The hexadecant sector rule based on the first-order static coupling model must be applied to dipeptide and tripeptide complexes with some caution. It is derived assuming nearly D_{4h} microsymmetry within the metal ion–donor atom cluster, and the model on which it is based ignores the possible consequences of symmetry reductions caused by dissimilarities between the amino, peptide, and carboxyl ligand moieties. These ligand groups cannot contribute directly to metal d–d optical activity since they lie in symmetry planes of the metal ion–donor atom cluster; however, they can significantly distort the nodal surfaces of the d–d spectroscopic states and indirectly influence the interactions between the metal ion and other dissymmetrically distributed ligand groups. In second-order extensions of the static coupling model,[6,7] the nonchiral parts of the ligand environment mediate the interactions between the metal ion and the chiral parts of the environment. These second-order treatments lead to socalled "mixed" sector rules in which the positional coordinates of two different perturbing groups appear simultaneously. In the dynamical coupling model employed in the present study, the second- and third-order terms accommodate the indirect influence which the nonchiral parts of the ligand environment may have on the chiroptical properties of the metal d–d transitions. Our results suggest that these higher order terms are essential to accurately calculating the d–d rotatory strengths and that two- and three-way interactions must be included in the basic physical model.

Acknowledgments. This work was supported in part by the Petroleum Research Fund, administered by the American Chemical Society, the National Science Foundation, and the Camille and Henry Dreyfus Foundation (through a Teacher–Scholar Grant to F.R.).

References and Notes

(1) See R. Bruce Martin in "Metal Ions in Biological Systems", Vol. 1, H. Sigel, Ed., Marcel Dekker, New York, N.Y., 1974, Chapter 4 and references therein.
(2) C. J. Hawkins, "Absolute Configuration of Metal Complexes", Wiley-Interscience, New York, N.Y., 1971, Chapter 5.
(3) J. A. Schellman, *J. Chem. Phys.*, **44**, 55 (1966).
(4) S. F. Mason, *J. Chem. Soc. A*, 667 (1971).
(5) S. F. Mason, in "Fundamental Aspects and Recent Developments in Optical Rotatory Dispersion and Circular Dichroism", F. Ciardelli and P. Salvadori, Ed., Heyden, New York, N.Y., 1973, Chapter 3.6.
(6) F. S. Richardson, *J. Chem. Phys.*, **54**, 2453 (1971).
(7) F. S. Richardson, *Inorg. Chem.*, **10**, 2121 (1971).
(8) F. S. Richardson, *J. Phys. Chem.*, **75**, 692 (1971).
(9) F. S. Richardson, *Inorg. Chem.*, **11**, 2366 (1972).
(10) R. W. Strickland and F. S. Richardson, *Inorg. Chem.*, **12**, 1025 (1973).
(11) H. C. Freeman, *Adv. Protein Chem.*, **22**, 257 (1967).
(12) C. Yeh and F. S. Richardson, *Inorg. Chem.*, in press.
(13) E. G. Höhn and O. E. Weigang, Jr., *J. Chem. Phys.*, **48**, 1127 (1968).
(14) I. Tinoco, *Adv. Chem. Phys.*, **4**, 113 (1962).
(15) J. A. Schellman, *Acc. Chem. Res.*, **1**, 144 (1968).
(16) D. Caliga and F. S. Richardson, *Mol. Phys.*, **28**, 1145 (1974).
(17) F. S. Richardson, D. Caliga, G. Hilmes, and J. J. Jenkins, *Mol. Phys.*, **30**, 257 (1975).
(18) F. S. Richardson, G. Hilmes, and J. J. Jenkins, *Theor. Chim. Acta (Berlin)*
(19) (a) J. W. Richardson, W. C. Nieuwpoort, R. R. Powell, and W. F. Edgell, *J. Chem. Phys.*, **36**, 1057 (1962); (b) J. W. Richardson, R. R. Powell, and W. C. Nieuwpoort, *ibid.*, **38**, 796 (1963).
(20) E. W. Wilson and R. B. Martin, *Inorg. Chem.*, **10**, 1197 (1971).
(21) J. M. Tsangaris and R. B. Martin, *J. Am. Chem. Soc.*, **92**, 4255 (1970).
(22) C. J. Hawkins and C. L. Wong, *Aust. J. Chem.*, **23**, 2237 (1970).

Effect of Counterion Substitution on the Type and Nature of Nematic Lyotropic Phases from Nuclear Magnetic Resonance Studies

K. Radley,[1a] L. W. Reeves,*[1b] and A. S. Tracey

Chemistry Department, University of Waterloo, Waterloo, Ontario N2L 3G1 *(Received December 16, 1974; Revised Manuscript Received June 23, 1975)*

Publication costs assisted by the National Research Council of Canada

Nematic lyotropic phases have been prepared using mixed detergents with the decyl sulfate anion. The phases have been studied by observing Li-7, Na-23, Cs-133, and D-2 nuclear magnetic resonance (NMR) spectra. The NMR signals all show first-order quadrupole splittings. The studies of the nematic phases were designed to investigate the influence of the counterion and temperature variation. The ternary phase sodium decyl sulfate–decanol–D_2O was modified by substituting the cations Li^+, K^+, Rb^+, Cs^+, NH_4^+, and $C_2H_5NH_3^+$ for Na^+ in varying proportion, but sustaining the mole fractions of detergent, decanol, and D_2O. Phase changes do occur as a result of counterion effects and two types of nematic phase can be distinguished. A type I nematic phase is slow to respond to orienting forces in a magnetic field, but does form a single liquid crystalline sample with the uniaxial nematic axis aligned parallel to the magnetic field direction. The second type II phase observed, is more mobile and orients much more rapidly in a magnet but with the nematic axis perpendicular to the field direction. At certain temperatures and compositions of counterions the two types of nematic phase can coexist. Type I nematic phases do not preserve their orientation while spinning about an axis perpendicular to the magnetic field direction but remain oriented when the spinning axis coincides with the field axis. They are suitable as orienting media for solutes to be investigated in NMR spectrometers with superconducting solenoids. Type II nematic phases, after a short initial period in the magnetic field, retain their single liquid crystalline properties while spinning in both parallel and perpendicular arrangements to the field. Nematic phases have been prepared with three different cations Li^+, Na^+, and Cs^+. Variation of the lithium decyl sulfate content of these nematic media induces the type I to type II phase transition. The changes in quadrupole splitting and the rates of change of quadrupole splitting with concentration at the phase change type I to type II indicate that relatively small changes in microdegree of order near the ions accompanies the perpendicular change in alignment. The temperature dependence of phase changes with the pure ternary phase sodium decyl sulfate–decanol–D_2O contrasts with that of a phase prepared with added sodium sulfate and ethylene carbonate. These differences indicate a type I phase without additives and a type II phase with the additives.

Introduction

There has been a recent revival of interest in lyotropic liquid crystals[2-9] because of their importance as crude membrane models[10-15] and as part of a renewed activity in liquid crystal studies. The nuclear magnetic resonance (NMR) tool is particularly appropriate[2-4,10-15] in these investigations since it gives a view of these interesting materials at the molecular and ionic level. Until a short time ago[6,15] no mesophases had been prepared with mixed counterion content. We shall show in this study that mixed detergents with a common detergent ion, but different counterions, do form nematic liquid crystals which, however, undergo phase changes with changes in counterion concentrations. The nature of the counterion which resides in the mobile component of the electrical double layer (edl) is thus shown to be an important factor for determining the type and stability of these phases.

Most of the NMR studies of lyomesophases[16-24] have been made on liquid crystalline materials where no X-ray diffraction data are available to describe the type of superstructure. The NMR technique has been used to define the direction of the nematic axis.[18,25] X-Ray diffraction studies of nematic lyomesophases in the middle soap region[26,27] reveal a superstructure array of semiinfinite cylinders on hexagonal or face centered cubic lattices. The middle soap region of lyomesophase systems contains[28-30] nematic phases which orient in an applied magnetic field and those which do not orient at any measureable rate. The randomly oriented phases lead to powder pattern type NMR spectra.[29] The nematic phases reported here do orient in a magnetic field and the homogeneity of the ordering increases with the time the sample spends in the magnetic field.

Partially Averaged Nuclear Quadrupole Splitting

Provided there is an anisotropic site, the degeneracy of the Zeeman transitions is lifted to give $2I$ transitions ($I > \frac{1}{2}$) with the intensity distribution $[I(I + 1) - m(m + 1)]$.[31-33] The separation of the transitions is determined by the nuclear quadrupole coupling constant. In all the practical cases discussed in this paper the nuclear quadrupole coupling energy is negligibly small compared with the nuclear Zeeman energy. In this case the frequencies of the transitions are given by

$$\nu_m = (m - \tfrac{1}{2})\nu_Q(3\cos^2\theta - 1)\tfrac{1}{2} \qquad (1)$$

for changes in magnetic quantum number $m - 1 \rightarrow m$. θ is the angle between the principal axis of the electric field gradient and the magnetic Zeeman field direction. ν_Q is a measure of the coupling energy between the nuclear quadrupole moment (eQ) and the electric field gradient (eq).

$$\nu_Q = \frac{3(e^2qQ)}{2I(I-1)h} \qquad (2)$$

It is further assumed that in our studies there is negligible assymetry in the quadrupole coupling tensor[33] and one parameter (eq) is sufficient to define the coupling energy.

From (1) when $m = \frac{1}{2}$ the transition frequency is unperturbed from the Zeeman transition. All other transitions depend on the angular factor $\frac{1}{2}(3\cos^2\theta - 1)$ which becomes averaged to S_{zz}, the degree of orientation of the electric field gradient in a uniaxial nematic medium. If there is a constraint direction in the liquid crystal, which may be varied in angle Ω to the magnetic field, then an angular dependence can be obtained for a single liquid crystal sample as in

$$\nu_m = (m - \tfrac{1}{2})\nu_Q S_{zz}\tfrac{1}{2}(3\cos^2\Omega - 1) \quad (3)$$

S_{zz} becomes the degree of orientation with respect to this constraint direction. In the present study we shall show that some nematic samples are sufficiently viscous to remain oriented for a short time when rotated with respect to the magnetic field. Equation 3 is then appropriate. In some liquid crystalline samples the torques applied by the magnetic field to the macroscopic diamagnetic anisotropy are insufficient to overcome the frictional viscosity forces within the sample and homogeneous alignment or single crystal behavior is not achieved. In this case a randomly oriented microcrystalline nematic phase persists even in the Zeeman field. The constraint direction Ω remains random leading to a powder type spectrum[31] for each pair of transitions displaced from the spectral center. The appropriate line shape then becomes

$$g(\Delta\nu) = \frac{1}{2\sqrt{3}\alpha}\left(1 \pm \frac{\Delta\omega}{\alpha}\right)^{-1/2} \quad (4)$$

where

$$\alpha = \left[\frac{(m - \tfrac{1}{2})\nu_Q}{2}\right]$$

and

$$-2 \leq \frac{\Delta\omega}{\alpha} \leq +1 \text{ for } \alpha > 0$$

$$-1 \leq \frac{\Delta\omega'}{\alpha} \leq +2 \text{ for } \alpha < 0$$

For a spin 1 case a typical Pake type[32] doublet results. The peak separations in the present study for single crystal behavior is related to ν_Q directly but for $I = \frac{3}{2}$ the separation between the outer transitions has been used and this is equal to $2\nu_Q$. Two special cases of eq 4 are important namely $\Omega = 0°$ for parallel alignment to the field and $\Omega = \pi/2$ for a perpendicular orientation. Separation of peaks decrease in magnitude by a factor 2 in going from parallel to perpendicular directions of order. There is also a sign change which we cannot detect. Another important point is the comparison of powder diagram to perpendicular and parallel order. In the former case there is no change in peak separation on forming a single liquid crystal but in the latter the splitting doubles.

Samples placed for the first time into the Zeeman field are a priori polycrystalline in their alignment directions. The time taken to achieve a single crystal spectrum after remaining in the field varies between an interval too short to measure to an interval which is too long to detect. The observation of initial and final states gives therefore information on perpendicular or parallel alignment to the single crystal. The intermediate line shapes are informative of the kinetics of the magnetohydrodynamic process of ordering. We do not address ourselves to this problem at this time.

Experimental Section

(a) *Preparation of Decyl Sulfates.* In previous work[34,35] sodium decyl sulfate NaDS was prepared by the sulfonation of 1-decanol, using an SO_3 complex in a suitable polar solvent, followed by neutralization with NaOH and purification by recrystallization from ethanol. In the present work cold concentrated H_2SO_4 (100 g) was used to sulfonate frozen decanol (50 g) at 0°C. The H_2SO_4 used was purchased from J. T. Baker. The 1-decanol also obtained from J. T. Baker was dried by shaking with anhydrous Na_2SO_4. The decanol was then decanted off and double distilled prior to sulfonation. The sulfonated decanol was poured over ice (200 g) and neutralized by slowly pouring in cold 6 M NaOH aqueous solution and stirring to avoid local heating. This solution was evaporated to dryness by letting it stand in the fumehood. The mixture of Na_2SO_4 and NaDS, obtained as a white solid, was boiled with absolute ethanol and the Na_2SO_4 was filtered off. The ethanolic solution of NaDS was evaporated to dryness on a rotary evaporator. NaDS, obtained as an off-white impure solid, was purified by recrystallization from (1) 90% ethanol and water and (2) 80% ethanol and water, followed by drying under vacuum. The yield was 50 g.

Other decyl sulfates were prepared by ion exchange. An ion-exchange column of about 1 mol capacity was prepared using Dowex 50W-X8 cation exchange resin as previously described by Reeves and coworkers.[2a,3,10] The column was washed with sufficient 3 M H_2SO_4 and then by distilled water. The aqueous decyl sulfuric acid solution so obtained was neutralized immediately using a sufficient amount of the solid metal carbonate or the hydroxide solution in the case of the ammonium ions. The solutions were evaporated to dryness by letting them stand in a fumehood. The solids so obtained were recrystallized from the appropriate solvents. Mixed solvents were preferred, since these gave the highest yields and larger crystals. Most yields were greater than 90%, e.g., CsDS from ethanol–ethyl acetate mixtures.

The structures of the decyl sulfates were characterized and their purity was determined using proton NMR taken on a Varian HA-100 spectrometer. The spectrum was that of a typical α-decyl-substituted chain which was reproducible for each decyl sulfate. Care was taken to search out impurities which might have been introduced during the preparation but none were found, when due care was taken with the preparation.

(b) *Phase Preparation.* The phases were prepared by weighing out the appropriate components into 10–17-mm test tubes with a 2–4-mm constrictions in the middle. The tubes were sealed off and used directly in the NMR spectrometer after phases had formed. The components were mixed to form a homogeneous phase, by centrifuging the fluid back and forth several times through the constriction in the tube, at slightly elevated temperatures. When the samples had been weighed out and homogeneously mixed they were all thermostated at 27°C, the temperature of the box surrounding the magnet.

(c) *Phase Compositions.* A standard ternary phase of 35.9 wt % sodium decyl sulfate, 7.2 wt % decanol, and 56.9 wt % D_2O of nematic properties was prepared. In the phases in which counterions are partially substituted the exchange of sodium for another ion was made on a mole for mole basis by weighing out mixtures of the detergent com-

ponent. At least four and sometimes six samples of the same composition were weighed out independently to test the reproducibility of the results.

In phases prepared with three counterions Li^+, Na^+, and Cs^+ the standard weight percent of decanol and water was used and the usual sodium decyl sulfate was replaced on a mole substitution basis, 50% by cesium decyl sulfate with 25 mol % of the sodium decyl sulfate in the standard phase retained. The remaining 25 mol % of the detergent normally used was lithium decyl sulfate. This standard phase with three detergents was further increased in lithium decyl sulfate content. A large addition of the third detergent was possible within the nematic range and the composition changes were expressed merely in mole ratio percent of the lithium decyl sulfate in a pure ternary phase of this detergent. Such a complex mixture of five components is difficult to express in simple terms of concentration and indeed not necessary as the purpose was to investigate possible phase changes with strong variation of Li^+ ion content.

Two samples typical of solvent and solvent plus solute for studying oriented molecules[16] were investigated at different temperatures. The pure standard ternary phase sodium decyl sulfate–decanol–water represents the nematic solvent sample and to a 1 g sample of this was added 0.05 g of ethylene carbonate and 0.07 g of sodium sulfate.

(d) *NMR Spectrometer.* All the alkali metal ion and ^2D quadrupole splittings were measured using a Varian Model VF-16 wide-line NMR spectrometer. All spectra were recorded on a Hewlett-Packard 7004A X–Y recorder. The sweep speed, power, leakage, and modulation broadening was determined individually for each sample in order to obtain a spectrum with maximum intensity in derivative mode. The samples were left in the magnet long enough to orient, varying from 0.5 hr, to at times 24 hr in order to obtain sharp single crystal spectra. A careful check was kept on the magnet box temperature and spectra were not recorded unless the box temperature was 27 ± 0.5°C.

The maximum field of the magnet was 10000 G. The magnet was usually operated at a lower field, in order that the alkali metal ions and ^2D resonances could be observed at radiofrequencies of 4–8 MHz. The rf unit was driven with a frequency synthesizer (ND.30M Schomandall 300 Hz–30 MHz). The spectra were calibrated by off setting the frequency synthesizer and retaking spectra without stopping the chart. For calibration a spectrum was swept at least twice upfield and twice downfield. The accuracy of the peak positions in the recorded spectra was estimated to be ±10 Hz for ^7Li, ±5 Hz for ^2D, ±10 Hz for ^{133}Cs, and ±100 Hz for ^{23}Na.

At a certain magnetic field ^2D, ^{23}Na, and ^{133}Cs have resonances in the frequency range 4–8 MHz. With a suitable sample containing each of the nuclei, all three resonances could be recorded consecutively with only minor spectrometer adjustments and without disturbing the sample. The probe was interchanged in order to record ^7Li NMR at the same field. This technique enables the comparison of the quadrupole splitting of several nuclei at an identical magnetic field, at the same temperature, and at a given age.

Two samples were run at various temperatures. These sample tubes were 11-mm o.d. and were held in an enclosed 17-mm o.d. sample holder, with an inlet and an outlet tube, through which regulated hot or cold air was blown as required. The samples were allowed to equilibrate for about 2 hr at each temperature before a spectrum was recorded. The temperature was measured by means of a thermocouple placed 1 cm from the sample. The temperature was controlled to within ±0.3°C.

Results

(a) *Counterion Substitution Experiments.* The NMR signals of Li-7, Na-23, and Cs-133 in monatomic ions and D-2 in the deuterium oxide used to make up the phases were observed. Typical spectra for single liquid crystalline nematic phases are reproduced in Figure 1. In Figure 1a the Na-23 resonance is a 3:4:3 triplet, in Figure 1b the D-2 resonance is a 1:1 doublet, in Figure 1c the Li-7 resonance is a 3:4:3 triplet (distorted because the H_1 field is partly saturating and the signal overmodulated), and in Figure 1d the Cs-133 resonance is a 7:12:15:16:15:12:7 heptet. In studying the effect of counterions on the stability and types of phases formed the standard phase mentioned in the Experimental Section was modified by substitution on a mole for mole basis of one detergent, sodium decyl sulfate by another decyl sulfate with a different counterion. The following counter ions K^+, Rb^+, NH_4^+, $C_2H_5NH_3^+$, and Cs^+ were used in this substitution process. The signal strength of the remaining Na-23 became weak enough with the equipment available to render good measurement difficult after 50% substitution of sodium for another ion. In some cases a transition to an isotropic phase occurred before 50 mol % substitution of the total detergent was achieved. Rubidium and potassium decyl sulfates are sparingly soluble in water and phases of the mixed detergents became isotropic before 50 mol % substitution occurred. Cesium, ethylammonium, and ammonium decyl sulfates are very soluble in water and nematic phases were obtained well beyond the 50 mol % substitution limit imposed by spectrometer sensitivity.

Results of these experiments are reproduced in Figure 2. It is interesting to note that there is some effect of ageing in the samples.

The behavior of the sodium quadrupole splitting as the second ion replaces sodium in the nematic medium is quite characteristic of the replacement ion even though in most cases the substitution involves another alkali metal ion. For all substituted ions except NH_4^+ there is a sharp drop in the quadrupole coupling as the second ion is substituted in small concentration. All curves show a sharp discontinuity or break at some concentration or other in the range investigated. In the case of Cs^+, Rb^+, and K^+ a sharp break in the curve occurs between 5 and 7 mol % of the substituted ion. The concentration increase in the replacement ion beyond this point causes an increase in the magnitude of the sodium quadrupole splitting, most strongly for Cs^+, less so for Rb^+, and very little for K^+. A second discontinuous change in the curve for K^+ occurs at ~15 mol % replacement of Na^+ for K^+. The curve corresponding to NH_4^+ replacement does not fall steeply initially but does have a discontinuous break at 20 mol % in the new samples and ~30 mol % in the aged samples.

The deuterium magnetic resonance results in curves 2c are remarkably similar in shape to those in 2b. The discontinuities and breaks in the curves occur at the same points of concentration for both D-2 and Na-23 resonances except in a few unusual cases (cf. K^+). The ratios of sodium to deuterium splittings are plotted in Figure 2d. This ratio increases in a roughly linear and coincident fashion for all three alkali metal ion replacements after 5 mol % substitution. There is a break in the ratio curve (Figure 2d) at ~5 mol % replacement as indicated by the upper dotted line. This break corresponds to the discontinuities for the same

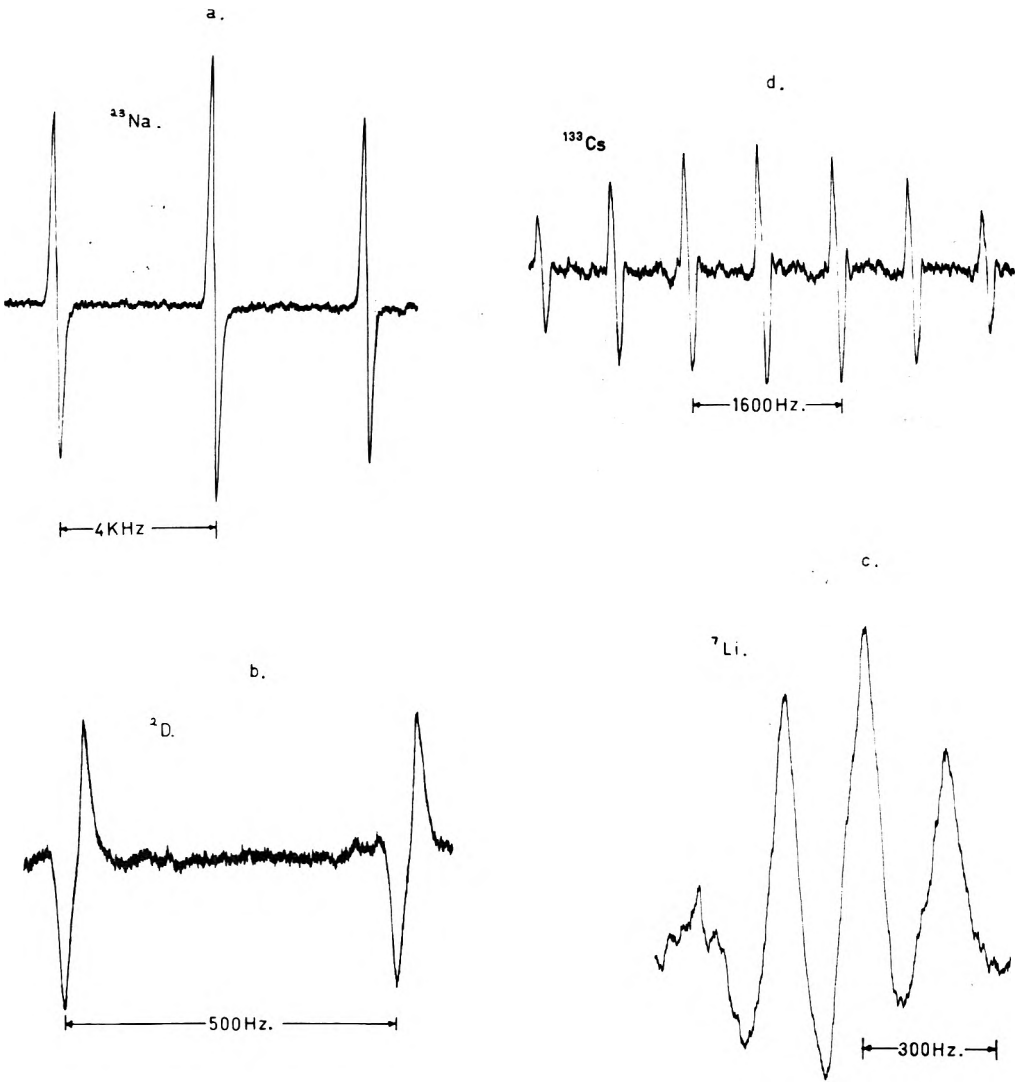

Figure 1. Selected spectra for lyotropic nematic phases reported in this study (a) Na-23, (b) D-2, (c) Li-7, and (d) Cs-133. The multiplicities and intensities are explained in the text.

ions in Figure 2b and 2c. The ammonium ions NH_4^+ and $C_2H_5NH_3^+$ are distinct from one another in their behavior in the ratio plot 2d but the break in the ratio curve for NH_4^+ clearly reproduces at the same concentration as in the other Figure 2b and 2c. The lower dotted horizontal line corresponds to the ratio of quadrupole couplings in the pure standard ternary phase. The ratio plot for $C_2H_5NH_3^+$ follows this rather closely. In all other cases of ion substitution there is a strong tendency for the ratio $(\Delta\nu_Q^{Na}/\Delta\nu_Q^{D})$ to increase as the substituent ion is increased in concentration.

(b) *Effect of Temperature on Two Selected Phases.* At lower temperatures both phases described in the Experimental Section start out as solids. The results in Figure 3 correspond to the studies of the ternary standard phase with sodium decyl sulfate in comparison with a phase containing electrolyte (Na_2SO_4) and an organic solute, ethylene carbonate. Such results are a useful guide to those contemplating the study of oriented molecules in lyotropic nematic phases. The temperature dependence of the sodium and deuterium magnetic resonance splittings are very similar and again have discontinuities at the same point ~17°C for the ternary phase. A pronounced broad maximum in the quadrupole splittings occurs for both nuclei in the region 29–33°C (Figure 3a and 3b). The ternary phase becomes isotropic above 40°C. The ratios of sodium to deuterium splittings at varied temperature are plotted as curve I in Figure 3e.

In Figure 3c and 3d the ternary phase contaminated with the electrolyte and an organic additive has quite a distinct behavior as the temperature is changed. The phase remains nematic up to higher temperatures ~50°C and has no phase change at the lower temperatures. The magnitude of the quadrupole splittings are much smaller indicating a lower degree of orientation of the components of the phases. A maximum in order is indicated from the sodium spectra at ~26°C. This maximum is not reproduced in the deuterium quadrupole couplings. Ratios of sodium to deuterium quadrupole couplings are lower in the contaminated phase at all temperatures (Figure 3e).

(c) *Studies of Phases with Three Different Counterions.* The standard phase described in the Experimental Section has a composition 54.3 wt % water, 7.6 wt % decanol, and 38.1 wt % sodium decyl sulfate. If lithium decyl sulfate replaces sodium decyl sulfate on a mole for mole basis in the phase then the weight composition becomes 55.9 wt % water, 7.8 wt % decanol, and 36.3 wt % lithium decyl sulfate while corresponding figures for complete replacement with

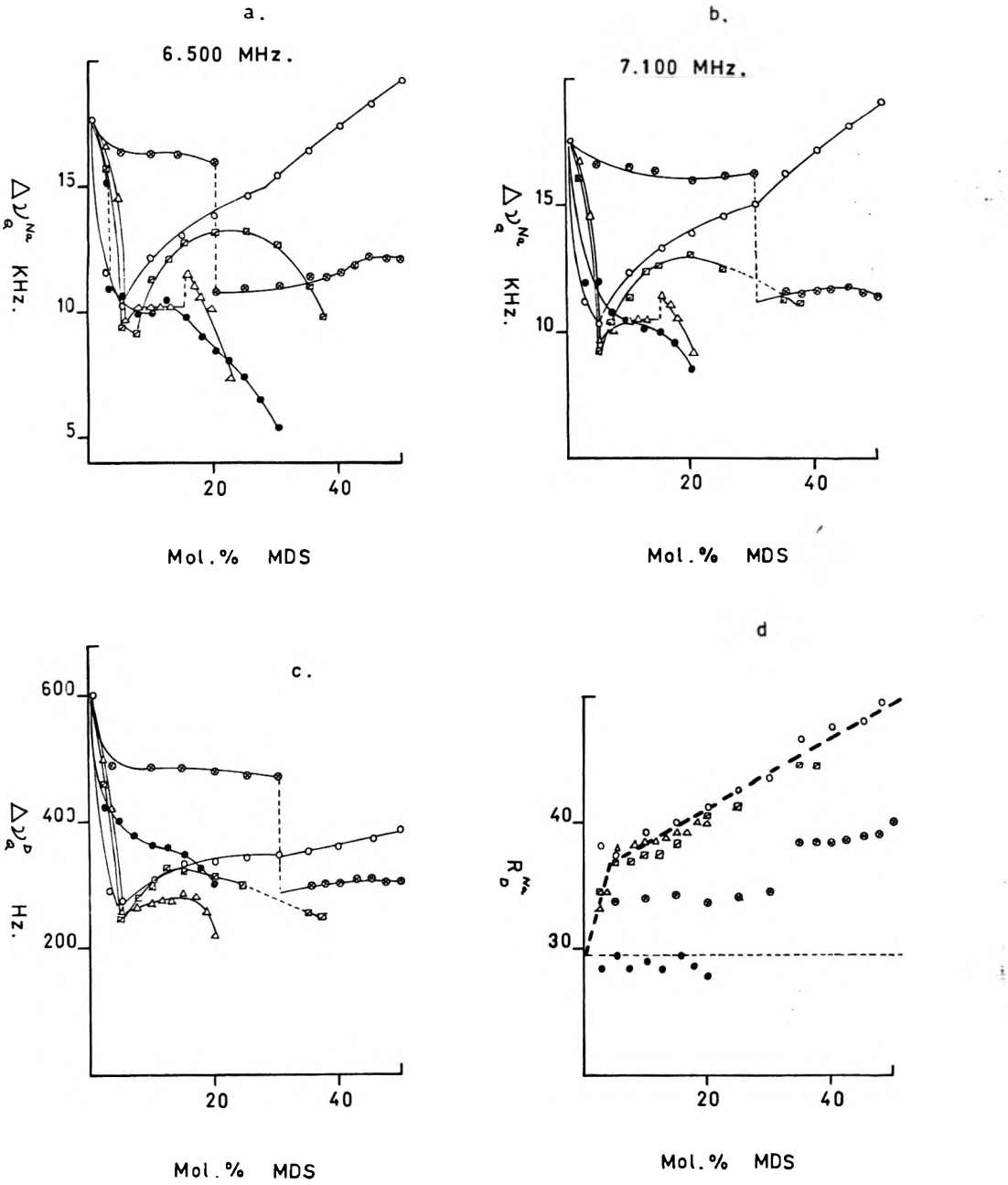

Figure 2. Sodium-23 and deuterium-2 quadrupole splittings measured for nematic phases with counterion substitution. (a) Mole percent of the substituted detergent MDS in the total detergent used to prepare the standard phase vs. sodium-23 quadrupole splittings. The points are identified according to the following ion substitutions: (O) Cs^+, (□) Rb^+, (△) K^+, (⊕) NH_4^+, and (●) $C_2H_5NH_3^+$. (b) Measurements made 6 months later on the same phases as in (a) at a frequency 7.1 MHz for Na-23. (c) Measurements of the deuterium resonance made at the same magnetic field as in (b) and at the same time by dialling 4.1 MHz after observation of the Na-23 resonance. (d) The ratio of the sodium to deuterium quadrupole splittings for measurements displayed in parts b and c of the figure. Samples were stored in a thermostat at the magnet temperature of 27°C.

cesium decyl sulfate are 46.7 wt % water, 6.54 wt % decanol, and 46.7 wt % cesium decyl sulfate. Phases with all three ions were prepared in which the lithium detergent was most strongly varied in concentration. The weight of water was always 1 g, decanol 0.14 g, cesium decyl sulfate 0.50 g, sodium decyl sulfate 0.20 g, and the lithium decyl sulfate weight was varied between 0.1 and 0.29 g in different phases. The quadrupole splittings for four nuclei in these phases are presented in Figure 4. The mole percent lithium decyl sulfate is a composition parameter represented as the fraction percent of moles of lithium decyl sulfate which would be present in a standard pure lithium counterion phase. This mole percent parameter is one of convenience to show the behavior of all four nuclear resonances with composition. The four curves shown in Figure 4 all have breaks at the same composition and are of the same general shape.

Ratios of Li-7 quadrupole splittings to both Cs-133 and Na-23 splittings vary by only about 8% over the compositions studied and no sudden discontinuity appears in the curve corresponding to the break at ~71 mol % LiDS in all curves of Figure 4. The ratio of Li-7 splittings to deuterium splittings changes by almost a factor of 2 over the composition range investigated.

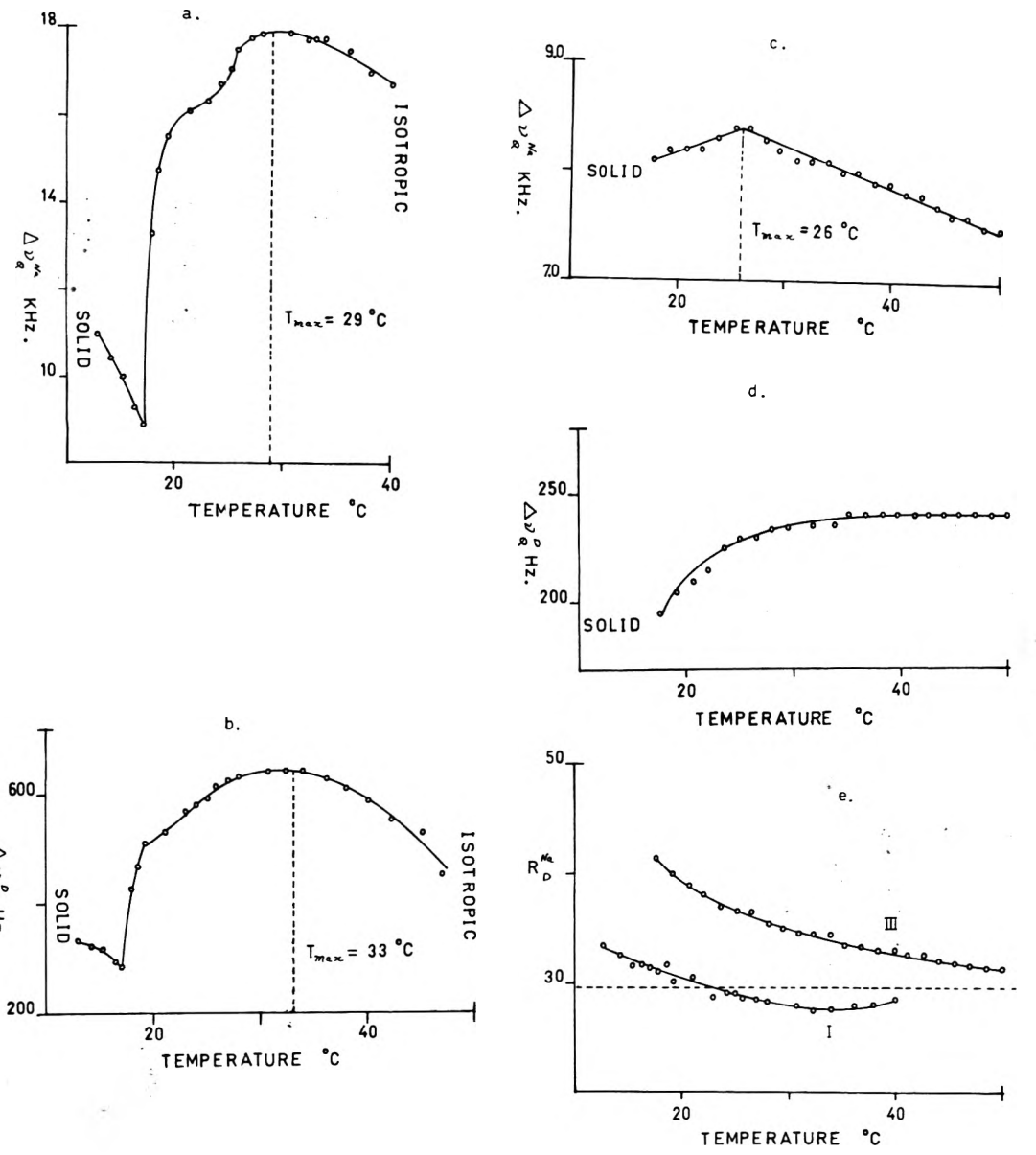

Figure 3. The temperature dependence of sodium and deuterium nuclear quadrupole splittings in two nematic phases. (a) and (b) correspond to studies of the ternary standard phase with sodium decyl sulfate–decanol–D_2O. (c) and (d) correspond to studies of the ternary phase with sodium sulfate and ethylene carbonate additives as described in the text. (e) shows ratios of sodium to deuterium quadrupole coupling for the ternary phase curve I and contaminated phase curve III.

Discussion

The discontinuities and breaks in the dependence of quadrupole coupling constant on sample composition represent sudden changes in the microorder and/or the uniaxial direction at or near the respective nuclear sites in the phases. Such precipitous changes are evidently changes in the phase superstructure, i.e., phase changes. The NMR signal is therefore, in this manner, a tool to investigate the possible nematic phases present in these lyotropic systems.

The results in Figure 2 show that the pure ternary phase with sodium decyl sulfate undergoes large changes in microorder at both the sodium and deuterium positions when the substitution for another ion occurs. For all other ions substituted except ammonium there is an initial very rapid fall in order over the first 5–8% substitution. In this range of 5–8% substitution a phase change occurs for Cs^+, Rb^+, and K^+ substitution. A phase change for NH_4^+ substitution occurs around 20 mol % in fresh samples and ~28 mol % in samples aged for 6 months. The phase change for the more organic ion $C_2H_5NH_3^+$ is somewhat ill defined but probably occurs around 15 mol % substitution in the total detergent.

The influence of simple counterion exchange on the stability and type of nematic phases was recently published in the form of a communication.[15] The present study considerably enlarges the original observations. Confirmation that the discontinuities in Figures 2–4 correspond to phase changes is shown in Figure 5. The disordering which occurs at most phase changes is accompanied often by loss of signal for all but the central transition of the sodium spectrum. This corresponds to randomization of the factor $\frac{1}{2}(3\cos^2\Omega - 1)$ from eq 3 for two coexisting phases. Sometimes broad satellite peaks do occur but in rare cases, the samples yield two clear sets of satellites for coexisting homogeneously ordered phases. In Figure 5 the two triplets for

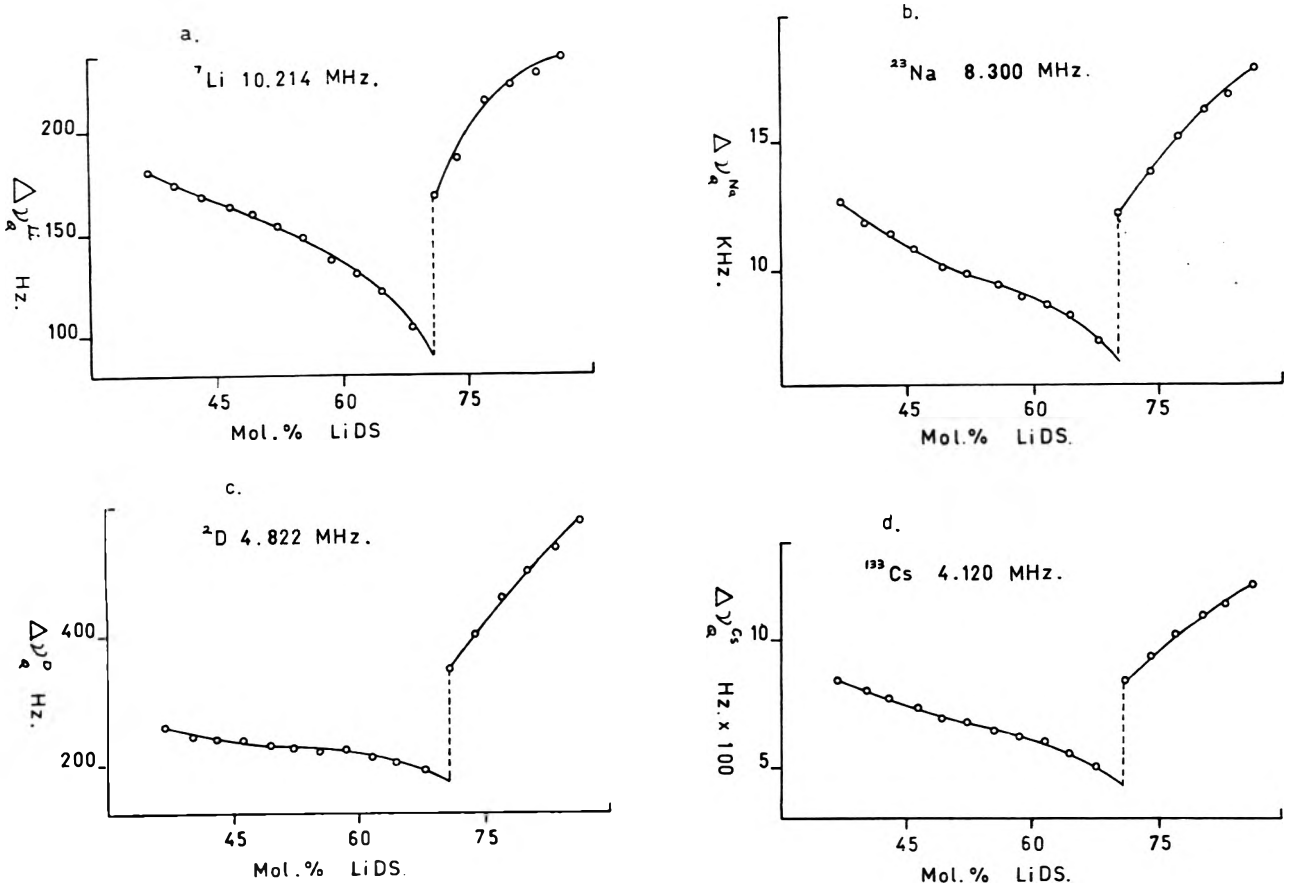

Figure 4. The dependence of the nuclear quadrupole splitting in a limited range of composition variation for lyotropic nematic phases prepared with three different counterions, Li^+, Na^+, and Cs^+. The variation of composition is represented by the change in lithium decyl sulfate in the phase expressed as a mole ratio percent of its concentration in a pure ternary phase of the standard mole composition for Li^+. The other two ions vary much more slowly in concentration with these phases as explained in the text.

Na-23 and two doublets for D-2 spectra are clearly visible for a region of discontinuity in the previous figures. Spectra were taken on the same sample by dialing one nucleus after the other.

There is considerable doubt in the literature regarding the different types of liquid crystalline phases which are formed in ternary soap systems.[23] Low angle X-ray diffraction work[26,27] has not been performed on these particular systems nor on magnetically oriented samples. We can definitely identify two types of nematic phase in this study which can coexist at a phase change. Coexistence of two nematic phases does not occur in the more simple thermotropic nematic mesophases. The pure ternary phase with 100% sodium decyl sulfate in the detergent component is designated in this study as nematic phase type I. After substitution of the sodium counterion a phase change occurs to nematic phase type II. The identity of phase type I for 0–8 mol % substitution is assured for all substituent cations used because nuclear quadrupole couplings change in a continuous manner back to the pure ternary phase (see Figure 2). There are no discontinuities in the dependence. After the phase change to type II the proof of a single phase type must await the definitive X-ray diffraction work. It is reasonable to assume that a single type II nematic phase has the same superstructure for all substituent cations. The further analysis of results reported here tend to confirm this assumption.

The differences between type I and type II nematic phases was investigated by studying the effect of spinning and nonspinning samples in the conventional iron magnet and cryogenic magnet spectrometers. In conventional spectrometers the spinning axis is perpendicular to the field while in the cylindrical solenoid of a cryogenic magnet the lines of force are parallel to the rotation axis. The deuterium doublet from the D_2O component was used to monitor the effect of rotation.

For both types of phases in a conventional magnet spectrometer the deuterium doublet took powder pattern form when the samples were first placed in the spectrometer. Type I phases responded more slowly to the orienting effect of the magnetic field but in 30 min for typical cases a single crystal pattern for the deuterium doublet had replaced the powder spectrum for both type I and type II mesophases. The transitions were not as sharp in the single crystal alignment for type I until a day or so had passed in the magnet. The quadrupole splitting for type I in the single crystal form was twice the separation of the doublet in the powder pattern indicating a parallel alignment to the magnetic field direction of the axis of the principal electric field gradient. The uniaxial direction of type I phases is thus parallel to the magnetic field direction. The powder diagram splitting for type II phases from whatever composition origin was always the same as the single crystal splitting. The type II phases all have the uniaxial nematic axis therefore perpendicular to the magnetic field.

After orientation of the type I phases in a conventional magnet the reorientation parallel to the field direction was sufficiently slow to allow the single crystal doublet to be

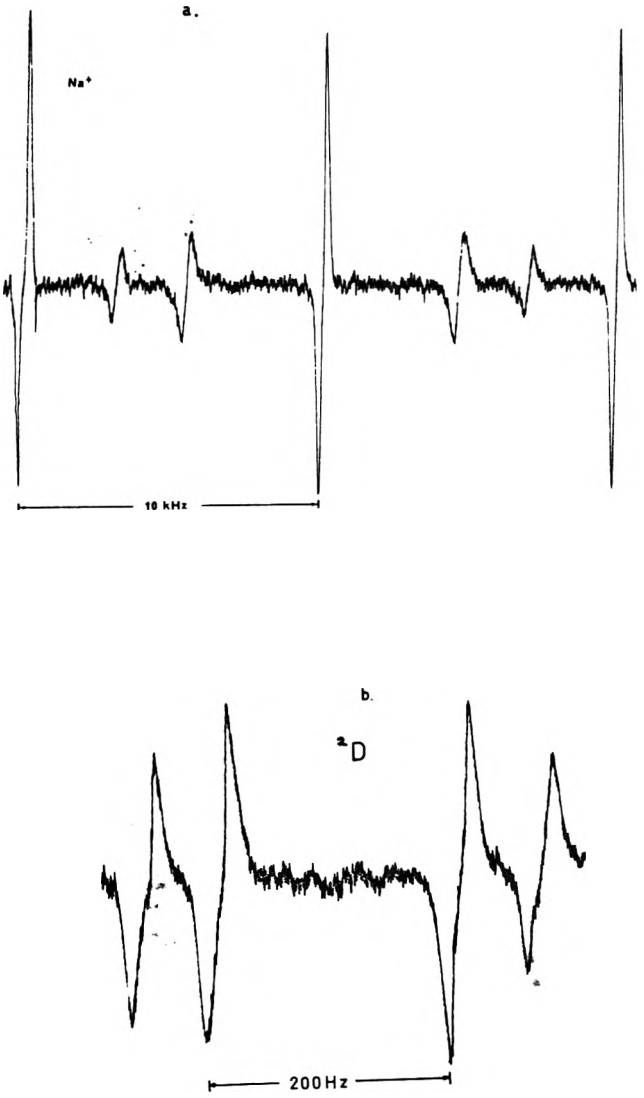

Figure 5. Sodium (a) and deuterium (b) NMR spectra in a region where two nematic phases coexist. Usually transitions removed from the spectral center are too broad to detect with the measurement conditions we used in this work. The upper spectrum (a) shows ±10 kHz calibration markers at the left and right of the spectrum. The two phases present exhibit two different quadrupole splittings and a coincident central transition. The deuterium spectrum (b) shows two doublets with the same intensity ratios as in part a of the figure for the satellite transitions.

studied as a function of angle of rotation of the tube. The dependence of the quadrupole splitting was a $(3\cos^2\Omega - 1)$ dependence with $\Omega = 0$ along the field direction. This confirms parallel alignment to the field of type I phases in the manner indicated earlier in the paper. The reorientation of type II phases was either too rapid to detect any rotation diagram or much less likely the phase chose always to orient in the particular perpendicular direction along the tube axis by some surface force effect. Observation of type II phases during sample spinning perpendicular to the field was initially accompanied by some line broadening which rapidly disappeared and was replaced by sharp transitions with improved resolution over stationary samples. It is suggested that the sample rotation at 10–80 Hz persuades the orientation to take up the unique perpendicular direction to the field in the spinning axis but that this process is not instantaneous. Spinning samples of type I at any measureable angular velocity about an axis perpendicular to the field always destroys the orientation.

The phases studied and illustrated in Figure 3a and 3b are identifiable as type I above 17°C and type II at the lower temperatures below the discontinuity. In the phases with three counterions, Li^+, Na^+ and Cs^+ which were illustrated in Figure 4, the high quadrupole splittings with greater than 72 mol % lithium decyl sulfate are type I phases while at lower lithium counterion contents the phases fall into the type II class. At the abrupt phase change in these five-component mixed detergent nematic fluids the Cs-133, Li-7, and Na-23 quadrupole splittings change by close to a factor 2. This is indicative of only small changes in the microdegrees of order of components but a change by 90° in the uniaxial alignment direction.

Further experiments were carried out to compare the alignment of a 2% methanol solute in the ternary standard phase (type I) and in the ternary phase to which 5 wt % sodium sulfate electrolyte was added (type II). The spectrum of the oriented methanol was observed in both a conventional and cryogenic magnet system Varian HR220 to determine the direction of uniaxial alignment. In type II with the added electrolyte the spinning of samples up to 80 Hz to improve resolution was possible in both spectrometers. In the absence of added electrolyte, spinning at 80 Hz to enhance resolution was still possible in the superconducting solenoid but in a Varian HA100 conventional iron magnet spectrometer the orientation of the methanol was destroyed at all spinning velocities. The dipole–dipole coupling constant was the same in all cases where alignment was preserved for both spinning and nonspinning experiments.

Further evidence of a change of 90° in the uniaxial alignment direction is obtained by observing the slope change $(d\Delta\nu/dc)$ for the three alkali metal resonances in Figure 4. The ratio of slopes before and after the phase change is always close to −2. Thus the microdegree of order which leads to distortion of these spherical ions remains approximately the same each side of the phase transition but the direction of alignment changes by 90°.

The nature of these two oriented type I and II phases in magnetically oriented samples should be investigated by low angle X-ray diffraction techniques. Further speculation beyond our present conclusions would be premature.

The nuclear quadrupole splitting of deuterium located in the water of these phases does derive from the degree of orientation of the principal axis of the electric field gradient tensor at the nuclear site. The nuclear quadrupole splittings of the alkali metal ion nuclei derive from a distortion of the spherical ions in a uniaxial manner by the nematic nature of the phase.[36] The degree of orientation in the deuterium case and the amount of distortion in the spherical case are both related to the microdegree of orientation at the nuclear sites as indicated in this study. Further comment and study on this aspect will be published soon.

References and Notes

(1) (a) This research generously supported by the National Research Council of Canada (NRCC) and the Defense Research Board of Canada (DRB). (b) In partial fulfillment for the degree of Ph.D., University of Waterloo, 1974.
(2) (a) L. W. Reeves, J. Sanches de Cara, M. Suzuki, and A. S. Tracey, *Mol. Phys.*, **25**, 1481 (1973); (b) L. W. Reeves, J. M. Riveros, R. A. Spragg, and J. R. Vanin, *ibid.*, **25**, 9 (1973).
(3) L. W. Reeves and A. S. Tracey, *J. Am. Chem. Soc.*, **96**, 1198 (1974).
(4) L. W. Reeves, A. S. Tracey, and M. M. Tracey, *J. Am. Chem. Soc.*, **95**, 3799 (1973).
(5) H. J. C. Berendsen and H. T. Edzes, *Ann. N.Y. Acad. Sci.*, **204**, 459

(1973).
(6) G. Lindblom and B. Lindman, *Mol. Cryst. Liq. Cryst.*, **22**, 45 (1973).
(7) J. Charvolin, P. Manneville, and B. Delache, *Chem. Phys. Lett.*, **23**, 345 (1973).
(8) J. Seelig and L. W. Niedberger, *J. Am. Chem. Soc.*, **96**, 2069 (1974).
(9) J. Seelig and W. Niederberger, *Biochemistry*, **13**, 1584 (1974).
(10) L. W. Reeves and A. S. Tracey, *J. Am. Chem. Soc.*, **96**, 365 (1974).
(11) L. W. Reeves, M. Suzuki, A. S. Tracey, and J. A. Vanin, *J. Inorg. Chem.*, **13**, 999 (1974).
(12) F. Fujiwara, L. W. Reeves, A. S. Tracey, and L. A. Wilson, *J. Am. Chem. Soc.*, **96**, 5249 (1974).
(13) D. M. Chen, L. W. Reeves, A. S. Tracey, and M. M. Tracey, *J. Am. Chem. Soc.*, **96**, 5349 (1974).
(14) F. Fujiwara, L. W. Reeves, and A. S. Tracey, *J. Am. Chem. Soc.*, **96**, 5250 (1974).
(15) D. M. Chen, K. Radley, and L. W. Reeves, *J. Am. Chem. Soc.*, **96**, 5251 (1974).
(16) K. D. Lawson and T. J. Flautt, *J. Am. Chem. Soc.*, **89**, 5489 (1967).
(17) P. J. Black, K. D. Lawson, and T. G. Flautt, *J. Chem. Phys.*, **50**, 542 (1969).
(18) P. J. Black, K. D. Lawson, and T. J. Flautt, *Mol. Cryst. Liq. Cryst.*, **7**, 201 (1969).
(19) R. C. Long, K. R. Long, and J. H. Goldstein, *Mol. Cryst. Liq. Cryst.*, **21**, 299 (1973).
(20) R. C. Long and J. H. Goldstein, *Mol. Cryst. Liq. Cryst.*, **23**, 137 (1973).
(21) R. C. Long, *J. Magn. Resonance*, **12**, 216 (1973).
(22) S. A. Barton, M. A. Raza, and L. W. Reeves, *J. Magn. Resonance*, **9**, 45 (1973).
(23) P. A. Winsor, *Chem. Rev.*, **68**, 1 (1968).
(24) G. J. Den Otter, W. Heijser, and C. MacLean, *J. Magn. Resonance*, **13**, 11 (1974).
(25) M. A. Raza and L. W. Reeves, *J. Magn. Resonance*, **8**, 222 (1972).
(26) V. Luzzati, H. Mustacchi, and A. E. Skoulios, *Nature (London)*, **180**, 600 (1957).
(27) V. Luzzati, H. Mustacchi, and A. E. Skoulios, *Discuss. Faraday Soc.*, **25**, 43 (1958).
(28) K. O. Lawson and T. J. Flautt, *J. Phys. Chem.*, **72**, 2066 (1968).
(29) A. Johannson and T. Drakenberg, *Mol. Cryst. Liq. Cryst.*, **14**, 23 (1971).
(30) J. Charovolin and P. Rigny, *J. Phys. C*, **30**, 4-76 (1969).
(31) E. A. C. Lucken, "Nuclear Quadrupole Coupling Constants", Academic Press, New York, N.Y., 1969.
(32) M. H. Cohen and F. Reif, *Solid State Phys.*, **5**, 321 (1957).
(33) C. P. Slichter, "Principles of Magnetic Resonance", Harper and Row, New York, N.Y., 1963.
(34) K. J. Mysels and P. Kapanan, *J. Colloid Interface Sci.*, **16**, 481 (1961).
(35) C. M. Suter, U.S. Patent 2098114 (1937); *Chem. Abstr.*, **32**, 191 (1938).
(36) D. Bailey, A. D. Buckingham, L. W. Reeves, and A. S. Tracey, *J. Magn. Resonance*, **18**, 344 (1975).

Electron Spin Resonance Studies of Ion Pair Complexes Involving the Tetracyanoethylene Anion Radical

M. P. Eastman,* D. A. Ramirez, C. D. Jaeger, and M. T. Watts

Department of Chemistry, The University of Texas at El Paso, El Paso, Texas 79968 *(Received July 5, 1974; Revised Manuscript Received September 22, 1975)*

Publication costs assisted by The University of Texas at El Paso

ESR studies of ion pair complexes formed in benzene by salts of tetracyanoethylene (TCNE) and complexing agents such as crown ethers and cryptands are reported. The values of the ^{23}Na and ^{39}K hyperfine splitting constants are given for the tight ion pair complexes formed from MTCNE salts and the crown ethers 18-crown-6, the A and B isomers of perhydrodibenzo-18-crown-6, and dibenzo-18-crown-6. ESR line width data indicate that the complex formed by NaTCNE and perhydrodibenzo-18-crown-6 (isomer A) exists in more than one ion pair form. A possible model for the structure of the crown ether complexes is discussed. No alkali metal hyperfine splittings are observed for the complexes formed in benzene by cryptand-222 and NaTCNE or KTCNE. ESR data indicate that cryptand-222 is more effective than the antibiotic valinomycin or the 18-crown-6 type crown ethers in terms of its ability to shield alkali metal cations from the $TCNE^-$ anion. ESR evidence is presented for the formation of ion pair complexes involving crown and cryptand complexed NH_4^+ cations. The relaxation times at room temperature for the 18-crown-6 complex with NaTCNE are $T_1 \sim T_2 \sim 2$ μsec. The question of the aggregation of ion pair complexes is discussed.

Introduction

Recently a number of papers have appeared in the literature describing the chemistry of the macrocyclic and macrobicyclic ligands known as crown ethers and cryptands.[1-22] Among these studies are a number describing the reactions of crown ether complexed alkali metal salts in low dielectric constant solvents.[1,9-16] For example, it has been demonstrated that perhydrodibenzo-18-crown-6 (PHDB) and 18-crown-6 (18C6) can dissolve potassium permanganate in benzene to produce a very efficient oxidizing agent with properties different from those of potassium permanganate in water.[9] Solutions of potassium acetate or potassium fluoride dissolved in benzene by the use of 18C6 are characterized by the presence of poorly solvated or "naked" anions.[13,14] Studies of a number of reactions indicate that the naked fluoride ion can act as a nucleophile or as a base. Crown ethers and cryptands can also be used to produce the radical ions of benzene and of toluene by dissolving alkali metals in these nonpolar solvents.[17,18] The resulting species apparently exist in solution as complexed ion pairs with electron transfer properties very dependent on the nature of the alkali metal complexing agent. However, in spite of the large number of studies of alkali metal complexing agents, there is at present relatively little known about the structure of crown ether or cryptand ion pair complexes in low dielectric media and the relationship of their structure to their reactivity.

In recent papers we reported that the alkali metal salts of tetracyanoethylene (MTCNE) when dissolved in benzene by means of crown ethers or the antibiotic valinomycin form tight ion pair complexes, and that the ^{23}Na hyperfine splitting of these complexes depends strongly on the complexing agent employed.[19,20] The purpose of this paper is to present detailed data on the properties and methods of formation of a number of MTCNE ion pair complexes in benzene and to extend the results when warranted to other ion pair complexes.

Experimental Section

Details of the ESR spectrometer and methods used in determining g values have been published elsewhere.[20,21] The pulse ESR studies were carried out on an instrument described in the literature.[22]

The dibenzo-18-crown-6 (DBC) was purchased from Aldrich Chemical Co. and was purified by recrystallizing twice from toluene and drying under vacuum. The melting point of the purified material was 163–164°C. The crown ethers PHDB (isomers A and B) and 18C6 were supplied by H. K. Frensdorff of E. I. duPont de Nemours and Co., Inc. The hexaoxadiamine macrobicyclic commonly known as cryptand-222 (C222) was kindly provided by Dr. Alex Popov. The TCNE salts were prepared as described in the literature.[23] The benzene and toluene used in these experiments were dried and stored over sodium ribbon.

Both quartz and Pyrex sample tubes were employed in this work. These sample tubes were cleaned by previously reported techniques to determine whether ions from the wall of the sample tube were participating in ion pair formation.[20] Such effects have previously been noted by Graceffa and Tuttle[24] and were also noted in the course of these experiments.

Results and Discussion

No ESR signals due to free radicals in solution could be obtained from mixtures of solid NaTCNE and benzene. In the presence of the crown ethers or C222, small amounts of NaTCNE could be dissolved in benzene to produce yellow solutions which yielded distinctive ESR spectra characteristic of the $TCNE^-$ anion radical. In all of the spectra obtained, the four nitrogen nuclei in the $TCNE^-$ were completely equivalent with a temperature independent hyperfine splitting of 1.57 ± 0.01 G. The spectra obtained from solutions containing crown ethers showed the interaction of the unpaired electron on the $TCNE^-$ with one ^{23}Na nucleus. The spectrum of the $TCNE^-$ in solution containing C222 showed no hyperfine splitting due to ^{23}Na.

In all of the experiments an excess of complexing agent was present in solution and in most cases undissolved NaTCNE was evident. Previously published results have shown that complexing agents of the type used in these experiments form 1:1 complexes with Na^+ and K^+ ions.[1,20,21,25–28] These observations together with the ESR spectra obtained suggest that an equilibrium for the formation of crown or crypt complexed ion pairs might be written

$$(CA) + (NaTCNE)\ \text{solid} \rightleftarrows [CANa^+\text{–}TCNE^-] \quad (1)$$

where CA is the complexing agent. Experiments at a constant nominal NaTCNE concentration of 1×10^{-4} M in which the concentration of several crown ethers was varied from 2×10^{-4} to 5×10^{-3} M showed an increase in radical concentration with increasing crown ether concentration. In these experiments there was no dependence of the ^{23}Na hyperfine splitting (A_{Na}) on crown ether concentration. Furthermore, published data indicate that when KF is dissolved in benzene by 18C6, eq 1 applies.[13] However, it should be noted that conductance studies on an asolectin membrane system indicate that 3:1 CE–cation complexes are formed when alkali metal cations are solubilized in the membrane.[29] The results reported here do not preclude the formation of 3:1 or similar complexes. The results do, however, clearly indicate that the cation and anion are not separated when crown ether complexes are formed, and that the value of A_{Na} is not affected by the concentration of complexing agent.

Figure 1 shows the value of the ^{23}Na hyperfine splitting (A_{Na}) from about 0 to 200°C for the crown complexes investigated. At room temperature all the sytems investigated yielded an isotropic g value of 2.00278 ± 0.000003 and line widths for the individual hyperfine lines of about 30 mG. Even at 200°C no decomposition of the complexes was noted. The values of A_{Na} obtained did not depend on the method of preparing the sample tube.

Figure 1 shows that the type of crown ether employed in complex formation has a profound effect on the value of A_{Na} at low temperatures and that the differences in A_{Na} values are decreased at higher temperatures. At 195°C the value of A_{Na} falls in the range 0.340 ± 0.035 G for all of the complexes studied. In general, the value of A_{Na} for PHDB(A) and DBC increases with temperature while the value for 18C6 and PHDB(B) decreases with temperature. DBC is seen to have the greatest temperature dependence with A_{Na} being given over the temperature range 30–195°C by the exponential expression $A_{Na} = 1.97e^{-858/T}$.

At temperatures below 35°C the $M = \pm 3/2$ lines of each ^{23}Na quartet in the spectrum of the PHDB(A) complex were broadened relative to the $M = \pm 1/2$ lines. At 35°C the $M = \pm 3/2$ lines were about 10% broader than the $M = \pm 1/2$ lines while at −10°C they were about 80% broader. This type of line width effect is characteristic of a situation in which two or more ion pair forms are in rapid equilibrium.[30] No evidence of a similar line width effect was obtained for the PHDB(B) and 18C6 complexes. In order to investigate the line width effects over a wide temperature range, the complexes were prepared in a 2:3 toluene–benzene mixed solvent system. A mixed solvent system was chosen for this work because, in general, the solubility of the complexes in pure toluene was not great enough for study by ESR. Figure 2 shows the value of A_{Na} for the PHDB(A), PHDB(B), and 18C6 complexes in the mixed solvent system. Over the temperature range investigated only the PHDB(A) complex showed the line width effect characteristic of rapidly converting ion pair forms. The values of A_{Na} measured above 5°C in the mixed solvent system differed little from the values obtained in pure benzene.

The above data for the crown ether complexes suggest a structure for the ion pair in which the oxygen atoms of the crown ether and the nitrogen atoms of the $TCNE^-$ are in parallel planes and the alkali metal ion lies along the line joining the centers of the $TCNE^-$ and CE molecules. In most respects this model is similar to that advanced by Smid et al. for crown ether complexed fluorenyl ion pairs.[25–27] This proposed structure places the metal cation in the nodal plane of the wave function for the unpaired electron on $TCNE^-$ (thus explaining the relatively small values of A_{Na}) and also allows the four nitrogens in $TCNE^-$ to be equivalent.[31] Since the sign of the alkali metal hyper-

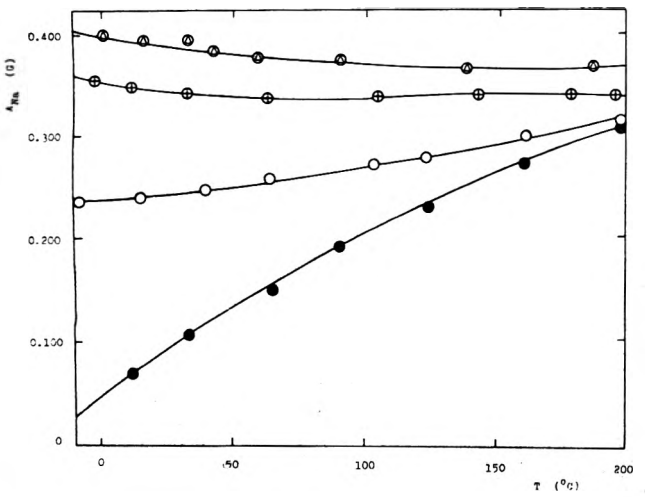

Figure 1. A_{Na} as a function of temperature for the (Δ) 18C6, (+) PHDB(B), (O) PHDB(A), and (●) DBC complexes with NaTCNE in benzene.

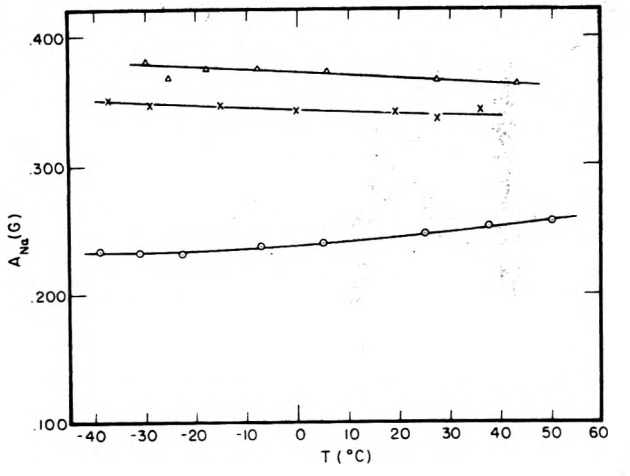

Figure 2. A_{Na} as a function of temperature for the (Δ) 18C6, (X) PHDB(B), and (⊙) PHDB(A) complexes with NaTCNE in 2:3 toluene–benzene mixtures.

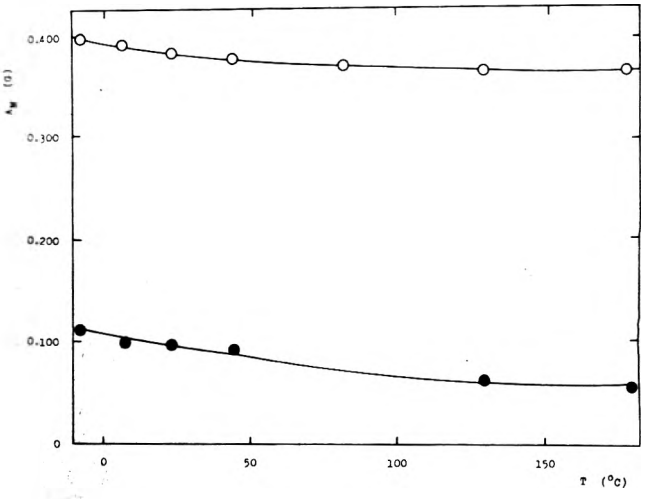

Figure 3. A_M as a function of temperature for the 18C6 Na^+–$TCNE^-$ (O) and 18C6K^+–$TCNE^-$ (●) complexes in benzene.

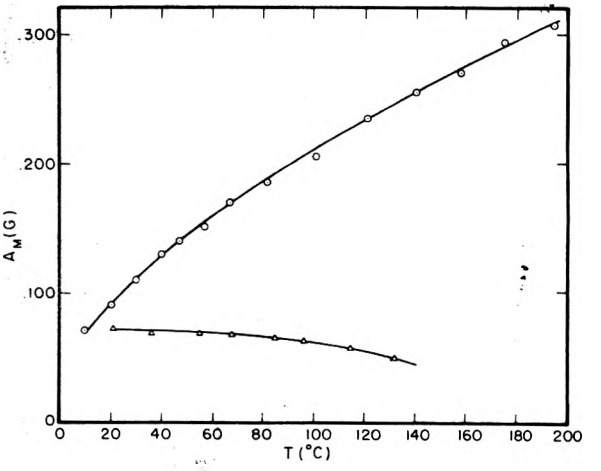

Figure 4. A_M as a function of temperature for the DBCNa^+–$TCNE^-$ (⊙) and DBCK^+–$TCNE^-$ (Δ) complexes in benzene.

fine splitting constant is not known, the mechanism by which unpaired spin density is transferred to the alkali metal nucleus cannot be determined. Possible mechanisms have recently been reviewed.[32]

According to the above model, the tight ion pair complex formed by PHDB(A) (cis–syn–cis isomer)[33] can have two possible nonequivalent structures. In one structure the $TCNE^-$ anion is found on the same side of the crown ether as the alkyl groups joined to the crown; in the other structure the alkyl groups point away from the anion. The crown ethers 18C6 and PHDB(B) (cis–anti–cis isomer)[34] form complexes in which the possible structures, in terms of anion position, are equivalent.

Tight ion pair complexes similar to those formed by NaTCNE have been formed using KTCNE. Figure 3 shows the value of A_M for the 18C6 Na^+–$TCNE^-$ complex and for the 18C6 K^+–$TCNE^-$ complex. Figure 4 shows A_M for the complexes DBCNa^+–$TCNE^-$ and DBCK^+–$TCNE^-$. From these figures it is seen that the 18C6 complexes have similar temperature dependences while the DBC complexes do not. A further comparison of these complexes may be made by calculating the s orbital spin density (ρ_M^{ns}) on the alkali metal cations by means of the expression[30,35]

$$A_M = Q_M \rho_M^{ns} \qquad (2)$$

Here Q_M represents the splitting expected from unit population of the outer shell's orbital of the alkali metal in question. Calculations using published Q_M values yield at 30°C for the 18C6 complexes $\rho_K^{4s} = \rho_{Na}^{3s} = 1.2 \times 10^{-3}$; for DBC the values are $\rho_K^{4s} = 9.2 \times 10^{-4}$, $\rho_{Na}^{3s} = 3.7 \times 10^{-4}$.[36] The temperature dependence of A_M and the calculation of ρ for the 18C6M^+–$TCNE^-$ complexes suggest that 18C6Na^+–$TCNE^-$ and 18C6K^+–TCNE have very similar structures. By the same criteria the structure and properties of DBCNa^+–$TCNE^-$ and DBCK^+–$TCNE^-$ complexes appear different. This would seem to indicate that the structure of the complexes formed are quite sensitive to the size of the cation, in relation to the flexibility of the crown ether, to the nature of the dipolar field set up by the crown ether oxygen and to the size of the "hole" in the crown.

The PHDB(A)K^+–$TCNE^-$ complex showed no evidence of existing in more than one ion pair form in benzene or toluene–benzene mixed solvent systems. In general the ^{39}K hyperfine splittings were found to be less sensitive to crown ether structure than the ^{23}Na hyperfine splittings. For example, at room temperature the K hyperfine splitting for PHDB(B)K^+–$TCNE^-$ complex (0.104 G) is 1.19 times that observed for the PHDB(A)K^+–$TCNE^-$ complex. For the

corresponding NaTCNE complexes the Na hyperfine splittings differ by a factor of 1.35 at room temperature. Thus, it is possible that the PHDB(A)K^+–$TCNE^-$ complex exists in the same forms as the PHDB(A)Na^+–$TCNE^-$ complex but the values of the ^{39}K hyperfine splitting for the forms differ only slightly. Another possibility is, of course, that the PHDB(A)K^+–$TCNE^-$ complex has one preferred form.

The complexes formed in benzene by KTCNE and C222 showed a temperature independent line width of 0.057 G and no evidence for unresolved ^{39}K hyperfine splitting. The complex formed by NaTCNE and C222 produced similar spectra with no resolvable ^{23}Na hyperfine splitting. Both complexes showed completely equivalent nitrogen in the $TCNE^-$ with A_N = 1.57 G. Thus, it is not clear from the ESR spectra to what extent the C222 complexed cation and the $TCNE^-$ anion are associated in solution. Studies of MTCNE complexes with antibiotic valinomycin (VM) at room temperature in benzene have yielded A_K = 0.025 G for the VMK^+–$TCNE^-$ complex and A_{Na} = 0.276 G for the VMNa^+–$TCNE^-$ complex.[19,37] A comparison of the above hyperfine data with that from the crown ether complexes (see Figures 3 and 4) clearly indicates that C222 is the most effective complexing agent studied in terms of the ability to shield the complexed K^+ and Na^+ cations from the $TCNE^-$ anion. Valinomycin is more effective than the crown ethers in shielding complexed K^+ from $TCNE^-$ but surprisingly only about as good as crown ethers at shielding complexed Na^+ from $TCNE^-$.

The 18C6Na^+–$TCNE^-$ complex has also been studied by pulse ESR in an effort to determine the effect of crown ether complexation on relaxation times. At room temperature $T_1 \sim T_2 \sim 2$ μsec for the 18C6Na^+–$TCNE^-$ complex in benzene. The relaxation times previously reported for the K^+TCNE^- loose ion pair in dimethoxyethane are $T_1 \sim T_2 \sim 8$ μsec.[38-40] Clearly the formation of tight ion pair complexes has a strong effect on the relaxation time for the $TCNE^-$ radical. Additional studies of this problem are in progress.

It is also possible to produce complexed ion pairs by letting crown or C222 solubilized iodides react with neutral TCNE in benzene. A possible mechanism for this reaction is

$$(MI)_{solid} + CA \rightleftarrows CAM^+\text{–}I^- \quad (3)$$

$$CAM^+\text{–}I^- + TCNE \rightleftarrows CAM^+\text{–}TCNE^- + \tfrac{1}{2}I_2 \quad (4)$$

This technique has worked with sodium iodide, potassium iodide, and with ammonium iodide. The values of A_{Na} and A_K from ion pairs produced by this method using crown ethers are the same as those obtained by MTCNE salts solubilized in benzene with crown ethers. The ion pairs formed from ammonium iodide using crown ethers and C222 as the complexing agent yield the nine-line spectrum characteristic of the $TCNE^-$ radical. Line shape analysis shows the hyperfine line to be Gaussian with peak-to-peak first derivative line widths in the range 0.050–0.100 G. No temperature dependence of the line shapes has been noted in the range 10–100°C.

A possibility which should be considered in this work is the formation of aggregates of complexed ion pairs in the benzene. Smid et al. have reported formation of CE separated fluorenyl ion pair aggregates in ethereal solvents at concentrations around 10^{-2} to 10^{-3} M.[27] Crown ether complexed fluorenyl tight ion pairs were shown not to form aggregates under these conditions. The preceding observations were explained in terms of a less stable structure for crown complexed tight ion pair aggregates compared to crown separated ion pair aggregates. If aggregates formed in the case under study here, it would be expected that there would be an aggregation of crown complexed tight ion pairs. This would lead to $TCNE^-$ radicals being close enough to each other to produce appreciable line broadening from dipolar interactions or Heisenberg spin exchange.[38] The line widths observed at room temperature for the crown ether complexes were typically about 0.030–0.040 G. In a number of solvents the line widths for the $TCNE^-$ anion radical at low concentrations fall in the range of 8–35 mG.[20,38] Thus, the line width data provides no evidence for the formation of CE–NaTCNE aggregates. It should also be noted in regard to the question of aggregation that crown ethers prevent or inhibit the dimerization of MTCNE salts in tetrahydrofuran.[21] The data obtained for the VM and crypt complexed ion pairs also offer no evidence for aggregation.

The apparent close proximity of the crown ether, the cation, and the anion in the crown ether complexes suggest that it might prove possible to synthesize crown ethers which would form complexes with alkali metal salts in such a way that the anion portion of the complex could react only with well-defined substrate structures. A recent article by Cram and Cram has described other aspects of crown ether "host-guest" chemistry.[41]

Acknowledgments. Dr. H. K. Frensdorff of E. I. duPont de Nemours and Co. generously provided the PHDB and 18C6 crown ether used in this work. Dr. Alex Popov kindly provided the C222. The pulse ESR studies were carried out by Dr. Paul Percival at Varian Associates. Helpful discussions with Dr. Josef Michl are gratefully acknowledged. This research was supported by the Robert A. Welch Foundation of Houston, Texas.

References and Notes

(1) C. J. Pederson, *J. Am. Chem. Soc.*, **89**, 7017 (1967).
(2) J. L. Dye, M. G. DeBacker, and V. A. Nicely, *J. Am. Chem. Soc.*, **92**, 5226 (1970).
(3) J. L. Dye, M. T. Lok, F. J. Tehan, R. B. Coolen, N. Papadakis, J. M. Ceraso, and M. G. DeBacker, *Ber. Bunsenges. Phys. Chem.*, **75**, 659 (1971).
(4) J. N. Roitman and D. J. Cram, *J. Am. Chem. Soc.*, **93**, 2231 (1971).
(5) M. J. Maskornick, *Tetrahedron Lett.*, 1797 (1972).
(6) R. A. Bartsch and K. E. Wiegers, *Tetrahedron Lett.*, 3819 (1972).
(7) R. C. Helgeson, K. Koga, J. M. Timko, and D. J. Cram, *J. Am. Chem. Soc.*, **95**, 3021, 3023 (1973).
(8) A. L. Kurts, P. I. Dem'yanov, I. P. Beleskaya, and O. A. Reutov, *Zh. Org. Khim.*, **9**, 1313 (1973).
(9) D. J. Sam and H. E. Simmons, *J. Am. Chem. Soc.*, **94**, 4024 (1972).
(10) M. Svaboda, J. Hapala, and J. Zavada, *Tetrahedron Lett.*, 265 (1972).
(11) E. Shchori and J. Jagur-Grodzinski, *J. Am. Chem. Soc.*, **94**, 7957 (1972).
(12) D. J. Sam and H. E. Simmons, *J. Am. Chem. Soc.*, **96**, 2250 (1974).
(13) L. Liotta and P. Harris, *J. Am. Chem. Soc.*, **96**, 2250 (1974).
(14) F. L. Cook, C. W. Bowers, and C. L. Liotta, *J. Org. Chem.*, **39**, 3416 (1974).
(15) J. W. Zubrick, B. I. Dunbar, and H. D. Durst, *Tetrahedron Lett.*, **No. 1**, 71 (1975).
(16) D. Landini, F. Montanari, and F. M. Pirisi, *J. Chem. Soc., Chem. Commun.*, 879 (1974).
(17) G. Kaempf, S. Raynal, A. Collet, F. Schue, S. Boileau, and J. Lehn, *Angew. Chem., Int. Ed. Engl.*, **13**, 611 (1974).
(18) M. A. Komarynsky and S. I. Weissman, *J. Am. Chem. Soc.*, **97**, 1589 (1975).
(19) M. P. Eastman, *J. Chem. Soc., Chem. Commun.*, 789 (1974).
(20) M. T. Watts, M. Lu, and M. P. Eastman, *J. Phys. Chem.*, **77**, 625 (1973).
(21) M. T. Watts, M. L. Lu, R. C. Chen, and M. P. Eastman, *J. Phys. Chem.*, **77**, 2959 (1973).
(22) M. Huisjen and J. S. Hyde, *Rev. Sci. Instrum.*, **45**, 669 (1974).
(23) (a) O. W. Webster, W. Mahler, and R. E. Benson, *J. Am. Chem. Soc.*, **84**, 3678 (1962); (b) R. Melby, R. J. Hardy, R. H. Hertler, W. Maher, R. E. Benson, and W. E. Mochel, *ibid.*, **84**, 3374–3387 (1962).
(24) P. Graceffa and T. R. Tuttle, Jr., *J. Chem. Phys.*, **50**, 1908 (1969).
(25) K. H. Wong, G. Konizer, and J. Smid, *J. Am. Chem. Soc.*, **92**, 666 (1970).

(26) U. Takaki, T. E. Hogen Esch, and J. Smid, *J. Am. Chem. Soc.*, **93**, 6760 (1971).
(27) U. Takaki, T. E. Hoger Esch, and J. Smid, *J. Phys. Chem.*, **76**, 2152 (1972).
(28) C. J. Pedersen and H. K. Frensdorff, *Angew. Chem., Int. Ed. Engl.*, **11**, 16 (1972).
(29) G. Eisenman, G. Szabo, S. Ciani, S. McLaughlin, and S. Krasne, *Prog. Surf. Membr. Sci.*, **6**, 139 (1973).
(30) J. H. Sharp and M. C. Symons in "Ions and Ion Pairs in Organic Reactions", Vol. 1, M. Swarc, Ed., Wiley-Interscience, New York, N.Y., 1972, p 177.
(31) J. Feuer, Ph.D. Thesis, Texas Tech University, 1970.
(32) J. L. Sommerdyk and E. de Boer in "Ions and Ion Pairs in Organic Reactions", Vol. 1, M. Swarc, Ed., Wiley-Interscience, New York, N.Y., p 321.
(33) N. K. Dalley, D. E. Smith, R. M. Izatt, and J. J. Christensen, *J. Chem. Soc., Chem. Commun.*, 90 (1972).
(34) D. E. Fenton, M. Mercer, and M. R. Truter, *Biochem. Biophys. Res. Commun.*, **48**, 10 (1972); M. Mercer and M. R. Truter, *J. Chem. Soc., Dalton Trans.*, 2215 (1973).
(35) The assumption of a positive value for A_M and consequently a positive spin density on the alkali metal cation is implicit in eq 3. Confirmation of this assumption rests on a measurement of the sign of A_M. At the present time such measurements have not proved possible due to the small solubility of the complexes in benzene. It should also be noted that eq 3 neglects direct overlap effects and that the values of Q_M used to calculate ρ_M do not take into account the effect of possible s orbital contraction in the alkali metal cation. The limitations of (3) are discussed in more detail in several review articles.[30,32]
(36) J. P. Goldsborough and T. P. Kohler, *Phys. Rev. A*, **133**, 135 (1965).
(37) M. P. Eastman, C. D. Jaeger, D. A. Ramirez, S. L. Kelly, and P. W. Percival, *J. Magn. Reson.*, in press.
(38) M. P. Eastman, R. G. Kooser, M. R. Das, and J. H. Freed, *J. Chem. Phys.*, **51**, 2690 (1969).
(39) M. R. Das, S. B. Wagner, and J. H. Freed, *J. Chem. Phys.*, **52**, 5404 (1970).
(40) D. L. Leniart and P. Percival, unpublished results.
(41) D. J. Cram and J. M. Cram, *Science*, **183**, 803 (1974).

Quadrupole Coupling Constants in Adsorbed Water. Effects of Chemical Exchange

H. A. Resing

Chemistry Division, Naval Research Laboratory, Washington, D.C. 20375 *(Received July 11, 1975)*

Publication costs assisted by the Naval Research Laboratory

Deuteron and proton NMR relaxation times are reported for water of various isotopic compositions adsorbed on NaX zeolite. The quadrupolar relaxation mechanism is shown to dominate the deuteron relaxation; a quadrupole coupling constant of 225 ± kHz is found for the deuterons in physically adsorbed water molecules. This method of supercooling liquids by use of the adsorbed state to obtain T_1 minima for quadrupolar nuclei is proposed as a new method for estimation of quadrupole coupling constants in liquids; the method is self-contained and requires no additional information on liquid state correlation times. The respective correlation times found for the diffusion and rotation processes differ from one another by less than a factor of 2 over a four decade range of correlation times. This implies a fundamental relation between the rotation and diffusion processes in liquid water. The effects of chemical exchange of the physically adsorbed water with a surface $Al(OH)_n$ species were observed; subject to certain assumptions, the Al–O–D bond angle is 121.5 ± 0.02° and the Al–O distance is 1.68 ± 0.20 Å in the complex. A formula for the effects of rotation about a single axis on the motional averaging of an arbitrary electric field gradient tensor is given.

I. Introduction

In the adsorbed state it is possible to vary the molecular mobility continuously from that characteristic of the liquid state to that characteristic of the solid state.[1-3] In the case of multilayer adsorption the adsorbed matter forms a state which is liquid-like in that (a) there is no long-range order,[4] and (b) there is high mobility at temperatures at which the normal liquid exists.[2] Thus, the adsorbed state may be used as an approximate model of the liquid state which may be supercooled to any desired degree and studied at leisure. Unfortunately, only molecular probes such as magnetic resonance, neutron scattering, or infrared spectroscopy may be used to study such adsorbed-liquid states, because the heterogeneous nature of the system precludes to a large extent the study of such bulk properties as viscosity and compressibility.

In this research the liquid under study is water, and a question asked is "What is the degree of coupling between the rotational and translational elementary motions?" These motions may to some extent be separated by means of the nuclear properties of the hydrogen isotopes available for study by nuclear magnetic resonance relaxation techniques. Deuterium interacts most strongly with its ambient electric field gradient; since this gradient arises mainly from within the molecule, reorientation of the gradient is synonymous with molecular reorientation.[5] The proton, in contrast, interacts only with its local dipolar magnetic field; since this field arises both from nuclei within and without the molecule, it can be reoriented both by molecular diffusion and rotation.[6] It is shown here that the correlation time for rotation, τ_r, and the correlation time for diffusion, τ_d, are the same within a factor of 2 of one another over a considerable temperature range in water adsorbed in zeolite 13-X.

The extension of the (adsorbed) liquid region to lower mobilities also simplifies the determination of nuclear quadrupole coupling constants. In the restricted liquid range of most substances it is sufficient to write the spin–lattice re-

laxation time[5] as $1/T_{1Q} = 3/2\pi^2(QCC)^2\tau$, where QCC is the quadrupole coupling constant and τ the correlation time (neglecting asymmetry of the quadrupole coupling tensor); in order to extract either the correlation time or the coupling constant it is thus necessary to know one or the other a priori.[7] This difficulty is of course removed if the T_{1Q} minimum can be observed; this is not possible for most liquids because freezing intervenes. In this work the minimum T_1 for the deuteron in adsorbed water has been observed. The value of the quadrupole coupling constant deduced agrees with the values found for liquid water and ice, indicating that the hydrogen bond structure of the zeolitic water is, on the average, little disturbed from that of the bulk phases.

Previous interpretations of the proton relaxation in this water–zeolite system furnished a detailed kinetic and structural model for a surface proton-containing species. The deuteron relaxation results presented here[8] furnish an effective quadrupole coupling constant for the surface species, which reinforces the model proposed.

II. Experimental Section

The water–zeolite 13-X specimens used are those prepared for the previous study,[9] namely, (a) $D_{1.33}H_{0.67}O$ adsorbed on a hydrolyzed, large-crystal specimen of zeolite NaX ($P/P_0 = 0.876$), and (b) normal water on another zeolite specimen from the same preparation ($P/P_0 = 0.809$). Because of the flatness of the isotherm, these specimens have essentially the same filling factor θ.

NMR relaxation measurements were carried out on a Bruker SXP spectrometer, modified to give short receiver dead time (~5 μsec) at 60 MHz. The spin–lattice relaxation time T_1 was measured by the 180–90 method; the spin–spin relaxation time by the CPMG method.[10] Low temperature free induction decays were used to estimate the rigid lattice second moment for the protons.[11] No attempt was made to find the second "phase" with short T_2 expected[12] for the deuteron transverse relaxation, primarily because of long dead time at 9.2 MHz. Temperature was measured with a copper–constantan thermocouple in contact with the sealed specimen tubes; the temperature of the gas stream was controlled by an Artronix proportional controller. The accuracy of the sample temperature measurement is estimated as ±0.5 K and the precision as ±0.2 K. On the basis of reproducibility the accuracy of relaxation time measurements is estimated at ±5%.

III. Results and Discussion

A. *Overview.* The measured relaxation times are presented in Figure 1. It has been shown previously[9] that there are two kinds of hydrogen "sites", those of physically adsorbed water molecules, and those of an "aluminate" surface species. In Figure 1 is plotted the mean lifetime, τ_{ex}, of a proton (deuteron) in the physisorbed water molecular state with respect to exchange with the surface species; this line divides Figure 1 into two parts: the lower right, where the protons in the water molecules relax independently of the surface species (and vice versa), and the upper left where a weighted average relaxation rate is observed. (Along the "exchange line" the measured "long T_2" is effectively equal to τ_{ex} and furnishes a method of studying kinetics of surface reactions.[13-15]) Therefore, it is convenient to discuss separately the rotation–diffusion motion of the physically adsorbed water on the one hand and the exchange kinetics and structure of the surface species on the other.

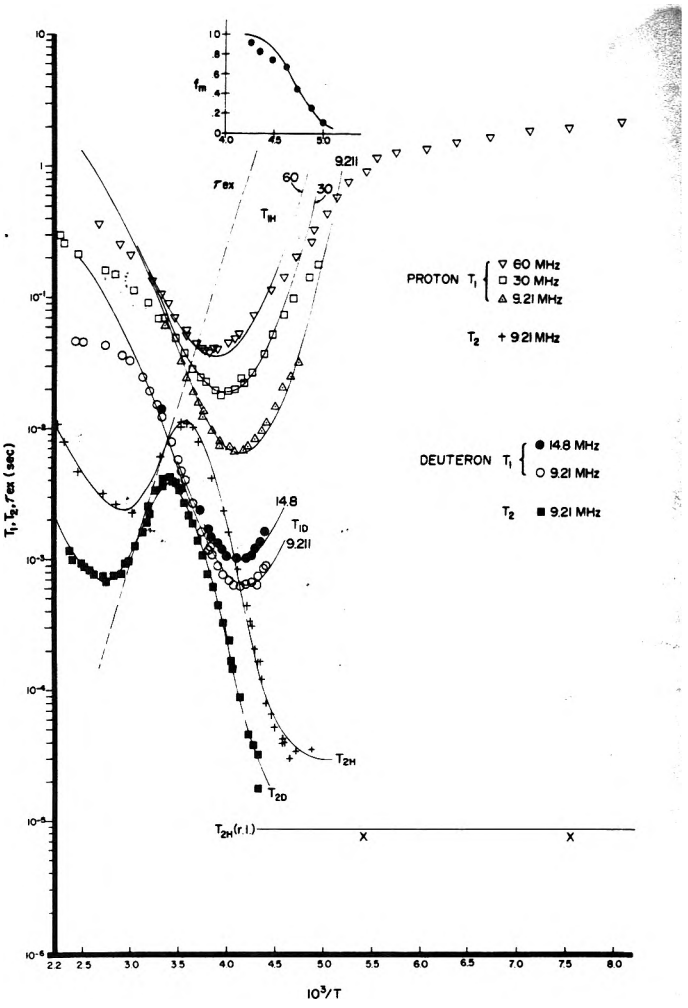

Figure 1. Relaxation times for protons in water and deuterons in $(D_{0.67}H_{0.33})_2O$ both adsorbed on NaX zeolite. The dashed line indicates the lifetime for exchange out of the physically adsorbed state. The solid lines represent least-squares fit of theory to the data; see text. The inset shows the fraction of physically adsorbed molecules in the "mobile state" with respect to the "apparent phase transition"; solid line is fit of theory.

B. *Relaxation Due to Molecular Motions of the Physically Adsorbed Water.* Bloembergen, Purcell, and Pound[6] (BPP) explained NMR relaxation by a dipolar relaxation mechanism in which molecular motion modulates internuclear dipolar magnetic fields and thereby induces the transitions in the energy levels of the system necessary for relaxation to thermodynamic equilibrium; such a mechanism holds for the protons of the physisorbed water. Quadrupolar nuclei such as deuterium interact also with electric field gradients and are thus relaxed also by a similar mechanism in which intramolecular electric fields are modulated by molecular rotation.[5] If only isotropic molecular rotation is considered, both mechanisms result in the following well-known mathematical forms[5] (limited in the case of quadrupolar nuclei to spin unity)

$$T_{1d(q)}^{-1} = \frac{2}{3}\sigma_{0d(q)}^2\left[\frac{\tau_r}{1+\omega^2\tau_r^2} + \frac{4\tau_r}{1+4\omega^2\tau_r^2}\right] \quad (1)$$

$$T_{2d(q)}^{-1} = \sigma_{0d(q)}^2\left[\tau_r + \frac{5\tau_r/3}{1+\omega^2\tau_r^2} + \frac{2\tau_r/3}{1+\omega^2\tau_r^2}\right] \quad (1b)$$

where

$$\sigma_{0d}^2 = \frac{3}{5}\gamma^2\hbar^2 I(I+1)\sum_j r_{ij}^{-6} \quad (2)$$

and

$$\sigma_{0q}^2 = (\mathrm{QCC})^2\left(1+\frac{\eta^2}{3}\right)(6\pi)^2/80 \quad (3)$$

$$(\mathrm{QCC}) = \left(\frac{eQ}{h}\frac{\partial^2 V}{\partial Z^2}\right) \quad (4)$$

Here QCC is the quadrupole coupling constant, the subscript d indicates dipolar, q quadrupole, and all the other parameters have their usual significance. The data of Figure 1 for the "molecular relaxation region" are in gross agreement with the predictions of (1): (a) at a given NMR frequency there is a minimum in T_1; (b) the value of T_1 at the minimum is proportional to the NMR frequency; (c) T_2 decreases monotonously as the temperature decreases; (d) in the extreme narrowing region $T_1 \simeq T_2$. Other aspects of these data can be accounted for if the BPP theory is extended by invoking a distribution of correlation times, namely, (a) for both protons and deuterons the ratio T_1/T_2 at the T_1 minimum is greater than the value of 1.6 predicted from (1); (b) at low temperatures such that $\omega\tau > 1$ for all ω, T_1 is not proportional to ω^2 as (1) predicts; and (c) before the onset of rigid lattice behavior in T_2 there is an apparent "two phase" transverse relaxation behavior for the protons. Concerning the last point, the fraction f_m of protons in the mobile phase (long T_2) is indicated in the inset of Figure 1. Such effects of a correlation time distribution have been seen in many adsorption and other systems.[16,17] The following equations, appropriate to a distribution of correlation times, were therefore fitted to the data:[18]

$$T_1^{-1} = \frac{2}{3}\sigma_0^2\int_0^\infty \mathrm{P}(\tau)\left[\frac{\tau}{1+\omega^2\tau^2}+\frac{4\tau}{1+4\omega^2\tau^2}\right]d\tau \quad (5)$$

$$T_2^{-1} = \frac{1}{3}\sigma_0^2\left\{3f_m^{-1}\int_{-\infty}^{\tau_c}\tau\,\mathrm{P}(\tau)\,d\tau + \int_{-\infty}^{\infty}\left[\frac{5\tau}{1+\omega^2\tau^2}+\frac{2\tau}{1+4\omega^2\tau^2}\right]\mathrm{P}(\tau)\,d\tau\right| \quad (6)$$

$$f_m = \int_0^{\tau_c}\mathrm{P}(\tau)\,d\tau \quad (7)$$

$$T_{2r} = \tau_c = (\sigma_0^2)^{-1/2} \quad (8)$$

In the above T_{2r} is the rigid lattice transverse relaxation time, τ_c is a "cutoff" value of the correlation time which divides the distribution into slow ($\tau > \tau_c$) and fast ($\tau < \tau_c$) moving molecules, and σ_0^2 is given by (2) or (3) above as appropriate. A mathematically simple distribution, adequate for the present and other cases,[16,17] is the log-normal distribution function, as

$$\mathrm{P}(\tau)\,d\tau = (B/\pi)\exp(-B^2Z^2)\,dZ \quad (9)$$

$$Z = \ln\tau/\tau^* \quad (10)$$

Here τ^* is the median correlation time, assumed to be given by a free volume law appropriate to liquids according to which

$$\tau^* = \tau_0\exp[A/(T-T_0)] \quad (11)$$

where τ_0 and A depend on molecular parameters and where T_0 is the temperature at which free volume disappears. A convenient expression for the inverse width parameter B is then[18]

$$B = \alpha(T-T_0) \quad (12)$$

There are thus five adjustable parameters necessary to fit the data for each hydrogen isotope; three to characterize the temperature dependence of the median correlation time, one to characterize the width of the distribution, and the appropriate second moment. *We wish to test initially the hypothesis that the proton and deuteron relaxation data in the molecular relaxation regime of Figure 1 are governed by one and the same correlation time.* (Discussion of the molecular motions represented by the correlation time is postponed until a later section.) Therefore, the "pertinent" data of Figure 1 were subjected to a non-linear least-squares fitting procedure[19] under two sets of assumptions; the resulting best fit parameters are given in Table I. By pertinent data is meant (a) those data clearly in the molecular relaxation regime, and (b) those T_1 data not affected by the low temperature "plateau", which is assumed to arise from an unrelated cause; thus the 60-MHz proton T_1 data points were only given a weight of 0.5 because they lie so close to the exchange line, i.e., to τ_{ex} extrapolated. First it was assumed that the hypothesis under test is true, which required a proton second moment, a deuteron second moment, a median correlation time τ^*, and a spread parameter. This first trial fitted the data to within ±15%. Second it was assumed that the deuterium median correlation time differed from that of the proton; this difference was allowed for by (a) assuming that the proton and deuteron correlation times are related by a scale factor and (b) by allowing an independent width parameter for the deuterons; thus only two new parameters were introduced. The second trial fitted the data to within ±13%, no significant improvement over the first. Further the deuterium correlation time is the same within a factor (=0.59) of the order unity of that for the protons, and the distribution widths for the protons and deuterons are essentially the same. Thus, the test hypothesis appears well verified.

In Figure 1 are plotted theoretical lines which represent the second fit referred to above. It can be seen that the model successfully accounts for T_1/T_2 ratio, frequency dependence, and apparent phase transition effect (relaxation times and mobile fraction). The fit, however, appears to show some systematic deviations, especially about the proton T_1 minima.

C. *The Quadrupole Coupling Constant.* The data of Figure 1 clearly reveal a T_1 minimum for the deuterons in the molecular relaxation range. This allows an estimate of the quadrupole coupling constant (QCC) for the physically adsorbed water molecules, which is presented in Table II where it is compared with those of bulk water and ice. Within experimental error it is the same as that in liquid water. Now the QCC is first of all a molecular parameter, depending on molecular electron densities.[20] Hydrogen bonding also plays a role in reducing the QCC from its free molecule value to that observed in condensed media.[21] An obvious conclusion is that the average hydrogen bonded configuration of the zeolitic water is the same as that of the normal liquid, despite the fact that many of the 30 or so molecules per large cage of the zeolite X structure must be adjacent to the oxide lined walls of the alumino-silicate framework. Perhaps hydrogen bonding to these oxide surface compensates for the missing water molecules. This technique of observing the T_1 minimum in the adsorbed state thus offers some promise for the determination of QCC's in molecules, even such polar ones as water.

TABLE I: Molecular Relaxation, Least-Squares Fit Parameters

Parameter	Units	Trial I value 6-parameter fit	Trial II value 8-parameter fit	Value expected
σ_{0d}^2	10^{10} rad^2 sec^{-2}	2.10 ± 0.07	2.03 ± 0.05	2.29[a]
σ_{0q}^2	10^{10} rad^2 sec^{-2}	19.4 ± 0.7	22.5 ± 0.8	23.5[b]
$\alpha_{hydrogen}$	10^{-3} K^{-1}	4.1 ± 0.1	4.4 ± 0.1	
$\alpha_{deuterium}$	10^{-3} K^{-1}	$\alpha_{hydrogen}$	4.1 ± 0.2	
τ_{0} hydrogen	10^{-13} sec	4.83 ± 1.3	1.86 ± 0.6	
τ_{0} deuterium	10^{-13} sec	τ_{0} hydrogen	(0.59 ± 0.08)τ_{0H}	
A	K	778 ± 60	650 ± 47	
T_0	K	166 ± 3	173 ± 3	
σ_x	%	15	13	

[a] V. I. Kvlividze, *Mater. Vses. Soveshch. Tseolitam, 2nd, 1964*, 42 (1964). [b] Reference 7.

TABLE II: Hydroxyl Quadrupole Coupling Constants (kHz)

Substance	QCC
Ice[a]	213–216
Liquid water[b]	230 ± 10
Zeolitic water[c]	225 ± 4
Surface hydroxyl	
(a) Direct	31[d]–22[e]
(b) Corrected for motion	241[d,f]
Aluminum hydroxides[g]	
(a) Boehmite	194 ± 10
(b) Diaspore	197 ± 10
(c) Bayerite	230 ± 10
(d) Gibbsite	224 ± 10
(e) Anodic oxide	214 ± 10

[a] P. Waldstein, S. W. Rabideau, and J. A. Jackson, *J. Chem. Phys.*, 41, 3407 (1964). [b] Reference 7. [c] From eq 3 and σ_{0q}^2 of Table I; error estimate is statistical only. [d] Calculated using correlation time for aluminate surface species of ref 9 and high temperature T_2 of present study. [e] Result of least-squares fit of this study in which Al–O–D bond angle Ψ was determined. [f] Calculated using QCC = 31 kHz and bond angle Ψ of Diaspore (AlOOH), $\Psi \sim 128°$ as estimated from ref 28. [g] Reference 26.

In the present instance by the observation of the T_1 minimum the necessary information about correlation times is furnished by the deuteron relaxation experiment itself. This is in contrast to, e.g., the work of Powles and Rhodes[7] in which it was necessary to obtain such information from other experiments. However, a necessary assumption here was that of a distribution of correlation times, and the value of T_1 at the minimum is strongly affected by such a distribution. For instance if eq 1, in which a single correlation time if assumed, is used to extract the QCC, a value of 148 kHz is obtained, which is significantly lower than that for bulk water and would imply an average structure with much stronger hydrogen bonds than in the liquid. However, as pointed out above, the distribution of correlation times is quite necessary to explain various features of the data. As far as the proton relaxation is concerned, the second moments deduced from T_1 are nonsensically too small, in terms of intramolecular bond distances, unless the correlation time distribution is invoked. These facts engender confidence in the application of the correlation time distribution and the ensuing results. However, unfortunately, in order to learn the width of the distribution a rather more detailed treatment of the relaxation times is required than merely the observation of the T_1 minimum; however, even this may be systematized, as has been pointed out.[22]

D. *Correlation Times for Diffusion and Rotation.* In condensed phases of spherical nonpolar molecules the processes of molecular rotation and diffusion may be entirely uncoupled; it is well known for such systems that even in the solid state[23] the molecules rotate with jump frequencies many orders of magnitude greater than those for translational diffusion. However, for irregularly shaped molecules it seems likely that diffusion and rotation are related; for example, in solid benzene[24] rotation about the hexad axis is "free", but rotation about other axes occurs only in the diffusion step. For polar or hydrogen bonded molecules, where there is also some friction between moving neighbors, it seems likely that diffusion and rotation might be intimately related also. It was pointed out by BPP[6] for instance that the jump times for rotation and diffusion in liquid water at room temperature are about the same, and we have previously[3,25] "assumed" that such is true at all temperatures in our treatment of relaxation data for adsorbed water. "Assumed" is perhaps too strong; the proton relaxation data more or less indicated this. However, now the deuteron relaxation times depend only on the molecular rotational correlation time;[5] and the proton relaxation times tell about diffusion as well.[6] Thus, a quantitative statement is possible as to the ratio of the jump time for rotation τ_r to that for the diffusion τ_d in liquid (adsorbed) water over a wide range of temperatures.

To develop the argument, examine first a hypothetical system in which the correlation time for diffusion τ_d is clearly different from that for rotation τ_r. Assume that both are given by the Arrhenius law

$$\tau_{r(d)} = \tau_0 \exp(H_{r(d)}/RT) \qquad (13)$$

where $\tau_0 = 10^{-12}$ sec for both processes (a standard assumption) and $H_d = 2H_r = 6.8$ kcal/mol. These correlation times are plotted vs. reciprocal temperature in Figure 2. First, the protons are relaxed by the dipolar mechanism; diffusion modulates the internuclear fields at a given proton arising from nuclei in other molecules; rotation modulates mainly the field at a nucleus arising from the intramolecular proton partner. Since the intramolecular and intermolecular fields are about equal to one another[6] the values of T_1 at the respective T_1 minima for diffusion ($10^3/T \sim 3$) and for rotation ($10^3K \sim 5.6$) will be roughly equal to one another, as is indicated in Figure 2. Note also the behavior of T_2 for this hypothetical proton system; at the lowest temperatures T_2 is representative of a completely rigid system; as the temperature is raised there is a transition to a T_2 value characteristic of rotating molecules fixed in position; further warming causes additional "motional narrowing", finally bringing T_2 equal to T_1. Note that it is only isotropic diffusion that can bring T_2 equal to T_1; in Figure 1 the successful fitting of the proton relaxation times to a model requiring $T_1 = T_2$ at the highest temperatures implies isotropic diffusion. The deuterons, on the other

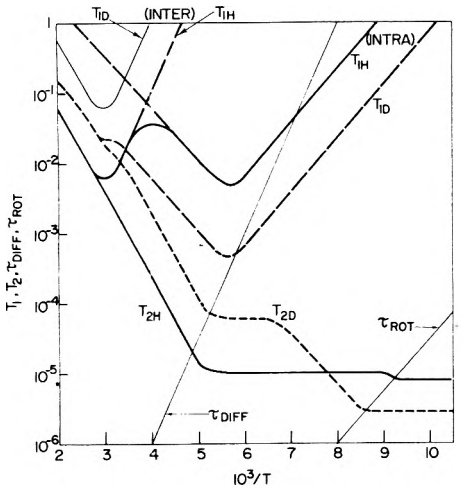

Figure 2. Relaxation times for protons and deuterons in a hypothetical water system in which the activation enthalpy for diffusion is twice that for rotation.

hand, are relaxed by a combination of dipolar and quadrupolar mechanisms. However, for the rotational motion the contribution of the dipolar process is negligible and has not been included in Figure 2; since the effective second moment for deuteron quadrupole relaxation is about ten times that for proton dipolar relaxation (Table I), the deuteron relaxation time is only one tenth as great as that for protons. Diffusion does not modulate the quadrupole coupling in the model of Figure 2, since the rotation averages the field gradient completely. Therefore, only dipolar coupling of deuterons to other deuterons and protons is modulated by diffusion, and because of the low gyromagnetic ratio of the deuterons this intermolecular contribution to the deuteron T_1 is very small, as indicated in Figure 2. The most obvious feature of Figure 2 is that the main deuteron T_1 minimum is displaced to a much lower temperature with respect to the proton T_1 minimum caused by diffusion at which $T_1 \simeq T_2$. This is in marked contrast to Figure 1 in which the experimental proton and deuteron spin–lattice relaxation times have their respective minima at the same temperature. It is clear from Figure 2 that sweeping H_r from $H_d/2$ to equality with H_d will (a) sweep τ_r into equality with τ_d and (b) therefore will sweep the low temperature rotational minima to higher temperatures and finally to a temperature such that all T_1 minima coincide; this is in agreement with experiment. *It is this coinciding of proton and deuteron T_1 minima that established directly that correlation times for diffusion and rotation are practically the same.* In section III.B it was shown that the median proton correlation time is less than a factor of 2 greater than that for the deuterons; this ratio is the best quantitative estimate available of the difference between diffusional and rotational correlation times in liquid water. *This difference appears to be independent of temperature, and implies a fundamental connection between rotational and translational diffusion processes in this hydrogen bonded system.*

E. *The Surface Complex.* At relatively low temperatures the long T_2 represents the motion of the physically adsorbed molecules, as just discussed. The short T_2, which would represent the intrinsic motions of the surface complex in this and the intermediate temperature range, was not seen for the deuterons because of experimental "dead-time" limitations, although it was seen and properly accounted for in the previous proton study.[9] At intermediate temperatures the long T_2 measures directly the lifetime of a deuteron (proton) in the physically adsorbed state with respect to exchange with the surface complex. At the highest temperatures of this study the long (and only) deuteron T_2 is the inverse of the "average relaxation rate over both proton environments".[13] It is the purpose of this section to discuss the intermediate and high temperature deuterium relaxation data of this study, especially in terms of the structure of the surface complex.

Because the intrinsic transverse relaxation rate for the surface complex is so great, it dominates the average (referred to above) at the high temperatures and the relaxation rate is given in theory by[2,9,13]

$$T_2^{-1} = P_b T_{2b}^{-1} \tag{14}$$

$$= P_b \sigma_{ob}^2 \tau_b \tag{15}$$

where P_b is the fraction of the deuterons (protons) which are in the surface complex, and where T_{2b}, σ_{ob}^2, and τ_b are, respectively, the intrinsic relaxation time, the second moment, and the correlation time of the surface complex or "b" phase. The new structural information gained here about the surface complex arises from the deuteron second moment, viz. quadrupole coupling constant.

Proton second moments, due to both like and unlike nuclear spins, were previously determined[9] via eq 15. It was concluded[9] that (a) the surface complex consists of $Al(OH)_n$ units, where n is at least two, and (b) that the hydroxyl groups are rotating rapidly about the aluminum–oxygen bond vector, which gives partial motional narrowing effects on the second moment. The additional motions of the surface complex responsible for the correlation time in eq 15 are rotation of the whole complex (τ_r) and the exchange reaction itself (τ_{ex}), where[6]

$$\tau_b^{-1} = \tau_r^{-1} + \tau_{ex}^{-1} \tag{16}$$

It is necessary to include both of these independent processes (as well as fast hydroxyl group rotation) to fit the total data suite. This model, based on the proton study,[9] allows predictions about the deuteron second moment; the quadrupole coupling constant should be close to those found for various aluminum hydroxides (Table II)[26] and the fast hydroxyl rotation should give rise to motional narrowing effects.

The effect of rapid molecular motion on a field gradient tensor is simply to replace the tensor by its average over the motion;[5,21,27] this average will now be developed. In the absence of any nuclear motion let the electric field gradient at the site of a deuteron be given by the tensor (V_{ij}) of largest principal value V_{zz}' and asymmetry parameter η. Assume that the z' principal axis associated with principal value V_{zz}' makes an angle θ with a "laboratory" axis z. Form the unit vector $\mathbf{y}'' = \mathbf{z}' \times \mathbf{z}/\sin\theta$. Let the y' axis be the principal axis associated with the principal value V_{yy}', taken as the second largest in absolute magnitude. Let $\beta = \cos^{-1}(\mathbf{y}'\cdot\mathbf{y}'')$. Now let the body in which the tensor is embedded rotate stochastically about the z axis so that over time all orientations about z are equally likely, and average the tensor elements over the motion, i.e., over all orientations. The result is a new, axially symmetric tensor of which the principal value largest in absolute magnitude is

$$V_{zz}'' = FV_{zz}' \tag{17}$$

$$F = \tfrac{1}{2}[3\cos^2\theta - 1 - \eta(\sin^2\beta - \cos^2\beta)] \qquad (18)$$

with principal axis along the rotation axis. Via eq 4 the quadrupolar coupling constant is multiplied by the same factor and the effective second moment is reduced by F^2. The reduction factor F is plotted vs. θ (for extreme values of η and β), in Figure 3; the value of the "magic angle", i.e., that angle θ for which $F = 0$, can be seen to cover a range of 90°, depending on the values of the asymmetry parameter and orientation angle β. Further, the angle θ for a given reduction factor F is a multiple valued function of F. Clearly the second moment alone will not suffice to find V_{zz}', θ, η, and β. The orientation of the tensor within the molecular framework of the surface complex must be specified.

The working hypothesis is that the deuterons exist in the surface complex as hydroxyl groups;[9] fortunately the properties of hydroxyl groups can be easily summarized.[21] First, the z' principal axis lies along the oxygen–deuterium bond direction; thus θ in (18) is the complement of the Al–O–D bond angle. Second, the y' principal axis is perpendicular to the Al–O–D plane; thus $\beta = 0$. Third, the asymmetry parameter η is generally near a tenth; it is hereafter neglected. Finally, the value of the quadrupole coupling constant depends to a large extent on hydrogen bond strengths and lengths; for hydroxyl groups in various solid aluminum hydroxides the QCC's are in the neighborhood of 200 kHz[26] (see Table II), about the same as those in liquid water or ice. There is little information available on Al–O–D bond angles; in diaspore[28] the Al–O–D angle is about 128°, but in this structure it is not even clear that there is an Al–O bond in the valence sense, since each Al has six roughly equidistant oxygen or hydroxyl nearest neighbors. Nevertheless, 128° is sufficiently close to the "magic bond angle" of 125.26° so that appreciable motional averaging of the field gradient tensor is expected (see Figure 3). For instance, using the proton correlation time[9] for motion of the complex, and the proton fraction in the complex ($P_b = 0.17$), and taking $\eta = 0$ and $\theta = 128°$, gives a full QCC for the deuteron of 241 kHz; whereas the assumption of no motional averaging gives QCC = 31 kHz; clearly the former, based on motional averaging, due to fast hydroxyl group rotation is in better agreement with expectation for OH groups.

The aim of this section is to specify as completely as possible the structure of the surface complex under the hypothesis that it is an $Al(OH)_n$ group. The deuteron second moment (under the assumption of motional averaging, as outlined above) depends only on the bond angle Ψ (see Figure 4), if a "full" QCC is given; the "full" QCC is assumed to be 240 kHz. The bond angle is assumed to be the smallest angle greater than $\pi/2$ which is consistent with eq 18. The proton second moment due to aluminum depends only on the aluminum–hydrogen distance (Figure 4), but motional averaging effects must be accounted for in this case also; the procedure has been outlined previously.[9] Specification of the Al–O–D(H) triangle requires three parameters, but there are only two independent data, the second moments; therefore the O–D distance was assumed to be 1.0 Å. To find the remaining two structural parameters the whole set of proton and deuteron relaxation times in the exchange region was subjected to a grand least-squares fitting procedure; the Al–O–D(H) triangle parameters found were the Al–O distance and the bond angle Ψ. These, and the other parameters necessary to describe the data are summarized in Table III (it can be seen that the resulting parameters agree within statistical error with those found

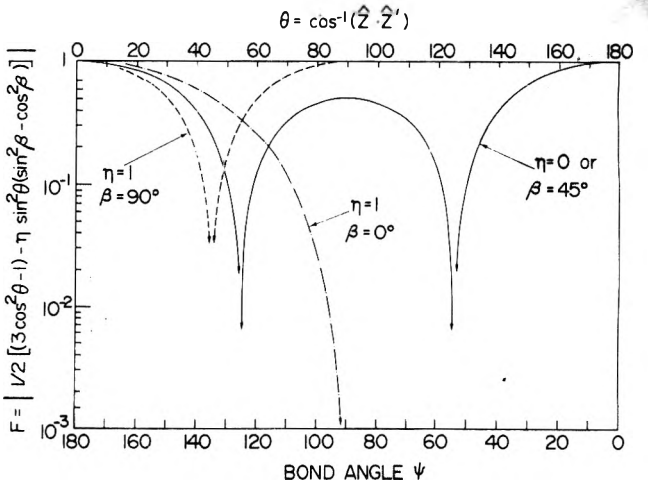

Figure 3. Reduction factor F (see text) for tensor principal value largest in absolute value as a function of θ, the angle between its principal axis and the rotation axis. Various extreme cases of asymmetry parameter and orientation angle β are given.

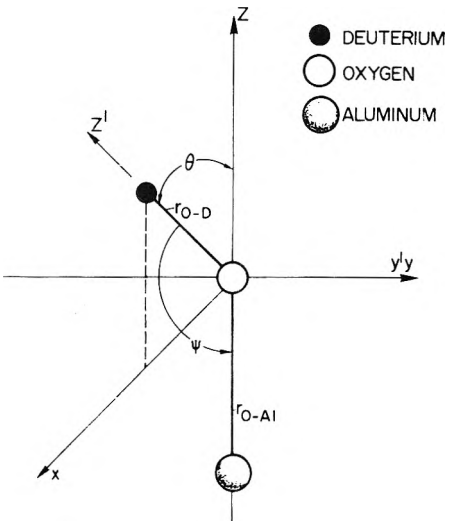

Figure 4. Diagram of Al–O–H; z' and y' axes are directions of principal axes of field gradient tensor which summarize past experience.

for the proton relaxation alone[9] for those parameters which were determined in this and the previous study). The fit to the data is illustrated in Figure 5. The bond angle of 121.5° is rather larger than the tetrahedral angle, but the Al–O distance of 1.68 Å agrees well (within rather large error) with the lengths of Al–O bonds in tetrahedral aluminosilicates.[29] The ensemble of assumed and found data is consistent with the hypothetical $Al(OH)_n$ structure with fast motional averaging due to hydroxyl group rotation.

With respect to the proton exchange reaction between the surface complex and the physically adsorbed water, the lifetime of a proton in a surface complex and that of a deuteron are the same within experimental error (Table III). Because of the heavier deuteron mass a longer deuteron lifetime might have been expected.

Finally, it has been pointed out that the protons of this complex are not very acidic, because their equilibrium configuration is in the $Al(OH)_n$ state;[30] this more or less agrees with the well-known amphoteric nature of $Al(OH)_3$. In contrast, the protons of hydrogen Y zeolite are very acidic; it

TABLE III: Surface Complex and Exchange Reaction, Structural and Motional Parameter Estimates

Parameter		Units	H data only[a]	H and D data[b]
τ_{0r}	preexponential factor for surface complex rotation	10^{-8} sec	5.4 ± 6	5.3^{+10}_{-3}
H_r	activation enthalpy for surface complex rotation	kcal/mol	3.08 ± 0.6	3.2 ± 0.6
$\tau_{0\,ex}$	preexponential factor for proton exchange out of surface complex	10^{-12} sec	1.9 ± 3.3	$4.9^{+5}_{-2.4}$
H_{ex}	activation enthalpy for proton (deuteron) exchange out of surface complex	kcal/mol	12.0 ± 1	11.4 ± 0.4
$\sigma_{0\,Al}$	that part of the proton intramolecular nuclear dipolar second moment of the surface complex arising from nonproton nuclei	10^8 rad^2 sec^2	4.13 ± 3	3.4 ± 1.3
r_{Al-O}	the aluminum–oxygen bond length in the surface complex	Å	1.65[c]	1.68 ± 0.20
λ	a ratio: that part σ_{OH}^2 of the proton intramolecular second moment in the surface complex due to protons divided by σ_{0Al}^2		0.64 ± 0.18	0.62 ± 0.20
σ_{0D}^2	the effective deuteron second moment for the surface complex arising from quadrupolar interactions	10^8 rad^2 sec^{-2}		30 ± 10
θ	the Al–O–D bond angle	deg	109[d]	121.49 ± 0.01
f_r	the exchange time (τ_{ex}) for protons, divided by that for deuterons at identical P/P_0			1.01 ± 0.06

[a] Data of ref 9. [b] This study. [c] Assumed, based on tetrahedral Al–O bond lengths in zeolites as given in ref 29. [d] Assumed tetrahedral angle.

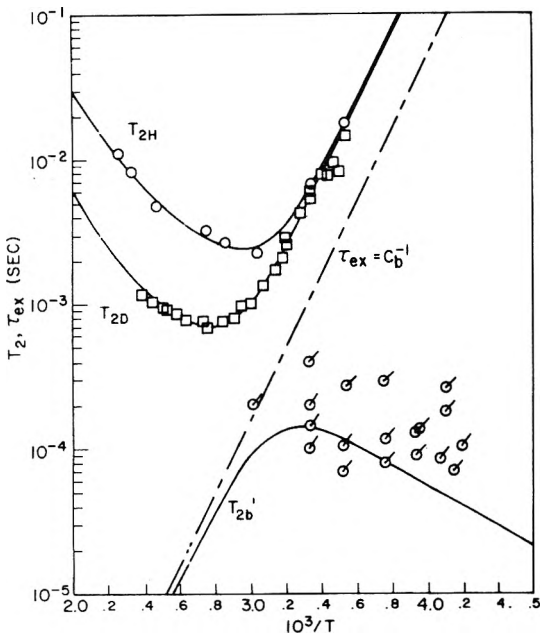

Figure 5. T_2 for protons and deuterons in the exchange region. The solid lines represent best fit of theory to experiment. The lifetime of a proton (deuteron) in the surface complex is indicated as τ_{ex}.

appears that upon adsorption of methanol on this zeolite the equilibrium lies with the formation of $CH_3OH_2^+$ ions.[31]

IV. Conclusions

The principal conclusions of this study are as follows.

(1) A new technique for estimating quadrupole coupling constants in molecules is demonstrated. It involves a greater attainable degree of supercooling of the liquid state by means of adsorption on solids, which allows a minimum in T_1 to be observed, thus no additional information on correlation times is required.

(2) The processes of molecular rotation and diffusion in liquid water appear to be intimately related. The correlation times for these processes for water adsorbed in a 13-X zeolite are equal to one another within a factor of 2 over almost a four decade range of correlation times.

(3) A structure proposed previously for the surface complex formed within the zeolite cages by hydrolysis has been further verified by deuteron relaxation results. The Al–O–D bond angle in this complex was estimated.

(4) The averaging effects of rotation about a single axis for an arbitrary field gradient tensor were worked out.

Acknowledgments. Helpful conversations with J. S. Murday are acknowledged. Thanks are due to Mrs. Brenda Russell for preparing the manuscript for publication.

References and Notes

(1) H. A. Resing, J. K. Thompson, and J. J. Krebs, *J. Phys. Chem.*, **68**, 1621 (1964).
(2) H. A. Resing, *Adv. Mol. Relaxation Processes*, **1**, 109 (1968).
(3) H. A. Resing and J. K. Thompson, *Adv. Chem. Ser.*, **No. 101**, 473 (1971).
(4) H. D. Simpson and H. Steinfink, *J. Am. Chem. Soc.*, **91**, 6225 (1969); J. J. DeBoer and I. E. Maxwell, *J. Phys. Chem.*, **78**, 2395 (1974).
(5) A. Abragam, "The Principles of Nuclear Magnetism", Oxford University Press, London, 1965, p 467 *ff*, also p 346 *ff*.
(6) N. Bloembergen, E. M. Purcell, and R. V. Pound, *Phys. Rev.*, **73**, 679 (1948).
(7) J. G. Powles and M. Rhodes, *Proc. Colloq. AMPERE*, **14**, 757 (1967).
(8) For other deuteron resonance studies of the adsorbed state see S. J. Seymour, M. I. Cruz, and J. J. Fripiat, *J. Phys. Chem.*, **77**, 2847 (1974).
(9) J. S. Murday, R. L. Patterson, H. A. Resing, J. K. Thompson, and N. H. Turner, *J. Phys. Chem.*, **79**, 2674 (1975).
(10) H. Y. Carr and E. M. Purcell, *Phys. Rev.*, **94**, 630 (1954).
(11) G. W. Parker, *J. Chem. Phys.*, **58**, 3274 (1973).
(12) In analogy with the proton relaxation times of ref 9.
(13) J. R. Zimmerman and W. E. Britten, *J. Phys. Chem.*, **61**, 1328 (1957).
(14) D. E. Woessner, *J. Chem. Phys.*, **39**, 2783 (1963).

(15) H. A. Resing, *J. Phys. Chem.*, **78**, 1279 (1974).
(16) J. K. Thompson, J. J. Krebs, and H. A. Resing, *J. Chem. Phys.*, **43**, 669 (1965).
(17) S. G. Bishop and P. C. Taylor, *Solid State Commun.*, **4**, 1323 (1972); K. Bergmann and K. Demmler, *Colloid Polym. Sci.*, **252**, 193 (1974); M. A. Butler and H. J. Guggenheim, *Phys. Rev. B.*, **10**, 1778 (1974); S. K. Garg, S. R. Gough, and D. W. Davidson, *J. Chem. Phys.*, in press; H. A. Resing, *Can. J. Phys.*, in press.
(18) H. A. Resing, *J. Chem. Phys.*, **43**, 669 (1965).
(19) The fitting procedure was discussed previously in ref 3.
(20) C. H. Townes and B. P. Dailey, *J. Chem. Phys.*, **17**, 783 (1949).
(21) T. Chiba, *J. Chem. Phys.*, **34**, 947 (1963); **41**, 1352 (1964); R. Blinc and D. Hadzi, *Nature (London)*, **212**, 1307 (1966).
(22) L. J. Lynch, K. H. Marsden, and E. P. George, *J. Chem. Phys.*, **51**, 5673 (1969).
(23) For example, H. A. Resing, *Mol. Cryst. Liq. Cryst.*, **9**, 101 (1969).
(24) D. E. O'Reilley and E. M. Peterson, *J. Chem. Phys.*, **56**, 5536 (1972).
(25) H. A. Resing and R. A. Neihof, *J. Colloid Interface Sci.*, **34**, 480 (1974).
(26) J. Y. Wei and A. J. Maeland, *J. Chem. Phys.*, **60**, 3718 (1974).
(27) H. W. Dodgen and J. L. Ragle, *J. Chem. Phys.*, **25**, 376 (1956).
(28) W. R. Busing and H. A. Levy, *Acta Crystallogr.*, **11**, 798 (1958).
(29) D. H. Olson and E. Dempsey, *J. Catal.*, **13**, 221 (1969).
(30) J. J. Fripiat estimates a pK_a of about +5; private communication.
(31) P. Salvador and J. J. Fripiat, *J. Phys. Chem.*, **79**, 1842 (1975).

Nitrogen-14 Nuclear Quadrupole Resonance in Nitrogen–Silicon Compounds

Ellory Schempp* and Ming Chao

Department of Crystallography, University of Pittsburgh, Pittsburgh, Pennsylvania 15260 *(Received September 8, 1975)*

Publication costs assisted by the National Science Foundation

Nuclear quadrupole resonance frequencies of ^{14}N in several compounds containing nitrogen–silicon bonds have been measured. The data show quadrupole coupling constants considerably larger than would be expected on the basis of the ^{35}Cl NQR frequencies in Si–Cl bonds. The results are compared with other amines and are interpreted in terms of a planar configuration at the nitrogen in silyl amines. The NQR data indicate considerable ionic character in the N–Si bonds, but only a modest degree of pπ–dπ bonding.

Nuclear quadrupole coupling constants (NQCC) in molecules are closely correlated with molecular electronic structure and are particularly sensitive to variations in the electronegativity of the atomic species directly bonded to the atom containing the quadrupolar nucleus. In using coupling constants to extract chemical bonding information, it is useful to have data from a wide range of bonding configurations; however, nuclear quadrupole resonance (NQR) spectroscopy of ^{14}N has been largely concerned with N–C, N–H, N–N, and N–O bonds.[1] We report here the first ^{14}N NQR results in several compounds containing the nitrogen–silicon bond. Since silicon has no natural isotopes with spin greater than one-half, there is no possibility of NQR with Si and the nature of silicon bonds must be inferred from its bonds to other species. The results of NQR investigations in Si–Cl compounds have been reviewed previously.[2,3]

The experimental data, presented in Table I, were obtained at 77 K; the compounds are liquid at room temperature. For nuclei with spin unity, as ^{14}N, there are two NQR frequencies, ν_+ and ν_-, which are related to the NQCC e^2qQ and the asymmetry parameter η of the electric field gradient tensor by[1]

$$e^2qQ = \frac{2}{3}(\nu_+ + \nu_-)$$
$$\eta = \frac{3(\nu_+ - \nu_-)}{(\nu_+ + \nu_-)} \qquad (1)$$

The experimental details have been given previously;[1,4] the samples were obtained commercially and purified by distillation only if the initial search failed to yield NQR lines.

In the cyclic hexamethyltrisilazane $(Me_2SiNH)_3$ the $\nu_\pm$ lines appear with a threefold splitting, consistent with a distortion of the ring which makes the three nitrogens inequivalent. Although other crystallographic possibilities are not ruled out, nearly axial distortion is indicated by the fact that the lines appear as a close doublet separated from another line about 50 kHz higher; such a configuration has been observed in other cyclosilazanes.[5,6] The lines were paired using pulsed double resonance techniques.

Azidotrimethylsilane, Me_3SiN_3, shows similar splittings due to inequivalent sites. We attribute the NQR lines to the nitrogen in the Si–N bond of Me_3SiNNN on the basis of comparison with the microwave results in HN_3.[7] In addition, we find that this compound can crystallize in two different forms; when the sample is cooled rapidly from room temperature to 77 K, NQR lines are found at 3148, 3083, 2928, and 2920 kHz. However, on warming just to the melting point (ca. −63°C) and recrystallizing, the lines appear at 3136, 3096, 2956, and 2935 kHz. Since no unusual broadening is observed in either case, the effect is probably not due to disorder or strain.

Discussion

In the case of Si–Cl bonds, the ^{35}Cl NQR frequencies are just about one-half the frequencies seen in the corresponding C–Cl compounds,[3,8] cf. 16.506 MHz in Me_3SiCl vs. 31.065 MHz in Me_3CCl; 18.571 MHz in H_2SiCl_2 vs. 35.991 MHz in H_2CCl_2. However, substitution of Si for C in analogous bonds to nitrogen does not lead to comparable reductions in the nitrogen nuclear quadrupole coupling constant; e^2qQ = 4855 kHz for Me_2NSiMe_3 (Table I) which is only 6.5% smaller than the 5194 kHz in Me_2NMe. Although the Cl–Si NQR data may be interpreted in terms of a low effec-

TABLE I: ^{14}N NQR Data in Several Compounds Containing N–Si Bonds[a]

Compound		Frequencies $\nu_{\pm}$, kHz	e^2qQ, kHz	η
N,N-Dimethylaminotrimethylsilane $(CH_3)_2NSi(CH_3)_3$		4184.05 3098.22	4854.85	0.4473
N,N-Diethylaminotrimethylsilane $(C_2H_5)_2NSi(CH_3)_3$		4160.38 3046.47	4804.57	0.4636
Hexamethyltrisilazane $[(CH_3)_2SiNH]_3$		2463.42 2418.53 2415.52 1628.43 1548.30 1537.36	2669.23[b]	0.6452[b]
Trimethylsilylazide[c] $(CH_3)_3SiN_3$	I	3147.80 3083.47 2927.60 2919.67	4026.18[b]	0.0953[b]
	II	3136.34 3096.41 2956.17 2935.33	4041.42[b]	0.0844[b]

[a] The frequencies were measured at 77 K and are accurate to ±0.05 kHz. [b] Average values. [c] NQR lines are found in I or II depending on the crystallization history; see text.

tive electronegativity for Si and possibly $d\pi$–$p\pi$ bonding, the nitrogen results require more explanation. For example, the coupling constants in the series of substituted amines[9-11] Me_2NH (4369 kHz), Me_2NSiMe_3 (4855 kHz), Me_2NMe (5194 kHz), Me_2NCl (6333 kHz) suggest an effective electronegativity for Si with respect to N which is intermediate between hydrogen and carbon. However, if this were all, then the asymmetry parameter in the silicon compound (0.45) should also be intermediate between the value in Me_2NH (0.32) and Me_2NMe (0) (η reflects the departure from trigonal symmetry, and hence the difference in occupancy of the three bonds, about the direction defined by the lone pair).

However, the nitrogen silyl compounds probably have a planar sp^2 configuration at the nitrogen,[5,6,12-15] whereas the alkyl amines have the pyramidal sp^3 form. Since the nitrogen lone pair electrons make the dominant contribution to the field gradient, a comparison of coupling constants must take into account the fact that when the lone pair electrons are in a nearly pure p orbital, their contribution to q_{zz} is 4/3 larger than when they are in an sp^3 orbital. Referred to an sp^2 basis, and assuming no consequent change in the bond polarities, Me_2NH would have e^2qQ = 5825 kHz. If N–Si σ bonds are more polarized toward nitrogen than N–H bonds, as expected on the basis of a lower electronegativity for Si, substituting the trimethylsilyl group for hydrogen could reduce this coupling constant to the 4855 kHz observed in Me_2NSiMe_3.

If, in addition, there is loss of charge from the nitrogen lone pair orbital to the vacant Si 3d orbitals, e^2qQ for the nitrogen will be further reduced. Evidence for such $p\pi$–$d\pi$ interaction comes from the planarity of the heavy atom skeleton and the short N–Si bond lengths in $(H_3Si)_3N$,[14] $(H_3Si)_2NMe$,[12] and Cl_3SiNMe_2,[13] from low values of the dipole moments[16-19] which suggest a two-way charge transfer, and from NMR experiments.[20-22]

Overall, the NQR data in Me_2NSiMe_3 can probably be most usefully compared with the data for the amino nitrogen in 4-dimethylaminopyridine:[23] e^2qQ = 4799 kHz, η = 0.025, vs. 4855 kHz, η = 0.45 in the silyl amine. Here the configuration is close to planar[24-28] and owing to conjugation with the ring there is some loss of charge from the amino lone pair. Both cases, however, display very much less $p\pi$ delocalization than occurs in *N*-methylpyrrole,[1] where e^2qQ = 2393.1 kHz and η = 0.171.

There are, thus, two parts to the explanation of the observed NQR results in the silylamines: the polarity of the N–Si σ bond and the degree of $p\pi$–$d\pi$ bonding. Another question concerns the relative σ bond polarity in Si–Cl bonds compared with Si–N bonds. In spite of several inadequacies, the Townes and Dailey model remains the most generally reliable scheme for the interpretation of quadrupole coupling constants in terms of bond populations. Accordingly, if the nitrogen σ bonds are written as sp^2 hybrid orbitals and electron occupancies b and b′ are assigned to the N–C and N–Si σ bonds, the NQR parameters can be expressed as[1]

$$a = \alpha + \frac{2}{3}b + \frac{1}{3}b' \qquad b' = b + \alpha\eta \tag{2}$$

where a is the nitrogen $p\pi$ occupancy and α is the reduced coupling constant, (e^2qQ_{exp}/e^2q_pQ); the coupling constant per p electron, e^2q_pQ, for nitrogen is taken as 8.4 MHz.[1] In order to estimate b' and a, the N–C σ population b must be known and, unfortunately, no reliable value for an sp^2 configuration is available: for sp^3 Me_3N, $b \simeq 1.17$, whereas for the nitrogen in pyridine, $b \simeq 1.29$ has been found. In the first case, eq 2 give for the N–Si bond in Me_2NSiMe_3 $b' \simeq 1.43$, and for the π charge a = 1.84, or a transfer of 0.16 e from the nitrogen $p\pi$ to the silicon d orbitals. In the second case for b = 1.29, $b' \simeq 1.55$, a = 1.95, suggesting a much smaller $p\pi$–$d\pi$ interaction. By comparison, in 4-dimethylaminopyridine for b = 1.17, we find a = 1.74, and for b = 1.29, a = 1.86 for the amino π-charge density. This contrasts with $a \simeq 1.5$ in the highly conjugated *N*-methylpyrrole. The N–Si bonding thus appears to be characterized by strong polarization of the N–Si σ bond and rather weak

$p\pi$–$d\pi$ bonding, weaker at least than the $p\pi$–$p\pi$ bonding in aminopyridines.

This conclusion is borne out by the results in hexamethylcyclotrisilazane, where e^2qQ (2.67 MHz) is only about half that in Me_2NSiMe_3, owing to the presence of three readily polarizable bonds. Using the previous model, and taking the N–Si occupancy $b' \simeq 1.5$ e gives $b'' = 1.3$ for the N–H σ bond, close to the value in Me_2NH, and $a = 1.75$. The π loss from the nitrogen is seen to be somewhat greater in this case where each nitrogen is bonded to two silicon atoms, and suggests a slight degree of aromatic character for the silazane ring with a silicon d occupancy of about 0.25 e.

The bond population discussion above indicates an approximately 20% increase in the nitrogen σ occupancy in going from N–C to N–Si. It is difficult to estimate an analogous change in σ polarity in the case of C–Cl and Si–Cl bonds since the coupling constant is related to three unknown parameters,[1] the σ charge b, the π occupancy, and the s character of the chlorine bonding orbital, $\alpha = (2 - b)(1 - s) - \pi$. If there is no $d\pi$–$p\pi$ bonding, and if $s \simeq 0.2$ for both the carbon and silicon cases, we find $b_C \simeq 1.29$ and $b_{Si} \simeq 1.62$ in Me_3CCl and Me_3SiCl, or an increase of about 25%. However, Kaplansky and Whitehead[29] have pointed out that the Cl s character probably increases in the Si bonds, to perhaps 0.45; they find $b_C = 1.26$ and $b_{Si} = 1.45$, or an increase of only 15%. If $\pi \neq 0$, which Kaplansky and Whitehead doubt, b_{Si} would be still smaller. The most that can be concluded, therefore, is that the σ polarization toward nitrogen in N–Si bonds is comparable to the σ polarization toward chlorine in Si–Cl bonds.

The ^{14}N quadrupole coupling constants in the silyl amines can thus be qualitatively accounted for on the basis of considerable N–Si σ polarization in a planar sp^2 configuration with a relatively small degree of $p\pi$–$d\pi$ bonding.

Acknowledgment. Supported by the National Science Foundation, University Science Development Grant No. GU-3184.

References and Notes

(1) E. Schempp and P. J. Bray in "Physical Chemistry", Vol. IV, D. Henderson, Ed., Academic Press, New York, N.Y., 1970.
(2) E. A. C. Lucken, "Nuclear Quadrupole Coupling Constants", Academic Press, London, 1969.
(3) E. A. C. Lucken in "Structure and Bonding", Vol. 6, C. K. Jørgensen, et al., Ed., Springer-Verlag, New York, N.Y., 1969.
(4) E. Schempp and P. J. Bray, *J. Magn. Reson.*, **5**, 78 (1971).
(5) G. W. Adamson and J. J. Daly, *J. Chem. Soc. A*, 2724 (1970).
(6) G. S. Smith and L. E. Alexander, *Acta Crystallogr.*, **16**, 1015 (1963).
(7) R. A. Forman and D. R. Lide, *J. Chem. Phys.*, **39**, 1133 (1963).
(8) I. P. Biryukov, M. G. Voronkov, and I. A. Safin, "Tables of NQR Frequencies", Chemistry Publishing House, Leningrad, 1968.
(9) P. J. Haigh, P. C. Canepa, G. A. Matzkanin, and T. A. Scott, *J. Chem. Phys.*, **48**, 4234 (1968).
(10) C. T. O'Konski and T. J. Flautt, *J. Chem. Phys.*, **27**, 815 (1957).
(11) E. Schempp, *Chem. Phys. Lett.*, **8**, 562 (1971).
(12) C. Glidewell, D. W. H. Rankin, A. G. Robiette, and G. M. Sheldrick, *J. Mol. Struct.*, **4**, 215 (1969).
(13) W. Airey, C. Glidewell, A. G. Robiette, G. M. Sheldrick, and J. M. Freeman, *J. Mol. Struct.*, **8**, 423 (1971).
(14) K. Hedberg, *J. Am. Chem. Soc.*, **77**, 6491 (1955).
(15) M. Yokoi and K. Yamasaki, *J. Am. Chem. Soc.*, **75**, 4139 (1953); M. Yokoi, *Bull. Chem. Soc. Jpn.*, **30**, 100 (1957).
(16) T. Moeller, Ed., "Inorganic Synthesis", Vol. V, McGraw-Hill, New York, N.Y., 1957, pp 58–59.
(17) R. L. Cook and A. P. Mills, *J. Phys. Chem.*, **65**, 252 (1961).
(18) K. Schaarschmidt, *Z. Anorg. Allg. Chem.*, **310**, 78 (1961).
(19) I. Yu. Kokoreva, Ya. K. Syrkin, E. D. Babich, and V. N. Vdovin, *Zh. Struct. Khim.*, **8**, 1102 (1967).
(20) E. W. Randall, C. H. Yoder, and J. J. Zuckerman, *Inorg. Chem.*, **6**, 744 (1967).
(21) J. Mack and C. Yoder, *Inorg. Chem.*, **8**, 278 (1969).
(22) H. Vahrenkamp and H. Noeth, *J. Organometal. Chem.*, **12**, 281 (1968).
(23) R. A. Marino, L. Guibé, and P. J. Bray, *J. Chem. Phys.*, **49**, 5104 (1968).
(24) T. C. W. Mak and J. Trotter, *Acta Crystallogr.*, **18**, 68 (1965).
(25) J. Tanaka and N. Sakabe, *Acta Crystallogr., Sect. B*, **24**, 1345 (1968).
(26) G. J. Bullen, D. J. Corney, and F. S. Stephens, *J. Chem. Soc., Perkin Trans. 2*, 642 (1972).
(27) J. L. DeBoer and A. Vos, *Acta Crystallogr., Sect. B*, **24**, 720 (1968).
(28) M. Chao, E. Schempp, and R. D. Rosentein, *Acta Crystallogr.*, in press.
(29) M. Kaplansky and M. A. Whitehead, *Mol. Phys.*, **16**, 481 (1969).

Nitroxide Spin Probes on Smectite Surfaces. Temperature and Solvation Effects on the Mobility of Exchange Cations

Murray B. McBride[1]

Department of Land Resource Science, University of Guelph, Guelph, Ontario, Canada *(Received June 30, 1975)*

Electron spin resonance (ESR) studies of the paramagnetic probe cation, protonated 4-amino-2,2,6,6-tetramethylpiperidine *N*-oxide, exchanged on the surfaces of a smectite (layer silicate) have revealed important properties of the silicate surface. The probe cation is motionally restricted by its association with the external exchange surfaces on fully solvated smectites, and is restricted and oriented to an even greater degree in interlamellar regions, especially as the distance between silicate sheets is decreased. The type of interlamellar solvent alters the molecular orientation, with water apparently allowing the hydrocarbon fraction of the probe ion to associate closely with the silicate surfaces. In addition, the species of exchangeable metal ion present on the surfaces has an effect on the probe's mobility and orientation. The mobility of the probe is greatly reduced on the hydrated smectite surfaces at temperatures below 0°C, a fact attributed to the migration of water from between the silicate sheets and the reduction of thermal motion. Similar low-temperature ESR studies of smectite exchanged with Cu^{2+} demonstrate the transition from a solution-like to a solid-like environment between the silicate plates in the −25° to −50°C temperature range. The ESR spectra are supported by x-ray diffraction data which allow the spacings between smectite plates to be determined.

Introduction

The use of electron spin probes in membrane biophysics has recently gained impetus because of the availability of stable nitroxide radicals as probe molecules. The anisotropic g tensors and hyperfine splitting values (A) of the nitroxide probes, as well as the solvent dependence of g and A, permit considerable information to be obtained from electron spin resonance (ESR) spectra of the probes when doped into membrane systems.[2,3] Effective viscosities of the local environments of the spin probes can be estimated from the degree to which anisotropies in the ESR spectrum are averaged by molecular tumbling.

Paramagnetic cations such as Mn^{2+} and Cu^{2+} have been utilized as spin probes to characterize the environment of exchangeable cations adsorbed on smectite surfaces.[4,5] These ions exist as $Mn(H_2O)_6^{2+}$ or $Cu(H_2O)_6^{2+}$ complexes in fully hydrated smectites, and demonstrate solution-like tumbling mobility in interlamellar regions. However, lowered relative humidities produce rigidly oriented hydration complexes of these ions as the interlamellar regions collapse until only about one to two monolayers of water remain between the silicate sheets.

In the present study, an attempt is made to relate the mobility of exchange cations on smectites to the extent of dehydration of the smectite. Dehydration is achieved both by lowering the relative humidity, and by freezing the clay at various temperatures between 0 and −50°C. A protonated nitroxide spin probe is doped into Na^+-, H^+-, and Mg^{2+}-saturated smectite at about the 5% level of exchange, and used to estimate the interlamellar mobility. In addition, the rotational mobility of the spin probe on fully solvated smectites is determined.

Materials and Methods

A California hectorite (<2-μ particle size), with chemical formula and exchange capacity previously reported,[5] was saturated with Na^+ and Mg^{2+} exchange ions using excess quantities of aqueous chloride salt solutions. Excess salt was then washed from the clay suspensions by centrifuging and discarding the supernatant until a negative $AgNO_3$ test for chloride was obtained. The H^+-saturated hectorite was prepared by passing Na^+ hectorite through an acid resin column; however, partial decomposition of this acid hectorite probably resulted in some Mg^{2+} moving from the structure into exchange positions. An aqueous solution of the spin probe (4-amino-2,2,6,6-tetramethylpiperidine *N*-oxide), referred to here as Tempo, was titrated with HCl past the equivalence point (as determined by a pH meter) in order to protonate the amine group of the probe. Known quantities of this cationic form of the probe were added to the Mg^{2+}- and Na^+-saturated hectorites to produce clays doped at about the 5% level of exchange capacity. The clays were then washed several times in distilled water to remove chloride and neutral probe molecules. Aqueous suspensions of the doped hectorites were dried on polyethylene sheets to produce oriented, self-supporting films to be used for ESR studies.

The ESR spectra were recorded for oriented films of hectorite in quartz tubes using an X-band Varian E-12 spectrometer. Sample temperature was controlled to ±1°C between 20 and −100°C by flowing nitrogen gas cooled by liquid nitrogen through the sample cavity and using a variable heating element. Hectorite suspensions dried on glass slides produced well-oriented films for x-ray diffraction.

A GE XRD-6 diffractometer with Ni-filtered Cu radiation was used to determine the basal spacings of these films under various conditions of solvation. The temperature of the clay films could be controlled by drying the clays on aluminum foil and mounting these foil-supported films on the sample holder. The holder was then placed in contact with an apparatus that varied the temperature using a reservoir of liquid nitrogen and a variable heating coil. A thermocouple attached to the sample holder allowed the temperature at the sample to be determined to ±1°C. Thus, the sample temperature could be varied from +20 to

−50°C while a slight excess of water was maintained on the clay films during the cooling process by covering the films with cellophane.

Results and Discussion

Nitroxide Spin Probes on Smectites under Various Conditions of Solvation. The nitroxide spin probes are observed to tumble rapidly enough in aqueous solution at 25°C to completely average anisotropies in g and hyperfine splitting (A) values. As a result, a three-line ESR spectrum is obtained centered on g_0 (average g) and with splitting value A_0 (average A). The correlation time, τ_c, for the tumbling of Tempol has been calculated to be 0.1×10^{-10} sec in water at 25°C.[6] A similar correlation time is expected for Tempo$^+$, the protonated form of Tempo, and is verified by the observation of a symmetrical three-line spectrum resulting from rapid molecular tumbling (Figure 1). However, the protonated probe can occupy exchange sites on hectorite surfaces and may demonstrate reduced mobility in the adsorbed state.

The spectra of Figures 2 and 3 for Tempo$^+$-doped Na^+ and Mg^{2+} hectorite demonstrate the loss of rotational mobility of Tempo$^+$ adsorbed on silicate surfaces that are solvated with H_2O or 95% ethanol (EtOH). Orientation of the hectorite films with the plane of the silicate sheets parallel ($\parallel$) and perpendicular ($\perp$) to the magnetic field, H, produces considerably different line positions and values of A for the hectorites equilibrated at 100% relative humidity (Figure 2), an effect that is much less evident for the hectorites solvated in 95% EtOH (Figure 3). This anisotropic behavior is more pronounced as the relative humidity of equilibration is reduced, a result demonstrated by the spectra of Na^+ and Mg^{2+} hectorite at 93%, 75%, and 33% relative humidities (Figures 4 and 5).

Closer analysis of the ESR spectra of Figures 2 and 3 reveals that the three sharp resonance lines are superimposed on a broad spectrum representing immobilized Tempo$^+$. The actual intensity of this broad spectrum is greater than is apparent from the spectra because of its greater line widths relative to the widths of the sharper resonance lines. The intensity of the broad spectrum is lowest when the hectorites are fully solvated in water or 95% EtOH (low-field and high-field shoulders of Figures 2 and 3) but increases as the relative humidity is decreased (Figures 4 and 5). Apparently, two distinct types of Tempo$^+$ are present on the hectorite surfaces: probe ions that are essentially immobilized and probe ions that are much less motionally restricted.

Analysis of the narrow-line spectra of Tempo$^+$ on fully solvated hectorites allows calculation of correlation times from the following equations:[6]

$$\tau_1 = \frac{-2211 W_0 R_-}{H_0}$$

$$\tau_2 = 0.65 W_0 (R_- - 2)$$

where τ_1 and τ_2 are two estimates of τ_c, the correlation time in nanoseconds, W_0 is the line width of the central peak (G), and H_0 is the magnetic field (G). $R_\pm = (h_0/h_{+1})^{1/2} \pm (h_0/h_{-1})^{1/2}$ where $h_{0,+1,-1}$ = height of the middle, low, and high field peaks, respectively. The calculated values of τ_c are given in Table I for Na^+, H^+, and Mg^{2+} hectorites solvated in water and 95% EtOH. Because of the anisotropy of the spectra, the τ_c values do not always agree for the perpendicular and parallel orientations of the silicate sheets.

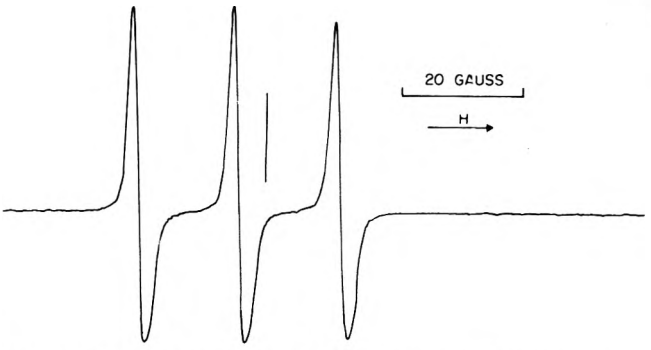

Figure 1. ESR spectrum at 20°C of the nitroxide spin probe, Tempo$^+$, in aqueous solution acidified to pH 2.4. The vertical line on this spectrum (and following spectra) represents the position of g = 2.00.

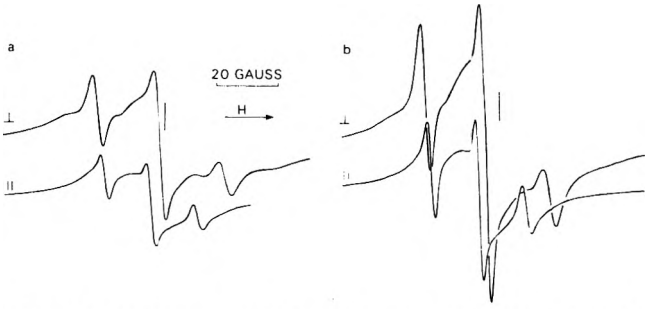

Figure 2. ESR spectra at 20°C of the nitroxide spin probe, Tempo$^+$, doped at the ~5% exchange level into (a) Na^+ hectorite equilibrated at 100% relative humidity; (b) Mg^{2+} hectorite equilibrated at 100% relative humidity.

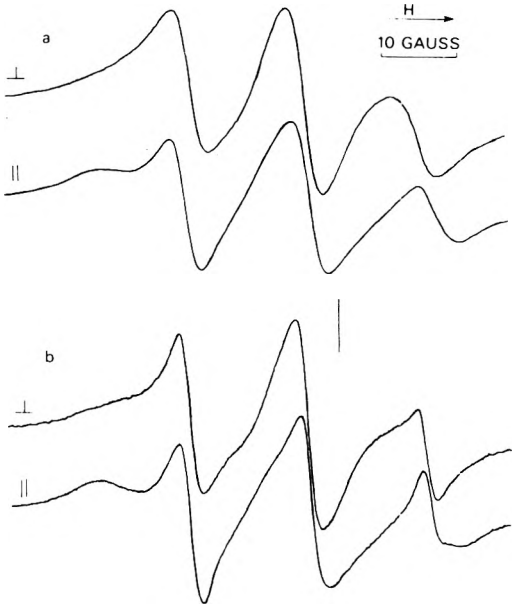

Figure 3. ESR spectra at 20°C of the nitroxide spin probe, Tempo$^+$, doped at the ~5% exchange level into (a) Na^+ hectorite solvated in excess 95% ethanol; (b) Mg^{2+} hectorite solvated in excess 95% ethanol.

In general, the values of τ_c are in the range of $1–5 \times 10^{-9}$ sec, meaning that the tumbling mobility of the nonimmobilized Tempo$^+$ is reduced by a factor of 100–500 when compared with the probe in aqueous solution. However, a number of trends are apparent from Table I. The correlation time is always greater for the hydrated systems than for the

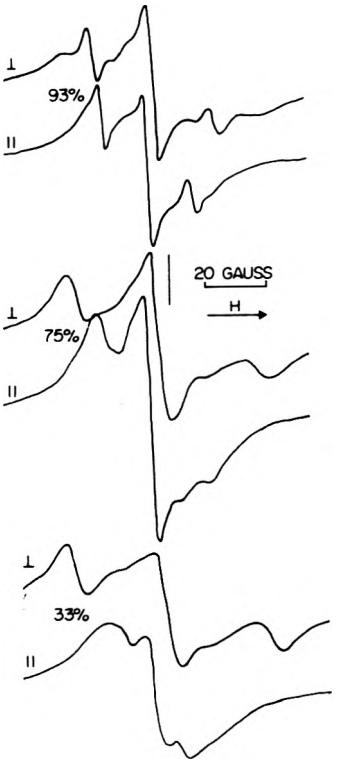

Figure 4. ESR spectra at 20°C of the nitroxide spin probe, Tempo$^+$, doped at the ~5% exchange level into Na^+ hectorite equilibrated at 93, 75, and 33% relative humidity.

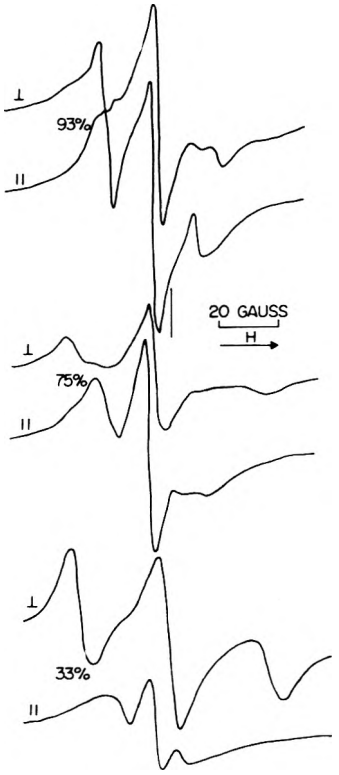

Figure 5. ESR spectra at 20°C of the nitroxide spin probe, Tempo$^+$, doped at the ~5% exchange level into Mg^{2+} hectorite equilibrated at 93, 75, and 33% relative humidity.

solvated (EtOH) systems despite the greater distances between silicate sheets for hectorites (Na^+, Mg^{2+}, H^+) wetted in water than for those solvated in 95% EtOH (Table II). The basal spacings of the hectorites show that the interlamellar distance is ≈7.5 Å in 95% EtOH, and at least 10.5 Å in water. If Tempo$^+$ occupies interlamellar positions, steric hindrance of tumbling would be expected for the EtOH-solvated hectorites especially, since the Tempo$^+$ molecule is about 8 Å in length. Because the probe tumbles more rapidly on the EtOH-solvated than on the water-solvated hectorite, it is likely that the spectra of the mobile probe represent Tempo$^+$ on external surfaces rather than in interlamellar regions while the broad spectra (immobilized probe) represent Tempo$^+$ sterically restricted from tumbling in the interlamellar spaces. The immobile fraction of Tempo$^+$ increases relative to the mobile fraction as the relative humidity is lowered from 100 to 93% (Figures 2, 4, and 5) as evidenced by the increase in the intensity of the broad "rigid glass" spectrum.[2] Lowering the relative humidity further to 75 and 33% essentially eliminates all evidence of mobile Tempo$^+$ (Figures 4 and 5). Essentially all of the probe at 33% relative humidity is restricted, either in interlayers as the silicate sheets collapse together (thereby eliminating most of the external surfaces that were present in fully solvated hectorites), or on partially dehydrated external surfaces.

TABLE I: Calculated Rotational Correlation Times (nsec) of Tempo$^+$ Doped into Solvated Na^+, H^+, and Mg^{2+} Hectorite[a]

Exchange form of hectorite	Wetting solvent	Correlation time, τ_c of Tempo$^+$ (× 10^9 sec)			
		τ_1		τ_2	
		⊥	∥	⊥	∥
Na^+	H_2O	1.7	2.6	3.9	3.8
Na^+	95% EtOH	1.4	2.0	2.3	2.4
H^+	H_2O	2.9	1.4	5.2	2.9
H^+	95% EtOH	1.2	1.3	1.8	1.5
Mg^{2+}	H_2O	3.3	1.5	5.9	3.4
Mg^{2+}	95% EtOH	0.9	1.0	1.6	1.7

[a] ⊥ and ∥ represent the orientation of the hectorite films to the magnetic field, *H*.

Another trend apparent from Table I is the dependence of correlation times upon the exchangeable cation that largely occupies the hectorite surface. Thus, for EtOH-solvated hectorite, τ_c decreases in the order $Na^+ > H^+ \geq Mg^{2+}$ for both perpendicular and parallel orientations of the hectorite. For hydrated hectorite, τ_c follows the order $Mg^{2+} \geq H^+ > Na^+$ for the perpendicular orientation and the order $Na^+ > Mg^{2+} \geq H^+$ for the parallel orientation. In general, the H^+ and Mg^{2+} hectorite seem to behave similarly (similar τ_c values) while Na^+ hectorite has different behavior, probably because of the weak energy of solvation of Na^+ relative to Mg^{2+} (or H^+). Therefore, the correlation time of the probe on EtOH-solvated Na^+ hectorite may be lengthened as a result of the ability of Tempo$^+$ ions to closely approach and be adsorbed to the weakly solvated silicate surface. In contrast, the strong solvation of Mg^{2+} and H^+ ions could more effectively inhibit probe–surface interactions by producing a layer of solvent molecules strongly attracted to the surface exchange cations through ion–dipole forces. (The similarity between the τ_c of Mg^{2+} and H^+ hectorite may be at least partly due to acid decomposition of H^+ hectorite to produce a (Mg^{2+}, H^+) hectorite.) The τ_c values of the hydrated hectorites depend on the orientation of the silicate sheets relative to *H* as well as the exchangeable cation (Table I). The orientation effect

on τ_c is a result of preferred alignment of the probe ion on the hydrated silicate surfaces, an effect that is much reduced on the EtOH-solvated surfaces.

From the spectra recorded in Figures 2, 3, 4, and 5, it is obvious that orientation of the hectorite films with the plane of the silicate sheets parallel and perpendicular to the external magnetic field, H, produces spectra with different hyperfine splitting values (A). Since the largest value of A, A_{zz}, is expected when H is parallel to the nitroxide z axis of the spin probe,[3] and is observed with H perpendicular to the fully hydrated hectorite films (Figure 2), the N–O bond axis of Tempo$^+$ is demonstrating a tendency to orient parallel to the hydrated silicate surfaces. If the hyperfine splitting value, A, is given as the distance in gauss between the low field line and the central line of the narrow spectrum, then $A_\parallel$ and $A_\perp$ are defined as the values of A for the two principal orientations of the hectorite films relative to H. The difference, $A_\perp - A_\parallel$, is denoted as ΔA, and is directly related to the degree of order of the nitroxide probe.[7] Thus, for perfect alignment of the z axis of the nitroxide normal to the silicate surface with no molecular motion, $\Delta A = A_{zz} - A_{xx} = 31.8 - 7.6 = 24.2$ G, assuming that $A_{xx} \sim A_{yy}$. The principal values of A (A_{xx}, A_{yy}, and A_{zz}) were determined for di-*tert*-butyl nitroxide oriented in a host crystal.[7]

The values of ΔA for fully-hydrated Na^-, H^+, and Mg^{2+} hectorite are 5.1, 3.4, and 3.2 G, respectively. Molecular tumbling and imperfect orientation result in ΔA values much below the maximum possible. As for correlation times, H^+ and Mg^{2+} hectorite have similar values of ΔA, while Na^+ hectorite has a higher value. This result indicates that Tempo$^+$ is better aligned on the Na^+ hectorite film, suggesting that the probe ion is spending a fraction of its time adsorbed directly on the silicate surfaces, allowing the longest dimensions of the probe to align with the surfaces. Again, the strongly hydrated surfaces of H^+ and Mg^{2+} hectorite may deter such direct adsorption.

The values of ΔA for H^+, Mg^{2+}, and Na^+ hectorite solvated in EtOH (−0.5, −0.6, and −1.3 G, respectively) are much smaller than those for the hydrated hectorites and indicate near-random tumbling of the mobile fraction of adsorbed Tempo$^+$. Since $A_\parallel > A_\perp$ for these systems (the reverse of hydrated systems), ΔA has a negative sign, and the probe has a slight preference for an orientation with the N–O axis of the nitroxide normal to the solvated silicate surfaces. As with the hydrated hectorites, the larger ΔA for the Na^+ hectorite is evidence for more direct probe–surface contact allowed by the weak solvation energy of Na^+.

The broad ESR spectrum representing immobilized Tempo$^+$ is observed even in the fully solvated systems (Figures 2 and 3) as the low- and high-field shoulders of the spectrum are partially separated from the more narrow spectrum of mobile Tempo$^+$. With the hydrated systems these shoulders are more intense for the perpendicular orientation, but the reverse is true with the EtOH-solvated systems. Thus, immobilized Tempo$^+$ has $A_\perp > A_\parallel$ on hydrated hectorites and $A_\parallel > A_\perp$ on EtOH-solvated hectorites. This orientation dependence, observed even on fully solvated hectorites, is further evidence that the immobilized probes are restricted in interlamellar regions. Using the positions of the low-field and high-field resonances of the broad spectrum, one can determine A_{zz} to be 34 G for both EtOH-solvated and hydrated systems, a value agreeing closely with the expected 32 G. Apparently, even the fully solvated hectorites immobilize part of the probe ions, but the type of solvent determines the alignment of these ions with the surface as indicated by the opposite dependence of A on orientation of hydrated and EtOH-solvated systems.

Since the alignment relative to the silicate sheets of both the mobile and immobile fractions of Tempo$^+$ is reversed when the solvent is changed from water to EtOH, it is evident that the probe–surface interaction is greatly influenced by the solvent. The hydrophobic nature of Tempo$^+$ is demonstrated by fully saturating the exchange sites on hectorite with the probe ion. The resulting basal spacing (Table II) for dry hectorite shows that the probe ions hold the clay plates about 5.7 Å apart, suggesting that the Tempo$^+$ molecules form a monolayer and are oriented in a way that minimizes the basal spacing. The Tempo$^+$-saturated hectorite does not expand appreciably in water, but does swell in 95% EtOH (Table II), indicating the hydrophobic nature of the adsorbed Tempo$^+$ arising from the hydrocarbon nature of the molecule.[8] Therefore, water molecules cannot compete as readily with Tempo$^+$ for adsorption sites on the silicate as can ethanol molecules. The hydrocarbon nature of ethanol may reduce the preference of the methyl groups of Tempo$^+$ to approach the silicate surfaces, thereby causing the molecule to assume an "upright" position on the external surfaces that permits considerable freedom of motion. The positively charged end of the Tempo$^+$ molecule is electrostatically attracted to the surface so that totally random motion is not achieved. In contrast, the hydrophobic portion of Tempo$^+$ associates closely with external silicate surfaces in the presence of water because of the lack of hydrocarbon–water attraction and the probe tends to lie "flat" on the surfaces. This model of interaction explains the large positive values of ΔA for the mobile fraction of Tempo$^+$ on hydrated systems, and the small negative value of ΔA on EtOH-solvated systems.

The immobilized Tempo$^+$ on the solvated hectorites is oriented in the same general sense as the mobile Tempo$^+$ on the same systems, but the alignment is much more rigid and pronounced. Steric hindrance of molecular tumbling combined with maximized probe–surface interaction can account for the orientation of the immobilized probes if it is assumed that these probe ions are in interlamellar regions. In the EtOH-solvated H^+, Na^+, and Mg^{2+} hectorites, the N–O bond axis of immobilized Tempo$^+$ tends to orient normal to the silicate sheets. Since the interlamellar distance is ~7.5 Å (Table II), the ~8.0-Å long probe could bridge across interlamellar space with the $-NH_3^+$ end of the molecule "keyed" into an hexagonal cavity of one surface[9] and the other end adsorbed to the adjacent surface by the attraction between the silicate oxygen atoms and methyl groups. In the hydrated H^+, Na^+, and Mg^{2+} hectorites, the N–O axis of immobilized Tempo$^+$ tends to orient parallel to the silicate sheets. The interlamellar distance of ~10.5 Å could allow restricted molecular tumbling since the interlamellar region has a viscosity similar to that of water;[5] however, the maximum probe–surface interaction is achieved when the molecule lies "flat" on an interlamellar surface with the $-NH_3^+$ group "keyed" into the surface. The rigid glass spectrum of immobilized Tempo$^+$ indicates that molecular motion is absent or very slow on the ESR time scale, i.e., $\tau_c^{-1} \ll |A_{zz} - A_{xx}| \sim 7 \times 10^7$ sec^{-1}.[3] Thus, "immobilized" Tempo$^+$ can be defined as probe ions with rotational correlation times considerably longer than 10^{-8} sec. The restrictions of the interlamellar region on rotation

TABLE II: Basal Spacing of Na^+-, Mg^{2+}-, H^+- and $Tempo^+$-Exchanged Hectorites under Various Conditions of Solvation

Exchange form[a]	Basal spacing, Å		
	Air dry	Wet in H_2O	Wet in 95% EtOH
H^+	14.2	19.6	17.7
Na^+	13.2[b]	(18.0)[b]	16.9
Mg^{2+}	14.2	20.0	16.9
$Tempo^+$	15.2	15.8	17.3

[a] The Na^+, H^+, and Mg^{2+} exchange forms were doped with ~5% $Tempo^+$ on the exchange sites. [b] These diffraction peaks were broad, indicating random interstratification. Bracket indicates a possible second-order peak of a ~36-Å basal spacing.

could easily account for an order of magnitude increase in τ_c, when the correlation times for the mobile and immobile fractions of $Tempo^+$ are compared. Evidently, the "immobilized" $Tempo^+$ may still have considerable motional freedom in the solvated interlamellar regions.

As the relative humidity is reduced from 100%, the fairly narrow spectrum of mobile $Tempo^+$ is gradually replaced by the broad spectrum of immobilized $Tempo^+$ (Figures 4 and 5). Thus, at 93% relative humidity, the narrow spectra of Mg^{2+} and Na^+ hectorite have the same values of ΔA as they did at 100% relative humidity. However, the increased intensity of the broadened spectrum suggests that silicate sheets are moving together to reduce external surface area. At 75% relative humidity, little evidence remains of the more mobile $Tempo^+$, and a fairly well-oriented, restricted probe with ΔA = 11 G predominates (Figures 4 and 5). Further reduction of the relative humidity to 33% further restricts and orients the probe in collapsed interlamellar regions, increasing ΔA to 21 G (close to the maximum of 24.2 G). Thus, $Tempo^+$ on Na^+ and Mg^{2+} hectorite at low relative humidity has virtually no mobility and almost perfect orientation of the nitroxide z-axis normal to the silicate surfaces, an alignment that permits maximum collapse of the interlayers. The relationships of the parameters ($A_\parallel$, $A_\perp$, ΔA) of the dominating spectrum at each relative humidity is shown in Figure 6.

Spin Probes on Frozen Smectite Systems. Since the spin probe, $Tempo^+$, is able to report the degree to which its tumbling is restricted and the molecular orientation that it adopts, a study was made of the effect of low temperatures on the $Tempo^+$-doped Na^+ and Mg^{2+} hectorite. Wet smectites are known to partially dehydrate upon freezing due to the migration of interlamellar water from between the clay plates.[10] After Mg^{2+}-, Cu^{2+}-, and Na^+-saturated hectorites were wetted in water, the interlamellar collapse just below 0°C was observed by x-ray diffraction (Figure 9). However, Na^+ hectorite showed somewhat greater collapse than the Cu^{2+} and Mg^{2+} hectorites, probably because of the low hydration energy of Na^+. More than two monolayers of interlamellar water were maintained by the Mg^{2+} and Cu^{2+} hectorites to temperatures below −40°C. Much of this water is probably inner- and outer-sphere water of hydration, too strongly held by the cations for freezing to remove it.

The $Tempo^+$-doped Na^+ and Mg^{2+} hectorites (excess water present) have ESR spectra that reflect the collapse of the interlayers below 0°C. At 0°C, most of the mobility of $Tempo^+$ is lost as shown by the broadened spectra of Figures 7 and 8 in comparison with the spectra of Figure 2. Lowering the temperature from 0 to −50°C gradually con-

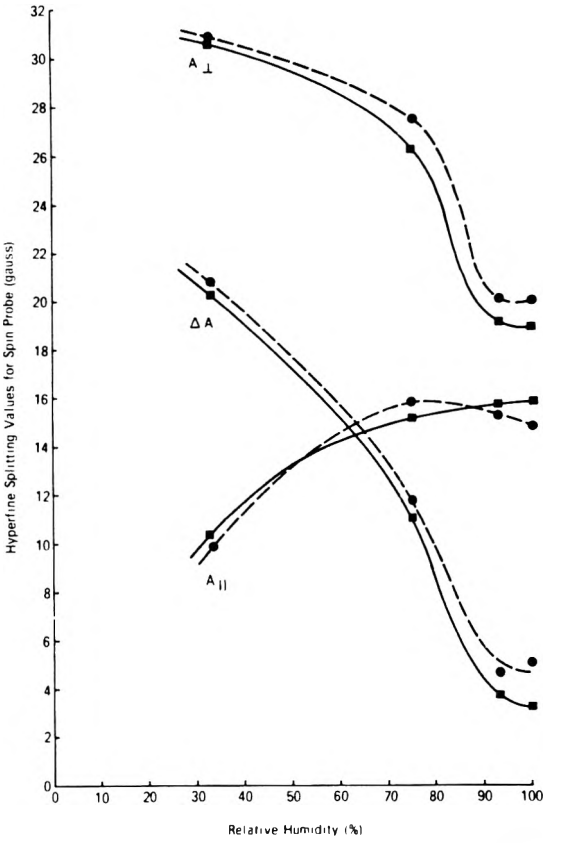

Figure 6. Relationship of the hyperfine splitting parameters ($A_\parallel$, $A_\perp$, ΔA) of the dominant ESR spectrum of $Tempo^+$ to the relative humidity. The circles (●) and squares (■) represent $Tempo^+$-doped Na^+ and Mg^{2+} hectorite, respectively.

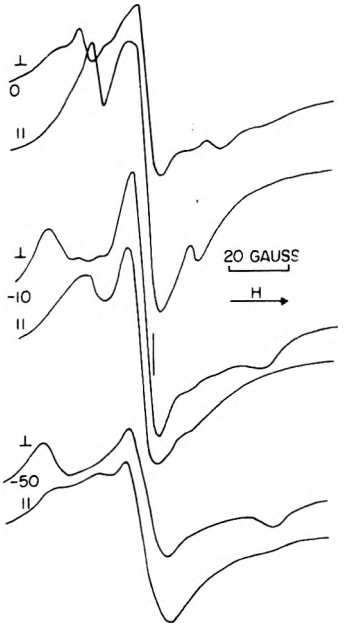

Figure 7. ESR spectra of $Tempo^+$ doped into Na^+ hectorite, equilibrated at 100% relative humidity and recorded at 0, −10, and −50°C.

verts the spectra from those representing partially immobilized and oriented $Tempo^+$ molecules, to those representing $Tempo^+$ in solid matrix. The spectra at −50°C for Na^+ and Mg^{2+} hectorites are very similar to the rigid glass

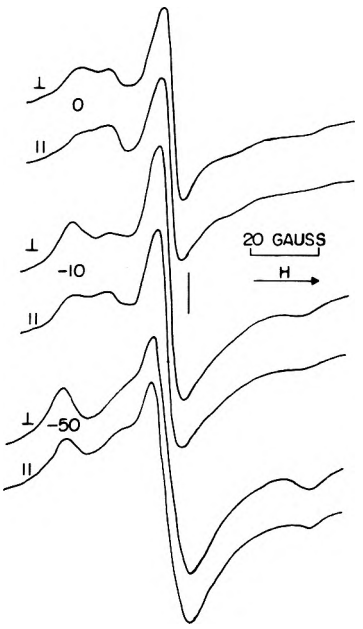

Figure 8. ESR spectra of Tempo$^+$ doped into Mg^{2+} hectorite, equilibrated at 100% relative humidity, and recorded at 0, −10, and −50°C.

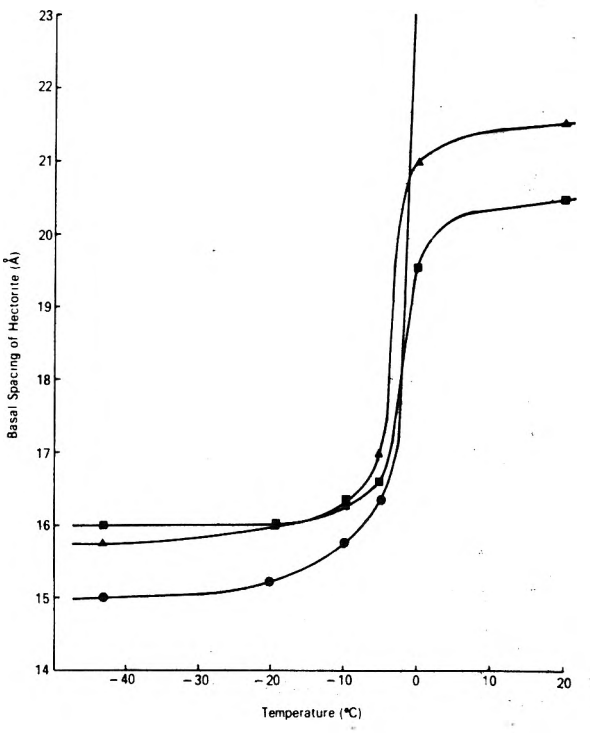

Figure 9. The basal spacings of hectorites exchanged with Na^+ (●), Mg^{2+} (▲), and Cu^{2+} (■) after wetting in water and lowering the temperature, determined by x-ray diffraction.

spectrum[2] except for some orientation of the probe. All of the spectra on frozen clays indicate partial ordering of Tempo$^+$ on the silicate surface so that the N–O axis is approximately parallel to the surface. However, Tempo$^+$ is less oriented in Mg^{2+} hectorite than in Na^+ hectorite at all temperatures below 0°C (Figures 7 and 8). This result probably arises from the fact that Mg^{2+} hectorite has a greater basal spacing than Na^+ hectorite at subzero temperatures (Figure 9), thereby allowing some freedom of alignment of Tempo$^+$ in interlayers that are wider than those of air-dry Mg^{2+} hectorite. At −50°C, the thermal motion of Tempo$^+$ practically ceases, and Tempo$^+$ is "frozen" in near-random orientations in the interlayers of Mg^{2+} hectorite.

Temperature Effects on the Mobility of Exchangeable Cu^{2+}. In addition to Tempo$^+$, Cu^{2+} can be used as a spin probe on the exchange sites of hectorite at subzero temperatures. Thus, Cu^{2+} hectorite powder was solvated in water and the ESR spectra were determined between 0 and −100°C (Figure 10). At room temperature, Cu^{2+} tumbles rapidly as the hexaaquo complex in wet hectorite, producing an isotropic signal near $g = 2.17$.[4] In these spectra of frozen hectorite, an isotropic signal at $g = 2.17$ is observed between 0 and −25°C. Therefore, much of the Cu^{2+} is in the hexaaquo form in this temperature range and is free to tumble or undergo rapid Jahn-Teller distortion, thereby averaging the anisotropy of the g and A tensors. Since the basal spacing varies from about 19.5 to 16.0 Å in the 0 to −25°C temperature range, the $Cu(H_2O)_6^{2+}$ ion has enough interlamellar space to undergo axial distortion or rotation as in free solution. Beginning at 0°C and persisting through to −100°C, a weak anisotropic signal showing $g_\parallel$ and $g_\perp$ components is apparent (Figure 10). The vertical lines demark the position of two low-field weak resonance positions of $g_\parallel$ (the two high-field hyperfine lines are obscured in the resonance at $g = 2.17$) as well as the position of $g_\perp$ (near the free electron signal). Analysis of the anisotropic portion of the spectrum gives $g_\parallel = 2.31$, $g_\perp = 2.04$ and the hyperfine splitting value, $A/C = 0.0151$ cm^{-1}. However, in

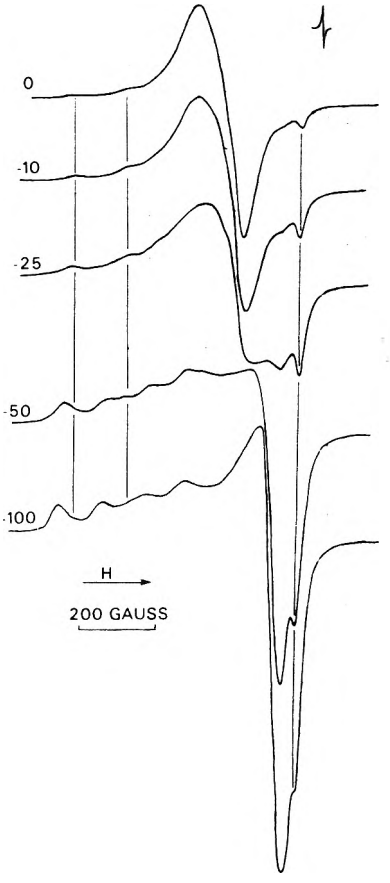

Figure 10. Cu^{2+} ESR spectra of powdered Cu^{2+} hectorite after wetting in water and lowering the temperature. The sample temperatures (°C) are noted and the vertical lines represent the positions of two hyperfine lines for $g_\parallel = 2.31$ and the position of $g_\perp = 2.04$. A free electron signal at $g = 2.0023$ is shown.

the temperature range between −25 and −100°C, a similar anisotropic spectrum becomes stronger until it dominates at −100°C (Figure 10). The values for $g_\parallel$ and $g_\perp$ are found to be 2.37 and 2.08, respectively, while A/C = 0.0125 cm^{-1} for this strong anisotropic spectrum. Investigations of oriented films of Cu^{2+} hectorite indicate that the z axis of the hydrated Cu^{2+} complex is normal to the silicate sheets for both the observed anisotropic spectra. However, the resonance with $g_\perp$ = 2.04 was very weak after the oriented films had been equilibrated at 100% relative humidity, and the isotropic (g = 2.178) resonance observed at 20°C became less symmetrical in shape until the anisotropic spectrum began to appear at −25°C. Between −25 and −50°C, the spectrum of oriented Cu^{2+} ($g_\perp$ = 2.08, $g_\parallel$ = 2.37) replaced the g = 2.178 resonance and was very evident at −100°C. Since the average g value is given as $g_0 = \frac{1}{3}g_\parallel + \frac{2}{3}g_\perp$, then g_0 = 2.177 for the strong anisotropic Cu^{2+} signal, but g_0 = 2.130 for the weak Cu^{2+} signal. Thus, tumbling $Cu(H_2O)_6^{2+}$ averages the anisotropic g tensor to give g = 2.178, but restriction of the $Cu(H_2O)_6^{2+}$ in a contracting interlamellar region by lowering the temperature below −25°C prevents rotational motion and causes alignment of the z axis of the complex normal to the silicate sheets. The restricted motion separates the $g_\parallel$ and $g_\perp$ components of the g tensor, but g_0 remains the same as that for rapidly tumbling $Cu(H_2O)_6^{2+}$. The weak anisotropic resonance with $g_\perp$ = 2.04 and $g_\parallel$ = 2.31 may represent a planar $Cu(H_2O)_4^{2+}$ complex that has been immobilized on the surface of the silicate, either by strong adsorption forces or by collapse of a few interlayers to produce monolayers of water between the clay plates.

Two anisotropic spectra of Cu^{2+} have been observed on dehydrated zeolites with $g_\perp$, $g_\parallel$, and A values very similar to those reported in this study.[11] The loss of the isotropic signal by lowering the temperature was also observed as the asymmetric signal ($g_\perp$ = 2.10, $g_\parallel$ = 2.38) became more intense. Dehydration (by heating) produced both the anisotropic spectra, and the one with $g_\perp$ = 2.05 and $g_\parallel$ = 2.32 was assigned to square-pyramidal or square-planar Cu^{2+}. Simplified crystal field theory appears to confirm the assignment of these spectra to square-planar and tetragonal symmetries of hydrated Cu^{2+}. For the d^9 distorted octahedral complexes of Cu^{2+}, it can be shown that

$$g_\parallel = 2\left(1 + \frac{4\xi}{\Delta_1}\right)$$

$$g_\perp = 2\left(1 + \frac{\xi}{\Delta_2}\right)$$

where the spin–orbit coupling energy, ξ, for Cu^{2+} is 829 cm^{-1}, Δ_1 is the energy separation between $d_{x^2-y^2}$ and d_{xy}, and Δ_2 is the separation between $d_{x^2-y^2}$ and d_{xz}, d_{yz}.[12] For $g_\perp$ = 2.08 and $g_\parallel$ = 2.37, Δ_1 and Δ_2 are calculated to be about 18000 and 20000 cm^{-1} without making corrections for covalency. For $g_\perp$ = 2.04 and $g_\parallel$ = 2.31, Δ_1 and Δ_2 are about 21000 and 39000 cm^{-1}, respectively. These energy levels suggest that tetragonally distorted octahedral $Cu(H_2O)_6^{2+}$ accounts for the main ESR spectrum ($g_\perp$ = 2.08) in frozen clays, while square-planar $Cu(H_2O)_4^{2+}$ produces the weak spectrum ($g_\perp$ = 2.04) in the clays.[13,14] The distinct orientation of the tetragonally distorted $Cu(H_2O)_6^{2+}$ with the elongated z axis normal to the silicate plates has been observed in air-dry systems and reasons for the orientation have been discussed.[15] The basal spacing of the Cu^{2+} hectorite below 0°C is near 16 Å, leaving enough interlamellar space for the octahedral complex to orient as described. Thus, below −25°C, the hydrated interlayer of Cu^{2+} hectorite essentially becomes a crystalline solid.

Conclusions

The mobility of the spin probe cation, $Tempo^+$, in hectorite depends on both the quantity and type of solvent in the interlamellar regions. The spin probe as an exchange cation on external surfaces of fully hydrated hectorites is several hundred times more restricted than in dilute aqueous solution, and also tends to orient on the silicate sheets to permit maximum interaction between methyl groups of $Tempo^+$ and silicate oxygens while allowing close approach of the $-NH_3^+$ group to the surface. Removal of interlamellar water at low relative humidities causes increased orientation and decreased tumbling mobility of $Tempo^+$ due to the collapse of the interlamellar space. Cooling the hectorites to −50°C also produces decreased molecular tumbling because of the restrictions of layer collapse as well as the reduced thermal motion. Hectorites solvated in ethanol produce different orientation effects for $Tempo^+$ than is observed for the hydrated systems. The N–O bond axis of the molecule, rather than tending to align with the silicate plates as it does in hydrated clays, shows a tendency to orient normal to the plates, although the tumbling motion in ethanol is closer to random than in water. It is suggested that the methyl groups of $Tempo^+$ prefer to interact with the solvent (ethanol) rather than the external surface oxygen atoms of the silicate, and this results in considerable mobility as well as a different molecular alignment from that observed in hydrated hectorites. It is evident that the nature of the solvent can greatly alter the cation–surface interaction. Specific molecular alignments of the probe with the external surfaces are apparently preferred over others, and these alignments can reveal important properties of the adsorbing surfaces. However, probe ions in interlamellar regions are oriented and motionally restricted to a greater extent than those on the external surfaces.

When the ESR spectrum of exchangeable Cu^{2+} on hydrated hectorite is used as an indicator of the interlamellar hydration structure, distinct transitions are observed between +20 and −100°C. Much of the $Cu(H_2O)_6^{2+}$ demonstrates rotational or distortional freedom to temperatures lower than −25°C, suggesting a non-rigid, solution-like interlayer. As the temperature is lowered from −25°C, a larger proportion of the Cu^{2+} is motionally restricted and strongly oriented as $Cu(H_2O)_6^{2+}$ in interlayers containing about two monolayers of water. At −100°C, essentially all of the Cu^{2+} is restricted, a result of the migration of water from between clay plates at low temperatures which allows the plates to impose order on the $Cu(H_2O)_6^{2+}$ complexes. The results indicate that interlamellar water is highly structured when only two monolayers of water occupy the interlayer.

Acknowledgments. The author wishes to acknowledge the technical assistance of Mr. R. McBride for design of the cold-temperature x-ray diffraction apparatus. Gratitude is expressed to Dr. M. Fujimoto for the use of the ESR spectrometer and variable temperature attachment.

References and Notes

(1) Address correspondence to this author at the Department of Agronomy, Cornell University, Ithaca, N.Y. 14853.
(2) O. H. Griffith, L. J. Libertini, and G. B. Birrel, *J. Phys. Chem.*, **75**, 3417 (1971).

(3) C. F. Chignell, *Aldrichimica Acta*, **7**, 1 (1974).
(4) D. M. Clementz, T. J. Pinnavaia, and M. M. Mortland, *J. Phys. Chem.*, **77**, 196 (1973).
(5) M. B. McBride, T. J. Pinnavaia, and M. M. Mortland, *Am. Mineral.*, **60**, 66 (1975).
(6) F. Sachs and R. Latorre, *Biophys. J.*, **14**, 316 (1974).
(7) P. Jost, L. J. Libertini, V. C. Hebert, and O. H. Griffith, *J. Mol. Biol.*, **59**, 77 (1971).
(8) A. D. Keith and W. Snipes, *Science*, **183**, 666 (1974).
(9) R. G. Gast and M. M. Mortland, *J. Colloid Interface Sci.*, **37**, 80 (1971).
(10) D. M. Anderson and P. Hoekstra, *Soil Sci. Soc. Am. Proc.*, **29**, 498 (1965).
(11) J. Turkevich, Y. Ono, and J. Soria, *J. Catal.*, **25**, 44 (1972).
(12) A. Carrington and A. D. McLachlan, "Introduction to Magnetic Resonance", Harper and Row, New York, N.Y., 1967, p 158.
(13) J. T. Richardson, *J. Catal.*, **9**, 178 (1967).
(14) J. E. Huheey, "Inorganic Chemistry: Principles of Structure and Reactivity", Harper and Row, New York, N.Y., 1972, pp 321–337.
(15) M. B. McBride, T. J. Pinnavaia, and M. M. Mortland, *J. Phys. Chem.*, in press.

X-Ray Diffraction and Electron Spin Resonance Studies of Single Crystals of Copper(II) Doped L-Cystine Dihydrochloride Dihydrate

Shiro Kominami,[1] Peter Riesz,*

Laboratory of Physiology, National Cancer Institute, National Institutes of Health, Bethesda, Maryland 20014

Toshiyuki Akiyama,[2] and J. V. Silverton

Laboratory of Chemistry, National Heart and Lung Institute, National Institutes of Health, Bethesda, Maryland 20014

(Received July 2, 1975)

Publication costs assisted by the National Institutes of Health

Crystals of Cu^{2+} doped L-cystine dihydrochloride dihydrate were grown from L-cystine–HCl solutions containing a high concentration of Cu^{2+} ions. X-ray analysis of the crystal structure and ESR studies of crystals with doped Cu^{2+} ions were performed. The crystals belong to space group $P2_1$ with a = 5.882(1), b = 13.182(1), c = 9.390(1) Å, and β = 90.77(2)°. The structure refinement was carried out to R = 0.051 and the positions of all atoms excluding Cu^{2+} ions were determined. From the ESR data, two distinct Cu^{2+} complexes, Cu^{2+}(A), and Cu^{2+}(B), were identified. One of the water molecules and a Cl^- ion were found to be the ligands for Cu^{2+}(A) ion. The principal values for **g** and hyperfine, A(^{63}Cu), tensors for the Cu^{2+}(A) complex were 2.058, 2.073, and 2.343, and 17, 23.5, and 127 G, respectively. The principal g values for the Cu^{2+}(B) complex were 2.02, 2.08, and 2.22. The dope sites for Cu^{2+}(A) and Cu^{2+}(B) ions were located in the crystal structure. The effects of Cu^{2+} ions on crystal growth are discussed.

Introduction

ESR studies of Cu^{2+} doped crystals of various amino acids have shown that Cu^{2+} ions are usually located at approximately square-planar sites formed by two carboxyl groups and two amino groups.[3-6] In crystals of L-histidine hydrochloride monohydrate, the Cu^{2+} ions are in a compressed octahedral ligand field produced by a carboxyl group, a water molecule, two Cl^- ions, and two amino groups.[7] No detailed information about crystals of Cu^{2+}-doped, sulfur-containing amino acids has been reported previously.[8] Attempts to prepare crystals of Cu^{2+} doped cystine·2HCl were made, but all the crystals which contained Cu^{2+} ions were found to be crystals of L-cystine dihydrochloride dihydrate with the space group $P2_1$. These are different from the previously investigated crystals of L-cystine dihydrochloride which have space group $C2$.[9,10] In this work, a crystal structure determination of L-cystine dihydrochloride dihydrate ($P2_1$) and ESR studies of dope sites for Cu^{2+} ions were performed to provide information on Cu^{2+} ions in a sulfur-containing amino acid crystal and also to attempt to understand the role of Cu^{2+} ions in changing the crystal structure. The crystal structure is almost isomorphous with that of L-cystine dihydrobromide dihydrate[11] which had not been reported at the inception of this work. Two distinct ESR signals of Cu^{2+} ions, Cu^{2+}(A) and Cu^{2+}(B), were observed in the Cu^{2+} doped L-cystine dihydrochloride dihydrate crystals and the dope sites of Cu^{2+} ions were located in the crystal structure. It is inferred that the complex formation of Cu^{2+} ions with cystine molecules stabilizes a particular configuration of L-cystine molecules.

Experimental Section

Procedure for Growing Crystals. Single crystals of Cu^{2+} doped L-cystine dihydrochloride dihydrate, $HOOCCH(NH_2{\cdot}HCl)CH_2SSCH_2CH(NH_2{\cdot}HCl)COOH{\cdot}2H_2O$, were obtained from degassed 5 N HCl solutions containing 0.8 M cupric chloride and 0.5 M L-cystine dihydrochloride by slow cooling. The deoxygenation was necessary to prevent the oxidation of L-cystine. A significant amount of cysteic acid was found by amino acid analysis of crystals grown from aerated solutions, whereas crystals which were grown from the carefully deoxygenated solutions did not contain any detectable amount of cysteic acid. A high concentration of Cu^{2+} ions in the HCl solutions was required to obtain Cu^{2+} doped L-cystine dihydrochloride dihydrate

TABLE I: Positional ($\times 10^4$) and Thermal Parameters ($\times 10^3$) for Heavier Atoms[a]

Atom	IUPAC name	x/a	y/b	z/c	U_{11}	U_{22}	U_{33}	U_{12}	U_{13}	U_{23}
S(a)	S_1^{γ}	−7497(2)	−2747(1)	−3631(1)	29(1)	24(1)	13(0)	8(0)	−6(0)	−5(0)
S(b)	S_2^{γ}	−6055(2)	−1566(1)	−2544(1)	24(1)	18(0)	19(0)	1(0)	3(0)	1(0)
C(1a)	C_1^{β}	−3961(8)	−8858(4)	−7115(4)	34(2)	22(2)	13(2)	−1(2)	0(2)	3(2)
C(1b)	C_2^{β}	−2361(7)	−6648(4)	−9101(4)	27(2)	22(2)	16(2)	−7(2)	−3(2)	4(2)
C(2a)	C_1^{α}	−3700(7)	−4052(4)	−3508(4)	27(2)	18(2)	13(2)	0(1)	−6(2)	0(2)
C(2b)	C_2^{α}	−105(7)	−1331(3)	−1067(4)	24(2)	15(2)	11(2)	−1(2)	−1(1)	0(1)
C(3a)	C_1	−2741(7)	−5020(4)	−2865(4)	29(2)	22(2)	13(2)	0(2)	−3(2)	2(2)
C(3b)	C_2	−1664(7)	−1835(3)	0(4)	27(2)	20(2)	15(2)	−3(2)	−3(2)	2(2)
N(a)	N_1	−3873(7)	−4145(3)	−5093(3)	31(2)	27(2)	12(1)	6(2)	−1(1)	2(1)
N(b)	N_2	−332(6)	−204(3)	−924(4)	29(2)	18(2)	17(1)	2(1)	−3(1)	3(1)
O(1a)	O_1'	−1502(7)	−5000(3)	−1829(4)	64(2)	36(2)	26(2)	8(2)	−24(2)	0(2)
O(1b)	O_2'	−2762(6)	−1387(3)	−9131(3)	33(2)	32(2)	22(1)	1(1)	7(1)	2(1)
O(2a)	O_1''	−3492(7)	−5829(3)	−3494(4)	41(2)	18(2)	32(2)	−1(1)	−10(1)	4(1)
O(2b)	O_2''	−1669(7)	−2828(3)	−220(4)	47(2)	19(2)	41(2)	−10(2)	12(2)	0(2)
O(W1)		−1805(8)	−7480(3)	−2493(4)	53(2)	27(2)	39(2)	4(2)	3(2)	6(2)
O(W2)		−2309(7)	−2167(3)	−6020(5)	47(2)	31(2)	45(2)	2(2)	0(2)	10(2)
Cl(1)		−1045(2)	0.0	−4296(1)	26(0)	47(1)	18(0)	1(1)	−3(0)	11(0)
Cl(2)		−4757(2)	−4111(1)	−8578(1)	32(1)	19(0)	32(1)	−3(0)	4(0)	5(0)

[a] The thermal parameter used was $\exp(-2\pi^2\Sigma_i\Sigma_j U_{ij}a_i^*a_j^*h_ih_j)$. No esd is given for the origin specifying y parameter of Cl(1).

crystals. Crystals of L-cystine dihydrochloride (*C*2 form), which were grown from HCl solutions of low Cu^{2+} ion concentration, did not contain any detectable amount of Cu^{2+} ions. The Cu^{2+} doped crystals of L-cystine dihydrochloride dihydrate have a pale green color. These crystals are not stable in air and disintegrate into powder. Crystals of L-cystine dihydrochloride dihydrate ($P2_1$) could be easily distinguished from those of L-cystine dihydrochloride (*C*2), since the latter do not disintegrate under vacuum. The cupric ion concentration in the crystal was estimated from ESR measurements of a polycrystalline sample prepared from the single crystal by comparison with the ESR absorption of known amounts of cupric ions. The amount of cupric ion incorporated into the crystal depends on the length of time for growing the single crystal and varied from 10^{-4} to 10^{-3} cupric ions per cystine molecule. The Cu^{2+} concentration in the crystals is too low to allow detection of the copper atoms by x-ray methods. The deuterated crystals were formed in the same way from DCl solutions.

Structure Determination. The crystallographic data are as follows: space group $P2_1$; cell dimensions (least-squares refinement using reflections measured at $\pm\theta$) a = 5.882(1), b = 13.182(1), c = 9.390(1) Å; β = 90.77(2)°; V = 728 Å^3; Z = 2; d_x = 1.593 g/cc; d_m = 1.60(1) g/cc (flotation in *n*-propyl alcohol–tribromomethane solution); x-radiation, Cu Kα (graphite monochromator, λ 1.5418 Å); μ 4.69 cm^{-1}; crystal habit, monoclinic prismatic elongated along a; faces developed, {011} with additional minor development of {001}; diffractometer, Nonius CAD-4; crystal size for data collection, a sphere approximately 0.3 mm in diameter. The intensity data were collected by methods previously described.[12] The intensities of three standard reflections, (312), ($2\bar{6}2$), and (080), were measured sequentially at hourly intervals and also after every 51 reflections. There was no significant drop in the intensities of the standards. 1449 "observed" and 55 "unobserved" reflections at the 1σ level were used for structure determination and refinements.

The structure was solved by the heavy-atom method. Scattering factors for C, N, O, and Cl were taken from the International Tables of X-ray Crystallography[13] and, for H, from the work of Stewart et al.[14] The positions of two chlorine and two sulfur atoms were determined from a Patterson map. These four atom positions gave an R factor of 0.33 and at this stage the whole molecular framework could be seen in an F_o map. The structure was refined by full-matrix least-squares using anisotropic thermal parameters to R = 0.057 without including H atoms. All the hydrogen atoms could be seen in a difference map at this stage. The hydrogen atoms were then included in the refinement with isotropic thermal parameters and convergence was reached at an R factor of 0.051 (observed reflections only). Other indices at the end of the refinement were $\Sigma w^2(|F_o| - |F_c|)^2/(n - m)$ = 2.9 where n = number of observations and m = numbers of parameters and $R_w = (\Sigma w^2(|F_o| - |F_c|)^2/\Sigma w^2F_o^2)^{1/2}$ = 0.088. The final atomic positions are given in Tables I and II. The function minimized in the least-squares calculations was $\Sigma w^2(|F_o| - |F_c|)^2$ where w is defined in the work of Peterson and Levy.[15]

TABLE II: Positional Parameters for Hydrogen Atoms ($\times 10^3$)

Atom	x/a	y/b	z/c	$U(\times 10^2)$
H(1a)	−281(9)	−946(4)	−698(5)	2(1)
(1a′)	−416(12)	−882(6)	−831(7)	5(2)
(1b)	−318(10)	−620(5)	−979(6)	5(1)
(1b′)	−231(8)	−741(4)	−937(5)	4(1)
(2a)	−260(7)	−349(3)	−332(4)	1(1)
(2b)	−102(8)	−156(5)	−213(5)	2(1)
(0a)	−314(11)	−641(5)	−324(6)	3(2)
(0b)	−278(11)	−321(6)	−949(7)	6(2)
(Na)	−526(13)	−439(5)	−538(7)	4(2)
(Na′)	−259(12)	−463(6)	−549(8)	4(2)
(Na″)	−355(11)	−342(6)	−561(7)	5(2)
(Nb)	−172(12)	2(6)	−126(7)	4(2)
(Nb′)	−941(16)	13(8)	−154(9)	11(3)
(Nb″)	−976(11)	−1(5)	−8(7)	3(1)
(W1)	−31(13)	−762(7)	−314(8)	9(2)
(W1′)	−309(15)	−804(7)	−254(9)	11(3)
(W2)	−325(14)	−191(7)	−685(9)	8(3)
(W2′)	−168(13)	−167(7)	−539(8)	6(2)

ESR Measurements. Single crystals approximately 3 × 2 × 1 mm^3 were mounted on lucite rods each of which had an inclined surface prepared so that one of the crystallographic axes (a, b, or c^*) was parallel to the vertical axis of the rod. The crystals were rotated in the static magnetic field (H_0) around the a, b, and c* axes at intervals of 5 or 2.5°. All the ESR spectra were measured with a Varian E-9 X-

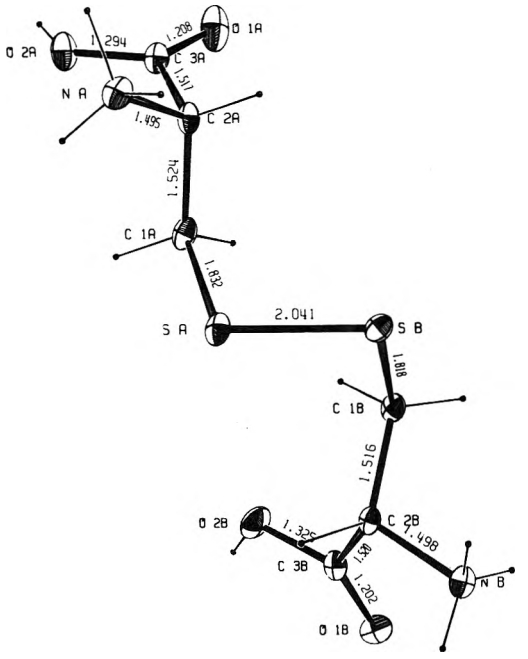

Figure 1. Molecular conformation and bond lengths of divalent cation of L-cystine in the crystal. The esd's are 0.002 Å for S–S bond, 0.004–0.005 Å for C–S bonds, and 0.005–0.007 Å for C–C bonds. This drawing was made with the ORTEP program,[16] using 30% probability ellipsoids. Hydrogen atoms are indicated by arbitrary spheres.

band spectrometer. A typical setting for measurements was the following: modulation frequency, 100 kHz; modulation amplitude, 2 G; microwave power, 20 mW. All the measurements were performed at 77 K using a Varian liquid nitrogen insert Dewar. Polycrystalline DPPH was used as the g marker. All the elements of the **g** and hyperfine tensors were obtained by least-square methods. The effects of quadrupole coupling and second-order effects on hyperfine splittings were neglected to obtain the elements of the tensors.[4]

Results

Structure of L-Cystine Dihydrochloride Dihydrate. The molecular structure and bond lengths of the divalent cation of L-cystine dihydrochloride dihydrate is shown as an ORTEP drawing[16] in Figure 1. The bond angles are listed in Table III. The averages of the bond lengths and angles among the chemically equivalent parts of L-cystine dihydrochloride dihydrate in the present study closely agree with those reported for L-cystine dihydrobromide dihydrate,[11] L-cystine dihydrochloride,[9,10] and L-cystine hydrobromide.[17] The values of the present work and those reported for hexagonal[18] and tetragonal[19] L-cystine crystals are also in reasonable agreement, except for the fact that, in the salts, the two C–O bonds are of different lengths unlike the situation in the free acid where the near equality was ascribed to a zwitterionic structure. While the dihydrobromide dihydrate and the present crystals are not exactly isomorphous, the agreement of bond lengths and angles is close and the fractional coordinates of the atoms are very similar if one allows for the differences in the axial labels and the origin. The torsion angles in the present structure (Table IV) are very similar to those for L-cystine dihydrobromide dihydrate; the biggest difference lies in the N(b)–C(2b)–C(3b)=O(1b) torsion angle which is −5° in the present structure and 0° in the dihydrobromide dihydrate.

TABLE III: Bond Angles (deg)

	$i = 1$	$i = 2$
$S_i\gamma-S_i\gamma-C_i\beta^a$	103.3(1)	99.5(2)
$S_i\gamma-C_i\beta-C_i\alpha$	114.1(3)	113.3(3)
$C_i\beta-C_i\alpha-N_i$	110.2(3)	110.5(3)
$C_i\beta-C_i\alpha-C_i$	108.8(4)	113.3(3)
$N_i-C_i\alpha-C_i$	110.3(4)	108.6(3)
$C_i\alpha-C_i-O_i'$	121.3(4)	124.5(4)
$C_i\alpha-C_i-O_i''$	112.9(4)	109.3(4)
$O_i'-C_i-O_i''$	125.7(5)	126.2(4)

[a] For the first angle $i = 1$ and $j = 2$, and for the second angle $i = 2$ and $j = 1$. In the nomenclature of this paper these angles correspond to S(b)–S(a)–C(1a) and S(a)–S(b)–C(1b), respectively.

TABLE IV: Torsion Angles (deg)

	IUPAC (1970) designation[a]	
$\tau(C_2\beta-S_2\gamma-S_1\gamma-C_1\beta)$	χ^3	−80
$\tau_2(S_i\gamma-S_i\gamma-C_i\beta-C_i\alpha)^b$	(χ_1^2, χ_2^2)	(−81, −71)
$\tau_2(S_i\gamma-C_i\beta-C_i\alpha-N_i)$	(χ_1', χ_2')	(−56, −85)
$\tau_2(S_i\gamma-C_i\beta-C_i\alpha-C_i)$		(−177, 153)
$\tau_2(N_i-C_i\alpha-C_i=O_i')$	(χ_1', χ_2')	(145, −5)

[a] See ref 22. [b] $\tau_2(S_j\gamma-S_i\gamma-C_i\beta-C_i\alpha)$ designates two equivalent torsion angles. For the first torsion angle $i = 1$ and $j = 2$, and for the second torsion angle $i = 2$ and $j = 1$. In the nomenclature of this paper these torsion angles correspond to τ[S(b)–S(a)–C(1a)–C(2a)] and τ[S(a)–S(b)–C(1b)–C(2b)], respectively.

Individual values of bond lengths in the present structure agree reasonably with those quoted by Sutton et al.,[20] except that the C–N bonds show the lengthening, first noted by Birnbaum,[21] usually present when a nitrogen atom is ionized. In the chemically equivalent parts of the present molecular structure, differences in the bond lengths are apparent but do not reach the 3σ level. Five pairs of angles are significantly different, however, S–S–C(1), C(1)–C(2)–C(3), C(2)–C(3)–O(1), C(2)–C(3)–O(2), and N–C(2)–C(3), and it is interesting that these are the same angles which show differences in the same sense in the dihydrobromide dihydrate, although there only two of the pairs were significantly different. It is much more likely that the effect of the unsymmetrical environment should be shown by the bond angles, in view of relative magnitudes of the force constants for bending and stretching of bonds. Since the trends are similar in both structures, one may conclude that the differences are real.

The average C–H, N–H, and O–H lengths in the present structure are 1.06, 0.97, and 0.99 Å with average esd's of 0.05, 0.08, and 0.08 Å, respectively. Possible hydrogen bonds are listed in Table V. On the bases of van der Waals radii[23] and hydrogen bond angles, ten hydrogen bonds appear probable. The remaining two hydrogen atoms, H(Nb') and H(W2), may also form hydrogen bonds but, since unique linkages cannot be assigned, the bonds may be weak bifurcated ones and in the case of H(Nb'), there may also be an additional electrostatic attraction. The N(a)–H(Na)- -Cl(1) and O(W2)–H(W2')- -Cl(1) bonds are also apparently relatively weak since the heavy atom distances are comparable with the appropriate sums of van der Waals radii, although H–Y distances are considerably less than van der Waals contacts. Both of the hydroxyl hydrogen atoms of the carboxyl groups appear strongly bonded to a Cl^- ion or the oxygen atom of water. One hydrogen atom of each amino group makes a strong H bond with an oxygen

TABLE V: Possible Hydrogen Bonds

Bond description[a] X—H---Y	$d_{H\cdots Y}$, Å	$d_{X\cdots Y}$, Å	X—H---Y, deg
O(2a)—H(0a)---O(W1)	1.76(7)	2.565(5)	165
O(2b)—H(0b)---Cl(2)	1.88(7)	2.935(4)	166
N(a)—H(Na)---Cl(1)^{I}	2.33(8)	3.239(4)	170
N(a)—H(Na')---Cl(1)	2.20(7)	3.164(4)	149
N(a)—H(Na'')---O(W2)	1.85(8)	2.903(6)	161
N(b)—H(Nb)---Cl(2)^{I}	2.37(7)	3.256(4)	159
N(b)—H(Nb')---Cl(2)	2.65(9)	3.360(4)	136
N(b)—H(Nb')---Cl(1)	2.76(8)	3.164(4)	117
N(b)—H(Nb'')---O(1a)	1.93(6)	2.801(5)	164
O(W1)—H(W1)---O(W2)^{II}	1.84(8)	2.841(6)	150
O(W1)—H(W1')---Cl(2)^{III}	2.17(9)	3.127(4)	149
O(W2)—H(W2)---O(1b)	2.27(8)	3.105(5)	139
O(W2)—H(W2)---O(2a)^{IV}	2.41(8)	3.065(6)	122
O(W2)—H(W2')---Cl(1)^{V}	2.46(9)	3.362(4)	159

[a] Symmetry operations are indicated as follows: None, x, y, z: I, $1 + x, y, z$; II, $-x, \frac{1}{2} + y, 1 - z$; III, $1 - x, \frac{1}{2} + y, 1 - z$; IV, $1 - x, -\frac{1}{2} + y, 1 - z$; V, $-x, -\frac{1}{2} + y, 1 - z$.

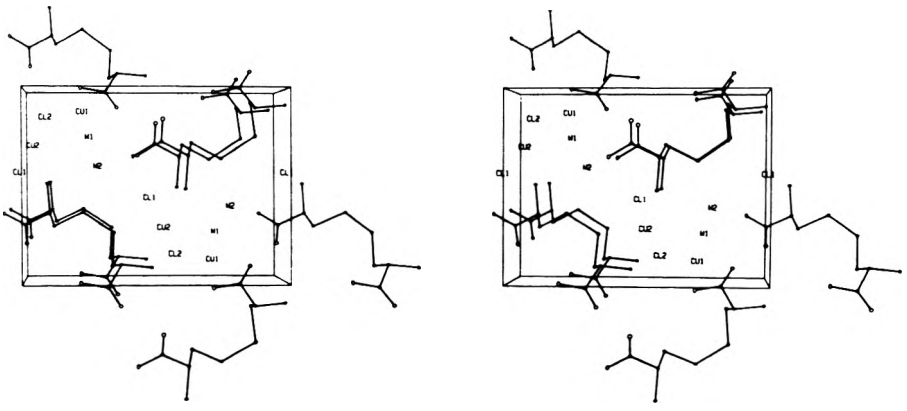

Figure 2. Packing diagram, stereo pair. The direction of projection is *a*. Cu^{2+}(A) and Cu^{2+}(B) are indicated as Cu1 and Cu2, respectively.

atom of a carboxyl group or a water molecule. The molecular packing is illustrated in Figure 2, which includes estimated positions of Cu^{2+} ions. The packing is similar to that reported for L-cystine dihydrobromide dihydrate.[9] It may be seen that N(b), Cl(1), N(a), and Cl(2) are almost in a plane. N(a), Cl(2), N(b)*, and Cl(1)* are also found to be almost coplanar, where N(a) and Cl(2) are in the same positions as in the former plane but N(b)* and Cl(1)* are one unit away along the *a* axis from the former N(b) and Cl(1) atoms. The former plane is almost a square with sides ranging from 3.2 to 3.4 Å. The latter plane is almost a rhombus whose four sides are from 3.2 to 3.3 Å with an acute angle of about 72°. The discrepancy of the atom positions from the planes for both groups of atoms is less than 0.2 Å. The angle between these planes is about 133°. The arrangement of these planes could be described as zigzag bands along the *a* axis. Cystine molecules stay between two zigzag bands. The hydrogen bonds from water molecules and carboxyl groups to Cl^- ions or amino groups appear to link the bands.

ESR Absorptions of Cu^{2+} Ions. The ESR spectra of Cu^{2+} ions in crystals of L-cystine dihydrochloride dihydrate which were grown in a few days are depicted in Figures 3 and 4. These crystals had concentrations of about 10^{-4} Cu^{2+} ions per L-cystine molecule. Two different kinds of ESR absorptions due to Cu^{2+} ions were distinguished, which will be called Cu^{2+}(A) and Cu^{2+}(B) absorptions. The integrated areas of Cu^{2+}(A) and Cu^{2+}(B) absorptions are almost the same. Only one set of ESR absorptions due to Cu^{2+}(A) ions was observed at all the orientations of the crystal with respect to the static magnetic field (H_0), although the symmetry of the crystal is $P2_1$.[24] This fact suggests that one of the principal axes of the Cu^{2+}(A) complexes should be parallel to the crystallographic *b* axis. Four hyperfine lines of Cu^{2+}(A) were split into four sets of four equally spaced lines with almost equal intensities, Figures 3c and 4c. This superhyperfine splitting due to some ligands was maximized at the orientation of H_0 parallel to the *b* axis, where the superhyperfine splitting became equal to that due to the ^{63}Cu nucleus, and the observed spectrum was simplified into seven lines with additional lines due to the ^{65}Cu isotope, Figures 3a and 4a. The theoretical intensities are shown by stick diagrams, where the hyperfine splittings due to $^{63,65}Cu$ nuclei and the superhyperfine splitting which gave four equally spaced lines were considered. The four equally spaced lines with equal intensities were attributed to a coupling with a nucleus of $I = \frac{3}{2}$. The only nuclei in this crystal with $I = \frac{3}{2}$ are $^{63,65}Cu$ and $^{35,37}Cl$. There was no indication of the copper–copper interactions which have been observed in other systems[25,26] and hence one of the ligands for Cu^{2+}(A) ions was identified as a Cl^- ion. ^{37}Cl isotope effects are possible in the ESR signals but were not identified.

The crystals grown from HCl (H crystals) and from DCl (D crystals) showed differences in ESR spectra at certain orientations. In the D crystals, Cu^{2+} ions showed only four lines due to hyperfine coupling with the ^{63}Cu nuclei with satellite lines due to ^{65}Cu nuclei as shown in Figure 4d. At the same orientation of the H crystals, four sets of multiple lines were observed as shown in Figure 3d. These addition-

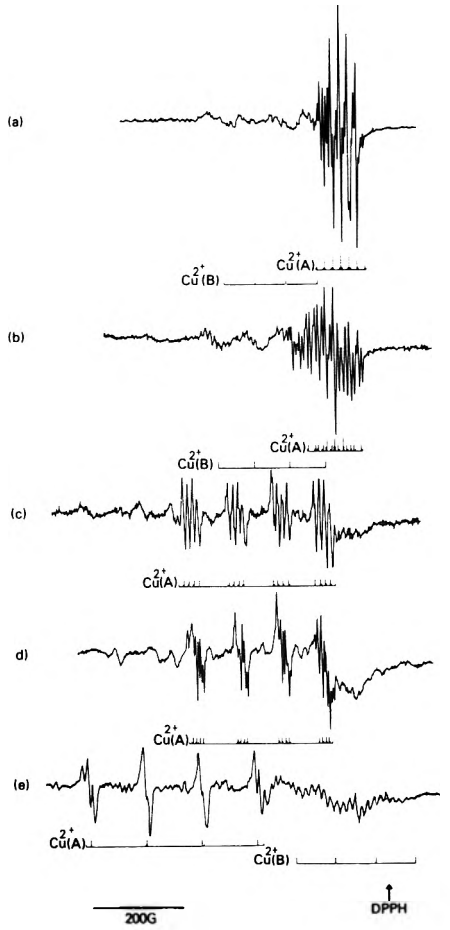

Figure 3. ESR spectra of Cu^{2+}-doped L-cystine dihydrochloride dihydrate at 77 K. The crystals were grown from HCl solutions in 2–3 days. (a) H_0 is parallel to the *b* axis. (b) H_0 is in the *bc** plane and 15° from the *b* axis. (c) H_0 is in the *bc** plane and 130° from the *b* axis. (d) H_0 is in the *ac** plane and 110° from the *a* axis. (e) H_0 is in the *ac** plane and 70° from the *a* axis.

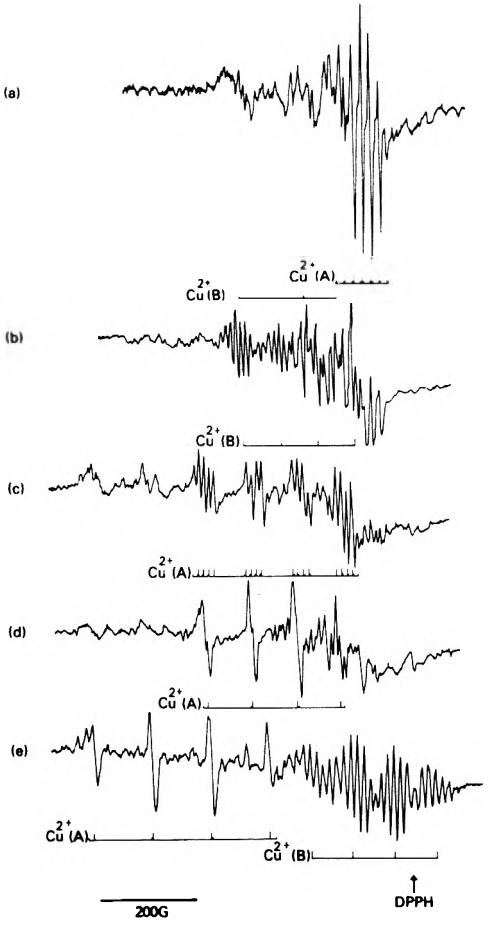

Figure 4. ESR spectra of Cu^{2+}-doped L-cystine dihydrochloride dihydrate at 77 K. The crystals were grown from DCl solutions in 2–3 days. (a) H_0 is parallel to the *b* axis. (b) H_0 is in the *bc** plane and 15° from the *b* axis. (c) H_0 is in the *bc** plane and 130° from the *b* axis. (d) H_0 is in the *ac** plane and 110° from the *a* axis. (e) H_0 is in the *ac** plane and 70° from the *a* axis.

al splittings in the H crystals are attributed to the superhyperfine coupling with exchangeable hydrogen atoms attached to or close to the ligand atoms. The spectrum could be explained in terms of superhyperfine splittings due to two nonequivalent hydrogen atoms and this interpretation is illustrated by a stick diagram below Figure 3d. The exchangeable hydrogen atoms in the crystal were those of amino groups, carboxyl groups, and water molecules. If amino groups were the ligands for Cu^{2+}(A) ions, the superhyperfine structure of a triplet or a combination of triplets due to the nitrogen nuclei ($I = 1$) would be expected in the D crystal as has been observed in other deuterated amino acid crystals.[4,5] However such a superhyperfine structure was not observed in the present study and hence the amino groups were eliminated as the ligands. The carboxyl groups could be the ligands but usually carboxyl groups are ionized to complex with Cu^{2+} ions[27] and therefore superhyperfine splitting due to exchangeable hydrogen atoms of carboxyl groups would not be expected. The most likely ligands are water molecules. It is not clear whether the two hydrogen atoms belong to one or two water molecules. The superhyperfine splittings due to the exchangeable hydrogen atoms were anisotropic and were not resolved at orientations where Cl^- superhyperfine splitting was well resolved. This would not be the case if the Cu^{2+}–Cl^- bond had the same direction as the Cu^{2+}–OH_2 bond. Furthermore the superhyperfine splittings due to the exchangeable hydrogen atoms were not resolved at the orientations where H_0 is close to the direction of the maximum *g* value.

The principal values and the direction cosines for **g**, ^{63}Cu hyperfine [**A**(^{63}Cu)], and ^{35}Cl superhyperfine [**A**(^{35}Cl)] tensors are listed in Table VI. The principal values of the **g** and hyperfine tensors are quite similar to those of Cu^{2+} ions in the square-planar ligand field observed in other Cu^{2+} doped amino acids.[3-5] The superhyperfine coupling tensor of the Cl^- ion is almost axially symmetric and hence the Cu^{2+}(A)–Cl^- bond is in the direction of the symmetry axis.[28] The Cl^- and H_2O ligand molecules should be in a plane which is perpendicular to the direction vector for maximum *g* value. The ligands other than these could be oxygen or sulfur atoms which would not give rise to any additional splittings.

The Cu^{2+}(B) absorptions were well resolved only at certain orientations of the D crystal, Figure 4b,e. Four sets of multiple lines were observed in the D crystal as shown in Figure 4e, but for the H crystal the lines were not well resolved at the same orientation, Figure 3e. This difference of Cu^{2+}(B) absorptions between in the H and D crystals indicates that some exchangeable hydrogen atoms may contribute to the ligand-hyperfine structures of Cu^{2+}(B) absorptions and also that at least one of the ligands may be the

TABLE VI: The g and Hyperfine Tensors and the Corresponding Direction Cosines for Assignments of Cu^{2+} Complexes in L-Cystine Dihydrochloride Dihydrate

g	A(^{63}Cu), G	A(^{35}Cl), G	Direction cosines a	b	c*
		Cu^{2+}(A)			
2.058	17	17	(0.0,	1.0,	0.0)
2.073	23.5	0–3[a]	(0.882,	0.0,	−0.471)
2.343	127	0–3	(0.471,	0.0,	0.882)
Cu^{2+}(A)–Cl(2)[b]			(−0.052,	±0.989,	−0.139)
O(W1)–O(2b)			(0.829,	∓0.100,	−0.550)
Z[c]			(0.559,	±0.144,	0.816)

g		Direction cosines a	b	c*
	Cu^{2+}(B)			
2.02 ± 0.02		(−0.71,	±0.39,	−0.58)
2.08 ± 0.02		(−0.41,	±0.43,	0.80)
2.22 ± 0.01		(0.57,	±0.81,	−0.15)
Cl(2)–Cl(1)		(−0.758,	±0.260,	−0.600)
N(a)–N(b)		(−0.527,	±0.297,	0.796)
Cu^{2+}(B)–S(b)[d]		(0.438,	±0.893,	0.102)

[a] A 3-G splitting was estimated from the line width. [b] The position of Cu^{2+}(A) ion was assumed to be at the middle of O(W1) and O(2b). [c] Z direction vector was calculated from the vector product of O(W1)–O(2b) and Cu^{2+}(A)–Cl(2) vectors. [d] The position of Cu^{2+}(B) ion was assumed to be at the center of the square formed by Cl(2), Cl(1), N(a), and N(b).

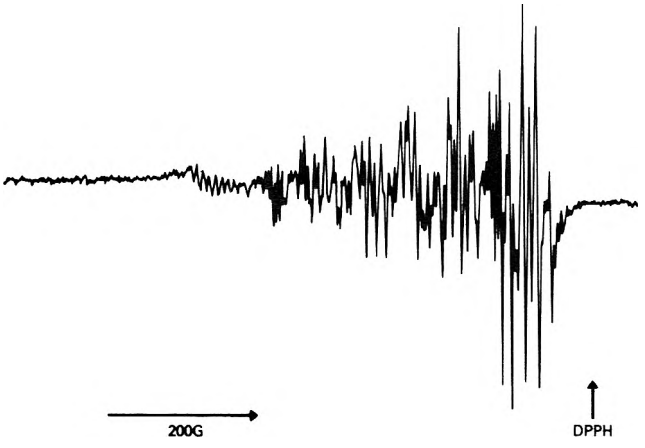

Figure 5. ESR spectrum of Cu^{2+}-doped L-cystine dihydrochloride dihydrate at 77 K. The crystals were grown from DCl solution in 2 weeks. H_0 is parallel to the *b* axis.

amino group of a cystine or a water molecule. Four sets of more than five lines were observed as shown in Figure 4e and these could not be attributed only to two equivalent amino nitrogen atoms which would give rise to four sets of five lines. Four sets of seven lines would be expected if two Cl^- ions were bound equivalently to the Cu^{2+} ions. The fact that well-resolved Cu^{2+}(B) absorptions were not observed at most of the orientations made it difficult to estimate the hyperfine tensor. The uncertainty in the assignments of the center of the absorptions is of the order of 10 G. An error of 10 G would result in $\Delta g = 0.007$ which is small in comparison with the observed change of the *g* value from 2.05 to 2.2 and hence the **g** tensor could be calculated. However a 10-G error is too large for a meaningful calculation of the hyperfine coupling whose estimated change is about 20 G. Table VI lists the principal values and direction cosines of the calculated **g** tensor. The principal *g* values are not exactly axial but the two smaller values are rather similar. The *g* values are closer to those observed for elongated octahedral or square-planar ligand fields than those for the compressed octahedral field.[29,30]

The ESR spectra shown in Figures 3 and 4 contain additional lines which cannot be explained by the Cu^{2+}(A) and Cu^{2+}(B) absorptions. These additional ESR signals increased if a longer time was taken to grow the crystals. A crystal which took 2 weeks to grow showed complicated absorptions, Figure 5, and the total Cu^{2+} ion concentration of this crystal was about 10^{-3} Cu^{2+} ions per cystine molecule. The concentration of Cu^{2+}(A) ions in this crystal was about a factor of 3 greater than in the crystals whose ESR spectra are shown in Figures 3 and 4. The contributions of the Cu^{2+}(B) absorptions could not be estimated because of overlapping of other signals. Figure 5 clearly shows the existence of several other sites where Cu^{2+} ions can complex in the crystal of L-cystine dihydrochloride dihydrate. This spectrum is too complicated to be analyzed at this stage.

Discussion

Dope Sites for Cu^{2+}(A) and Cu^{2+}(B) Ions. It was inferred that the Cu^{2+}(A) ion was in a square-planar ligand field

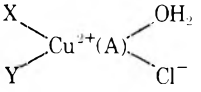

where X is a ligand which does not show any additional splittings and Y could be another H_2O molecule. A water molecule and a chlorine ion make one side of the square and the Cu^{2+}(A)–Cl^- bond direction is estimated to be parallel to the *b* axis. The bond lengths of the Cu^{2+}–OH_2 and Cu^{2+}–Cl^- bonds are usually in the range of 2.2–2.4 and 2.2–2.3 Å, respectively.[31-33] Hence the distance between the oxygen atom of the water molecule and the Cl^- ion in the square was calculated to be about 3 Å and the H_2O–Cl^- direction should be at an angle of about 45° to the *b* axis. The only pair of a water molecule and a Cl^- ion which can satisfy these conditions is a pair of H_2O(W1) and Cl(2) in the crystal. In a similar way, the third ligand can be identified to be the oxygen atom, O(2b), of the carboxyl group. However, no atoms could be found at the position where the fourth ligand was expected. It is possible that the molecular configuration is distorted around the Cu^{2+}(A) ion in the unit cells which actually contain the Cu^{2+} ions. In such

a unit cell an oxygen atom of the carboxyl group or a sulfur atom of the disulfide bond might be displaced to the position of the fourth ligand. The assumed positions for Cu^{2+}(A) ions are illustrated in Figure 2. The principal values for the **g** and hyperfine tensors for the Cu^{2+}(A) complex could also be explained as the Cu^{2+}(A) ion in an elongated octahedral field but the other two ligands required for an octahedral field are not present in the crystal structure. The estimated direction cosines for Cu^{2+}(A)–ligand bonds are listed in Table VI and are in good agreement with the principal directions of the **g** and hyperfine tensors. The direction of the Cu^{2+}(A)–Cl^- bond is not exactly parallel to the *b* axis and hence two Cu^{2+}(A) absorptions would be expected when H_0 is in the *ab* or *bc** plane. However, only one absorption for Cu^{2+}(A) ions was observed at these orientations. These results could also be explained if the situation in the unit cells actually containing Cu^{2+} ions was not exactly the same as that in the bulk structure given by the x-ray results.

The principal *g* values for Cu^{2+}(B) ions are listed in Table VI and they do not correspond exactly to the axially symmetric ligand field case, but for simplicity axial symmetry around Cu^{2+}(B) ions will be assumed. The direction for the maximum *g* value is the direction of the symmetry axis in the case of an elongated octahedral or a square-planar ligand field. A square made by two amino groups and two Cl^- ions could be found in the crystal and the direction perpendicular to the square was found to be almost parallel to the direction for the maximum *g* value. If we assume that the Cu^{2+}(B) ion is located in the center of the square, the calculated lengths of Cu^{2+}(B)–Cl^- and Cu^{2+}(B)–NH_2 bonds were 2.25 and 2.35 Å, respectively. These bond lengths are similar to those in other Cu^{2+} complexes.[32-35] A sulfur atom, S(b), of the disulfide bond is located at a position 2.9 Å away from the center of the square and the direction for the assumed Cu^{2+}(B)–S(b) bond is almost perpendicular to the square. This calculated length for the assumed Cu^{2+}(B)–S(b) bond is longer than those for reported Cu^{2+}–S bonds which range from 2.3 to 2.6 Å.[36,37] However a slight distortion of the molecular configuration might make this Cu^{2+}(B)–S(b) bond possible. The direction cosines for Cl(1)–Cl(2), N(a)–N(b), and Cu^{2+}(B)–S(b) bonds are listed in Table VI and they are in good agreement with the observed principal directions for the **g** tensor of Cu^{2+}(B) ions. The estimated positions of the Cu^{2+}(B) ions are illustrated in Figure 2. The sixth ligand for the octahedral ligand field around the Cu^{2+}(B) ion could not be located in the crystal structure. Complicated ligand hyperfine lines could be expected from this ligand field. At arbitrary orientations of the D crystal, four sets of 5 × 7 lines could be expected. These considerations explain why the Cu^{2+}(B) absorptions are not well resolved at most orientations.

Effect of Cu^{2+} Ions on Crystal Growth. The crystals usually grown from L-cystine–HCl solutions are L-cystine dihydrochloride crystals which belong to the *C*2 space group and this paper represents the first report of the occurrence of crystals of L-cystine dihydrochloride dihydrate in the $P2_1$ space group. Crystals of L-cystine·2HCl (*C*2 form) were also grown from solutions of low Cu^{2+} ion concentration in our experiments but these crystals did not contain any detectable amount of Cu^{2+} ions. More than 20 crystals of L-cystine·2HCl·$2H_2O$ ($P2_1$ form) were grown under slightly different conditions and all were found to contain Cu^{2+} ions. These facts suggest that Cu^{2+}–L-cystine complexes may be necessary to produce the $P2_1$ crystals of L-cystine·2HCl·$2H_2O$. The $P2_1$ molecular packing of the L-cystine·2HCl·$2H_2O$ may be a metastable configuration in HCl solution and Cu^{2+} ions may stabilize this configuration. This is supported by the observation that L-cystine·2HBr·$2H_2O$ crystals have an almost isomorphous structure.[9] A square made by two Cl^- ions and two amino groups plays an important role in the arrangement of H bonds as shown by x-ray studies. ESR studies located the Cu^{2+}(B) ion in the center of this square. Almost the same square is found in L-cystine·2HCl crystals (*C*2 form) but the surroundings of this square are different in crystals of L-cystine·2HCl·$2H_2O$ ($P2_1$ form). One of the sulfur atoms of the disulfide bond is located in a position 2.9 Å from the center of the square in L-cystine·2HCl·$2H_2O$ crystals ($P2_1$ form) but in L-cystine·2HCl crystals (*C*2 form) the distance between the center of the square and the nearest sulfur atom is 4.9 Å.[9,10] In L-cystine–HCl solutions containing a high concentration of Cu^{2+} ions, a Cu^{2+} ion may complex with two Cl^- ions, two amino groups of two cystine molecules, and one sulfur atom of the disulfide bond. It seems likely that Cu^{2+} ions stabilize a particular configuration of L-cystine molecules. The same configuration could be formed at the other ends of the cystine molecules with or without Cu^{2+} ions. A crystal could grow on a nucleus produced by several cystine molecules connected according to the same scheme. Only a very low concentration of Cu^{2+} ions could be introduced into the crystals and this may indicate that the Cu^{2+} ions play a role only in the inception of the crystal formation but do not produce a stable Cu^{2+}–complex crystal. This is consistent with the previous suggestion that the configuration of cystine molecules around the Cu^{2+} ion is somewhat different from the bulk conformation given by the x-ray results.

Acknowledgment. The authors wish to express their gratitude to Dr. Hideo Kon and Dr. Mitsuo Sato of N.I.A.M.D.D., NIH for valuable discussions. We thank Dr. Michiyo Morishita of N.I.C.H.H.D., NIH for amino acid analysis.

Supplementary Material Available: structure factor table for Cu-doped cystine (12 pages). Ordering information is given on any current masthead page.

References and Notes

(1) Department of Chemistry, Faculty of Science, Kyoto University, Kyoto, Japan.
(2) Faculty of Pharmaceutical Sciences, University of Tokyo, Tokyo, Japan.
(3) K. Takeda, Y. Arata, and S. Fujiwara, *J. Chem. Phys.*, **53**, 854 (1970).
(4) M. Fujimoto and J. Janecka, *J. Chem. Phys.*, **55**, 1152 (1971).
(5) M. Fujimoto and Y. Tomkiewicz, *J. Chem. Phys.*, **56**, 749 (1972).
(6) Y. Tomkiewicz and M. Fujimoto, *J. Chem. Phys.*, **56**, 3317 (1972).
(7) R. Hirasawa and H. Kon, *J. Chem. Phys.*, **56**, 4467 (1972).
(8) O. Dobozy, F. Guba, and T. Mandy, *Magy Kem. Foly.*, **68**, 1 (1962).
(9) L. K. Steinrauf, J. Peterson, and L. H. Jensen, *J. Am. Chem. Soc.*, **80**, 3835 (1958).
(10) S. C. Gupta, A. Sequeira, and R. Chidambaram, *Acta Crystallogr., Sect. B*, **30**, 562 (1974).
(11) R. E. Rosenfield, Jr., and R. Parthasarathy, *Acta Crystallogr., Sect. B*, **31**, 816 (1975).
(12) J. V. Silverton, G. W. A. Milne, P. E. Eaton, K. Nyi, and G. H. Temme, III, *J. Am. Chem. Soc.*, **96**, 7429 (1974).
(13) "International Tables for X-Ray Crystallography", Vol. III, Kynoch Press, Birmingham, England, 1962, p 201.
(14) R. F. Stewart, E. R. Davidson, and W. T. Simpson, *J. Chem. Phys.*, **42**, 3175 (1965).
(15) S. W. Peterson and H. A. Levy, *Acta Crystallogr.*, **10**, 70 (1957).
(16) C. K. Johnson, ORTEP ORNL-3794, Oak Ridge, Tenn., 1965.
(17) J. Peterson, L. K. Steinrauf, and L. H. Jensen, *Acta Crystallogr.*, **13**, 104 (1960).

(18) B. M. Oughton and P. M. Harrison, *Acta Crystallogr.*, **12**, 396 (1959).
(19) M. O. Chaney and L. K. Steinrauf, *Acta Crystallogr., Sect. B*, **30**, 711 (1974).
(20) L. E. Sutton, O. Kennard, H. M. Powell, and D. H. Whiffen, *Chem. Soc., Spec. Publ.*, **No. 18** (1965).
(21) G. Birnbaum, *Acta Crystallogr.*, **23**, 576 (1967).
(22) IUPAC–IUB Commission on Biochemical Nomenclature, *J. Mol. Biol.* **52**, 1 (1970).
(23) A. Bondi, *J. Phys. Chem.*, **68**, 441 (1964).
(24) A. D. Rae, *J. Chem. Phys.*, **50**, 2672 (1969).
(25) R. H. Dunhill and J. R. Pilbrow, *J. Chem. Phys.*, **45**, 1474 (1966).
(26) J. A. McMillan and D. J. Cravens, *J. Chem. Phys.*, **57**, 3268 (1972).
(27) M. E. Martell and M. Calvin, "Chemistry of the Metal Chelate Compounds", Prentice-Hall, Englewood Cliffs, N.J., 1956, p 35.
(28) J. H. M. Thornley, B. W. Mangum, J. H. E. Griffiths, and J. Owen, *Proc. Phys. Soc. London*, **79**, 1263 (1961).
(29) C. Chow, K. Chang, and R. D. Willett, *J. Chem. Phys.*, **59**, 2629 (1973).
(30) P. A. Narayama and K. V. L. N. Sastry, *J. Chem. Phys.*, **57**, 3266 (1972).
(31) D. E. Billing and B. J. Hathaway, *J. Chem. Soc. A*, 1516 (1968).
(32) M. J. Bew, D. E. Billing, R. J. Dudley, and B. J. Hathaway, *J. Chem. Soc. A*, 2640 (1970).
(33) R. J. Dudley and B. J. Hathaway, *J. Chem. Soc. A*, 2799 (1970).
(34) A. Dijkstra, *Acta Crystallogr.*, **20**, 588 (1966).
(35) J. F. Blount, K. A. Fraser, H. C. Freeman, J. T. Szymanski, and C. H. Wang, *Acta Crystallogr.*, **22**, 396 (1967).
(36) M. Bonamico, G. Dessy, A. Mugnoli, A. Vaciago, and L. Zambonelli, *Acta Crystallogr.*, **19**, 886 (1965).
(37) G. Narongiu, E. C. Lingafelter, and P. Paoletti, *Inorg. Chem.*, **8**, 2763 (1969).

Dielectric Dispersion in *n*-Propylbenzene

Thomas G. Copeland and Donald J. Denney*

Department of Chemistry, Hamilton College, Clinton, New York 13323 *(Received July 25, 1975)*

Publication costs assisted by Hamilton College

Dielectric dispersion in *n*-propylbenzene has been studied between 150 and 138 K over the frequency range 10^2 to 10^5 Hz. The results are described accurately by the Cole–Davidson skewed-arc function which has been used previously for a large number of liquids and has generally been interpreted as indicating the importance of cooperative intermolecular effects in the dynamical behavior. The interpretation of earlier work on similar compounds in terms of a few discrete relaxation times is examined.

Introduction

Static[1,2] and dynamic[3] dielectric properties of a number of alkyl benzenes have been measured at room temperature and above. The dispersion behavior is somewhat ambiguous because of the limited number of microwave frequencies used and the small values of dielectric increment and loss arising from the small dipole moments (0.1 to 0.5 D). Since viscosity studies by Barlow, Lamb, and Matheson[4] indicated that several of these alkyl benzenes would undercool it appeared that the dispersion spectrum could be examined in the audio-radiofrequency region at low temperatures and its character determined more easily. Of the three materials tried in this study (isopropylbenzene, *n*-butylbenzene, and *n*-propylbenzene) only the latter could be undercooled sufficiently.

A second reason for studying the dispersion behavior of these compounds is to enable comparisons to be made between the spectra of nonhydrogen bonded liquids with low and high dipole–dipole interactions. Extensive data are available for a number of aliphatic bromides[5–8] ($\mu \sim 2.0$ D). Dilution of the dipole interaction by solution measurements in a readily undercooled solvent (2-methylpentane) led to disappointing results since the resulting dispersion could not be characterized by any simple analytic function.[9] (The present authors believe this result was due to a combination of dispersions of solute and solvent which, though in quite different frequency ranges in the pure state at the same temperature, probably overlap significantly in the mixture because the molecular environments are similar.) With the alkyl benzenes the dipole interactions should be considerably smaller though differences in molecular shape and bond moment distribution may make it difficult to make precise quantitative estimates.

Experimental Section

n-Propylbenzene was deoxygenated by a stream of nitrogen and then distilled over P_2O_5 through a Vigreux column in a nitrogen atmosphere. The middle portion of the distillate was stored under nitrogen. This portion showed only one peak on the gas chromatograph and the static dielectric constant and refractive index at 20°C were in good agreement with literature values: $\epsilon_0 = 2.370$ (2.372[1b]), $n_D = 1.4921$ (1.4920[10]).

Dielectric constant (ϵ') and loss (ϵ'') measurements in the range 10^2 to 10^4 Hz were made with a General Radio 1620-A capacitance measuring assembly and extended to 10^5 Hz with a Cole–Gross bridge.[11] The three-terminal coaxial cell had a nominal air capacitance of 8 pF and calibration showed that stray capacitance effects were negligible. Temperature measurement and control were accomplished as described previously.[12] Static dielectric constants were measured from 298 to 138.3 K and dispersion parameters determined from 149.4 to 138.3 K. The *n*-propylbenzene could be cooled to the lowest temperature used and then reheated slowly through the melting point with no evidence of freezing, either visual or electrical.

For a given temperature, errors in the dielectric constant (assuming no error in the air capacitance) are estimated to be in the range 0.2–0.3% while loss values may have errors of 4–5% at the frequency extremes although 1–2% is more

likely in a wide range around the loss maximum. The room temperature air-capacitance value was used in all calculations. The listed temperature is estimated to be within 0.2° of the correct value.

Results

Complex plane plots of the data were asymmetric and were analyzed in terms of the Cole–Davidson equation[13]

$$\epsilon^* = \epsilon' - i\epsilon'' = \epsilon_1 + (\epsilon_0 - \epsilon_1)/(1 + i\omega\tau_0)^\beta \qquad (1)$$

where ϵ_0 and ϵ_1 are the low- and high-frequency limits of the dielectric constant, ϵ', ω is the angular frequency ($= 2\pi f$), τ_0 is a characteristic relaxation time, and β is a dimensionless parameter in the range 0 to 1.

The parameters τ_0, β, and ϵ_1 were determined with the aid of a GE TSS/645 computer. Trial values were incremented over a range consistent with the observed complex plane plots and the best fit was taken to be the set of parameters which minimized the function

$$S = \left[\frac{\Sigma_\omega((\epsilon'_{obsd} - \epsilon'_{calcd})/\epsilon'_{obsd})^2}{M}\right]^{1/2} + \left[\frac{\Sigma_\omega((\epsilon''_{obsd} - \epsilon''_{calcd})/\epsilon''_{obsd})^2}{M}\right]^{1/2}$$

where M is the number of frequencies. As shown in Table I, the values of S range from 0.01 to 0.045 with about 90% of the contribution from deviations in loss values. Calculated and observed values of ϵ' and ϵ'' for one temperature are plotted in Figure 1. The agreement for each frequency is well within the experimental errors cited above.

Table I lists a representative set of dispersion parameters taken from two runs. Generally ϵ_1 values are estimated to have a precision of ±0.005 and β of ±0.02. These estimates may be exceeded somewhat at the highest two or three temperatures in the dispersion region where the high-frequency portion of the spectrum is least well defined. τ_0, the cutoff relaxation time of the Cole–Davidson representation, has the temperature dependence generally observed for undercooled liquids in the region where the viscosity exceeds about 10^2 P (see Figure 2). The curve is slightly convex toward the abscissa in a log $\tau_0 - 1/T$ plot.

The asymmetry parameter, β, increases with increasing temperature but the temperature range is too small to allow any extrapolations. A value of $\beta = 1$ corresponds to the familiar Debye locus representing a single exponential relaxation process.

One interesting contrast between the relaxation behavior of *n*-propylbenzene and that in the aliphatic bromides lies in the apparent absence in the former of any appreciable deviations from the Cole–Davidson (skewed-arc) analytic function at high frequencies. One could argue that the lowest temperatures used were not such as to show these deviations in the frequency range used. However, comparison of the ϵ_1 values found here with values of n_D^2, n_∞^2 (refractive index extrapolated to zero frequency considering only electronic polarization), and ϵ_∞ (which adds to n_∞^2 a contribution due to atomic polarization) extrapolated to the same temperature region indicates there can be little contribution from high-frequency deviations. [Room temperature values of n_∞ are taken from Forziati[10] and the contribution from atomic polarization is based on Altshuller's[1b] assumption that the value for *n*-propylbenzene is the same as that for the nonpolar 1,3,5-trimethylbenzene. Values of n_D^2, n_∞^2, and ϵ_∞ in our temperature range were calculated assuming

TABLE I: Dielectric Dispersion Parameters for *n*-Propylbenzene

T, K	ϵ_0	ϵ_1	$10^6\,\tau_0$, sec	β	S
293.3	2.370				
248.9	2.465				
205.2	2.581				
149.4	2.777	2.466	2.58	0.75	0.033
147.4	2.786	2.472	5.58	0.74	0.010
146.4	2.790	2.474	8.12	0.74_5	0.018
145.3	2.794	2.475	13.0	0.72	0.021
144.5	2.797	2.475	18.5	0.74	0.045
143.5	2.803	2.477	31.8	0.71	0.025
142.5	2.806	2.478	50.4	0.71	0.033
141.5	2.812	2.477	76.5	0.71_5	0.024
140.5	2.815	2.478	141	0.67_5	0.019
139.5	2.820	2.480	254	0.65_5	0.027
138.3	2.824	2.479	473	0.63_5	0.037

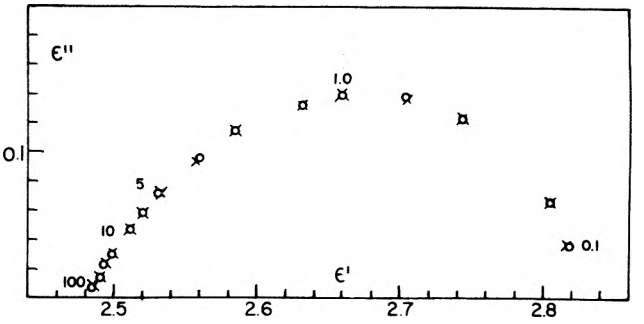

Figure 1. Complex plane diagram for *n*-propylbenzene at 139.5 K: O, observed values; ×, values from eq 1 using parameters in Table I. (Numbers beside points are frequencies in kHz.)

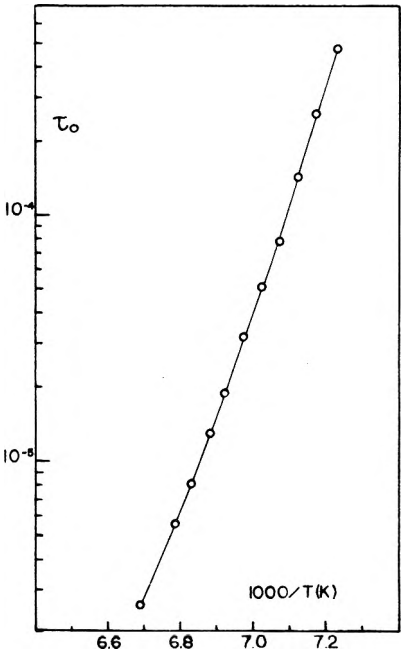

Figure 2. Log τ_0 (relaxation time parameter) vs. reciprocal absolute temperature for *n*-propylbenzene.

the Clausius–Mossotti relation for each to be temperature independent. Timmermans[14] gives density values for *n*-propylbenzene from 296 to 177 K and it is a linear function of T over this range. Also, Barlow et al.[4] found the density to be linear within 0.1% from 320 to 150 K. Extrapolation to the region of interest here (149 to 138 K) can be made

with an error estimated to be less than 0.5%.] The results are shown in Figure 3. In contrast to the usual observation, the observed ϵ_1 is slightly less than the calculated n_D^2 (0.3–0.8%) and about 2.5% less than the calculated ϵ_∞. Some of this discrepancy can be attributed to the temperature dependence of the geometric cell capacitance which decreases by about 0.25% in going from 298 to 95 K. The presence of voids in the glassy sample may also have made some contribution but the effect would have had to be reproducible since the ϵ_0 values in two separate runs were the same within 0.002. It is probable that the high value of ϵ_∞ is due to an overestimate of the atomic contribution to the molar refraction. In any event any high-frequency contribution to the orientation polarization, ordinarily estimated as $(\epsilon_1 - n_D^2)/(\epsilon_0 - \epsilon_1)$, would appear to be much less than the 3 to 5% observed for isoamyl bromide.

Altshuller[1b] calculated a dipole moment at 293 K of 0.35 using the Onsager equation with ϵ_∞ to account for the electronic and atomic contributions. At 149 K we calculate 0.32 using ϵ_∞ and 0.36 using ϵ_1. There do not seem to be any reliable vapor data.

Discussion

Hassell and Walker[3] interpreted their microwave data for several monoalkyl benzenes in the range 15–60°C in terms of two relaxation regions, each characterized by a single exponential. The interpretation was based on an apparent resolution of ϵ' vs. $\omega\epsilon''$ plots into two straight lines. Only six frequencies were available and, therefore, the resolution is not convincing. If one plots, in the same way, a dispersion corresponding to eq 1, one can obtain two reasonable "straight" lines within experimental error if the frequencies used are less than 4 or 5 times that of the loss maximum as in Hassell and Walker's data. The present work suggests that the resolution is not physically meaningful. The low temperature behavior of *n*-propylbenzene is similar to that found in many other liquids in which no specific association effects, e.g., H bonding, are present as indicated by the success of the Onsager equation in giving reasonable values for the dipole moment, values which are essentially constant over a wide temperature range. Although the temperature region here is much lower than that used by Hassell and Walker, work on isoamyl bromide[5,6,8] and *n*-octyl iodide[7] indicates that the basic character of the dispersion remains unchanged over a wide temperature interval with a continuous change in the parameters.

Although the dipole moment of *n*-propylbenzene and isoamyl bromide differ by a factor of about 6, there are no essential differences in the dispersion behavior, indicating that dipolar interactions based on the overall molecular moment play an insignificant role in determining this behavior. The β values in *n*-propylbenzene (0.64–0.74) are somewhat higher than those in isoamyl bromide (0.57–0.61) at temperatures where the dispersion frequencies are comparable but we are not prepared to speculate, at the present time, on the molecular origins of this difference.

Glarum,[6] Adam,[15] Anderson and Ullman,[16] and Zwanzig[17] have all proposed models of the dynamical behavior of dielectric fluids that, with appropriate choice of parameters, give rise to an asymmetric dispersion. The common feature in all of these models is the importance of intermolecular cooperative effects. Distributions of relaxation times due to intramolecular modes cannot be ruled out in all cases, especially at higher temperatures where the relative importance of cooperative effects may diminish, but there should be clear molecular reasons for invoking these and this does not appear to be the case for the simple monoalkyl benzenes.

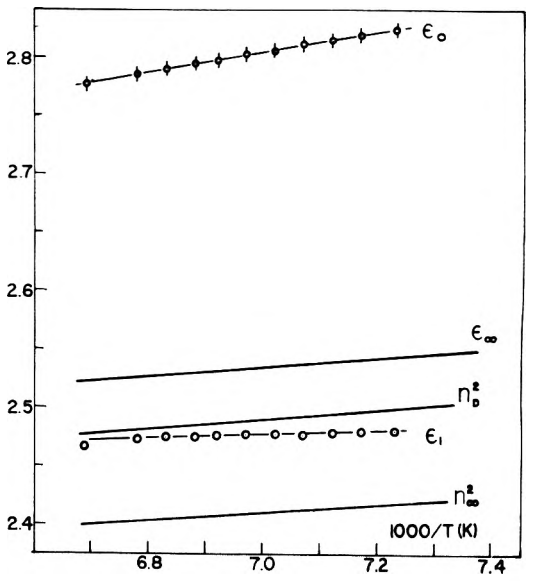

Figure 3. Dielectric constants and refractive indices for *n*-propylbenzene vs. reciprocal absolute temperature. The lines (ϵ_∞, n_D^2, n_∞^2) were calculated assuming temperature independence of the Clausius–Mossotti function.

Acknowledgment. This work was supported in part by the National Science Foundation URP Program.

References and Notes

(1) (a) A. P. Altshuller, *J. Phys. Chem.*, **57**, 538 (1953); (b) *ibid.*, **58**, 392 (1954).
(2) C. W. N. Cumper, A. I. Vogel, and S. Walker, *J. Chem. Soc.*, 3640 (1957).
(3) W. F. Hassell and S. Walker, *Trans. Faraday Soc.*, **62**, 861 (1966).
(4) A. J. Barlow, J. Lamb, and A. J. Matheson, *Proc. R. Soc. London, Ser. A*, **292**, 322 (1966).
(5) D. J. Denney, *J. Chem. Phys.*, **27**, 259 (1957).
(6) S. H. Glarum, *J. Chem. Phys.*, **33**, 639 (1960).
(7) F. I. Mopsik and R. H. Cole, *J. Chem. Phys.*, **44**, 1015 (1966).
(8) J. G. Berberian and R. H. Cole, *J. Am. Chem. Soc.*, **90**, 3100 (1968).
(9) D. J. Denney and J. W. Ring, *J. Chem. Phys.*, **44**, 4621 (1966).
(10) A. F. Forziati, *J. Res. Natl. Bur. Stand.*, **44**, 373 (1950).
(11) R. H. Cole and P. M. Gross, Jr., *Rev. Sci. Instrum.*, **20**, 252 (1949).
(12) D. J. Denney and J. W. Ring, *J. Chem. Phys.*, **39**, 1268 (1963).
(13) D. W. Davidson and R. H. Cole, *J. Chem. Phys.*, **19**, 1484 (1951).
(14) J. Timmermans, "Physico-chemical Constants of Pure Organic Compounds", Elsevier, New York, N.Y., 1950.
(15) G. Adam, *J. Chem. Phys.*, **43**, 662 (1965).
(16) J. E. Anderson and R. Ullman, *J. Chem. Phys.*, **47**, 2178 (1967).
(17) R. Zwanzig, *J. Chem. Phys.*, **38**, 2766 (1963).

Relative Stabilities of Bis(triphenylmethyl) Polysulfides

Richard D. Costa, John Tanaka, and David E. Wood*

Department of Chemistry, University of Connecticut, Storrs, Connecticut 06268 *(Received July 23, 1975)*

Publication costs assisted by the University of Connecticut Research Foundation

The relative stabilities of the bis(triphenylmethyl) di-, tri-, and tetrasulfides were studied by measuring their reactivity to oxygen at room temperature and measuring their thermal decomposition by EPR. About 25% of the disulfide in benzene solution was converted to the peroxide by reaction with air at room temperature for 8 h, whereas the tri- and tetrasulfides exhibited no reaction under these conditions. All of the polysulfides gave an EPR signal of the trityl radical when warmed in benzene solution. The temperatures of initial free radical appearance were 24, 75, and 66° for the di-, tri-, and tetrasulfides, respectively. Activation energies for the decomposition were also measured by EPR; they are 15, 80, and 30 kcal/mol for the di-, tri-, and tetrasulfides, respectively. The reason for this unusual order of stabilities is discussed.

Introduction

Although there is a report in the literature that bis(triphenylmethyl) disulfide in solution can react with oxygen to form bis(triphenylmethyl) peroxide,[1] no report exists with respect to the other bis(triphenylmethyl) polysulfides. The implication in Nakabayashi's paper[2] on the preparation of various bis(triphenylmethyl) polysulfides is that the higher sulfides are more stable than the disulfide. The only obvious way by which the disulfide might be predicted to be less stable than the higher polysulfides is a steric hindrance argument. There are other reasons, however, which might argue the reverse, namely, that the disulfide should be more stable than the higher polysulfides. The analogous bis(triphenylmethyl) peroxide is reasonably stable; furthermore, the strength of the S–S bond in polysulfides declines somewhat with length of the sulfur chain. The S–S bond dissociation energy in dimethyl disulfide is 67 kcal/mol[3] as compared to an average S–S bond energy of 36 kcal/mol for dimethyl tetrasulfide.[4] In the series of compounds, H_2S_2, H_2S_3, H_2S_4, H_2S_5, and H_2S_6 the average S–S bond dissociation energies in kcal/mol are 72, 64, 62, 62, and 62, respectively.[5]

In order to study the relative stabilities of the carbon–sulfur bond in bis(triphenylmethyl) polysulfides, the reactivities of the di-, tri-, and tetrasulfides were tested with respect to oxygen. The ease of thermal decomposition to form radicals was also studied using electron paramagnetic resonance.

Experimental Section

Bis(triphenylmethyl) Disulfide. The bis(triphenylmethyl) disulfide was prepared by condensation of triphenylmethylsulfenyl chloride with triphenylmethanethiol in a modification of the method described by Vorlander and Mittag.[6] A solution of approximately 4 g of triphenylmethanethiol dissolved in ~200 ml of hot 95% ethanol was placed in a large beaker and cooled to about 0° in an ice bath. A solution of 1.2 g of sodium hydroxide in 95% ethanol (25 ml) was then added. With further cooling and stirring, approximately 1 g of sulfuryl chloride was added to the solution. After the disulfide precipitate formed, it was filtered and washed successively with 95% ethanol and acetone. The bis(triphenylmethyl) disulfide melted with decomposition at 155–157° (lit. mp 155° dec). Purity was checked by thin-layer chromatography and infrared absorption.

Bis(triphenylmethyl) Trisulfide and Bis(triphenylmethyl) Tetrasulfide. Both compounds were obtained by the method of Nakabayashi.[2] The products were recrystallized several times from chloroform–methanol. Both compounds were light yellow crystals. The trisulfide melted at 146–147° (lit. mp 147–148°). The tetrasulfide melted at 147–149° (lit. mp 146–148°). Purity was checked by thin-layer chromatography and infrared spectroscopy.

Reaction of Bis(triphenylmethyl) Polysulfides with Oxygen. Approximately 0.5 g of bis(triphenylmethyl) disulfide was dissolved in 15 ml of dry benzene in a 50-ml two-necked flask equipped with a gas-inlet tube and vent. A stream of air was dried by passing it through a 45-cm column packed with silica gel. The air was then saturated with dry benzene and bubbled through the disulfide solution at room temperature. After about 2.5 h a small amount of white solid was noted on the sides of the reaction vessel. After about 5 h the solid was filtered, washed with CS_2, recrystallized from toluene, and dried under high vacuum. About 0.1 g of white crystals were obtained. The infrared spectrum (KBr) was identical with the Sadtler standard spectrum for bis(triphenylmethyl) peroxide. The crystals melted at 184–185° (lit. mp 185°). The tri- and tetrasulfides showed no reaction when treated similarly for 12 h.

EPR Spectra. EPR spectra were obtained with a Varian V-4502 100-kHz X-band spectrometer with 12-in. magnet and Fieldial MK II field regulation. Second-derivative presentation was used and the spectra were recorded on a Hewlett-Packard 15-in. X-Y recorder. Temperature was controlled by a Variar V-4547 cold gas apparatus and measured by means of a copper–constantan thermocouple.

The sample tubes consisted of thin-walled quartz tubing approximately 10 cm long and 4 mm in diameter which had been calibrated by volume per unit length. Known concentrations of about 10^{-2} M polysulfide in benzene were prepared on the vacuum line and the sample tubes were sealed off under vacuum.

In a typical procedure 4–6 mg of solid was weighed directly on a spatula and quantitatively transferred to the sample tube; then the spatula was reweighed and the sample weight was calculated by difference. The tube was then attached to the vacuum line and evacuated to a pressure of

about 10^{-6} mm. A small amount of dry benzene, which had been rendered free of dissolved oxygen by several successive deaerations, was then condensed in a ring just below the Pyrex-quartz graded seal. The liquid nitrogen level was lowered to the end of the tube and the benzene allowed to melt and flow down the sides of the tube, ensuring that any residual solid adhering to the inside of the constriction would be washed down. The tube was filled to the predetermined mark with benzene; then the liquid nitrogen level was raised to just below the 3mm constriction and the tube was sealed off and separated from the rest of the vessel. All samples were stored at −10° until just prior to use.

Threshold temperatures for radical formation were determined by placing the sample in the microwave cavity and slowly increasing the temperature while sweeping the magnetic field until a resonance signal was noted on the recorder.

Decomposition rates were obtained by placing a previously decomposed sample into the cavity and equilibrating the cavity and sample to the desired temperature. The signal was then optimized to include only the four center lines of the radical. A fresh sample was then placed in the cavity and the spectrum immediately recorded. A sweep width of 2.5 G was used with a sweep time of 2.5 min. This enabled the four lines of interest to be scanned at the rate of one complete scan per minute. Scanning was continued until the increase in radical concentration, as evidenced by the size of the signal, appeared to be negligible. The elapsed time to a reference line of each spectrum was recorded. Rates were determined at several different temperatures each for bis(triphenylmethyl) di-, tri-, and tetrasulfides.

Results and Discussion

The results obtained by Blicke[1] in forming bis(triphenylmethyl) peroxide by oxygenating a solution of bis(triphenylmethyl) disulfide in benzene solution were reproduced. However, under identical conditions only starting materials could be recovered from oxygenation of bis(triphenylmethyl) trisulfide or bis (triphenylmethyl) tetrasulfide for 12 h. This confirms the *qualitative* observations that the disulfide is less stable than the other polysulfides. The formation of peroxide from the bis(triphenylmethyl) disulfide leads one to expect that homolysis of the carbon–sulfur bond has occurred with the concomitant production of triphenylmethyl and triphenylmethyldisulfur radicals.

Samples of the polysulfides prepared as described in the Experimental Section readily yielded the EPR spectrum of triphenylmethyl radical.[7] Because of the possibility of radicals of the type $Ph_3CS\cdot$, $Ph_3CSS\cdot$, etc., a careful search was made for different radical species. The only radical which could be detected by EPR was the triphenylmethyl free radical. A sample taken directly from an EPR tube which had been heated for several hours at 38° showed TLC spots corresponding to unreacted disulfide and sulfur and a very dark spot which did not move from the origin (assumed to be trityl dimer). If the tube is kept sealed, radical signals are lost after several months at room temperature and cannot be generated even on heating. This apparently corresponds to the known acid- or base-catalyzed isomerization of trityl dimer.[8] These results indicate that sulfur–sulfur bond cleavage is insignificant with respect to carbon–sulfur bond cleavage. This is not surprising in that the dissociation energy of the sulfur–sulfur bonds in dimethyl and diethyl disulfides are only slightly less than the carbon–sulfur bond dissociation energies, and with *tert*-butyl disulfide the two bond dissociation energies become approximately the same.[3]

Threshold temperatures for radical formation were determined for each of the polysulfides. The threshold temperature was taken to be the lowest temperature at which the triphenylmethyl radical could be detected. For the di-, tri-, and tetrasulfides the observed threshold temperatures were 24, 75, and 66°, respectively. The low threshold temperature for radical formation observed for the disulfide explains the ease of peroxide formation on reaction with oxygen at room temperature. Presumably, the tri- and tetrasulfides would also form peroxides if reacted with oxygen at or above their respective threshold temperatures.

If the decomposition is assumed to occur according to the net reaction

$$RS_xR \xrightarrow{k} 2R\cdot + S_x \qquad (1)$$

and the trityl radicals exist in rapid equilibrium with their dimer[9]

$$R_2 \overset{C}{\rightleftharpoons} 2R\cdot \qquad (2)$$

then the relation of trityl radical concentration, [R·], to the rate constant, k, is

$$[R\cdot] = [C(RS_xR)_0(1 - \exp(-kt))]^{1/2} \qquad (3)$$

where $(RS_xR)_0$ is the initial concentration of polysulfide and $[R\cdot] \ll [R_2]$. The peak heights of the EPR signal are proportional to [R·] and they were observed to follow this type of rate expression (e.g., a rapid rise at first followed by a gradual increase to a limiting value). Linearization of the first part of the plot could be obtained by plotting the square of the EPR peak height vs. time as as can be seen mathematically by squaring eq 3 and expanding the exponential.

$$[R\cdot]^2/C(RS_xR)_0 = kt - k^2t^2/2 + k^3t^3/6 + \ldots \qquad (4)$$

The first term of this expansion is accurate for small kt. Typical values observed for k in this study were 10^{-3} to 10^{-4} s^{-1}. However, obtaining the value of k from either 3 or 4 requires the measurement of the absolute value of the free radical concentration and accurate knowledge of C at the various temperatures employed.[10] Since this is rather tedious and subject to large errors we used the following method which does not depend on absolute concentrations or the value of the equilibrium constant. Since the radical concentration is proportional to the square root of the amount of polysulfide decomposed, the half-life, $\tau_{1/2}$, of the reaction was determined by the time taken for the EPR signal to attain $0.5^{1/2}$ of its final value. The rate constant for the first-order reaction was then obtained from $k = 0.693/\tau_{1/2}$. Runs at several temperatures for each of the polysulfides thus yielded rate constants from which the activation energies for decomposition were obtained by use of the Arrhenius equation. The values are 15, 80, and 30 kcal/mol for the di-, tri-, and tetrasulfides, respectively. There are at least two major possible sources of error in this measurement: (a) the lag in attainment of thermal equilibrium in the sample can give an error in the effective starting time; (b) disproportionation of the trityl radicals or isomerization of the trityl dimers will give an error in the final free radical concentration, although this is only a problem at the higher temperatures. Although the size of these er-

rors is difficult to estimate, which makes the absolute values quoted uncertain, the relative magnitudes are certainly in the order shown.

A number of reasons can be put forth to explain why the disulfide should be at least as stable as the tri- and tetrasulfides. As noted in the Introduction, the average S–S dissociation energy decreases with increasing sulfur chain length in polysulfides. The steric repulsion between the triphenylmethyl groups in bis(triphenylmethyl) disulfide should not be an important factor in decreasing its stability in that bis(triphenylmethyl) peroxide, where oxygen has a smaller atomic radius than sulfur, is a reasonably stable compound. A cyclic transition state, possibly involving d orbitals, would be expected to occur more readily in the higher polysulfides, with the result of easier decomposition. However, if it is assumed that the energy of the products is greater than the energy of the reactants, then the energy as well as the geometry of the transition state can be assumed to resemble that of the products.[11] The energy and geometry of the triphenylmethyl radical is the same for all the polysulfide decompositions. The other product formed by a carbon–sulfur bond cleavage is the S_2, S_3, or S_4 species. Of these, S_2 is the most stable on the basis that, when S_8 is heated, S_2 is the species formed almost exclusively. Since the products trityl plus S_2 are more stable than the other products, trityl plus S_3 and trityl plus S_4, it is reasonable to expect the transition state going to trityl plus S_2 to be lower than for the others. This argument can then be extended to explain the greater instability of the tetrasulfide over the trisulfide. Since the S_4 formed in the decomposition is a "dimer" of two S_2 units, the reaction might be expected to exhibit a lower transition state energy than the trisulfide decomposition. The foregoing argument assumes that the rate-determining step is the cleavage of either one or both carbon–sulfur bonds, and if it is the former, then subsequent breaking of the remaining carbon–sulfur bond must be rapid since no EPR signals attributable to sulfur-containing radicals were observed.

References and Notes

(1) F. F. Blicke, *J. Am. Chem. Soc.*, **45**, 1965 (1923).
(2) T. Nakabayashi, J. Tsurugi, and T. Yabuta, *J. Org. Chem.*, **29**, 1236 (1964).
(3) H. Mackel, *Tetrahedron*, **19**, 1159 (1963).
(4) I. Kende, T. L. Pickering, and A. V. Tobiski, *J. Am. Chem. Soc.*, **87**, 5582 (1965).
(5) W. A. Pryor, "Mechanisms of Sulfur Reactions", McGraw-Hill, New York, N.Y., 1962, Chapter 3.
(6) D. Vorlander and E. Mittag, *Ber. Dtsch. Chem. Ges.*, **46**, 3453 (1913).
(7) H. S. Jarrett and G. J. Sloan, *J. Chem. Phys.*, **22**, 1783 (1954).
(8) R. D. Guthrie and G. R. Weisman, *J. Chem. Soc. D*, 1316 (1969).
(9) The equilibrium constant for the dissociation of trityl radical dimer in benzene at 23° is (2.92 ± 0.09) × 10^{-4} via EPR measurements: J. A. Weil, *Prepr. Pap. Int. Symp. Free Radicals*, **5**, 72-1-72-3 (1961).
(10) Recent spectrophotometric measurements have apparently settled the differences between various methods of obtaining the equilibrium constant for trityl radical and its dimer: K. S. Colle, P. S. Glaspie, and E. S. Lewis, *J. Chem. Soc., Chem. Commun.*, 266 (1975).
(11) G. S. Hammond, *J. Am. Chem. Soc.*, **77**, 334 (1955).

COMMUNICATIONS TO THE EDITOR

On the Correction Term for Interactions between Small Ions in the Interpretation of Activity Data in Polyelectrolyte–Simple Electrolyte Mixtures

Publication costs assisted by the Dalhousie Research Development Fund

Sir: The activity of the added simple electrolyte in polyelectrolyte–simple electrolyte mixtures is an important quantity for the understanding of polyion–small ion interactions, and for the description of the properties of small ions in biological fluids and in ion exchangers. Experimental results for the activity of the simple salt have been compared with semiempirical expressions such as the "additivity rule",[1-3] or with a theoretical "limiting law" derived by Manning.[4] When experimental activity data are compared with the additivity rule, the measured values and the predicted activities were made to conform in the limit of no polyelectrolyte in the solution.[3,5,6] In the case of the limiting laws a similar *empirical* correction, suggested by Manning,[4,7] has been applied.[8-11] Typically, this correction can be expressed as[8]

$$\ln \gamma_{\pm} = \ln \gamma_{\pm}^{PM} + \ln \gamma_{\pm}^{MM} \quad (1)$$

where $\gamma_{\pm}$, $\gamma_{\pm}^{PM}$, and $\gamma_{\pm}^{MM}$ denote respectively the mean molal activity coefficient of the added electrolyte, the contribution of the polyion–mobile ion interactions, and the contribution of the mobile ion–mobile ion interactions. Manning's limiting law only predicts $\gamma_{\pm}^{PM}$ because the work in charging the small ions is not considered in arriving at an expression for the free energy. It is the purpose of this communication to point out that the correction method given in eq 1, which leads to very satisfactory agreement of experimental data with the limiting law,[8-11] is also theoretically indicated by a comparison between Manning's limiting law and a result obtained for the total excess free energy obtained with a mode expansion method.[12-14]

It has been shown that both the cluster expansion method[15] and the mode expansion method[12] applied to polyelectrolyte solutions lead to an expression for the excess free energy of the form:[13,14,16]

$$F^{ex} = F_{PM}^{ex} + F_{MM}^{ex} \quad (2)$$

where F^{ex}, F_{PM}^{ex}, and F_{MM}^{ex} respectively represent the ex-

cess free energy of the solution due to all electrostatic interactions, the contribution of the polyion–mobile ion interactions, and the contribution of the mobile ion–mobile ion interactions. F_{PM}^{ex} is the polyion–mobile ion contribution which is well discussed by Manning,[4] leading to Manning's well-known limiting laws for solvent and solute activities and other thermodynamic properties. It consists mainly of two terms, one term is proportional to ln κ, where κ is the Debye–Hückel parameter

$$\kappa^2 = (4\pi e^2/\epsilon VkT) \sum_i n_i z_i^2 \quad (3)$$

(e is the elementary charge, ϵ the dielectric constant of the solvent, V the volume, k Boltzmann's constant, T the temperature, n_i the number of ions i in V, and z_i the valence of ion i), and the other term is the "condensation" term.[4,13,16] Using Anderson and Chandler's mode expansion method, eq 2 can be derived when the polymer concentration is low enough to neglect polymer–polymer interactions (a condition also required by Manning). This condition is also satisfied in the case of excess added electrolyte. Under these conditions and also assuming a rod model for the polyion F_{PM}^{ex} has been shown to be identical with Manning's result.[13] However, the mode expansion method also leads to an expression for the second term on the right-hand side of eq 2, F_{MM}^{ex}, given by[13]

$$-F_{MM}^{ex}/VkT = \kappa^3/12\pi + B_3^{(0)} + \ldots \quad (4)$$

The complete expressions for $B_3^{(0)}$ and higher terms are given in ref 13. The first term on the right-hand side of eq 4 is identical with the Debye–Hückel limiting law for mobile ions. $B_3^{(0)}$ and higher terms are correction terms for finite concentrations. The activity coefficient of ion i is given by

$$\ln \gamma_i = [\partial(F^{ex}/VkT)/\partial n_i]_{T,V,n_{j\neq i}}$$

Differentiation of (4) leads to (for the case of mono-monovalent added electrolyte)

$$\ln \gamma_\pm^{MM} = -\kappa e^2/(\epsilon kT) + C_3 + \ldots \quad (5)$$

where

$$C_3 = \partial B_3^{(0)}/\partial n_+ + \partial B_3^{(0)}/\partial n_-$$

Again, the first term on the right hand side of eq 5 is identical with the Debye–Hückel term for simple electrolytes, and the succeeding terms are identical with higher terms in the simple electrolyte case,[12,13] although here κ contains contributions from all mobile ions.

If we compare eq 1, 2, and 5, it is clear that the empirical correction to the limiting law, i.e., equating $\gamma_\pm^{MM}$ in eq 1 to the activity coefficient of the simple salt without added electrolyte, is justified by the mode expansion method result expressed in eq 5. Thus the mode expansion method yields an expression for the free energy contribution of the polyion–mobile ion interactions which is identical with Manning's limiting law, and gives an expression for the mobile ion–mobile ion interactions which justifies previous empirical corrections for these interactions. Equation 5 indicates that the correction term $\gamma_\pm^{MM}$ should be taken at the total mobile ion ionic strength rather than at the ionic strength of the added electrolyte only, however, in most systems studied so far this difference will be small.

Acknowledgments. We are grateful to the Killam Trust for the support of the first author (K.I.). This research is supported by the National Research Council of Canada.

References and Notes

(1) R. A. Mock and C. A. Marshall, *J. Polym. Sci.*, **13**, 563 (1954).
(2) M. Nagasawa, M. Izumi, and I. Kagawa, *J. Polym. Sci.*, **37**, 375 (1959).
(3) F. Oosawa, "Polyelectrolytes", Marcel Dekker, New York, N.Y., 1971.
(4) G. S. Manning, *J. Chem. Phys.*, **51**, 924 (1969).
(5) Z. Alexandrowicz, *J. Polym. Sci.*, **43**, 337 (1960).
(6) T. Ueda and Y. Kobatake, *J. Phys. Chem.*, **77**, 2995 (1973).
(7) G. S. Manning, "Polyelectrolytes", E. Selegny, Ed., D. Reidel, Dordrecht, 1974, p 9.
(8) J. D. Wells, *Biopolymers*, **12**, 223 (1973).
(9) J. D. Wells, *Proc. R. Soc. London, Ser. B*, **183**, 399 (1973).
(10) J. C. T. Kwak, *J. Phys. Chem.*, **77**, 2790 (1973).
(11) J. C. T. Kwak, M. C. O'Brien, and D. A. MacLean, *J. Phys. Chem.*, **79**, 2381 (1975).
(12) H. C. Andersen and D. Chandler, *J. Chem. Phys.*, **53**, 547 (1970).
(13) K. Iwasa, *J. Chem. Phys.*, **62**, 2967 (1975).
(14) K. Iwasa, *J. Chem. Phys.*, in press.
(15) J. E. Mayer, *J. Chem. Phys.*, **18**, 1426 (1950).
(16) G. S. Manning and B. H. Zimm, *J. Chem. Phys.*, **43**, 4750 (1963).

Department of Chemistry
Dalhousie University
Halifax, Nova Scotia, Canada B3H 4J3

Kunihiko Iwasa*
Jan C. T. Kwak

Received September 22, 1975

Inorganic Chemistry

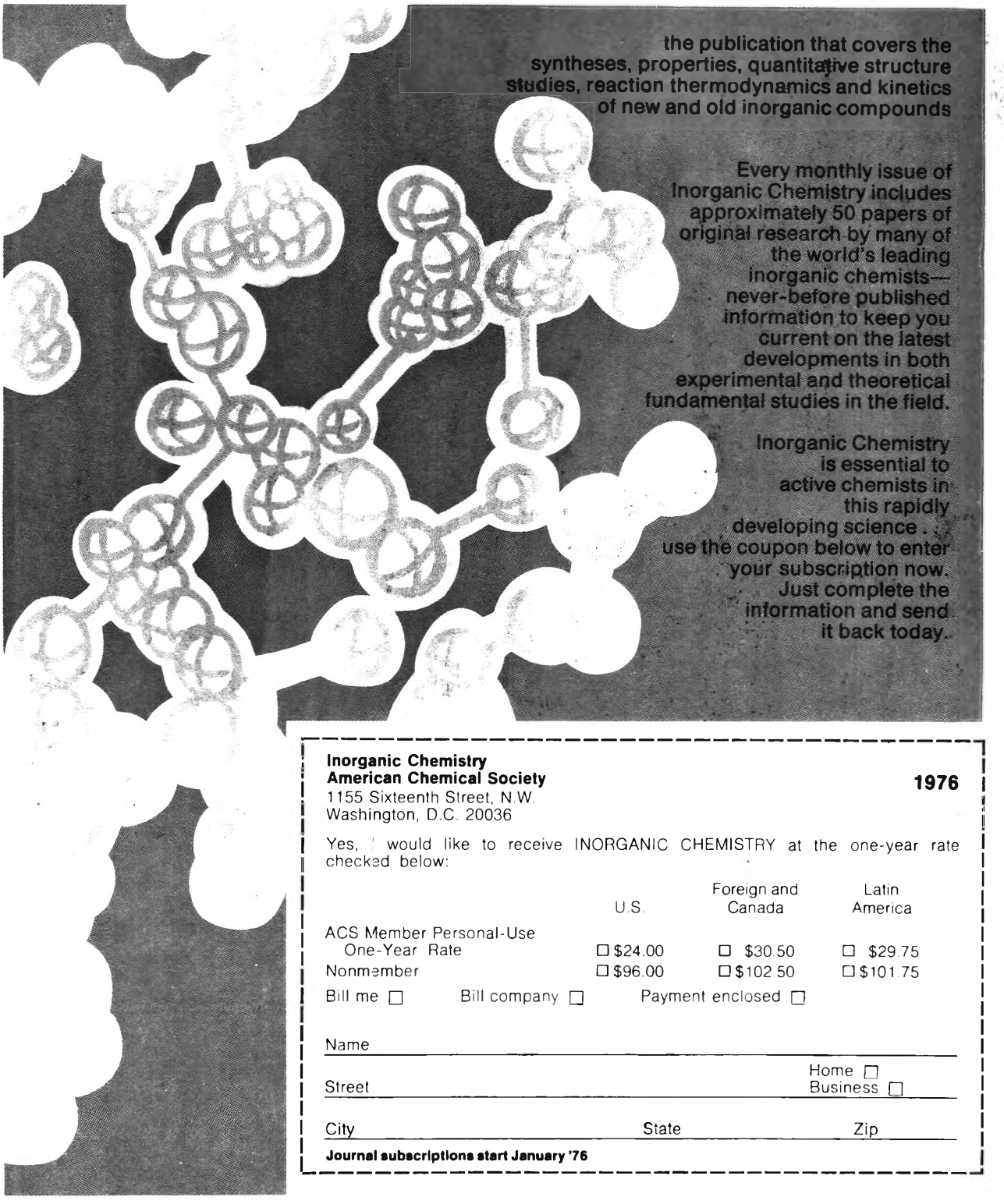

the publication that covers the syntheses, properties, quantitative structure studies, reaction thermodynamics and kinetics of new and old inorganic compounds

Every monthly issue of Inorganic Chemistry includes approximately 50 papers of original research by many of the world's leading inorganic chemists—never-before published information to keep you current on the latest developments in both experimental and theoretical fundamental studies in the field.

Inorganic Chemistry is essential to active chemists in this rapidly developing science . . . use the coupon below to enter your subscription now. Just complete the information and send it back today.

Inorganic Chemistry
American Chemical Society **1976**
1155 Sixteenth Street, N.W.
Washington, D.C. 20036

Yes, I would like to receive INORGANIC CHEMISTRY at the one-year rate checked below:

	U.S.	Foreign and Canada	Latin America
ACS Member Personal-Use One-Year Rate	☐ $24.00	☐ $30.50	☐ $29.75
Nonmember	☐ $96.00	☐ $102.50	☐ $101.75

Bill me ☐ Bill company ☐ Payment enclosed ☐

Name _____

Street _____ Home ☐ Business ☐

City _____ State _____ Zip _____

Journal subscriptions start January '76

COORDINATION POLYMERIZATION

A Memorial to Karl Ziegler

(Proceedings of the Symposium on Coordination Polymerization held at the American Chemical Society National Meeting, Los Angeles, California on April 3, 1974)

edited by JAMES C. W. CHIEN

CONTENTS: *G. Wilke*, Karl Ziegler, in Memoriam. *A. Zambelli*, A Few Considerations on Stereoregular Propylene Polymerization. *P. Pino, et al.*, Stereoselection and Stereoelection in α-Olefin Polymerization. *H. Schnecko, et al.*, The Number of Active Sites for the Polymerization of Ethylene, Propylene, and Butene-1 by Ziegler-Natta Catalyst. *Y U. Yermakov and V. A. Zakharov*, The Number of Propagation Centers in Solid Catalysts for Olifin Polymerization and Some Aspects of Mechanism of Their Action. *S. Fuji*, Ethylene Polymerization with the Catalysts of One and Two Component Systems Based on Titanium Trichloride Complex. *P. J. T. Tait*, A Kinetic Model for Heterogeneous Ziegler-Natta Polymerization. *F. S. Dyachkovskii*, Homogeneous Complex Catalysts of Olefin Polymerization. *D. G. H. Ballard*, Transition Metal Alkyl Polymerization Catalysts. *T. Keii*, Kinetic Approach to Elucidate the Mechanism of Ziegler-Natta Polymerization. *G. Henrici-Olivé and S. Olivé*, Chain Transfer in Ziegler Type Polymerization of Ethylene. *J. C. W. Chien and J. T. T. Hsieh*, Supported Ziegler-Natta Catalysts. *P. Teyssié, et al.*, Stereospecific Polymerization of Diolefins by h^3-Allylic Coordination Complexes.

1975, 304 pp., $16.00/£8.30

HIGH TEMPERATURE VAPORS

Science and Technology

by JOHN W. HASTIE

A Volume in the MATERIALS SCIENCE AND TECHNOLOGY Series

This book examines the basic aspects of important practical areas of application for the growing science of high temperature vapor phase chemistry, introducing the vapor phase to materials science and technology.

Major high temperature problem areas of application selected for discussion include chemical vapor transport and deposition, the vapor phase aspects of corrosion, combustion, and advanced energy systems. There is also a brief discussion of the utility of extraterrestrial high temperature species. A special chapter offers perhaps the first extended analysis of the high temperature chemistry aspects of combustion; the variety of combustion problems and applications deriving from the formation of high temperature inorganic species further exemplifies the practical utility of high temperature vapor phase chemistry.

1975, 498 pp., $35.00/£17.50

CHEMISORPTION AND MAGNETIZATION

by P. W. SELWOOD

Chemisorption and Magnetization is essentially a completely revised and updated edition of the author's 1962 publication, *Adsorption and Collective Paramagnetism*. Professor Selwood describes in detail the experimental techniques and interpretation of results involved in using magnetic measurements to gain information about chemisorbed molecules on certain kinds of solid surfaces. The method outlined here is applicable to ferromagnetic solids and especially to nickel metal; there is no restriction on the kind of adsorbate for which the method may be used. The book covers the literature to the end of 1974, and gives numerous applications to particle size determination.

1975, 192 pp., $19.50/£10.15

ANNUAL REPORTS ON NMR SPECTROSCOPY, Volume 6A

edited by E. F. MOONEY

NMR spectroscopy is used in all branches of science where precise structural determination is required or where the nature of interactions or reactions in solution is being studied. *Annual Reports on NMR Spectroscopy* familiarizes the specialist and non-specialist alike with new applications of the technique in all branches of chemistry, including biochemistry and pharmaceutics.

CONTENTS: *G. A. Webb*, Nuclear Magnetic Resonance Spectroscopy of Paramagnetic Species. *K. C. Ramey, et al.*, General Review of Nuclear Magnetic Resonance. *T. A. Crabb*, Nuclear Magnetic Resonance of Alkaloids. *D. F. Ewing*, Two-Bond Coupling between Protons anc Carbon-13.

1975, 510 pp., $40.00/£15.50

MOLECULAR ASSOCIATION, Volume 1

edited by R. FOSTER

Here is the first of a new series of volumes designed to keep pace with current developments in molecular association. This book provides up-to-date critical reviews of experimental and theoretical studies of those molecular interactions which are often loosely referred to as "complexes". The contributiors cover those reactions which are too weak to be described generally as involving the formation and breaking of classical chemical bonds.

CONTENTS: *Z. G. Soos and D. J. Klein*, Charge-Transfer in Solid State Complexes. *N. Kulevsky*, Dielectric Properties of Molecular Complexes in Solution. *K. M. C. Davis*, Solvent Effects on Charge-Transfer Complexes. *R. S. Davidson*, Photochemical Reactions Involving Charge-Transfer Complexes.

1975, 379 pp., $30.50/£11.80

N.B.: Postage plus 50¢ handling charge on all orders not accompanied by payment.
Prices subject to change without notice.

ACADEMIC PRESS

A Subsidiary of Harcourt Brace Jovanovich, Publishers
111 FIFTH AVENUE, NEW YORK, N.Y. 10003
24-28 OVAL ROAD, LONDON NW1 7DX